Hybridization of Electrical Resistance Tomography to Population Balance Model for Accurate Bubble Column Reactor Hydrodynamic Parameter Predictions

Olubode Caleb Adetunji

Thesis Presented for the Degree of

DOCTOR OF PHILOSOPHY

In the Department of Chemical Engineering

UNIVERSITY OF CAPE TOWN

MARCH 2016

Abstract

A novel approach of obtaining bubble size and spatial distribution is developed by hybridising techniques of Electrical Resistance Tomography and the Gas Disengagement Technique using a Population Balance as a framework. As a result, detailed hydrodynamic predictions suitable for Bubble Column Reactor (BCR) optimisation results with minimal computing effort.

Electrical Resistance Tomography (ERT) is a technique for creating 3D images of objects occurring in space. The images are obtained through current stimulations through a body surface electrodes and measurements of resulting voltage signals due to interior spatial conductivity field distribution. The use of ERT imaging method for hydrodynamic parameter predictions in a BCR has a benefit of yielding high temporal resolution but low spatial resolution. The low spatial resolution in electrical imaging accounts for underestimated or overestimated hydrodynamic parameter predictions similar to results obtained from the use of alternative techniques.

The population balance model (PBM) is a mathematical framework with which the spatial transport of properties of bubble population can be described. The PBM also allows for the description of the time-variant bubble population properties by a division of bubble population into size classes. Moreover, the PBM allows for the inclusion of models of bubble coalescence and breakage phenomena, which affect the distribution of bubble population properties during bubble swarming. The included source terms enable accurate modelling of the bubble evolution either in a steady or unsteady state fluid flow regime.

The objective of the present study is to develop an ERT interpretation technique yielding a high accuracy reconstruction of bubble population distribution through coupling ERT measurements to a PBM. It is hypothesized that a higher accuracy interpretation of ERT measurements will result from coupling ERT measurements to a PBM. The ERT technique has the capacity to image the steady and time-dependent gas void fractions in column sections as bubbles swarm and during dynamic gas disengagement (DGD). This ERT potential is explored in hybridizing ERT and a PBM in the present work.

The PBM was used to model a steady state 2-phase (air-water) fluid system operated in a semi-batch mode. The interactive fluid system was set-up in a Perspex cylindrical experimental BCR of height 1.545 m and diameter 0.29 m. The experiment was set-up to

measure hydrodynamic parameters in a BCR for varied superficial gas velocities ranging from 0.005 – 0.016 m/s on the interval of 0.001 to 0.01 m/s.

An essential bubble population property for the hydrodynamic predictions is the bubble number density distribution (BNDD) $n(v,z)$. The BNDD is defined such that $n(v,z)\Delta z\Delta v$ is the number of bubbles between axial position z and $z+dz$ having a volume between v and $v+dv$. The hybridization of the ERT measurements to a PBM followed these sequences of measurements and computations:

1) A calibration of the local static gas void fractions measured by the ERT method and the differential pressure method;

2) An analysis of the transient gas void fractions in the process of DGD to determine the bubble size distribution in the column;

3) A simulation of bubble swarming in the column by the PBM method using the boundary condition of results in step 2;

4) Solving a model of the process of DGD in the column using the initial condition of results obtained in step 3.

The first step in the sequences of computations is a validation of the usefulness of ERT method for the measurement of the local gas void fractions in the column. The second, third and fourth steps highlight measurements and computations required to determine the $n(v,z)$ by the ERT and PBM hybrid method during bubble evolution. The criteria in resolving the $n(v,z)$ were that the $n(v,z)$ satisfies a validated static and dynamic gas void fractions measured by the ERT method.

Having determined the $n(v,z)$ for varied superficial gas velocities within a range of experimental accuracy by the used equipment, the hydrodynamic parameters were predicted from the known $n(v,z)$. The predicted hydrodynamic parameters are the local gas void fractions, gas-liquid interfacial area, volumetric gas-liquid mass transfer rates, Sauter Mean Bubble Diameter and intensity of mixing depending superficial gas velocity. The predicted hydrodynamic parameters computed from the resolved $n(v,z)$ by the hybrid of ERT and PBM are consistent with findings in the literature, where alternative methods were utilized.

Thus, the inadequacies of the ERT method to measure hydrodynamic parameters useful for enhanced designing and scaling-up of BCRs have been addressed by the fusion ERT and a PBM.

Acknowledgements

It is with a deep sense of gratitude that I wish to recognise the input of my primary supervisor, Associate Professor Randhir Rawatlal, to this study. His conception of the idea, his suggestions and guidance as well as his criticism of my ideas in the course of this work are commendable. Indeed, you are endowed with capacity at training research scholars. Your kind gesture expressed by the provision of the bursary for this project from your research purse is appreciated.

I wish to thank Professor Andy Adler of the Dept. of System and Computer Engineering, Carleton University, my co-supervisor, for his generosity expressed in covering a part of the cost of my research visit to his laboratory at Carleton University, Ottawa, Canada. Prof. Adler's guidance and suggestions with regards to the development of the electrical resistance tomography (ERT) imaging algorithm cannot be overemphasised. I wish to also appreciate the great support of Associate Professor Aubrey Mainza, my co-supervisor at the University of Cape Town, for proof-reading my thesis.

The suggestions and assistance rendered by the following people in various capacities in the course of this study are worthy of recognition and commendation: Yasin Mamatjan, Post Doctoral Research Fellow and Peyman Rahmati at Carleton University, Granville de la Crus and staff members at the Mechanical Workshop Unit at University of Cape Town (UCT). The involvement of Bill Randall of the Electronic Workshop Unit, Dept. of Chemical Engineering, UCT, on this project in varied forms including facilitating the use of the ERT data acquisition hardware is appreciated.

Ultimately, I bless God for my parents for believing in the vision, regular encouragements and prayers through the entire study. You are great to have.

Contents

Table of Contents

List of Figures

List of Tables

Nomenclature

Roman symbols

a_b	Characteristic acceleration of deformation $[ms^{-2}]$
C	Concentration of a bubble class $[kgm^{-3}]$
u_b	Characteristic velocity of deformation $[ms^{-1}]$
t_b	time taken for a bubble to break-up $[s]$
F_e	Force acting on a bubble surface $[kgms^{-2}]$
u	Electric potential $[Volts]$
ξ	Electrical conductivity $[S/m]$
E	Electric field $[Volts/m]$
E_L	Liquid phase dispersion rate $[m^2s^{-1}]$
E_G	Gas phase dispersion rate $[m^2s^{-1}]$
I	Electric current $[Amperes]$
E_l	Electrode area $[m^2]$
Z_l	Electrode impedance [Ω]
V_l	Constant voltage on electrode $[Volts]$
V	Vector of voltage measurements $[Volts]$
$F(\xi)$	Non-linear forward operator $[Volts]$
I	Identity matrix
A_i	Area of a discrete finite element $[m^2]$
P	Pressure $[kgm^{-1}s^{-2}]$
h	Height of the column $[m]$
g	Acceleration due to gravity $[ms^{-2}]$

L_T and L_B The top and bottom positions of the pressure legs on the column $[m]$

W Weight of fluid phase $[kgms^{-2}]$

U Superficial gas velocity $[ms^{-1}]$

$U_{b\infty}$ Single bubble rise velocity $[ms^{-1}]$

$f(d_b)$ Volume fraction of bubbles with size between d_b and $d_b + dd_b$ $[m^3]$

L Height of section of a column $[m]$

H_L Liquid height $[m]$

t Time $[s]$

$d^l_{t_{min}}$ Mean bubble diameter size disengaging at certain time at section l of the column $[m]$

d_{32}^{ERT} Sauter Mean bubble diameter measured by the ERT technique $[m]$

n Bubble number density distribution $[m^{-3}]$

f_1 Probability of a particle being in a state $[unit]$

r Size of a bubble $[m]$

J Flux of mass of volume fraction of bubbles in a class flowing per unit area per unit time $[kgm^{-2}s^{-1}]$

Q Mass of volume fraction of gas bubbles in a reference class $[kg]$

K_L Volumetric liquid-phase mass transfer coefficient $[mS^{-1}]$

L_x Size of large energy containing eddies $[m]$

a Specific gas-liquid interfacial area $[m^{-1}]$

D_l Diffusivity of liquid $[m^2s^{-1}]$

v_l kinematic viscosity of liquid $[m^2s^{-1}]$

g Acceleration due to gravity $[ms^{-2}]$

D Diameter of the column $[m]$

d_{vs} Volume-surface mean bubble diameter $[m]$

t_m Mixing time of multiphase mixture $[s]$

V_R Dispersion volume $[m^3]$

k Wave number $[m^{-1}]$

γ_g Molar mass of gas phase $[kg/kmol]$

$\dot{n}$ Molar flux transferred out of the bubble $[kmol/(m^2 s)]$

$\dot{Q}$ Total molar flow rate of a bubble class $[kmol/s]$

R_j Reaction rates resulting in generation of bubble sizes $[kmol/(m^2 s)]$

u_o Gas velocity through the gas distributor orifices $[m/s]$

d_o Gas distributor orifice diameter $[m]$

Greek symbols

ξ Conductivity distribution in a domain $[s/m]$

ζ Particle state $[unit]$

∇ Spatial gradient operator $[1/m]$

σ Surface tension of water-air $[kgs^{-2}]$

ρ Density of fluid phase $[kgm^{-3}]$

∅ Intensity of mixing $[unit]$

ε_g Gas holdup fractions $[unit]$

$\varepsilon \; or \; e'$ Energy dissipation rates $[m^2 s^{-3}]$

Δ Differential operator

ρ_l Density of water $[kgm^{-3}]$

v_D Drift flux velocity $[m/s]$

μ_L Viscosity of liquid $[kgm^{-1}s^{-1}]$

μ'_n Expectation value of a variable to power n $[unit]$

μ_G Viscosity of gas $[kgm^{-1}s^{-1}]$

l Diameter of large vortices $[m]$

η kolmogorov micro scale of viscous dissipation $[m]$

Subscript

L or lig or sc Liquid

G or g Gas

a Aerated phase

DP Differential pressure transmitter reading

ERT Electrical resistance tomography

b Bubble

bs Small bubbles

bL Large bubbles

d Eddies of viscous dissipation

e Large energy containing eddies

gos Gas holdup fraction composing of small bubbles

goL Gas holdup fraction composing of large bubbles

x Cross sectional area of section of a column

L Cross sectional area of section of a column occupied by large bubbles

S Cross sectional area of section of a column occupied by small bubbles

T Tank

j Period of bubble disengagement

Δt Differential time-step

z Axial length of a column

m Mixture fluid phase

p Gas phase

Superscript

i Section of the column or electrode layer

DGD Dynamic gas disengagement

b Bubble

g Gas

$'$ Local property of parameters

$ERT - DGD$ Electrical resistance tomography measurements captured in the process of dynamic gas disengagement

$PBM - SS$ Population Balance Model data captured at steady state

$ERT - SS$ Electrical resistance tomography data captured at steady state

$M - DGD$ Data captured from a model of process of dynamic gas disengagement

ERT/PBM Hybrid of ERT and a PBM data

Subscript

C Reactor column

i Electrode layer plane or column section

j Bubble size class

Chapter 1: Introduction

1.1. Motivation and aims of study

The relevance of applications of Electrical Resistance Tomography (ERT) to chemical industries is related to its capacity to measure the presence of a substance in 2D or 3D in pipes and vessels. The ERT imaging of the substances is usually obtained at a low capital cost rate, in a non-radioactive, simple and non-invasive manner. Conductivity measurements can in principle be interpreted to yield the concentration and even temperature across a vessel. However, a transferral of its use in chemical process systems from the research environment to real-life process monitoring has been slow owing to lack of fidelity in the reconstructed images. The reconstructed images are expected to describe the spatial distribution of conductivity contrasting of the multiphase components within pipes and vessels. The low spatial resolution is a major contributing factor to limited applications of the technique in chemical industry.

To address the challenges of ERT applications to chemical process systems, ERT data capturing sequences or advanced reconstruction algorithms are often developed and implemented. To date, there is a lack of adequate measurement or reconstruction technique which allows for robust applications of ERT measurements to multiphase chemical process systems.

However, it is possible to interpret the low spatial resolution of ERT images but adequate for gas holdup measurements to determine the mean bubble rise velocity. The possibility is based on a finding in literature that shows a relationship between volume to surface mean bubble diameter and arithmetic mean of bubble rise velocity in the form

$$0.59\frac{\overline{U_b}^2}{g} = 0.59\frac{\left(v_D/\bar{\varepsilon_g}\right)^2}{g} = d_{vs} \qquad (1.1)$$

The expression of Eq.(1.1) indicates that the arithmetic mean bubble rise velocity, $\overline{U_b}$, equals the ratio of the drift flux of gas, v_D, to the cross-sectional averaged gas holdup, $\bar{\varepsilon_g}$ (Fukuma, et al., 1987). This finding suggests that the ERT capability to measure gas void fractions at high temporal resolution could be explored for determining bubble properties that depend

on the bubble rise velocity. The knowledge of the bubble rise velocity is essential in calculating the hydrodynamic parameters in a bubble column reactor (BCR).

Furthermore, the ERT imaging technique produces images with high temporal resolution while the solution of a PBM yields a high spatial resolution of constituent substances in a multiphase reactor system. Thus a hybridization of ERT and PBM is envisaged for an enhanced interpretation of ERT measurements. A hybrid of ERT and PBM that yields images with high temporal and high spatial resolution is envisioned for useful accurate prediction of bubble column hydrodynamic parameters.

It is also anticipated that a hybrid model of ERT with a PBM will allow more accurate measurements of the spatial distribution of bubble size, bubble number densities and gas holdup parameters. These results will be further analysed to estimate the overall mass transfer, total gas-liquid interfacial area and total reaction rates in a BCR compared with using ERT measurements only.

This novel high accuracy interpretation of ERT measurement will lead to the direct benefit of expanding the spectrum of applications of ERT techniques in chemical industries. Typical targeted chemical processes are crystallization processes, packed beds processes and fluidized beds processes which are inherently multiphase and complex hydrodynamic processes. In addition, the novel interpretation approach will ensure an accelerated pace in the transferral of ERT techniques from the research environment to a real-life application on a commercial basis.

Many multiphase reactions are set-up in a BCR for cost effectiveness due to the low energy requirement, lack of moving parts and low capital cost of maintenance. A developed low-cost ERT and PBM hybrid technique that enables bubble population parameter measurements will contribute to the applications of the ERT technique in multiphase process systems. A coupling of the ERT to PBM will also contribute to a novel approach for prediction of useful parameters for describing the performance of bubble columns.

1.2. Basic principle of tomography

In the field of imaging, production of tomography images of an object refers to imaging sections of the object through the use of any form of a penetrating wave as in Figure 1.1. Allan Cormack at the Department of Physics, at the University of Cape Town in early 1950 (Wikipedia, 2014) developed the theoretical underpinning of X-ray computed tomography (CT). The CT produces tomography images from X-ray images of a specific area of an object allowing the interior of an object to be viewed. With a view to taking Allan Cormack's invention into a real application, Godfrey Hounsfield in 1971 (Wells, 2005) built the first CT scanner and found Cormack's theoretical calculations valid. Allan Cormack and Godfrey Hounsfield's independent efforts in the invention of CT were rewarded with the award of Nobel Prize in Physiology or Medicine in 1979 (Wikipedia, 2014). The tomography method has been found useful in Radiology, Archaeology, Biology, Atmospheric Science, Geophysics, Oceanography, Plasma Physics, Materials Science, Astrophysics, Quantum Information, and other sciences since its invention (Wikipedia, 2014).

In ERT, the penetrating wave is a diffuse electric field and its perturbation is interpreted by an ERT algorithm to create images for the monitoring or visualization of the interior objects (e.g. vessels or reactors).

Figure 1.1. Basic principle of tomography : superposition free tomographic cross sections S1 and S2 compared with the projected image P.

Imaging the constituent interior materials of a body using the ERT technique requires current stimulation and measurements of voltage signals through periphery electrode rings due to the interior medium conductivity. Image creation by the ERT technique requires solving a mathematical problem classified into forward and inverse "problems".

The forward problem entails modelling the sensed voltage signals on the boundary electrodes due to a sequence of current stimulation for a known simulated interior

conductivity distribution. In the inverse problem, the actual conductivity distribution is sought from an iterative algorithm that optimizes the simulated voltage with the measured voltage given the same current stimulation scheme.

X-Ray CT is generated from X-Ray images, which are produced by passing a collimated beam of radiation through an object in a straight line and measuring the attenuation of the beam. The attenuation of the beam is affected by matter that lies along its path. The X-Ray images are then created from the measured attenuation coefficient of the collimated beam of radiation. The X-Ray CT is local and yields high spatial resolution because the opaqueness or density of pixels or voxels of created images affects only some of the attenuation measurements. Notably, the collimated beams of radiation (signal) have high frequency and high energy with a limited occurrence of scattering. When a low-frequency signal is propagated through an object, the phenomenon of signal scattering need be taken to account in addition to the signal attenuation by matter along its path (Lionheart, et al., 2004).

The ERT imaging method requires passing a low frequency direct or alternating current through a conductive object medium and measurement of voltage owing to the changes in the conductivity of the object medium. The low-frequency current bombarding the object medium makes a change in the conductivity of the object medium to have some effects on any measurement captured at the object surface. The distortion in any surface measurement by a change in the conductivity of the object medium makes ERT non-local and yielded low spatial resolution images (Lionheart, et al., 2004). ERT is therefore also known as a “soft field” tomography technique because an electric current propagates diffusely in the body in the form of electric field as depicted in Figure 1.2. (Tao, et al., 2008).

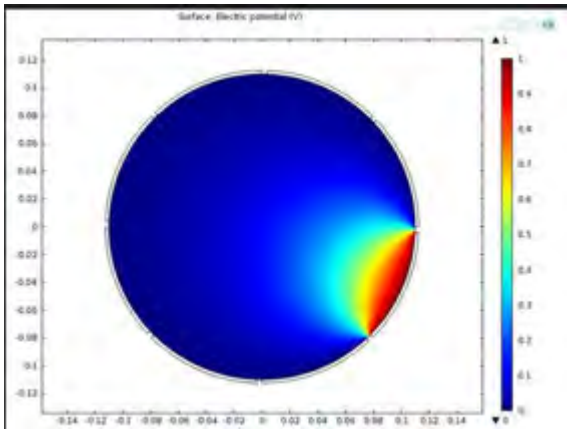

Figure 1.2. A 2D cross-section of the surface of the electric field distribution generated by a pair of electrodes on a ring of 8 electrodes during ERT data measurements.

An illustration of equipment required for ERT data capturing is presented in Figure 1.3. The data acquisition system interfaces between the personal computer and the layers of electrodes. It houses the multiplexing module hardware for multiple rings data measurements. It loads the measurement sequences table for current injection and voltage measurement through periphery electrodes on the body and returns measured voltage data to the PC for image reconstruction. The PC hardware stores a C++ programme that controls the voltage data measurements and ERT imaging software for either 2D or 3D output. Preference for the use of a non-conducting body within which a 2 or 3-phase dispersion process is set-up is often suggested as shown in Figure 1.4 and Figure 1.5. The use of a conducting body (metal pipes or tank) or vessel will require the electrical insulation of the body electrodes.

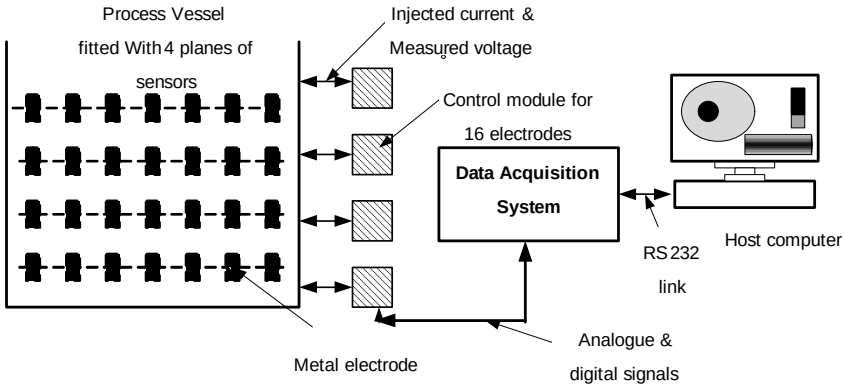

Figure 1.3. The components of electrical resistance tomography equipment.

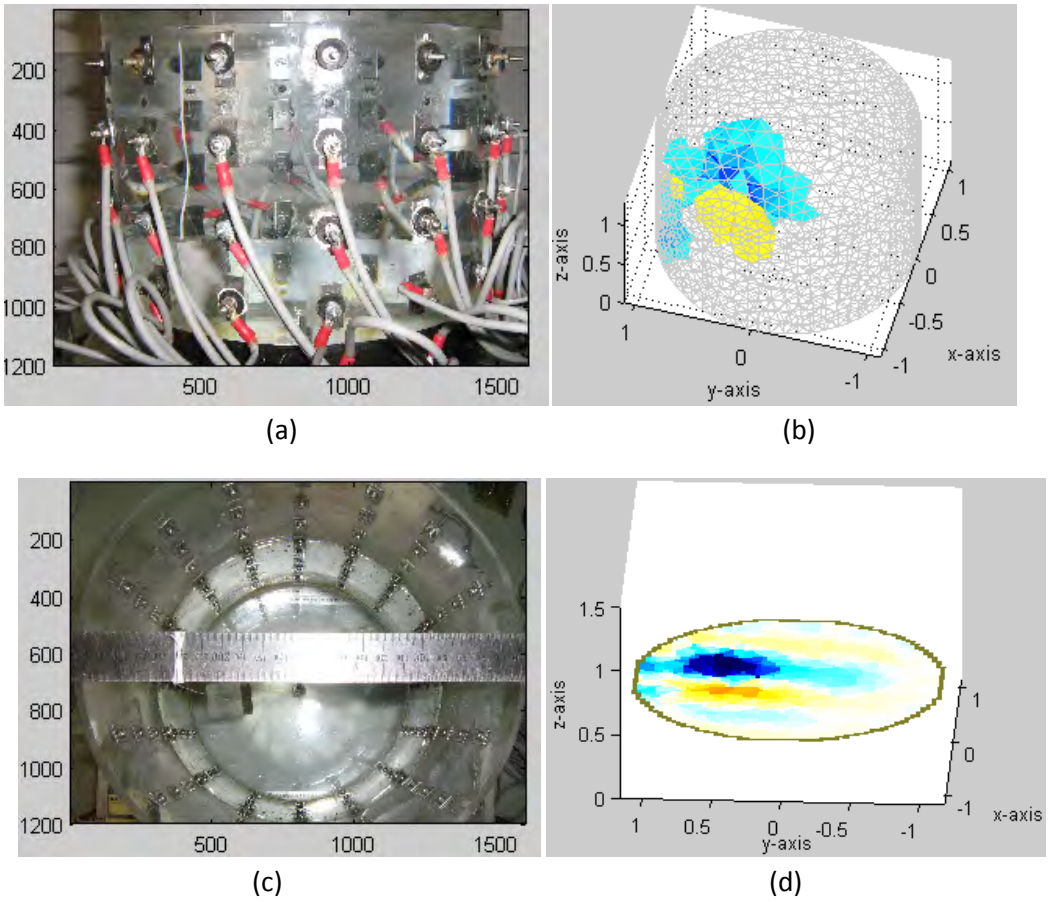

Figure 1.4. An ERT rig containing a suspended cuboid solid object in a saline solution of conductivity 0.2 S/m orientated as follows: a) Front view of the ERT rig; b) ERT 3D image of the object; c) Plan view of ERT rig; d) A 2D slice of the object's image.

1.3. Bubble column reactor (BCR) operations

In the field of chemical engineering, BCRs are important multiphase contactors. These are cylindrical vessels with a gas distributor at the bottom (Figure 1.5). The gas is sparged in the form of bubbles into either a liquid phase or a liquid-solid suspension. Much preference is given to BCRs both in design and operation over other reactors because excellent interfacial multiphase mixing at high heat and mass transfer rates are achievable. Furthermore, BCRs are often used since they require little maintenance and low operating costs due to lack of moving parts and their compactness (Kantarci, et al., 2005).

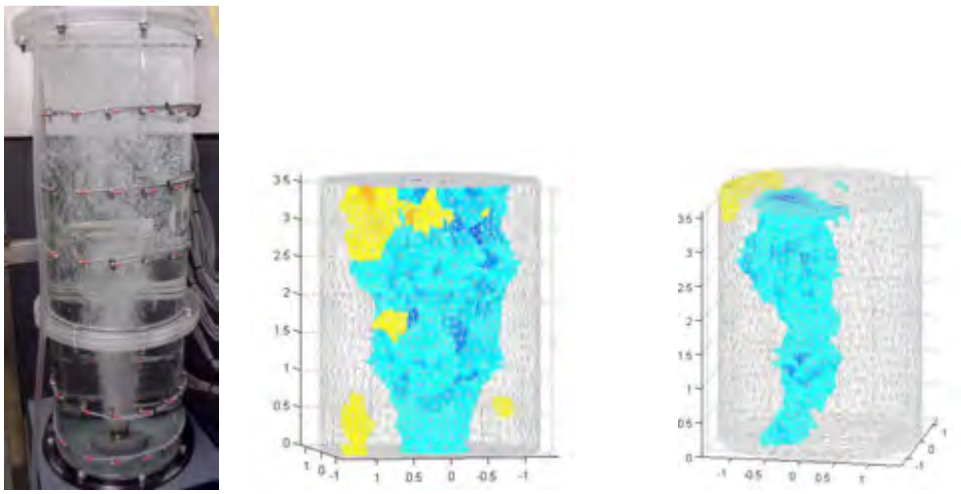

(a) (b) (c)

Figure 1.5. Air dispersion in a BCR (as in a) during operation and its ERT 3D images using Gauss-Newton algorithm with Tikhonov regularization (as in b); using Gauss-Newton algorithm with image element and data frame correlation for regularization (as in c).

An increase in production and optimal performance of BCR for biochemical processes and biological wastewater treatment could be achieved through the use of a scaled-up or an upgraded BCR. For example, processes such as oxidation, chlorination, alkylation, polymerization and hydrogenation are known to be mass-produced at a cost-effective rate when the reaction systems are set-up in an upgraded BCR. The BCR maintains the durability of catalyst or other packing materials when a catalytic process is a set-up in it. The possibility of online adding or withdrawing of catalyst to processes in BCRs and their operation capability in a plug-free mode make BCRs the multiphase contactor of choice.

A study on gas holdup by (Luo, et al., 1999) and (Veera, et al., 2004) as well as bubble characterization studies by (Prakash, et al., 2001) and (Essadki, et al., 1997) highlight these

BCRs operation parameters as requirements for proper BCR design and scale-up. In addition, a mass transfer study is also important as indicated in the work of (Behkish, et al., 2002) and (Vandu & Krishna, 2004).

Furthermore, the design and scale-up of a BCR are dependent on accurate estimation of heat and mass transfer characteristics, mixing characteristics and chemical kinetics of the reacting system. These parameters are in turn functions of an accurately determined total interfacial area in a multiphase gas-liquid system. Accordingly, a technique that could enable accurate computation of the total interfacial area would promote effective designing of a BCR for cost effective production purposes. While there are chemical reaction techniques for the measurement of a total interfacial area in a mixture system, the uncertainty in the accuracy of the reported values are high.

1.4. Essence of population balance model (PBM) in the accurate prediction of BCR hydrodynamic parameters

The population balance model (PBM) allows the description of the changes in properties of countable entities in space and time under the influence of governing phenomena. The PBM accounts for the interaction of the countable entities during their transport or diffusion in a BCR. In the present study, the countable entities of interest are the bubble size classes having a distribution of bubble number density that change as bubble population swarm axially in a BCR. The changes in the bubble number density distribution (BNDD) are due to phenomena of bubble coalescence and breakup.

The PBM is an unsteady state partial differential equation that describes the time-varying spatial transport of countable entities (BNDDs) on the account of bubble coalescence and breakage phenomena. In this case, the bubble coalescence and breakage phenomena are the PBM source term model. The solution of the steady or unsteady state PBM will yield a distribution of which the change in BNDD in space only or in space and time respectively could be determined. Moreover, when the radial variation of the BNDD as bubble swarm axially is insignificant, a PBM in 1D space could describe the changes in the BNDD along the column axial direction.

The BNDD is the product of the total number of bubbles in the gas phase and the probability density distribution of bubble population belonging to the predetermined bubble size

classes. Since hydrodynamic parameter predictions depend on BNDD, accurate determination of local and global BNDD will allow for accurate prediction of column hydrodynamic parameters. These are the gas-liquid interfacial area available for gas-liquid reactions, volumetric gas-liquid or liquid-gas mass transfer rates and the degree of multiphase mixing locally or globally.

The application of ERT for the measurement of gas holdup has been validated. However, its use for the measurement of the total interfacial area in a 2 or 3-phases system has been hindered by the low spatial resolution of ERT reconstruction. Through a simulation approach, gas holdup and total interfacial area of a 2 or 3-phases system in a BCR could not be determined singularly by the PBM. Therefore, it is anticipated that ERT fused with a PBM will yield the total interfacial area estimate at a low capital cost and in a non-invasive manner. This will be a contribution to a new method of hydrodynamic parameter predictions from this work.

1.5. Advantages of the use of ERT to determine hydrodynamic parameters in a BCR

ERT is a high temporal imaging technique applicable to imaging objects in the interior of a BCR based on conductivity distribution changes either during an online bubble evolution or in the process of dynamic gas disengagement (DGD). The DGD process is observed after the gas inlet into either an initially steady state or unsteady state fluid flow system is turned off. ERT has been used to study homogeneous and heterogeneous flow regime in a BCR in order to investigate the effect of increasing superficial gas velocity on gas void fraction locally and globally.

The ERT technique yielded results of increasing gas void fraction with an increase in superficial gas velocity in the column. The results were validated using the differential pressure (DP) measurement technique. ERT has a high temporal resolution allowing accurate measurements of the time-dependent changes in gas void fraction locally or globally during DGD process. The measured changes in the gas void fraction by the ERT technique in the process of DGD could be interpreted to determine BNDD of bubble size classes in a BCR. However, ERT's low spatial resolution has rendered the technique to be inadequate to measure other BCR hydrodynamic parameters. Notably, the gas dispersion process leading

to bubble swarming events in a BCR could either take place at a steady state or unsteady state.

1.6. Benefits of hydrodynamic parameter predictions in a BCR

Multiphase reactors are often used in chemical, petrochemical and biochemical industries both at commercial scale and pilot scale to set-up multiphase reactions. Multiphase reactors can typically be categorised into two groups: Fixed beds and slurry phase reactors, and Slurry bubble column reactors (SBCRs) and stirred tank reactors (STR). Fixed bed or packed bed columns are characterised by the stationary solid phase. In trickle bed columns, the gas and liquid flow downwards through a packed catalyst. A slurry BCR (SBCR) is characterised with fine solid phase catalyst particles suspended in a liquid phase by gaseous phase dispersion into a column through a gas sparger. The SBCRs are gaining many applications in industries over the fixed bed reactors for the following competitive benefits: 1) higher product yield due to efficient reaction rate per unit volume; 2) enhanced temperature control, higher gas holdup and mass transfer rates.

Examples of multiphase reactions often carried out at commercial scales include the production of cyclohexanol / cyclohexanone from cyclohexane by chemical companies, benzoic acid / benzaldehyde from toluene, production of styrene via MBA, oxidation of propylene, Fischer-Tropsch synthesis, hydro-cracking and hydro-isomerisation processes (Behkish, 2004). Improved designing of a BCR and its scaling up are important subjects that affect multiphase reactions in terms of cost of processes, product yield with time and energy consumption. In order to effectively scale-up a BCR, sufficient knowledge of the kinetics of the processes, its hydrodynamic parameters as well as mass transfer characteristics must be known. More importantly, adequate design and scale-up of industrial reactors that ensure high space-time yields require information on the hydrodynamic parameters, mass and heat transfer coefficients. Such information is useful for the determination of the pressure, gas throughput, reactor diameter and slurry concentration needed.

Chapter 2: Literature review

A review of literature is presented in section 2.1 to give an account of the mathematical development of ERT forward and inverse problems. Section 2.2 highlights previous attempts to develop an ERT algorithm that yields high spatial resolution in addition to its inherent high temporal resolution. Given the most efficient ERT algorithm developed till date, a review of literature in section 2.3, section 2.4 and section 2.5 enumerate applications of the ERT algorithms in industries, in Medicine and Geophysics and in Biomedical research respectively.

The findings on the experimental and modelling approaches to quantify hydrodynamic parameters in a BCR for its scale-up and enhanced designing are reviewed in section 2.6. Since the hydrodynamic parameter measurements by experimental approaches or from empirical correlations yield an over-estimate or under-estimate values, the PBM is envisaged to yield accurate results. This is envisaged owing to the reported development of the PBM in literature that indicates the path to bubble coalescence and breakage rate models were considered as in section 2.8. In sections 2.9 and 2.10, the derivation of the PBM and the development of its source terms models (i.e. bubble coalescence and breakage rate models) are reviewed respectively. Notably, publications that are relevant to the core scope of this study only have been reviewed.

2.1. Mathematical description of ERT forward and inverse problems

The applications of the ERT technique to image the constituents in a body is based on changes in the electrical conductivity (or resistivity) distribution of the space within the interior. The ERT technique yields a scan of the constituent substances within a body owing to disturbance of a homogeneous conductive medium by the constituent substances. Usually, in order to obtain an ERT image of the substances within a body, a small amplitude current signal is driven through pairs of periphery electrode to generate periphery electrical potential difference due to the conductivity distribution in the body interior. The act of current injection through electrode pairs and measurement of voltage signals on the

electrode system caused by the interior conductivity distribution can be predicted by the Gauss's law in electromagnetism.

The ERT forward problem is modelled using the Poisson's equation of the form of Eq.(2.1). It is derived from the integral form of the Divergence Theorem that describes the Gauss's law in an integral form when applied to the electric vector field as in Eq.(2.2). The physical meaning of Eq.(2.2) is that the outward flux of an electric field through a closed surface is equal to the volume integral of the divergence of the electric field over the region inside the surface.

$$\nabla \cdot (-\varepsilon \nabla \emptyset) = \rho \tag{2.1}$$

$$\iiint_V (\nabla \cdot E) dV = \oiint_S (E \cdot n) ds \tag{2.2}$$

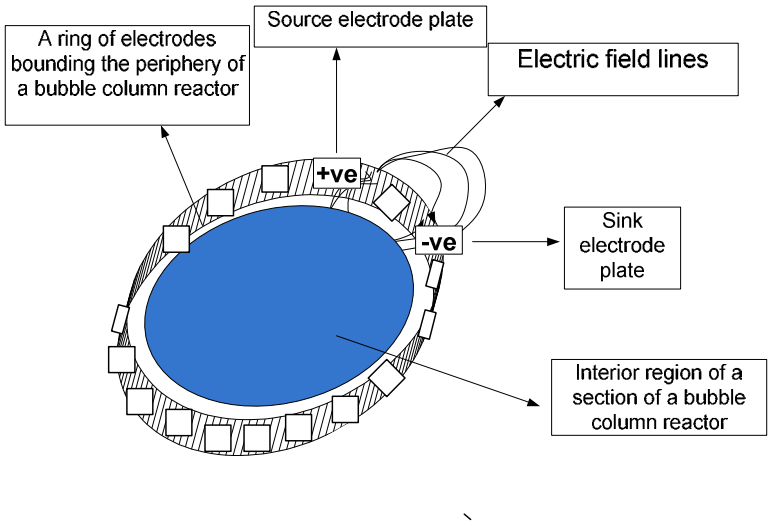

Figure 2.1. Diagrammatical illustration of a stimulation of small amplitude of current (mA) through ring of electrode plates on the periphery of a BCR.

By the diagrammatic illustration of Figure 2.1, Eq.(2.1) relates the flow of charge density (current $I[Ampere]$) on the periphery electrode pairs to the periphery electric potential $\emptyset[Volts]$ owing to the interior conductivity distribution $\varepsilon\,[Sm^{-1}]$. At the boundary of a column section between electrode plates, Eq.(2.1) will take the form of Eq.(2.3) while on the periphery electrode plates, Eq.(2.1) will be of the form Eq.(2.4).

$$\nabla \cdot (-\varepsilon \nabla \emptyset) = 0 \tag{2.3}$$

$$\nabla \cdot (-\varepsilon \nabla \emptyset) = I \tag{2.4}$$

The ERT inverse problem could be modelled using the Newton Raphson's algorithm (Eq.(2.5)) with an included Tikhonov regularization parameter that results in the Levenberg - Marquadt algorithm of Eq.(2.7).

$$f(\xi) = {}^{1}/_{2}\,(F(\xi) - V)^{*}\,(F(\xi) - V) = {}^{1}/_{2}\,\|F(\xi) - V\|_{2}^{2} \tag{2.5}$$

$$h_{LM} = (F'(\xi)^{*}F'(\xi) + \lambda I)^{-1}\,F'(\xi)^{*}\big(V - F(\xi)\big) \tag{2.6}$$

$$\xi_{k+1} = \xi_{k} + h_{LM} \tag{2.7}$$

The Newton Raphson's algorithm has been applied to a number of industrial research works that were set-up in a bubble column reactor owing to its low capital cost, its portability, non-invasiveness and its high temporal resolution.

The described mathematical formulation of the ERT forward and inverse problems will be solved in this work by the finite element method (FEM) using electrical impedance and diffuse optical reconstruction software (EIDORS). EIDORS is an open source software coded in MATLAB and Octave that will be utilized for imaging the dispersion.

2.2. Progression in the development of ERT imaging algorithms

The progression of the ERT algorithm development begins with an understanding that images of objects are created by optimising an actual measured voltage and a model voltage signals taken on the boundary of a body. While actual voltage signals are captured on the periphery of a body, the model voltage is calculated by the method of finite element method (FEM). The computation of the model voltage signal is the required data from the solution of ERT forward problem. In the forward problem, the sensed voltage signal on the surface of a column is sought given the interior conductivity distribution and known current stimulation signals.

The model voltage sensed on the surface of the reactor by the FEM is based on the Poisson's equation. The Poisson's equation relates the divergence of the gradient of the electric potential at a point in a static electric field to the charge density that generates the electric field. The derivation of the Poisson's equation is presented in section 2.2.1.

2.2.1. Physics of ERT forward problem

The ERT forward problem could be solved through an analysis of the physical law governing electrical potential, conductivity distribution and charge density in a body system. The relationship among these quantities is provided for by the Poisson's equation. The derivation of the Poisson's equation used for modelling the ERT forward problem is as follows.

According to Carl Friedrich Gauss (Gauss, 1965), the net electric flux through a closed surface is equal to $1/\varepsilon$ times the net electric charge enclosed within the closed surface as in Eq.(2.8)

$$\emptyset_E = \frac{Q}{\varepsilon} \tag{2.8}$$

In Eq.(2.8) , $\emptyset_E$ is the electric flux $[Nm^2C^{-1}]$ through a closed surface S enclosing any volume V $[m^3]$; Q is the total charge $[C]$ enclosed within the surface; and ε is electric constant $[C^2N^{-1}m^{-2}]$ that equals electrical conductivity in a conductive medium. The net electric flux $\emptyset_E$ through a closed surface S is also the surface integral of the electric field as in Eq.(2.9) , where $E$is the electric field $[Vm^{-1}]$and dA $[m^2]$ is the vector of an infinitesimal element area.

$$\emptyset_E = \oiint_S E \cdot dA \tag{2.9}$$

Since the flow of electric field (electric flux) is defined as an integral of the electric field, Eq.(2.9) is referred to as the integral forms of Gauss's Law. By Gauss's Law, the distribution of electric charge can be found if the electric field is known everywhere within a body. Conversely, if the distribution of charge is known, Gauss's Law can be used to compute the electric field provided that the electric field passes through the surface in a uniform way. This requirement that the electric field passes through the surface in a uniform way is to ensure a symmetric electric field such that if the total flux is known, the electric field can be deduced at every point. Eq.(2.9) can, therefore, be interpreted to mean the charge in any given region can be deduced by integrating the electric field to find the flow of the electric field.

2.2.2. Divergence theorem

The flux of a vector field through a surface to the variation of the vector field inside the surface is related by the Divergence Theorem (Halliday & Resnick, 1970). The Divergence Theorem describes the Gauss's Law in an integral form when applied to electric vector field as in Eq.(2.10) . The physical meaning of Eq.(2.10) is that the outward flux of an electric field through a closed surface is equal to the volume integral of the divergence of the electric field over the region inside the surface. The Divergence Theorem is related mathematically by Eq.(2.10) where the left-hand side stands for the total of the sources of the electric field in volume V, while the right-hand side means the total flow of electric field across the boundary ∂V.

$$\iiint_V (\nabla \cdot E) dV = \oiint_S (E \cdot n) ds \tag{2.10}$$

From Eq.(2.10) , Since electric field, E, can be related through the Coulomb's Law as in Eq.(2.11) ,

$$E = \frac{Q}{A\varepsilon_o} \tag{2.11}$$

where A is the surface area covered by the unit vector pointing from the particle with charge Q to the electric field evaluation point and ε_o is electric constant. Evaluating the integrands in Eq.(2.10) , we obtain

$$(\nabla \cdot E)V = \frac{QA}{A\varepsilon_o};\ \nabla \cdot E = \frac{Q}{V\varepsilon_o} = \frac{\rho}{\varepsilon_o} \tag{2.12}$$

The electric potential $\emptyset$ at a point r in a static electric field E is given by the line integral of the form

$$\Delta\emptyset = -\int_c E \cdot dl \tag{2.13}$$

When Eq.(2.13) is differentiated

$$\nabla\emptyset = -E; E = -\nabla\emptyset \tag{2.14}$$

Substituting Eq.(2.14) into Eq.(2.12) ,

$$\nabla \cdot (-\nabla\emptyset) = \frac{\rho}{\varepsilon_o} \tag{2.15}$$

When the electric constant ε_o is a function that varies with the spatial variable of the domain, Eq.(2.15) is of the form of Eq.(2.16) , which is referred to as the Poisson's equation.

$$\nabla \cdot (-\varepsilon \nabla \emptyset) = \rho \qquad (2.16)$$

The technique of addressing the ERT forward problem described by the Poisson's equation using FEM is described in the following sections. The solution of the forward problem which is required for solving the inverse problem is also based on FEM analysis.

2.2.3. Gauss-Newton algorithm (forward and inverse solver)

The ERT forward and inverse problem are usually solved using FEM analysis. In order to use the FEM approach, a target section of the column will be discretised to either a piecewise smooth tetrahedral elements (imaging in 3D) or a piecewise smooth triangular elements (imaging in 2D) (Adler, et al., 2008). Conductivity distribution in the interior of a column section is achieved by assigning conductivity values on all discrete elements that span the discretised section of the column. The conductivity distribution will then be in the form of vector $\sigma \in R^{n_N}$, where R denotes a real number.

The act of imaging objects in the column using the ERT method could be achieved either using an absolute or a difference ERT algorithm. In the case of an absolute ERT algorithm, the voltage signal due to the heterogeneous conductivity distribution is required, while the difference algorithm requires the two voltage measurements resulting from homogeneous and heterogeneous conductivity distribution in the column interior. Findings in the literature show that the difference algorithm is more often applied in biomedical and industrial research studies than absolute algorithm since it is a more accurate functional imaging technique (Andy & William, 2006).

Using the FEM to solve the forward problem based on difference algorithm, a change in conductivity distribution between the present conductivity distribution σ $[s/m]$ (heterogeneous conductivity distribution) and a reference conductivity distribution σ_0 can be represented by $x_i = \sigma_i - [\sigma_0]_i$. Thus, given a stimulated current signal, the resulting difference voltage measurement, y relates to the small change in conductivity distribution by the expression

$$y = Jx + n \qquad (2.17)$$

The ERT forward problem modelled, using the Poisson's equation of Eq.(2.16) is represented in matrix form using the FEM as in Eq.(2.17) . The J symbol in Eq.(2.17) denotes the Jacobian or sensitivity matrix of the form $J \in R^{n_M \times n_N}$, where n_M is the number of voltage measurements and n_N is the number of discrete elements in a domain. The notation n in Eq.(2.17) is the noise in the measurement, which is assumed to be uncorrelated white Gaussian of the form $n \in R^{n_M}$. The Jacobian matrix is called by the FEM according to the definition

$$J_{ij} = {\partial y_i}\Big/{\partial x_j} \tag{2.18}$$

The ERT inverse problem is defined as what conductivity distribution in the interior target section of the column produced the measured voltage signal captured at the periphery of a reactor given a known stimulation of current signal. The ERT inverse problem is mathematically ill-conditioned because the conductivity values on all image elements affect any voltage measurement made on periphery electrode pairs (William, et al., 2002). Thus, the system of Eq.(2.17) is under-determined since the number of discrete elements n_n is usually much higher than the number of measurements n_M. For an ERT generated image in 2D on a cross section of a reactor bounded by a ring of 16 electrodes, the number of discrete elements is the range of 828-1200 (coarse grid), while the minimum number of voltage measurements that could generate the image (a data frame) is 256 (16 x 16).

The inverse problem is usually solved by the inclusion of a regularization parameter in the inverse problem equation (Pinheiro, et al., 1998). This addresses the under-determined state of the system of equations in Eq.(2.17) so that images obtained that may be interpreted. The method of image creation by the inverse ERT algorithm where the differential measured voltage values and the stimulated current signals through the boundary electrodes are required is referred to as image reconstruction.

The aim of the image reconstruction by the regularization approach is to calculate a conductivity change estimate $\hat{x}_t$ that produced a measured voltage y_t using prior constraints of a "most likely" image for a measurement made at time t. The one step linear Gauss-Newton reconstruction algorithm (solver) was first introduced into ERT by (Tossavainen, et al., 2004) and that has gained wide usage is of the form

$$\|y - Jx\|^2_{\sum n^{-1}} + \|\hat{x} - x^o\|^2_{\sum x^{-1}} \tag{2.19}$$

The symbol x^o in Eq.(2.19) denotes the expected value of element conductivity changes. For difference ERT algorithm, x^o is zero since an assumption that the conductivity change may be equally positive or negative is made. The covariance matrix of the expected measurement noise is represented by $\sum_n \in R^{n_M \times n_M}$ in Eq.(2.19)

In many proposed models, the method of calculating the inverse of $\sum_x$ or $\sum_n$ is usually adopted instead of calculating $\sum_x$ and $\sum_n$ directly. The terminologies $W = \sigma_n^2 \sum_n^{-1}$ and $R = \sigma_x^2 \sum_x^{-1}$ were used to define the inverse of $\sum_x$ and $\sum_n$ respectively in the work by (Tao, et al., 2008). The symbols $\sigma_n$and σ_x respectively in the terminologies denote the average measurement noise amplitude and the apriori amplitude of conductivity change. While W models the relative measurement accuracy across channels, the regularization matrix R model the "unlikelihood" of image element configurations.

When Eq.(2.19) is solved with a definition of hyperparameter $\lambda = {\sigma_n}/{\sigma_x}$, a linearised one-step inverse solver is obtained as

$$\hat{x} = (J^T W J + \lambda^2 R)^{-1} J^T W y = By \tag{2.20}$$

The size of the matrix of terms to be inverted to calculate B in Eq.(2.20) is $n_N \times n_N$. In a situation where the size of n_N is of the order of 10^4 or10^5, the computation to calculate B will have a high demand for a much faster computer system and memory space.

In order to overcome the challenge in computing space and memory, the term B is usually re-written as in Eq.(2.21) (also referred to as Weinner filter)

$$B = PJ^T (JPJ^T + \lambda^2 V)^{-1} \tag{2.21}$$

where $P = R^{-1} = {\sum_x}/{\sigma_x^2}$ and $V = W^{-1} = {\sum_n}/{\sigma_n^2}$.The size of matrix to be inverted in Eq.(2.21) is $n_M \times n_M$, which is significantly less than $n_N \times n_N$ as required in Eq.(2.20)

The Gauss-Newton algorithm with the re-formulated Weinner filter will be used for image reconstruction of dispersion in this work owing to the less time for the computation of the Jacobian matrix.

2.2.4. Temporal imaging reconstruction algorithm

The temporal reconstruction algorithm calculates an image at a current measurement data frame using the data collected at earlier times and later times away from the current data frame. The temporal reconstruction algorithm is different from Kalman filter based algorithm of Eq.(2.20) which estimates image x_t based on measurement y_t and the previous image estimate x_{t-1}. The temporal algorithm creates a sequence of image frames as a single inverse problem using a regularization prior that accounts for both spatial and temporal correlation between image elements (Tao, et al., 2008). In order to calculate an image x_t at time t corresponding to measurement y_t, the image elements that resulted in the measurements within the neighbourhood of the target measurement frames are used.

If we let the concatenated sequence of measurement frames be an array $\widehat{y_t} = \left[y_{t-d}^T, y_{t-d+1}^T, \dots, y_t^T, \dots, y_{t+d-1}^T, y_{t+d}^T\right]$; and we let the concatenated sequence of corresponding images be $\left[x_{t-d}^T, x_{t-d+1}^T, \dots, x_t^T, \dots, x_{t+d-1}^T, x_{t+d}^T\right]$. For a given sequence of concatenated measurement frames $\widehat{y_t}$ and the corresponding concatenated images $\widehat{x_t}$ that yielded the measurement, $\widehat{y_t}$, the direct temporal forward model takes the form

$$\widehat{y_t} = \hat{J}\widehat{x_t} + \hat{n} \tag{2.22}$$

where $\hat{n} = [n_{t-d}^T, \dots, n_t^T, \dots n_{t+d}^T]$. In evaluating Eq.(2.22) the model structure could be considered to be constant, which makes the Jacobain J to be constant with respect to time. Thus, $\hat{J} = I \otimes J$, where the identity matrix I has size $2d + 1$ and $\otimes$ is the kronecker product.

Relating Eq.(2.22) of the temporal forward model to Eq.(2.17) of the direct ERT forward model, the one-step inverse image reconstruction algorithm becomes

$$\tilde{B} = \tilde{P}\tilde{J}^T(\tilde{J}\tilde{P}\tilde{J}^T + \lambda^2\tilde{V})^{-1} \tag{2.23}$$

where $\tilde{V} = I \otimes V$ and $\tilde{P} = \Gamma \otimes P$ and Γ is the temporal weight matrix of an image sequence $\tilde{x}$ and it is defined as

$$[\Gamma]_{i,j} = \mathrm{e}^{(|\mathrm{i}-\mathrm{j}|)/\gamma},\ i, j = -d, \dots, d \tag{2.24}$$

Using Eq.(2.24) , Eq. (2.23) could be re-written as in Eq.(2.25)

$$\tilde{B} = [\Gamma \otimes (PJ^T)][\Gamma \otimes (JPJ^T) + \lambda^2 (I \otimes V)]^{-1} \quad (2.25)$$

The one-step solution for the current image $\widehat{x_t}$ given $\tilde{B}$ is thus

$$\widehat{x_t} = \tilde{B}_o \widetilde{y_t} \quad (2.26)$$

where $\tilde{B}_o$ is the first row $n_M \times d + 1, \ldots, n_M \times (d + 1)$ of $\tilde{B}$ (Tao, et al., 2008).

With a view to accurately measure gas void fractions using the ERT technique, the ERT algorithm with temporal data frame correlation as the regularization parameter will be explored. An assessment of its accuracy will be made, which will justify the use of alternative algorithms.

2.2.5. Gauss-Newton algorithm with spatial image elements correlation and temporal data frames correlations

The regularization parameters for an image reconstruction matrix, mentioned in section 2.2.2, are usually developed using image prior models. A common assumption on the image prior model is that the image elements are independent as obtained in zeroth order Tikhonov prior (Yorkey, et al., 1987) and Noser prior (Cheney, et al., 1990). Alternatively, it is assumed that the image elements are locally correlated as reported by (Vauhkonen, et al., 1999).

The covariance matrix of the expected image $\sum_x$ is a diagonal matrix leading to inter-element correlation being zero when the elements are independent. However, when the elements are assumed to be locally correlated, $\sum_x$ is a sparse non-diagonal structure since only adjacent elements are considered correlated (Vauhkonen, et al., 1999). Two limitations were found to be associated with the stated correlation model. First, the correlations do not adequately reflect the scale of the correlations since image elements are correlated globally. Secondly, the spatial frequency of the conductivity distribution depends on the size of the image elements (Tao, et al., 2008), meaning that in a correlation model development, larger elements should have larger spatial correlation values.

The limitations of the correlation models lead to the development of a special prior model (either in 2D or 3D imaging) which account for full correlation model as in Eq.(2.27) (Tao, et al., 2008)

$$\left[P_N^{1/2}\right]_{i,i} = [J^T J]_{i,i}^{-P/2} \tag{2.27}$$

The sensitivity part of the prior image matrix P is $P_N^{1/2}$ in Eq.(2.27) and P is therefore defined as

$$P = P_N^{1/2} P_C P_N^{1/2} \tag{2.28}$$

where P_C is the exponential spatial correlation matrix of the form.

$$[P_C]_{i,i} = e^{\left(-\|r_i - r_j\|/\eta\right)} \tag{2.29}$$

The symbols r_i, r_j represent the centre of two image elements i and j, while η is an exponential constant of same unit distance $[m]$.

When the image elements correlation form of Eq.(2.28) is substituted into Eq.(2.19) , an image reconstruction algorithm with the spatial image prior either in 2D or 3D is obtained.

Furthermore, substituting Eq.(2.28) into Eq.(2.25) results in an image reconstruction algorithm with a spatial correlation in image elements and temporal correlation in data frames. If a spatial image element with correlation in 3D is substituted into Eq.(2.25) , the imaging algorithm is referred to as ERT algorithm with 4D regularization.

The ERT reconstruction algorithm involves solving an ill-conditioned residual equation resulting from optimising actual measured voltage signals to the forward problem model of the measured voltage. The ill-conditioning of the model system of equations arises from a disparity in the number of voltage measurements when related to the number of discretised elements that span a target column section. The target sections could be a cross section of the column in the case of 2D reconstruction or a target volume of column in the case of 3D reconstruction.

The disparity in the number of measured voltage signals (256 data for a frame collected from a ring) and discrete finite elements number (828 triangular elements in the case of 2D imaging) leads to non-uniform sensitivity regions within the domain to current signals stimulated at the column periphery. Thus, to improve the sensitivity of the region within the target sections of the column to current stimulated at the surface of the reactors, a small

diameter vessel or pipes within the range of 5 – 10cm were used by (Haibo, et al., 2007) and (Jin, et al., 2007). The use of large diameter BCR are often preferred because large gas throughput is involved (Kantarci, et al., 2005), and large conversion levels are achievable only with BCR with higher heights.

This limitation in the use of ERT to analyse bubble population parameters, restricting its effective use to a laboratory scale reactor system, is envisaged to be addressed by hybridizing ERT measurements to a model of a physical system in a BCR. A review of applications of ERT algorithms is presented in the next section to highlight benefits of ERT high temporal resolution, which make it an effective functional imaging tool both in industries and biomedical field. ERT technique was used in these fields to scan properties of physical substances in the interior of a body since its high temporal resolution is effective at monitoring the changes in the properties.

The ERT reconstruction algorithm in 3D with 4D regularization will be explored in this study for imaging the dispersed phase in a 2-phase air-water system. The intention is to evaluate the improvement in the spatial resolution of images with the included 4D regularization parameters. An efficient algorithm of such is expected to produce a graph of gas void fraction estimates depending on gas flow rates that can easily be validated or calibrated against available data. Should this algorithm be ineffective, other alternative algorithms without 4D regularization or in 2D will be explored for accurate gas void fraction measurements.

2.3. Industrial applications of ERT technique

The ERT technique has the potential for gaining more information on the bubble size distribution in a bubble column since an ERT estimate of gas void fraction values is as a result of perturbed conductivity field by entire bubble population. In the case of 2D image generation, the bubble size distribution will be from a cross-sectional area of the vessel, while in the case of 3D image reconstruction, the bubble size distribution will be from a given volume of a vessel. The Sauter Mean Bubble Size could be calculated from gas void fraction values using empirically determined correlation model for Sauter Mean Bubble Size as a function of gas void fraction values (Laari & Turunen, 2003).

Multi-component flow monitoring in real-time for an identification of areas of good and poor contact during velocity measurement of flow is possible by the ERT imaging technique (Robert, et al., 2002). ERT has been verified to be applicable for these studies: visualisation of intimate contact with two fluids within packed beds and monitoring of blockage that changes flow of fluids (Robert, et al., 2002); measurement of vortex formation from outside the hydrocyclones and detection of its faults (Williams, 1999); testing, validation and improving CFD codes(Pakzad, et al., 2008); and diagnosis of functioning of sparger and characterisation of flow in bubble columns reactors (Vijayan, et al., 2007). The ERT algorithm was applied by (Mann, et al., 1997) to monitor mixing from the resistivity property of the spatial distribution of different components, which provided a measure of homogeneity. ERT sensitivity to electrical changes can also provide information on the onset of crystallisation (Ricard, et al., 2005)

Pinheiro et al. (Pinheiro, et al., 1998) pioneered the industrial process tomography applications with the use of ERT 3D reconstructions for analysis of a multi-phase mixture. (Davidson, et al., 2004) applied ERT reconstructions in 3D to metal-walled filtration test platform, while (Stephenson, et al., 2007) explored ERT to determine the jet mixing characteristics in reactors. An investigation into fluid mixing in a stirred vessel through analysis of ERT 3D reconstructions was made by (Stephenson, et al., 2009), and further applications of the ERT 3D reconstruction to characterise gas holdup distribution in laboratory flotation cell was recorded in the work of (Jari, et al., 2011). ERT is employable for the monitoring of formation of the vortex from outside the hydrocyclones (Williams, 1999). In crystallization processes, ERT reconstruction has been analysed to gain an online visualisation of processes for controlling the final shape and size of crystals at the point of nucleation (Rodgers, et al., 2009). The ERT imaging technique was also employed in bubble columns and packed beds for monitoring of various flow patterns for hydrodynamic characterisation and monitoring of blockage, which change the flow of fluids and reduce its effectiveness (Bolton, et al., 2004). CFD models validation and its improvements for a reliable use have been made using ERT measured data (Pakzad, et al., 2008).

The ERT imaging method is superior to the optical technique for high gas void fraction measurements because bubbles nearer to the column wall may only be detected by optical technique (camera) at this flow regime. More so, in an opaque BCR, the optical approach is ineffective while the ERT technique is still useful for gas void fraction measurements. Since ERT has a low spatial but high temporal resolution, it is suitable for fast process monitoring

taking place in reactors. The ERT equipment set-up is portable and allows the visualisation of the interior of a body in a non-intrusive and non-radioactive means as well as at a low capital cost rate.

2.4. Medical and Geophysics applications of ERT technique

Earlier applications of ERT were based on analysis and interpretation of reconstructed conductivity images in 2D in Medicine and Geophysics as well as in industries. The errors in their assumptions were that the body under investigation was taken to be in 2D and the equipotential lines were analysed in image creation to be curves (2D) instead of surfaces (3D) (Andy & William, 2006). An example was the imaging of human forearm by (Barber, et al., 1983). The effective opposition to the flow of current due to resistor and reactance components caused, respectively, by the resistivity, capacitive and inductive properties of the 2 - phase systems is referred to as impeditivity. Since admitivity, the inverse of impeditivity, is the target distribution to be imaged in a human body, ERT is referred to as electrical impedance tomography (EIT) in medical applications.

Given that ERT is an effective functional imaging technique, it is utilized in medicine for the monitoring of patient's heart and lungs activities through the movement of conductivity contrasting of blood and air (Helga, et al., 2009). It also allows the monitoring of regional ventilation within the lungs faster than the blood gas approach (Tao, et al., 2008).

In geophysics, recent applications include the detection of underground mine workings by (Johnson, et al., 2003); and in the work of (Lesparre, et al., 2011), the inner structures of geological objects were imaged using ERT. Moreover, earlier 3D imaging algorithms were from the medical electrical impedance tomography (EIT) group, which include the work of (Goble, et al., 1992) and (Metherall, et al., 1996).

2.5. Recent industrial and biomedical applications of ERT

Industrial applications of ERT 2D reconstructions include respectively the work of (Jin, et al., 2007) who measured gas holdup profiles in a gas-liquid co-current bubble column using ERT. An analysed of bubble behaviour in bubble columns from ERT reconstructions has also been

made by (Haibo, et al., 2007). (Okonkwo, et al., 2012) reported the characterisation of a high concentration of ionic bubble column using ERT.

In the three applications of ERT reconstruction in 2D, the gas holdup values of the dispersed phase were calculated from ERT images using Maxwell's relation (Maxwell, 1873) of the form of Eq.(2.30) , where $\sigma_1$is the conductivity value of the continuous phase; σ_2 is the conductivity value of the dispersed phase; $\overline{\sigma_{mc}}$ is the average conductivity value of the mixture phase.

$$\varepsilon_g = \frac{2\sigma_1 + \sigma_2 - 2\overline{\sigma_{mc}} - \overline{\sigma_{mc}}\sigma_2/\sigma_1}{\overline{\sigma_{mc}} - \sigma_2/\sigma_1 + 2(\sigma_1 - \sigma_2)} \tag{2.30}$$

If the dispersed phase ($\sigma_2 = 0$) is a non-conductive material, Eq.(2.30) is simplified to

$$\varepsilon_g = \frac{2\sigma_1 - 2\overline{\sigma_{mc}}}{2\sigma_1 - \overline{\sigma_{mc}}} \tag{2.31}$$

The average value of the mixture conductivity $\overline{\sigma_{mc}}$ over the column cross sectional area A_c is given by Eq.(2.32)

$$\overline{\sigma_{mc}} = \frac{\int_{A_c} \sigma_{mc} dA_c}{A_c} \tag{2.32}$$

Findings in the literature on process tomography show that a robust utilization of ERT algorithms has been limited by the low spatial resolution of the images, particularly for smaller objects in the scale of bubble sizes. An improvement in spatial resolution of ERT images to the extent of accounting for countable entities in a BCR will in no less make ERT gain many industrial applications especially for BCR designing and scale-up.

In the Department of Chemical Engineering, University of Cape Town, some research studies have benefitted from the application of ERT 2D reconstructions. Stevenson (Stevenson, 2006) PhD thesis reported an analysis of particle suspension and mixing in biological systems using the ERT technique developed from a 2D algorithm. (Long, 2006) Master's thesis work complimented earlier application of ERT 2D reconstruction in the department, in a study conducted to accomplish an on-line velocity flow profiling system with a view to visualising the flow of slurries in 2D. Further, (Sudhakaran, 2010) explored the ERT 2D reconstruction in evaluating the influence of nozzle design on the gas holdup distribution in boiling bubble column reactors. Later, (Adetunji, 2011) harnessed the measurement sequences in 3D obtainable with the UCT ERT instrument to implement an advanced algorithm for enhanced

signal analysis in electrical resistance tomography using EIDORS toolbox to monitor fluid movement in 3D.

In Biomedical research, (Tao, et al., 2008) developed an ERT algorithm to improve the spatial resolution of reconstructed images since ERT algorithm has high temporal resolution and images are highly correlated especially in high-speed system. In their paper, entitled ''ERT 3D reconstruction with 4D regularization'', a prior model of the temporal correlations among images and 3D spatial correlations of image elements were used to improve the spatial accuracy of images. (Tao, et al., 2008) applied the ERT algorithm with 4D regularization to track the trajectory of a spherical conductive target of radius 1.5cm, which represented the bolus left ventricular ejection in a human body. The reconstructed images using this algorithm showed higher spatial accuracy than an algorithm without 4D regularization.

In this study, the effective algorithm will be determined by using the enumerated ERT algorithms to measure the gas holdup fractions at a target section of the column over range of gas flow rates. An efficient reconstruction algorithm of such is expected to yield a graph of increasing time and area average of conductivity distribution with an increase in gas flow rate since air is non-conductive. The time and area average of conductivity distribution means computing the product of the size of the finite element and the conductivity of such element for all elements and adding the result. The ratio of added result to the total volume of the column section in the case of 3D reconstruction is called volume average of conductivity distribution calculated for every data frame captured (256 data sets). For the same data size, in the case of 2D reconstruction, the ratio of added result to the total cross-sectional area of the column is called area average of conductivity distribution. The mean of either volume or area averages of conductivity distribution for all captured data frames will then be calculated to obtain time and area average of conductivity distribution.

In the context of this study, gas holdup fractions of the multiphase reaction system to be measured is set-up in a BCR. Multiphase reactions in a BCR often need to be optimised for cost-effective production and energy consumption purposes. Alternatively, the design and scale of geometric dimensions of component column parts could be adjusted to ensure a high product yield at a low capital cost and low energy consumption rate, while achieving higher heat and mass transfer.

Findings on studies to upgrade the BCR and studies on the development of correlation models for prediction of bubble population properties as well as hydrodynamic parameter

calculations are presented in the next section. In the sub-section of section 2.7, an illustration is given of the method of calculating the bubble number density distribution of bubble population sizes.

2.6. Design, scale-up and performance description of a BCR

Many studies on improving the performance of a BCR have focussed on design and scale-up because of its effects on the transport characteristics and complex hydrodynamic state in the reactor (Kantarci, et al., 2005). The design and scale-up of a BCR are dependent on the quantification of 3 main phenomena, namely: 1) Heat and mass transfer characteristics; 2) Mixing characteristics; and 3) chemical kinetics of the reacting system. Scale-up problems are known to originate from the scale-dependency of the fluid dynamic phenomena and heat and mass transfer properties.

Studies have shown that reactor performance is governed by reaction specific quantities and reactor specific phenomena. The reaction specific quantities such as physical properties of 2 fluid systems, stoichiometry, thermodynamics and kinetics are independent of reactor types and design. The reactor specific phenomena, however, are largely dependent on operating conditions, physical properties, reactor types and its geometric dimensions (Deckwer & Schumpe, 1993). Typically, in biotechnology and chemical industry, scale-up methods range from empirical know-how to know why based approaches. In recent times, the know-why based method is suggested to yield more reliable models than the know-how approaches (Deckwer & Schumpe, 1993). More often, mathematical models to describe the performance of the BCR are dependent on the variables of reaction kinetics, the number of reactive species and phases, the absorption reaction regime (mass transfer terms) and the fluid dynamics of the phases. In the classical models, the liquid and gas phase resident time distribution models (RTDs), measured by known methods are employed and utilized in characterizing the fluid dynamics of the systems, while the RTDs can be interpreted to be completely mixed, partially mixed or unmixed. The partial mixing of the fluid system often encountered can be described by tank-in-series models (with or without back flow between neighbouring cells) or by the one-dimensional axial dispersion model (ADM) (Deckwer & Schumpe, 1993).

The fluid dynamics of the gas phase in a BCR could be classified to homogeneous flow (bubbly flow) and heterogeneous flow (churn-turbulent flow) based on the superficial gas velocity of dispersion and bubble sizes in the continuous liquid phase. Bubbly (homogeneous

) flow exists at a low gas flow rate and it is characterised by almost uniform size bubbles having similar rise velocities. As the superficial gas velocity increases, the bubbly flows transits to the churn-turbulent regime described by a dispersion of larger bubbles rising with higher velocities through the bed of the small bubbles. Although in the ADM, all the individual mixing phenomena taking place in each phase are all lumped to an axial dispersion coefficient (a coarse simplification of reality), it has proven as and still an effective tool to model BCRs (Deckwer & Schumpe, 1993).

Thus, in predicting the hydrodynamic parameters by the hybrid of ERT and a PBM in this work, the tank-in-series model or the ADM approach will be explored to solve the PBM. The ADM approach is adopted since it is a valid tool to model BCRs particularly for hydrodynamic flow regime characterised with mixing phenomena.

2.7. Fluid dynamics and regime analysis of BCRs

The operations and performance of bubble column reactor (BCR) have been found to be highly affected by the fluid dynamic characteristics and the dominant fluid flow regime in the column. In addition to the three known regimes: Homogeneous (bubbly flow) regime, Heterogeneous (churn-turbulent) regime and the slug flow regime (Hyndman, et al., 1997), the ‘’foaming regime’’ also exist but rarely takes place in the bubble columns (Kantarci, et al., 2005).

The homogeneous flow regime is observed in a BCR operated in a semi-batch mode at low superficial gas velocities approximately less than 0.05m/s (Kantarci, et al., 2005). When this regime exists in a BCR, bubbles are seen to be of relatively uniform small sizes and rise velocities. Their sizes and rise velocities give rise to a uniform bubble distribution and relatively gentle mixing over the entire cross-sectional area of the column. Practically, during this flow regime, bubble coalescence and breakage are insignificant to the extent that bubbles sizes are influenced largely by sparger design and system properties (Thorat & Joshi, 2004). (Kawagoe, et al., 1976) reported that the gas holdup in the bubbly flow regime increases linearly with increasing superficial gas velocity.

As superficial gas velocity increases, the flow regime transits from bubbly to the churn-turbulent regime (heterogeneous regime), where the superficial gas velocity is greater than

0.05m/s in a batch column (Kantarci, et al., 2005). The regime is described by perturbed homogeneous gas-liquid system caused by the turbulent motion of gas bubbles and liquid recirculation. Due to high gas throughput in this regime, unsteady flow pattern and large bubbles with short residence times are formed by coalescence phenomena. In addition to bubble coalescence, bubble breakage processes could occur, leading to a wide size distribution of bubbles. The average bubble size is, thus, controlled by coalescence and breakup which is dependent on the energy dissipation rate in the bulk solution (Thorat & Joshi, 2004). It has been reported that the gas-liquid mass transfer coefficient is lower at churn-turbulent (heterogeneous) regime as compared to homogeneous flow.

Knowing when flow regime transits from bubbly to churn-turbulent regime in the column is important because significant changes are observed in the hydrodynamic behaviours of the system at this period. It is noticed that at this period liquid circulates upward at the centre of the column and downward near the column wall. This allows further entry to take place at the centre, which leads to the build-up of transverse hold-up profile that enhances liquid circulation. In measuring the liquid circulation and the transverse hold-up profiles, the ERT imaging technique is superior to the optical technique often used since the ERT technique does not require a transparent column.

2.7.1. Gas holdup and specific interfacial area

Gas hold-up is a dimensionless essential hydrodynamic parameter for column designing that determines the nature of transport phenomena in a bubble column system (Luo, et al., 1999). Gas holdup is the ratio of the volume occupied by the gas in a reactor section to the volume of the reactor section (local gas holdup); or the ratio of the volume occupied by the gas in the entire reactor to the reactor volume (global gas holdup). The axial holdup in a BCR could be determined from two differential pressure signals (Jin, et al., 2007). Based on an assumption that the values of the liquid acceleration terms and the wall friction terms are normally small and negligible, the mean gas holdup ($\overline{\varepsilon_g}$) is usually calculated using Eq.(2.33)

$$\overline{\varepsilon_g} = 1 - \frac{\Delta P}{\rho_l g \Delta H} \tag{2.33}$$

where ΔP is the differential pressure between two pressure sensor points $[Nm^{-2}]$, ΔH is the vertical distance between two pressure points $[m]$, ρ_l is the liquid density $[kgm^{-3}]$ and g is the acceleration due to gravity $[ms^{-2}]$ (Jin, et al., 2007). The spatial variation of the gas holdup, also called gas holdup profile, is a key factor that contributes to the rise in pressure variation and liquid recirculation (Kantarci, et al., 2005). Additionally, the magnitude of gas holdup radial gradients is known to depend on the superficial gas velocity, the column diameter, gas distribution design, physical properties of the system and operating conditions (Wu, et al., 2001) (Shah, et al., 1982). This assertion is supported given the gas holdup correlations by (Hughmark, 1967) and (Kawase, et al., 1992) respectively as in Eq.(2.34) and Eq.(2.35)

$$\varepsilon_g = \frac{1}{2 + \left(0.35/\mathrm{u_G}\right)\left(\rho_L \sigma/72\right)^{1/3}} \tag{2.34}$$

$$\frac{\varepsilon_g}{1+\varepsilon_g} = 0.0625\left(\frac{u_G}{\vartheta_l g}\right)^{1/4} \tag{2.35}$$

Akita and Yoshida (Akita & Yoshida, 1973) developed a model of integral hold-up (averaged over the entire volume of gas-in-liquid dispersion) following a correlation for many experimental data of the form

$$\frac{\varepsilon_g}{\left(1-\varepsilon_g\right)^4} = \propto \left(\frac{D_C^2 \rho_L g}{\sigma}\right)^{1/8} \left(\frac{D_C^3 g}{v_L^2}\right)^{1/12} \frac{U_G}{\sqrt{g D_C}} \tag{2.36}$$

where $\propto = 0.2$ for pure liquid and non-electrolyte solution; $\propto = 0.25$ for salt solutions in the range of $\varepsilon_G < 0.14$ within which the experiment was conducted. The model, Eq.(2.36) is valid for superficial gas velocity (U_G) in the range $0.003 - 0.4m/s$, liquid velocity (U_L) in the range of $0 - 0.044m/s$, column diameter (D_C) in the range of $0.152 - 0.6m$ and column height (H_C) ranging from $1.26 - 3.5m$.

Thereafter, (Hikita, et al., 1980) proposed a more accurate correlation model for gas holdup of the form of Eq.(2.36) by including the physical property of the gas phase, ρ_G, unlike the model of (Akita & Yoshida, 1973). The included ρ_G has been observed to reduce the deviation of the data fit from the experimental data from 15% to 4% when compared to model Eq.(2.37) The parameter $f = 1$ for non-electrolyte solution and for salt solution f was determined to be a function of ionic strength of solution.

$$\varepsilon_g = 0.672f\left(\frac{U_G\mu_L}{\sigma}\right)^{0.578}\left(\frac{\mu_L^4 g}{\rho_L\sigma^3}\right)^{-0.131}\left(\frac{\rho_G}{\rho_L}\right)^{0.062}\left(\frac{\mu_G}{\mu_L}\right)^{0.107} \quad (2.37)$$

Eq.(2.37) is valid for U_G within the range $0.042 - 0.38m/s$, $D_C = 0.1m$ and liquid height $H_L = 0.64m$. The correlations of (Akita & Yoshida, 1973) and (Hikita, et al., 1980) have been found suitable for gas holdup calculations for BCRs design purposes (Oztijrk, et al., 1987). In Ozturk's work, 50 different gas-liquid systems were measured, plotted and several correlations models in literature were tested to fit their data but the correlation of (Akita & Yoshida, 1973) and (Hikita, et al., 1980) yielded the best fit with a measurement error of 11%.

In the work of (Akita & Yoshida, 1973), Eq.(2.36) was further re-expressed as

$$\frac{U_G}{\sqrt{gD}} = 8.887\left(\frac{gD^2\rho_L}{\sigma}\right)^{-1/8}\left(\frac{gD^3}{v_L^2}\right)^{-1/12}\varepsilon_g^{\,10/9} \quad (2.38)$$

Eq.(2.39) and Eq.(2.40) were obtained from a correlation for average bubble size as a function of physical properties of the fluid state, column dimension and superficial gas velocity by (Akita & Yoshida, 1974). Thus, further simplification of Eq.(2.38) lead to the development of the specific interfacial area, a, in terms of properties of liquid, dimension of the column and gas holdup of Eq.(2.41) (Akita & Yoshida, 1974) for $\varepsilon_G < 0.14$.

$$a = 6\left(\frac{\varepsilon_g}{d_{vs}}\right) \quad (2.39)$$

$$\frac{d_{vs}}{D_C} = 26\left(\frac{gD_C{}^2\rho_L}{\sigma}\right)^{-0.5}\left(\frac{gD_C{}^3}{v_L^2}\right)^{-0.12}\left(\frac{U_G}{\sqrt{gD_C}}\right)^{-0.12} \quad (2.40)$$

$$aD_C = 1/3\left(\frac{gD_C{}^2\rho_L}{\sigma}\right)^{0.5}\left(\frac{gD_C{}^3}{v_L^2}\right)^{0.1}\varepsilon_G^{1.13} \quad (2.41)$$

The correlation of Eq.(2.40) is valid for column diameter up to $0.3m$ and superficial gas velocity up to about $0.07m/s$. The correlation of Eq.(2.40) is recommended for self-studied systems and most suitable for single orifice spargers (Shah, et al., 1982). In a two-phase multiphase system, the bubble sizes are known to be controlled by the balance between the bubble coalescence and breakup rates. The observation was confirmed by (Deckwer, et al., 1978) who found no significant difference in the d_{vs} in their experimental bubble size measurements at 3.5 and 6.0m above the sparger. Akita and Yoshida (Akita & Yoshida, 1974)

also observed no effect of orifice diameter on the d_{vs} in the bulk region away from the sparger (Helene, et al., 2006).

Eq.(2.41) shows a dependency on the column diameter as in $D_C^{0.3}$, which vanishes at larger column diameters (i.e. $D_C \geq 0.3m$). The physical quantity variables of Eq.(2.40) and Eq.(2.41) are kinematic viscosity of liquid (v_L) $[m^2 s^{-1}]$, surface tension (σ) $[kgs^{-2}]$, liquid density (ρ_L) $[kgm^{-3}]$, superficial gas velocity (U_G) $[ms^{-1}]$, gas hold-up (ε_G), column diameter (D_C) $[m]$ and the volume-surface mean bubble diameter (d_{vs}) $[m]$.

The empirically developed correlation of Eq.(2.41) can be explored for the computation of the specific gas to liquid interfacial area since it is valid within the operating range of the present work. The required gas void fractions will be computed from the resolved bubble number density distribution by the hybrid of ERT and a PBM. The proposed hybrid of ERT and a PBM is, thus, intended to address the operational limitation ranges of the correlation models for hydrodynamic parameter predictions. This will be accomplished through an accurate prediction of the BNDDs required for hydrodynamic parameter predictions overall operational conditions.

2.7.2. Superficial gas velocity

Superficial gas velocity is the average velocity of the gas that is sparged into a column, expressed as the ratio of volumetric gas flow rate to the cross-sectional area of the column. Gas holdup has been found to increase with increasing superficial gas velocity in both bubble column and slurry bubble column (Prakash, et al., 2001)(Li & Prakash, 2000)(Pino, et al., 1992)(Krishna, et al., 1997)(Hyndman, et al., 1997)(Schumpe & Grund, 1986)(Deckwer, et al., 1980)(Saxena, et al., 1990) and (Daly, et al., 1992). Furthermore, an increase in the gas holdup with superficial velocity has been found to be proportional in the bubbly flow regime (Lockett & Kirkpatrick, 1975) and (Kara, et al., 1982). However, in a churn-turbulent regime, the effects of superficial velocity on gas holdup are less significant (Kara, et al., 1982) and (Koide, et al., 1984).

Since the ERT imaging approach is based on the interior conductivity of a body, gas holdup fractions increase with gas flow rates is expected to lead to a decreasing magnitude of conductivity distribution in a non-conductive dispersed phase. This relationship will hold

over a wide range of gas flow rates. Thus, the hybrid technique is proposed to be useful for hydrodynamic predictions over wide fluid regimes including the churn-turbulent regime fluid flow.

2.7.3. Hydrodynamic parameters – mass transfer coefficients

The specific gas-liquid interfacial area a_s is related to the gas hold-up, ε_g, and the Sauter Mean Bubble Diameter, d_{vs}, assuming that bubbles are spherical in shape as in Eq.(2.42) .

$$a_s = {}^{6\varepsilon_g}\Big/_{d_{vs}} \tag{2.42}$$

The overall mass transfer rate per unit volume of the dispersion is dominantly controlled by the liquid-side mass transfer in a situation when the gas side possess negligible resistance (Kantarci, et al., 2005). The liquid-side mass transfer is the product of volumetric mass transfer coefficient, k_L, and interfacial area, a. (Fan, et al., 1985) reported that variation of $k_L a$ in a BCR is majorly due to variations in the interfacial area. Eq.(2.42) agrees with the findings of (Daly, et al., 1992) who stated that accurate computation of the specific gas-liquid interfacial area requires the information of the gas holdup and the bubble size distribution. In a gas-liquid multiphase system, the mass transfer from gas to liquid phase is an essential parameter to be optimised.

Additionally, the volumetric mass transfer coefficient is often used in the characterisation and designing of both industrial stirred and non-stirred gas-liquid reactors (Kantarci, et al., 2005). However, it has been realised that very few data are found dealing separately with mass transfer coefficient (k_L) and interfacial area (a) in a BCR (Bouaifi, et al., 2001), though (Akita & Yoshida, 1974) suggested the model of Eq.(2.43) . Most investigators' works have been limited to the determination of the volumetric mass transfer coefficient, $k_L a$. The separation of parameters k_L and a has been suggested to yield better comprehension of the gas-liquid mass transfer mechanism. Furthermore, an independent determination of k_L and a has also been proposed to allow for knowing which parameter between k_L and a contribute to mass transfer.

$$k_L = 0.5 g^{5/8} D_L^{1/2} \rho_L^{3/8} \sigma^{-3/8} d_{vs}^{1/2} \tag{2.43}$$

The data used to develop Eq.(2.43) had its bubble size range from 1.7 to 7.2mm in water, 1.3 to 5.4mm in glycol, and 1.1 to 4.5mm in methanol. Eq.(2.43) was proposed to be valid in a column diameter up to 60cm, superficial gas velocity up to 41cm/s and gas holdup up to 30%. Some of the developed correlations by researchers to predict mass transfer rates in a bubble column, based on the effects of operational parameters on mass transfer characteristics are stated in Eq.(2.44) and Eq.(2.45) The model of Eq.(2.45) (Akita & Yoshida, 1973) was found to be useful for large column diameter in the range 1 – 5.5m, while model Eq.(2.44) (Hikita, et al., 1981) was validated in a column of diameters 0.1 and 0.19m, where no significant effect on D_c was noticed.

$$k_L a = 14.9f\left(\frac{\mu_L}{\sigma}\right)^{1.76}\left(\frac{\mu_L^4}{\rho_L\sigma^3}\right)^{-0.248}\left(\frac{\mu_G}{\mu_L}\right)^{0.243}\left(\frac{\mu_L}{\rho_L D_L}\right)^{-0.604}\left({u_g}^{0.76}\mathrm{g}^{0.7520}\right) \tag{2.44}$$

$$k_L a = 0.6\left(\frac{\mu_L}{\rho_L}\right)^{0.5}\left(\frac{gD_C^2\rho_L}{\sigma}\right)^{0.62}\left(\frac{gD_C^3\rho_L^2}{\mu_L}\right)^{0.31}\left(\frac{{D_L}^{0.5}}{D_C^2}\right)\varepsilon_g^{1.1} \tag{2.45}$$

In Eq.(2.44) and Eq.(2.45) $\mu_{G,}\, D_{C,}\, \mu_L, \sigma$ are gas viscosity$[kg(sm)^{-1}]$, reactor diameter$[m]$, dynamic viscosity of liquid$[kg(sm)^{-1}]$ and surface tension $[kgs^{-2}]$ respectively; ρ_L, $\varepsilon_g$and D_L are respectively the density of the liquid $[kgm^{-3}]$, gas holdup $[unit]$, and the liquid phase diffusivity$[m^2s^{-1}]$. The value of f was approximated to be 1 in the case of non-electrolyte solutions (water, methanol, butanol and ionic solution) and a function ionic strength in the case of electrolyte solutions.

(Ozturk, et al., 1987) reviewed the two models of Eq.(2.44) and Eq.(2.45) by measuring 400 $k_L a$ value data in 50 different gas-liquid systems in a column diameter of 0.095m. Eq.(2.44) and Eq.(2.45) were observed to describe the experimental data with an error of 25 to 37%, even with an optimizer, the error was still greater than 20%. As a result of a high error in using Eq.(2.45) to correlate their results, (Ozturk, et al., 1987) developed the model of Eq.(2.46) by modifying Eq.(2.45) . In the development, the used surface-volume mean bubble diameter d_{vs} was assumed to be of a constant value of 0.003m rather than using the column diameter. Following a testing of the developed model of Eq.(2.46) with experimental data, the computed average error was 13.3%.

$$K_L a = 0.62\left(\frac{\mu_L D_L}{\rho_L}\right)^{0.5}\left(g\frac{\rho_L}{\sigma}\right)^{0.33}\left(\frac{g\rho_L^2}{\mu_L^2}\right)^{0.29}\left(\frac{u_g}{\sqrt{g}}\right)^{0.68}\left(\frac{\rho_G}{\rho_L}\right)^{0.04} d_{vs}^{-0.81} \quad (2.46)$$

A simulation model of bubble column reactor useful for prediction of gas hold-up and volumetric mass transfer coefficients was developed by (Shimizu, et al., 2000). In their model, gas hold-up and gas-liquid mass transfer rates were evaluated on the basis of bubble break-up and coalescence.

The concept of compartmentalisation of the column was adapted to determine the size distribution of a population of bubbles influenced by bubble breakage and coalescence at column sections. The gas hold-up of bubbles in a given dispersion volume V_R was calculated by adding the volume of all bubbles, V_{bi}, in V_R and dividing it by the dispersion volume V_R. The dispersion volume was made up of the sum of the volume of gas V_g and liquid V_l. Thus, the gas hold-up expression of Eq.(2.47) was obtained.

$$\varepsilon_g = \frac{V_g}{V_g + V_l} = \frac{\sum_i V_{bi}}{V_R} \quad (2.47)$$

In calculating the volumetric mass transfer coefficient, the specific gas-liquid interfacial area, a, relating the gas hold-up fractions was defined as Eq.(2.48) ,

$$a = \frac{6\varepsilon_g}{d_{vs}} \quad (2.48)$$

where d_{vs} was the Sauter Mean Diameter of bubbles.

Additionally, the Higbie penetration theory (Shah, et al., 1982) of Eq.(2.49) was used to calculate the liquid phase mass transfer coefficient K_L as in

$$K_L = \left(\frac{4D_L u_r}{\pi d_b}\right)^{\frac{1}{2}} \quad (2.49)$$

where D_L is diffusivity of liquid$[m^2 s^{-1}]$; u_r is bubble rise velocity$[ms^{-1}]$; and d_b is the bubble diameter $[m]$.

The gas-liquid volumetric mass transfer coefficient was then calculated by combining Eq.(2.48) and Eq.(2.49) to derive Eq.(2.50) .

$$K_L a = \sum_i \left(\frac{4D_L u_r}{\pi d_b}\right)^{\frac{1}{2}} \left(\frac{6\varepsilon_g}{d_{vs}}\right) \quad (2.50)$$

The experiment to validate the model of the BCR simulation by (Shimizu, et al., 2000) was set-up in a column with diameter 0.2m and height 1.7m. A 2-phase air-water dispersion system in a batch-wise operational mode, that ran until steady state was achieved, was set-up in the column. The steady state condition of the fluid was determined when there was a negligible change of gas holdup.

The density, viscosity and surface tension of water were measured by a Pycnometer, a Cannon-Fenske viscometer and the du-Noug ring method respectively. A pre-calibrated rotameter was used to measure a continuous sparged air-flow into the column. The gas hold-up measurements were made by the volume expansion method. The volume mass transfer coefficients were measured by the dynamic method. A fast response dissolved oxygen electrode was utilized for monitoring the change in the dissolve oxygen concentration.

The graph of the gas hold-up against the superficial gas velocity by the proposed model simulation of (Shimizu, et al., 2000) is shown in Figure 2.2, alongside the graphs from their experimental studies and other correlations in the literature as in Eq.(2.34) and Eq.(2.35) . In Figure 2.3, the graphs of the gas hold-up along the column axis for two superficial gas velocities of 0.01 m/s and 0.04m/s by the simulation model are shown. Similar graphs in Figure 2.2 and Figure 2.3 are shown in Figure 2.4 and Figure 2.5 respectively when the volumetric mass transfer coefficient was calculated instead of the gas holdup values.

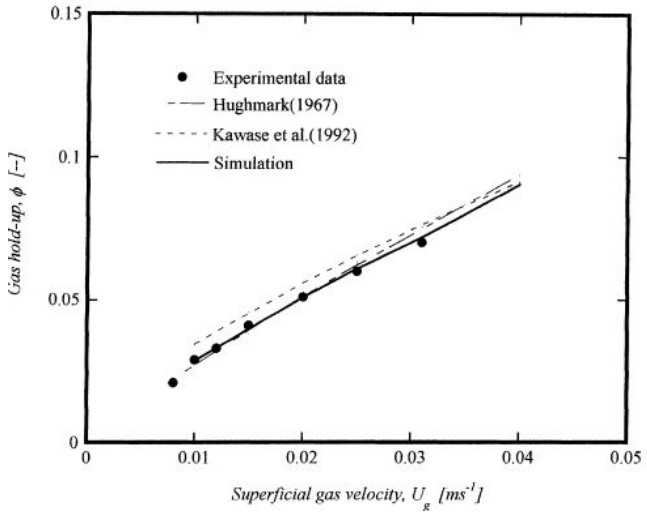

Figure 2.2. Gas hold-up in a 0.2m i.d column reactor

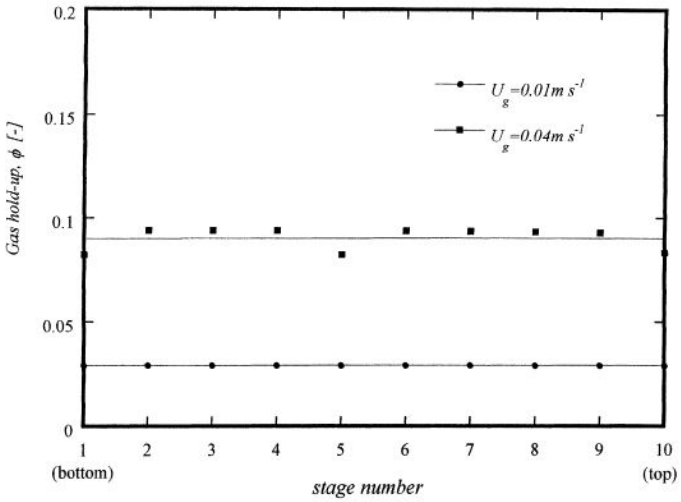

Figure 2.3. Axial distribution of gas hold-up in a bubble column reactor (D_C=0.2m)

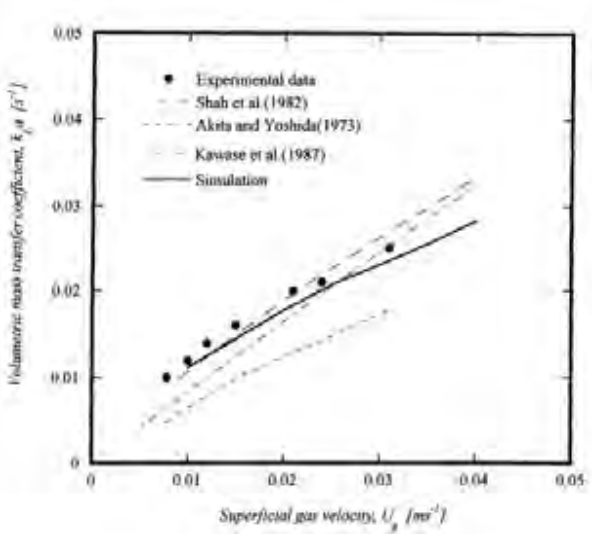

Figure 2.4. Gas-liquid mass transfer rates in a 0.2m i.d bubble column reactor.

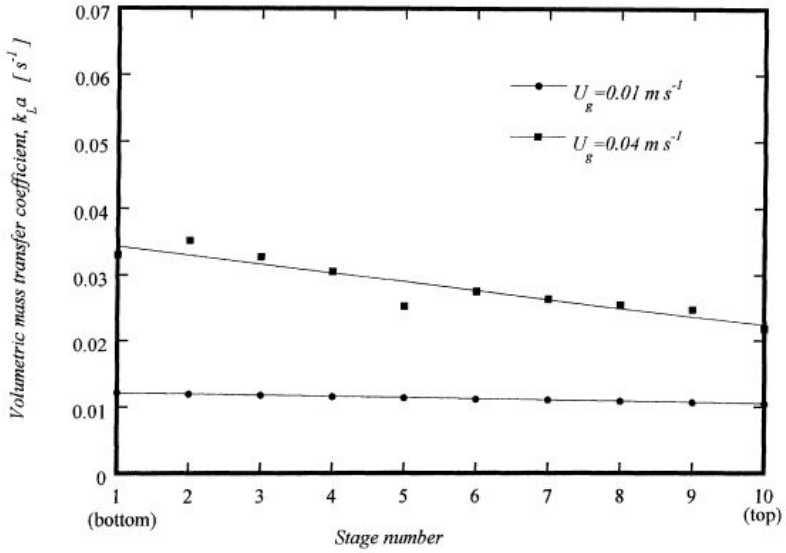

Figure 2.5. Axial distribution of gas-liquid mass transfer rate in a bubble column reactor (D_C=0.2m)

The theory supporting the development of the liquid phase mass transfer coefficient K_L of Eq.(2.43) will be explored since the K_L is valid with the operational conditions of the present work.

2.7.4. Liquid mixing in bubble column reactors

A review of the literature on liquid phase mixing in a bubble column reactor (BCR) indicates it has gained the attention of researchers in the last 57 years. It was observed that despite a number of newly proposed hydrodynamic models, the use of axial dispersion model (ADM)

to describe the liquid phase mixing in BCR is still common (Deckwer, et al., 1974). As an alternative to the use of axial dispersion coefficient to describe the mixing of the liquid phase in a BCR, some researchers characterised the mixing behaviour in a BCR by the mixing times. When a certain degree of homogeneity is achieved, the mixing time is then converted into a dispersion coefficient (E_L).

A theoretical relation was derived by (Baird & Rice, 1975) provide an interpretation for the experimental determination of E_L on the basis of dimensional analysis and Kolmogoroff's theory of isotropic turbulence of the form of Eq.(2.51)

$$E_L = k l^{4/3} \varepsilon^{1/3} \tag{2.51}$$

where k is a constant and the specific energy dissipation, ε $[m^2 s^{-3}]$, equals gU_G ($\varepsilon = gU_G$); l is appropriate diameter $[m]$ of large vortices. From Eq.(2.51) ,

$$E_L = k l^{4/3} (gU_G)^{1/3} \tag{2.52}$$

Eq.(2.52) showing the relation of E_L to D_C and U_G has been confirmed by (Kato & Nishiwaki, 1972) and (Deckwer, et al., 1974).

Mixing of the liquid phase was found to be caused by the combined phenomena of turbulent vortices, liquid entrainment in the wakes of rising bubbles, liquid circulation and radial exchange of flows. Hydrodynamic models which account for the radial liquid velocity and holdup profiles are more appropriate than lumping the various phenomena which differently contribute to mixing into a dispersion coefficient (E_L) (Deckwer & Schumpe, 1993). However, since some of the hydrodynamic models could be reduced to a dispersion model, the relation for E_L are usually derived and the results have been found to be striking agreement with the Eq.(2.51)

It was reported that in spite of many investigations carried out on liquid phase mixing, its effects on BCR performance are only minor and seemingly often over-estimated (Deckwer & Schumpe, 1993). Liquid phase mass transfer coefficient shows little sensitivity to considerable variations of E_L when evaluating mass transfer coefficients ($K_L a$) for measured steady state liquid phase concentration profiles (Deckwer, et al., 1983). Similarly, in a fast reaction absorption regime, reactor performance is not influenced at all by the liquid mixing as the reaction takes place at the gas-liquid interface (Deckwer, et al., 1983).

Given a slow reaction absorption regime where a gas phase component, for example A, reaching the liquid phase reactant B, a complete back mixing can be assumed for component B. This is as a result of the reaction time that is usually higher than effective mixing time. Whether or not a back-mixed liquid phase can be assumed for dissolved gaseous reactant, component A has been reported to depend on the ratio of characteristic time for mixing and mass transfer as in Eq.(2.53) (Deckwer, 1986).

$$\emptyset = \frac{mixing\ time}{mass\ transfer\ time} = \frac{f\left({}^{L^2}/_{\varepsilon_L E_L}\right)}{{}^{1}/_{K_L a}} \tag{2.53}$$

In Eq.(2.53) , $f = 1$, $\emptyset$ is the product of the Bodenstein $\left(\frac{U_L L}{\varepsilon_L E_L}\right)$ number and Stanton $\left(\frac{K_L a L}{U_L}\right)$ numbers that can be interpreted as the product of $\tau_m = \left({}^{L^2}/_{\varepsilon_L E_L}\right)$ and $\tau_{mT} = (K_L a)$.

Table 2.1 shows the values of $\emptyset$ for reactions typically carried out in BCRs for two reactor sizes (Deckwer, 1986).

Table 2.1. Typical values of the ratio of mixing to mass transfer time of BCRs in meters

Reaction	${}^{0.2}/_{2}$	${}^{1}/_{10}$
Isobutene hydration from C_4b cuts	3.6	9.4
Fischer Tropsch synthesis in slurry phase	10.6	28.2
Chlorination of toluene	0.04	0.1

The validity of the theoretically derived liquid dispersion coefficient by the experimental data suggests the model is useful for calculating intensity of liquid mixing. The model will be utilised in this study to determine the intensity of mixing for varied gas flow rates.

2.7.5. Gas mixing in bubble column reactors

More often, modelling of BCRs is conducted while neglecting the gas phase mixing. The gas phase mixing factor could only be ignored for a bench-scale reactors where the Bodenstein number $\left(Bo_G = {}^{U_G L}/_{\varepsilon_G E_G}\right)$ with E_G calculated from the available correlation being high, for example $Bo_G \gg 10$ (Deckwer & Schumpe, 1993). Mixing of the gas phase in BCRs is

attributable to different bubble rise velocities, bubble coalescence, break-up and circulation of bubbles (Deckwer & Schumpe, 1993).

ADM is often used to describe the global gas phase mixing by lumping all the various phenomena into the gas phase axial dispersion coefficient, E_G. Unlike the liquid phase mixing, gas phase mixing dispersion significantly affects the performance of BCRs. (Levenspiel, 1972) found that the influence of gas phase dispersion on conversion corresponds with single phase reactor for a fast reaction absorption regime (the diffusion regime).

However, given the significant effect of the gas phase dispersion on the performance of a reactor, comparative few reports have been made on the gas phase dispersion owing to the difficulty in determining the gas phase dispersion. (Mangartz & Th, 1980) (Anon., n.d.) developed a model for the gas phase dispersion coefficient (E_G) of the form of Eq.(2.54) , which was recommended by (Shah, et al., 1982)

$$E_G = 50 D_C^{3/2} \left(\frac{U_G}{\varepsilon_G}\right)^3 \tag{2.54}$$

(Field & Davidson, 1980) modified Eq.(2.54) from a study of gas phase dispersion in a 3.2m diameter bubble column to obtain a model of Eq.(2.55) .

$$E_G \propto D_C^{3/2} (U_G)^1 \tag{2.55}$$

Eq.(2.55) was derived theoretically by (Wachi & Nojima, 1990) on the basis of the recirculation theory of (Ueyama & Miyauch, 1979) and (Miyauchi, et al., 1981). (Wachi & Nojima, 1990) conducted an experiment to measure the gas-phase dispersion coefficient in an air/water system setup in bubble columns with diameters 0.2m and 0.5m to proposed Eq.(2.56)

$$E_G = 20 D_C^{3/2} U_G \tag{2.56}$$

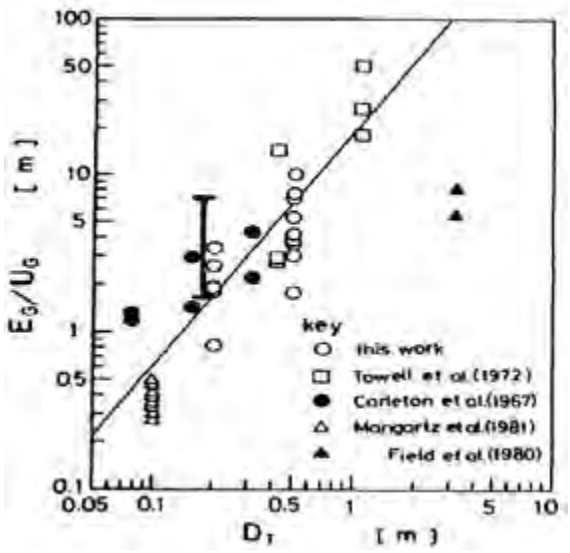

Figure 2.6. E_G /U_G against column diameter (taken from (Wachi & Nojima, 1990). The solid line shows data disparity, vertical solid line presents data field reported by (Grund, 1988) for aerated organic liquids.

In spite of a number of models for calculating the gas dispersion coefficient in a BCR, the plot of the experimental data used in developing these models show a large disparity in the data by nearly an order of magnitude. In fact, data from same authors using the same measuring techniques were noticed to be subject to large scatter of the factor of 5 (Deckwer & Schumpe, 1993).

Grund (Grund, 1988) carried out a study on measuring E_G data in a 15m diameter column with organic liquids and observed same large data scatter. The vertical line of Figure 2.6 illustrates the range of data measured by (Grund, 1988). Due to the inaccuracy in employing the proposed model of Eq.(2.54) Eq.(2.55) and Eq.(2.56) two-bubble class model was recommended by (Joseph & Shah, 1984) and (Shah, et al., 1985). In the recommendation, the ADM approach was adopted since it is applicable only for homogeneous bubbly flow and not for gas - phase dispersion measurement in a heterogeneous flow regime.

The developed model with consideration of two-bubble class models was expected to be more accurately implemented with an addition of appropriate dynamics of bubble coalescence and break-up (Shah & Deckwer, 1983). Moreover, it has been suggested that there is still a need for studies which support the development of structured hydrodynamic models of the gas phase in BCRs (Deckwer & Schumpe, 1993). Following the verification of

the developed E_G with experimental data, the theoretical basis for its development will be adopted in this work.

2.7.6. Hydrodynamic parameters - bubble characteristics

Bubble population, their gas holdup and their rise velocities have significant effects on changing the hydrodynamics of heat and mass transfer coefficients in a BCR (Kantarci, et al., 2005). Based on this, an accurate computation of these bubble population parameters will allow for accurate prediction of hydrodynamic parameters in a BCR system. Although methodologies have been explored to estimate bubble population properties, all of the methods were based on a 2-bubble class model proposed by (Krishna, et al., 1991). The proposed classification, however, limits the classification of bubble hold-up and rise velocity to two classes of large and small bubble groups.

The dynamic gas disengagement (DGD) is a widely accepted method to investigate bubble groups, bubble hold-up structures and their rise velocities. The DGD technique involves measurement of drop in dispersion height after turning off of gas flow into the column. An advanced analysis of the disengagement profile could yield information on separate bubble population classes contributing to the gas holdup (Schumpe & Grund, 1986). The central idea of the technique is that, different bubble classes in the dispersion can be determined provided that there are significant differences between their rise velocities. This idea was supported by the work of (Li & Prakash, 2000) who discovered that the rate at which instantaneous gas holdup drops depend on fraction and rise velocities of the different bubble classes. Thus, they noticed that an initially fast rising larger bubbles escaping from the bulk liquid lead to a fast drop in gas holdup. Subsequently, when all the larger bubbles had left the column, slower moving bubbles were seen disengaging at a slow rate coupled with the slow rate of drop in dispersion height.

The possibility of developing an advanced analysis of the disengagement profile provides a motivation to couple ERT measurements to gas disengagement process in this work. Such a coupling technique is anticipated to allow for higher bubble size classification in the column given ERT high temporal resolution.

2.7.7. Bubble size distribution

The diagram in Figure 2.7 illustrates the experimental set-up to measure bubble size distribution (BSD) by the photographic method carried out by (Akita & Yoshida, 1974). A set of experiments were carried out in 3 transparent acrylic resins of height 250cm and square cross sections: 7.7cm x 7.7cm, 15cm x 15cm and 30cm x 30cm. At the base of the column, a single orifice gas sparger was mounted where perforated and porous plates gas spargers were used with the 15cm x 15cm column. Notably, the air distributors of varied dimensions, pore diameters and pitch were changed, i.e. from perforated to porous plate spargers. The changing was done is a search of an air distributor that produces relatively uniform bubble size distribution at lower gas flow rates. A single orifice sparger was also tested to simulate more practical bubble evolution processes. In all the measurements, a gas chamber was installed at the base of the sparger plate at the bottom of the column for the purpose of minimizing the fluctuation of the gas pressure.

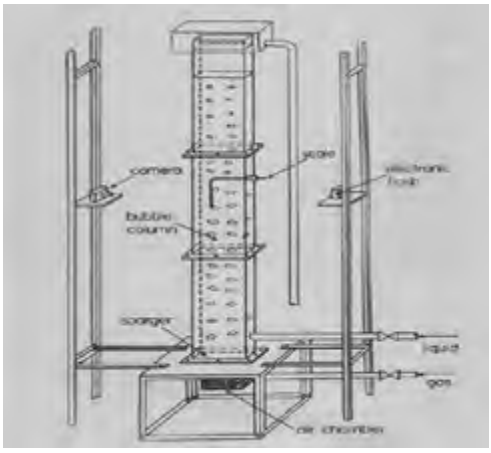

Figure 2.7. Experimental set-up for bubble size distribution model development (Akita & Yoshida, 1974)

Several experiments involving changing the liquid properties in the perforated and porous plates spargers were conducted. In the case of the experiment conducted in a single orifice sparger, the diameter of the orifice and the phase state of the system used are stated in Table 2.2.

In Figure 2.7, a blower located at the base of the column supplied the air (N_2) into the column for absorption and bubble size measurements. Optical cameras and electronic flash light systems placed at the opposite sides of the column were used to capture photographic images. These were further processed to determine the bubble sizes. The shapes of the bubbles were noticed to be non-spherical and were approximated by an oblate spheroid. The maximum and minimum dimensions of individual bubbles were then scaled on photographic prints. The sizes of bubble classes were represented by arithmetic mean x values of the maximum and minimum dimensions of bubble population in bubble classes scaled on the photographic images. The result of bubble size measurement for a run made using a single orifice sparger is tabulated in Table 2.3. Column 3 of Table 2.3 shows the number of bubbles in the range of bubble sizes stated in column 1. The geometric mean of the upper and lower limit of each bubble size range was calculated and presented in Column 2. Bubbles with major axis smaller than 0.8mm were ignored in the work since their contributions to the gas hold-up and interfacial areas were negligible.

Column 4 of Table 2.3 highlights the number of bubbles for each bubble size range as percentage, $\Delta F \times 100$, of the total number of bubbles, while column 5 gives the cumulative percentage, $F \times 100$, i.e. distribution function defined by

$$F(x) = \int_0^x f(x)dx \tag{2.57}$$

where $f(x)$ is the probability density function. The n^{th} moment of the distribution, μ_n', was defined by

Table 2.2. Experiments with single-orifice sparger (Akita & Yoshida, 1974)

Column Diameter	Orifice Diameter	Systems used	Temp (o_C)
7.7	0.30	Water-air (or oxygen)	20
7.7	0.30	Glycol-air (or oxygen)	20
7.7	0.30	Methanol-air (or oxygen)	20
7.7	0.30	Carbon tetrachloride - air	20
15.0	0.45	Water - air (or oxygen)	20
15.0	0.20	Water - air	20
15.0	0.10	Water - air	20
15.0	0.45	Water - air	5
15.0	0.45	Water - air	40
15.0	0.45	Glycol – air (or oxygen)	20
15.0	0.45	30 vol. % glycol - air	20
15.0	0.45	Methanol – air (or oxygen)	20
15.0	0.45	Carbon tetrachloride - air	20
30.0	0.50	Water - air	20

$$\mu'_n = \int_0^\infty x^n f(x)dx = \int_0^1 x^n dF \tag{2.58}$$

Columns 6 and 7 of Table 2.3 show respectively the second and third moment of the distribution of bubble sizes. The volume-surface of mean diameter of bubble swarm was calculated using the expression

$$d_{vs} = {\mu'_3}/{\mu'_2} \tag{2.59}$$

Where

$$\mu'_3 = \int_0^\infty x^3 f(x)dx = \sum_{i=1}^{N} \Delta\, \mu'_{3,i} \tag{2.60}$$

and

$$\mu_2' = \int_0^{\infty} x^2 f(x) dx = \sum_{i=1}^{N} \Delta \mu_{2,i}' \tag{2.61}$$

The function $\Delta\mu_{n,i}'$ was then defined as

$$\Delta\mu_{n,i}' = x^n \times \Delta f_i; i = 1,2,3, \dots N \tag{2.62}$$

where N is the number of largest class of bubble sizes.

Accordingly, the probability density function $f(x)$ was then found to be expressible as

$$f(x) = \frac{1}{\sigma x\sqrt{2\pi}} \exp\left(-\frac{1}{2}\left(\frac{ln(x) - m}{\sigma}\right)^2\right) \tag{2.63}$$

Combining Eq.(2.59) and Eq.(2.63) , one gets

$$\mu_n' = \exp\left(mn + \frac{\sigma^2 n^2}{2}\right) \tag{2.64}$$

The derivation of the volume-surface mean bubble diameter of Eq.(2.65) is based on the definition of Eq.(2.64) .

$$d_{vs} = {\mu_3'}/{\mu_2'} = e^{(m+2.5\sigma^2)} \tag{2.65}$$

The exponential of geometric mean of bubble size, m, and the standard deviation, σ, could then be expressed in terms of μ_3' and μ_2' in the forms

Table 2.3. Example of calculations for model development of bubble size distribution (Akita & Yoshida, 1974)

Range, mm	$x_,$, mm	No. of bubbles	$\Delta F_i \times 100$	$F \times 100$	$\Delta\mu_2', mm^2$	$\Delta\mu_3', mm^3$
0.9 – 1.0	0.945	260	8.225	8.23	0.074	0.07
1.1 – 1.5	1.27	450	14.24	22.47	0.230	0.29
1.6 – 2.0	1.78	416	13.16	35.63	0.417	0.74
2.1 – 2.5	2.29	452	14.30	49.93	0.750	1.72
2.6 – 3.0	2.79	454	14.36	64.29	1.118	3.12
3.1 – 4.0	3.52	479	15.15	79.44	1.877	6.61
4.1 – 5.0	4.53	241	7.624	87.06	1.565	7.09
5.1 – 6.0	5.53	141	4.461	91.52	1.364	7.54
6.1 – 8.0	6.98	145	4.589	96.11	2.235	15.60
8.1 – 10.0	8.99	58	1.835	97.94	1.483	13.33
10.1 – 15.0	12.3	40	1.265	99.21	1.914	25.54
15.1 – 20.0	17.4	18	0.5694	99.78	1.724	29.99
20.1 – 25.0	22.4	3	0.09491	99.87	0.476	10.67
27.0	27.0	1	0.03164	99.90	0.230	6.22
27.4	27.4	1	0.03164	99.94	0.237	6.50
30.0	30.0	1	0.03164	99.97	0.284	8.53
30.3	30.3	1	0.03164	100.00	0.290	8.79
D $= 15.0cm$	U_G $= 46.2\ m$ $/hr$	$\mathrm{d_{vs}}$ $= 9.24\mathrm{mm}$	d_g $= 2.32mm$	σ $= 0.744$	$\sum_{i=1}^{N} \Delta\mu_{2,i}'$ $= 16.268$	$\sum_{i=1}^{N} \Delta\mu_{3,i}'$ $= 150.35$

$$m = \frac{3}{2} ln\mu_2' - \frac{2}{3}\ ln\mu_3' \text{ and } \sigma = \sqrt{\frac{2}{3}} ln\mu_3' - ln\mu_2' \qquad (2.66)$$

The obtained values for d_{vs}, d_g and σ using Eq.(2.65) and Eq.(2.66) are stated in Table 2.3.

The determination of bubble size distribution by the photographic technique as done by (Akita & Yoshida, 1974) is liable to error due to the geometry of the cylindrical column boundary. The column curve surface will have to be accounted for in order to accurately resolve the bubble sizes. Besides, the technique cannot be used for bubble size analysis in an opaque multiphase system or column. However, the ERT technique, being a non-invasive imaging technique, is useful in both opaque and transparent columns. The method of analysis of the bubble size distribution by the photography approach will be adopted in this work for bubble size distribution analysis using ERT measurements.

2.7.8. Bubble rise velocity

Following an assumption that the shape of bubbles is spherical, the volume – surface mean bubble diameter, d_{vs}, has been correlated to the arithmetic mean of bubble length, $\overline{L_b}$, in the work of (Ueyama & Miyauchi, 1976) as

$$d_{vs} = 1.5\overline{L_b} \tag{2.67}$$

In a study to determine the relationship between d_{vs}, and the arithmetic mean bubble rise velocity, $\overline{U_b}$, conducted by (Ueyama & Miyauchi, 1976), (Akita & Yoshida, 1974) and (Koide, et al., 1966), their results were in agreement with that carried out by (Fukuma, et al., 1987). In the work of (Ueyama & Miyauchi, 1976) and (Fukuma, et al., 1987), a dual electro-resistivity probe method was implemented to study the relationship between $\overline{U_b}$ and d_{vs}. It was observed that all the data for both the gas-liquid and the gas-liquid-solid bubble column could be correlated by a Davies-Taylor type equation of the form

$$\overline{U_b} = 1.3\sqrt{g d_{vs}} \tag{2.68}$$

Eq.(2.68) could be re-expressed in the form of

$$0.59\frac{\overline{U_b}^2}{g} = d_{vs} \tag{2.69}$$

Furthermore, when Eq.(2.69) is simplified to include the drift flux of gas and the cross-sectional averaged gas hold-up, Eq.(2.70) is derived, where $\overline{U_b} = {}^{v_D}/_{\overline{\varepsilon_g}}$ (Fukuma, et al., 1987).

$$0.59\frac{\left(v_D/\bar{\varepsilon_g}\right)^2}{g} = d_{vs} \tag{2.70}$$

Review of literature on the relationship between the d_{vs} to the $\overline{U_b}$ in form of Eq.(2.70) indicates that the $\overline{U_b}$ equals the drift flux of gas, v_D, divided by the cross-sectional averaged gas holdup, $\bar{\varepsilon_g}$, (Fukuma, et al., 1987).

This means that it is possible to interpret the low spatial resolution of ERT images and its effectiveness for gas holdup measurements to determine the $\overline{U_b}$ from which hydrodynamic parameters in the reactor could be calculated. The bubble number density distribution (i.e. a countable entity) is influenced by phenomena of bubble coalescence and breakup, which affect bubble sizes as they swarm axially in a column. The bubble number density distribution in a column operating at either a steady or an unsteady state cannot be measured by an analysis of ERT images solely given its low spatial resolution.

Thus, an integration of a model of a physical system to ERT measurements is envisaged to yield a method of interpreting ERT images for the calculation of bubble population properties in a column. The PBM is an effective tool for modelling physical systems in a column because of its mathematical framework, described in section 2.8, includes paths for bubble breakage and coalescence. The developments of bubble coalescence and bubble breakage models are also reviewed following the review of the theoretical framework of PBM development.

2.8. Measurements of bubble population swarming parameters at steady state: Electrical Conductivity Probe Technique

Hydrodynamic parameter computations in a column require knowledge of the BNDD with respect to space and bubble size. The volumetric mass transfer rates, the specific interfacial area, the gas holdup fractions, the global mean bubble sizes and the intensity of mixing of the 2-phase fluid system are examples of the hydrodynamic parameters that depend on BNDD, physical properties of the fluid system and geometric dimensions of the column. The relationships of the hydrodynamic parameters to bubble population properties have been given in subsections of Section 2.7 of this chapter.

An experiment was conducted by (Luo, 1993) to measure bubble properties using a 5-point Electrical Conductivity Probe Technique set-up in a plexi-glass column with an inner diameter of 0.288m and a height of 4.33m. The gas distributor for the column was placed between the main column section and a stainless steel liquid inlet section. The 5-point conductivity micro-probe with a tip diameter of 0.3mm was then connected to a signal processing unit system. The system consisted of a real time signal recording and storage unit connected via an interface card to a personal computer. An oscilloscope was also used to calibrate the conductivity probe. The superficial gas and liquid velocities were varied within the range of 0.02 - 0.2 m/s and 0 – 0.02m/s respectively and measurement were made at two temperature values of $11\pm1^{o}C$ and $25\pm1^{o}C$. The measurements were then taken at two local axial lengths of 0.2 and 2.0m along the column height from the gas distributor respectively. At each level, measurements were made at varied radial positions from the centre (dimensionless radius) at 0.25, 0.5, 0.6, 0.7, 0.8, 0.9, and 0.95.

The conductivity probes generated signals for measurements due to the difference in electrical conductivity between the liquid phase and the gas phase. At the detection of a bubble in the liquid by the probe sensor, a square pulse of voltage was generated. A 1-point (sensor) probe had been used to determine the local gas void fraction, before an improvement of its fabrication lead to its use for measuring bubble sizes, bubble velocities and bubble frequencies. (Buchholz, et al., 1981) and (Yu & Kim, 1990) used a 2-point probe to measure bubble size distribution and bubble motion. The 2-point probes could only yield information on bubble chord lengths and not bubble volumes or their equivalent diameters. An enhanced design of the probe configuration with more point was then developed, which was useful for measuring bubble curvatures and their volumes in a vessel.

2.8.1. The 5-point probes of (Burgess & Calderbank, 1975)

The 5-point conductivity probes were first developed by (Burgess & Calderbank, 1975). It is usually connected to a digital computer in order to process the output voltage pulse signal sequences generated when a bubble approaches the probe sensor assembly as shown in Figure 2.8.

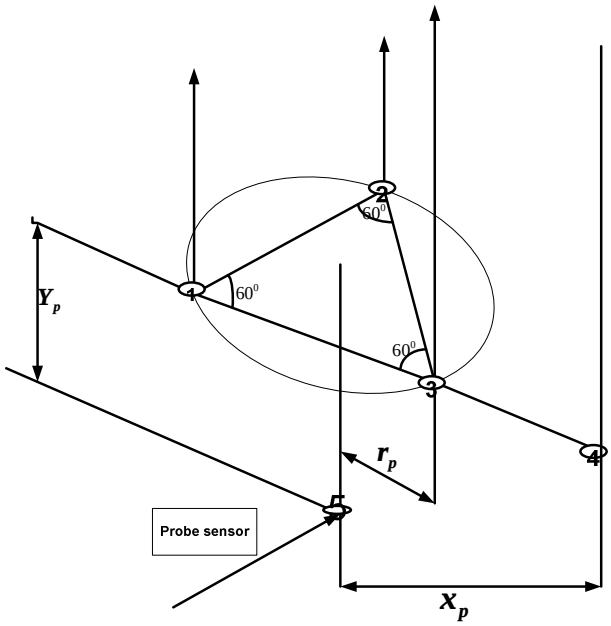

Figure 2.8. The spatial orientation of the probe tip developed by (Burgess & Calderbank, 1975).

Some of the advantages of the 5-point probes technique are as follow:

1) The probe systems calculate the position of a bubble relative to the central line by detecting the point at which it is struck by the bubble;

2) Using the 5-point conductivity probe technique, events of bubble collision, which are approximately symmetrical with the probe axis was referred to as true bubbles, otherwise, false bubbles. The events of true bubbles were accurately determined by conductivity probes;

3) The shape of a true bubble was calculated from the difference in signal lengths generated by different probe sensors. The use of the 5-point conductivity probes allows for more signals to be generated than the use of the 2-point probes sensors. Hence, bubble volumes may be estimated with higher accuracy from analysis of obtained data using the 5-point conductivity probes than from the 2-point conductivity probes. However, since bubbles encountered by the 5-point probes that are not symmetrical around the probe axis (i.e. false bubbles), a large number of bubbles were wasted by this technique.

Additionally, in measuring the bubble rise velocities, the technique assumes the bubble rise vertically through the column, when bubbles in true sense have a more randomly distributed direction. The limitation of the assumption on the direction of bubble rising, however, is a

source of error with respect to the number of true bubbles recorded by the 5-point conductivity probes system.

2.8.2. Measurement of bubble population parameters using (Burgess & Calderbank, 1975) probe design technique

The method of estimating bubble velocities and bubble sizes from obtained voltage pulse signals by the 5-point conductivity probes technique of (Burgess & Calderbank, 1975) is presented below. The presentation will describe the disadvantages of the technique.

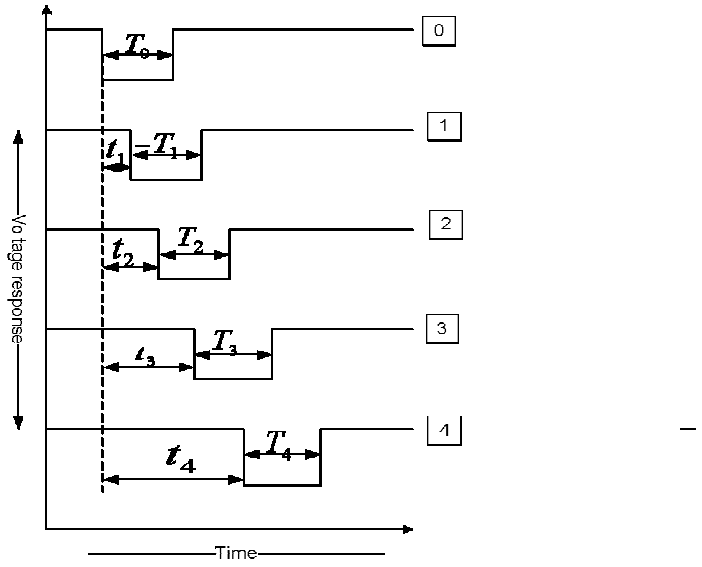

Figure 2.9. Pictorial representation of pulse sequences.

To calculate the bubble rise velocities of true bubbles, which are symmetrical around the probe axis (i.e. at probe sensor 5 in Figure 2.8), the expression of Eq.(2.71) is used. In Figure 2.8, the probes' separation axial length denoted by $y_p$is accurately known as well as the respective time lag (Figure 2.9) of detected subsequent signals t_i from a reference signal t_0.

$$U_{b,z} = \frac{3y_p}{t_1 + t_2 + t_3} \qquad (2.71)$$

Eq.(2.71) would have been accurate if the bubbles actually move vertically in the column since this is a basis assumption of Eq.(2.71) .However, when some bubbles move at an angle to the vertical, the model of Eq.(2.71) is inefficient to determine the bubble rise velocities.

(Luo, 1993) calculated the central vertical chord length of a true bubble, L_c, with the expression

$$L_c = U_{b,z} T_o^m \tag{2.72}$$

where $T_i^m (i = 0)$ is the modified pulse duration time for probe sensor i (Burgess & Calderbank, 1975) and was taken to represent the real pulse duration time by (Luo, 1993). As illustrated in Figure 2.8, the probe sensor 4 is used to measure the vertical distance, L_d (as in Eq.(2.73)), between the bubble leading surface at the centreline and at the radial position, x_p. It was also used to measure the bubble vertical length at this position L_e as in Eq.(2.74) .

$$L_d = U_{b,z} t_4 \tag{2.73}$$

$$L_e = U_{b,z} T_4^m \tag{2.74}$$

From the data of L_c, L_d, L_e and x_p, the bubble volume may accurately be calculated using the reported correlations (Tadaki & Maeda, 1961), (Clift, et al., 1978) and (Fan & Tsuchiya, 1990). The local gas holdup was measured using the signals of the central sensor by a correlation of the form

$$\varepsilon_G = \frac{\sum T_o^m}{t_{total}} \tag{2.75}$$

where $\sum T_o^m$ shows that the real pulse duration time for all signal responses including both true and false bubbles detected by the central sensors within a given measurement period t_{total} were considered.

2.8.3. The five-point probes of (Steinemann & Buchholz, 1984)

Steinmann and Buchholz (1984) upgraded the design of the 5-point conductivity probes by (Burgess & Calderbank, 1975) by placing the 4th electrode on the same radial position as the 1st – 3rd sensor as shown in Figure 2.10.

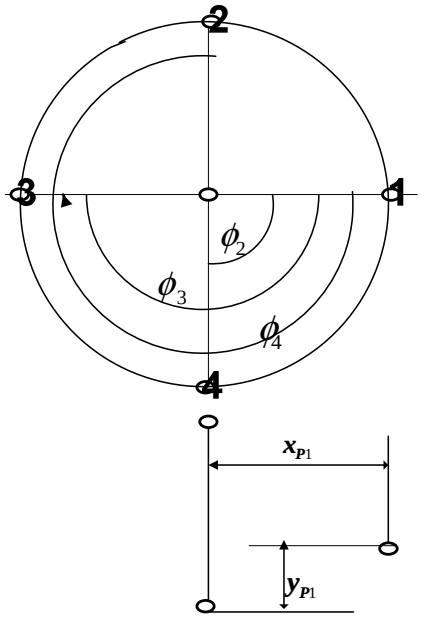

Figure 2.10. Probe sensor design of Steinmann and Buchholz (1984).

This new design by (Steinemann & Buchholz, 1984) enables a development of estimation methods for determining the direction of bubble motion. The bubble motion is an additional bubble property to bubble size distribution, bubble velocity and frequency of bubbles measurable by the 5-point probes design (Burgess & Calderbank, 1975). The bubble motion was determined through an analysis of the recorded voltage pulse sequences coupled with the principle of analytical geometry.

Unlike the 5-point probes design by (Burgess & Calderbank, 1975), the new design by (Steinemann & Buchholz, 1984) did not discard registered bubbles that were not symmetrical around the probe axis. The new design utilises voltage pulses due to both true and false bubbles. Although, the new design by (Steinemann & Buchholz, 1984) use more bubble signals than that by (Burgess & Calderbank, 1975), the complication of the method is suggested to be a source of error particularly when the bubble shapes depart largely from sphere or ellipsoid.

2.8.4. Measurement of bubble population parameters using (Steinemann & Buchholz, 1984) probe design technique

The information on a complete bubble motion including the absolute bubble velocity $U_{b,a}$, the angle between the probe axis and the bubble trajectory, θ, and the horizontal angle, φ,

as in Figure 2.11, are required for a reliable interpretation of the signal combinations using the design of (Steinemann & Buchholz, 1984).

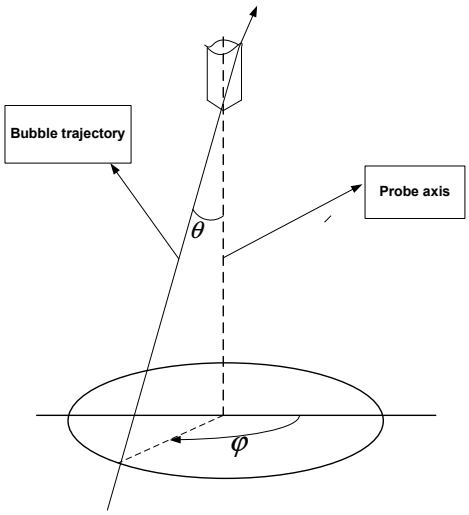

Figure 2.11. Definition of bubble movement parameters.

The horizontal angle φ, ranging from $0-360^0$, gives information about the direction of bubble motion, while the vertical angle, θ, ranges from $0-180^0$and takes the value of either 0^0or $180^0$to describe a situation when bubbles are vertically ascending or descending. The bubble motion parameters $U_{b,a}$, θ and φ were calculated by solving a non-linear system of equations that included the terms of probe signals and parameters of bubble geometry. The system of equations was over-determined since 3 unknown parameters $U_{b,a}$, θ and φ were solved from a system of 4 equations as in Eq.(2.76) . The over-determined problem which compensated for possible errors introduced by the determination of the pulse time was solved by a minimization approach.

$$U_{b,a} = \frac{2y_{pi}^{m}}{T_o + T_i}\ , i = 1,2,3,4 \qquad (2.76)$$

where $y_{pi}^{m} = y_{pi}\cos\theta - x_{pi}\sin(\varphi + \varphi_i) sin\theta$.

The coordinates of the bubble surface from the probe signals and the probe geometry were obtained from the known 3 parameters of bubble motion. (Steinemann & Buchholz, 1984) proposed a complex correlation for determining the coordinate of the bubble surface from known 3 parameters of $U_{b,a}$, θ and φ, assuming the bubbles were spheres or ellipsoids when rotated. The availability of the model for calculating the coordinates of the bubble surface, thus, motivated a derivation of a model for estimating bubble sizes.

The possibility of calculating the bubble rising velocity vertically from the known absolute bubble velocity, $U_{b,a}$, and the vertical angle, θ, instead of an assumption that bubbles rise vertically makes the technique of (Steinemann & Buchholz, 1984) more accurate than that of (Burgess & Calderbank, 1975). The long length of time required to solve the array of equations involved using the (Steinemann & Buchholz, 1984) technique is a demerit for using the method. Moreover, the induced large errors when the bubble shape departs significantly from a sphere or an ellipsoid are an additional demerit. Notably, the method of measurement of local gas holdup based on the technique of (Burgess & Calderbank, 1975) is similar to that of (Steinemann & Buchholz, 1984) as expressed in Eq.(2.75) .

2.8.5. Conclusions on the use of the Electrical Point Probe Technique for bubble population parameter measurements

The 5-point Electrical Conductivity Probe Technique is useful for measuring bubble velocity, bubble size distribution, the direction of bubble motion, bubble frequency and local gas holdup. However, the following demerits have been noticed in the use of the Electrical Point Probe Technique to measure bubble population parameters: 1) It is applicable only in a BCR system that has certain minimum electrical conductivity; 2) The probe technique suffers from error due to underestimation when used to measure gas holdup in the column; 3) Bubble parameters measurable by the probe technique are sensitive to pre-determined absolute velocity of bubbles, $U_{b,a}$, angle between the probe axis, the bubble trajectory, θ, and the horizontal angle φ. Thus, the correlation of (Steinemann & Buchholz, 1984) for calculating the bubble sizes from their coordinate values is dependent on the spherical or ellipsoidal shape of the bubbles. This proposition is supported by the wok of (Amin, et al., 2015) who noticed that the radial profiles of bubble frequency, bubble chord length and bubble rise velocity were relatively flat at low gas flow rates and parabolic at high gas flow rates. Any distortion of the shape of bubbles forms a source of error in the detected output voltage signals; 4) Estimation of the bubble motion and its shape require solving non-linear system of equations for each bubble, which takes a long time to solve.

Similar to the use of an oscilloscope to calibrate the conductivity probe, the ERT measurements will be calibrated using a differential pressure measurement method. However, the proposed ERT and PBM hybrid technique is intended to address the error in

the bubble parameter measurements using the conductivity probes given the assumptions associated with the technique.

2.9. Theoretical framework for PBM source terms development – bubble coalescence rate and breakage rate models

A Population Balance Equation (PBE) is one satisfied by the product density function of order one. The population of particles can increase in a closed system due to particle fission or particle agglomeration. In such cases, the individual particle state is described by a scalar variable x, which lies on the positive real line. Such variable may represent size variables of diameter and volume or mass. Particles can also grow as a result of mass transfer from the surrounding continuous phase at a rate $\dot{X}$ that depends on x.

2.9.1. Agglomeration of particle system

In this section, a derivation of the product density equation is made for a process in which the number of particles progressively decreases as a result of binary agglomeration (coalescence) between particles. It is assume a particle state of an individual particle is a scalar variable on the positive real line and grows at a rate $X(\dot{x})$. Thus, the probability that a particle of state x at time t agglomerates with a particle of state y (also at time t) during the time interval $(t, t+dt)$ is assumed to be given by $q(x,y)dt$, where $q(x,y)$ is symmetric with respect to x and y.

The first product density is derived by considering the various ways by which a particle may be in $(x, x+dx)$ at time $t+dt$ given by (Ramkrishna & Borwanker, 1973)

Prob. (there is a particle in $(x, x+dx)$ at $(t, t+dt)$)

$$= f_1(x, t+dt)dx \tag{2.77}$$

The ways are as follow:

1) Starting from conditions at time t, it is observed that a particle may be in state $(x - dx', x)$ at time t and may grow into the interval $(x, x+dx)$ if it does not agglomerate with any other particle in the population. The probability of this event occurring is

$$f_1(x-dx',t)dx'\left[1-\int_0^{\infty} f_1\,(\zeta,t|x-dx')q(x-dx',\zeta)d\zeta dt\right] \tag{2.78}$$

where $f_1(\zeta,t|x)d\zeta$ is the probability that there is a particle in state $(\zeta,\zeta+d\zeta)$ given that there is particle at state x. Eq.(2.78) may be rewritten as

$$f_1(x-dx',t)dx'-\int_0^{\infty} f_2\,(x-dx',\zeta;t)q(x-dx',\zeta)d\zeta dtdx' \tag{2.79}$$

where Eq.(2.79) involves a second order product density.

2) A second means of obtaining a particle in state $(x,x+dx)$ at time $(t,t+dt)$ is by agglomeration of two smaller particles during the time interval $(t,t+dt)$. The probability of this is given by

$$\frac{1}{2}\int_0^{x} f_2(x-y,y;t)\,q(x-y,y)dydxdt \tag{2.80}$$

which has a product density of order 2. The factor $^1/_2$ accounts for symmetry of integrand about $^x/_2$. Equating Eq.(2.77) to the sum of Eq.(2.79) and Eq.(2.80) and further simplification leads to the $f_1(x,t+dt)dx$ being re-expressed as Eq.(2.81)

$$\begin{aligned}\frac{\partial f}{\partial t}+\frac{\partial[f_1\dot{X}(x)]}{\partial x}=\frac{1}{2}\int_0^{x} f_1(x-y,t)f_1(y;t),q(x-y,y)dy\\ -f_1(x;t)\int_0^{\infty} f_1\,(\zeta;t)q(x,\zeta)d\zeta\end{aligned} \tag{2.81}$$

2.9.2 Bubble coalescence rate model development based on the framework

The three steps involved in the coalescence of two bubbles by the bubble coalescence theory are as follows:

1) Collision of bubbles and trapping of the liquid between them;

2) Flattening of bubble surface and drainage of the trapped liquid;

3) Coalescence of two bubbles.

The first step indicates that coalescence rate is connected to the collision rate. The duration of coalescence process is dependent on the flattening of bubble surface and drainage of the trapped liquids.

Bubble collision that leads to coalescence of bubbles are due to three cumulative bubble motion mechanisms:

1) Turbulence effects (random motion of bubbles due to turbulence in the liquid phase);

2) Buoyancy effects (collision of bubbles due to differences in rise velocities of bubbles of different sizes);

3) Laminar shear effects (collision resulting from bubbles of same size or different sizes located in different sections of the high and slow sections of the velocity field).

2.9.3. Turbulence driven collision rate

Turbulent collision rate describes the bubble motion in the liquid phase resulting in collision due to turbulence effect owing to the fluctuating turbulent velocity of the liquid phase. The expression for turbulent motion as a function of bubble size, concentration and velocity is given as

$$\theta_{ij}^{T} = n_i n_j S_{ij} (\bar{u}_{ti}^2 + \bar{u}_{tj}^2)^{1/2} \tag{2.82}$$

Here n_i, n_j are the concentrations $[m^{-3}]$ of bubbles of radius $[m]$ r_{bi} and r_{bj} respectively. The average turbulent fluctuating velocity of the bubble is represented by u_t $[ms^{-2}]$, while S_{ij} is the collision cross-sectional area $[m^2]$ of a pair of bubbles given as

$$S_{ij} = \frac{\pi}{4}(d_{bi} + d_{bj})^2 \tag{2.83}$$

The assumptions made in the development of turbulent collision rates are: 1) that the velocities of bubbles in Eq.(2.82) are taken to be the turbulent eddy velocity of the length scale of bubbles; 2) that the bubble sizes lie in the inertial sub-range; 3) and that turbulent collision rates are isotropic. The inequality expression for the inertial sub-range of bubble sizes that bubbles should satisfy is of the form

$$k_e \ll k_b \ll k_d \tag{2.84}$$

where, k_e, denotes the wave number $[m^{-1}]$ of the large energy containing eddies, k_b is the wave number corresponding to a bubble size and k_d is the wave number of eddies of viscous dissipation.

As found by (Batchelor, 1953), the wave number for energy dissipation (k_d) is equivalent to the inverse of the microscale of turbulence and was expressed as

$$k_d = 0.5\frac{\varepsilon^{1/4}}{\vartheta^{3/4}} \tag{2.85}$$

where ε is the energy dissipation per unit mass $[m^2 s^{-2}]$, ϑ, is the kinematic viscosity$[m^2 s^{-1}]$. The energy dissipation per unit mass is expressed as

$$\varepsilon = u_s \times g \tag{2.86}$$

The wave number of large energy, k_e, containing eddies is assumed to be the inverse of the size of the energy containing eddies, i.e. the diameter of the vessel. The turbulent velocity in the inertial sub-range of isotropic turbulence is expressed as

$$u_t = 1.4\varepsilon^{1/3} {d_b}^{1/3} \tag{2.87}$$

where d_b is the diameter of a bubble. When Eq.(2.83) to Eq.(2.87) are substituted into Eq.(2.82) , the turbulent collision rate of Eq.(2.82) becomes

$$\theta_{ij}^{T} = 0.089\pi n_i n_j \left(d_{bi} + d_{bj}\right)^2 \varepsilon^{1/3} \left({d_{bi}}^{2/3} + {d_{bj}}^{2/3}\right)^{1/2} \tag{2.88}$$

2.9.4. Buoyancy driven collision rate

Bubble coalescence driven by bubble buoyancy collision effects is as a result of bubbles of different sizes rising with varied velocity values. (Friendlander, 1977) modelled the buoyancy driven collision rate as

$$\theta_{ij}^{B} = n_i n_j S_{ij} (u_{ri} - u_{rj}) \tag{2.89}$$

where u_r is the rise velocity of bubble, which is given by the expression

$$u_r = \left(\frac{2.14\sigma}{\rho_l d_b} + 0.505 g d_b\right)^{1/2} \quad (2.90)$$

In Eq.(2.90) , the liquid density[kgm^{-3}] and surface tension [kgs^{-2}] are represented with the symbols ρ_l and σ respectively. Eq.(2.89) is applicable only to uncontaminated bubbles with mobile gas liquid interfaces (Azad & Sultana, 2006).

2.9.5. Laminar shear collision rate

Laminar shear collision rate results from the development of gross circulation pattern in a bubble column at a sufficiently high gas flow rates. The gross circulation pattern of the liquid phase produces a radial velocity distribution that enables bubbles situated at a high-velocity region to overtake or collide with other bubbles of the same size and rise velocity located at a slow velocity region. As defined by (Friendlander, 1977), the functional form of the collision rate due to laminar shear is of the form

$$\theta_{ij}^{LS} = {}^4/_3\, n_i n_j \left(r_{bi} + r_{bj}\right)^3 \left(\frac{d\overline{u_l}}{dR}\right) \quad (2.91)$$

where u_l is the liquid circulation velocity $[ms^{-1}]$, R is the radial coordinate of the column $[m]$ and $\frac{d\overline{u_l}}{dR}$ is the average shear rate $[s^{-1}]$. The average shear rate is found by averaging the local shear rate over the radial dimension of the column with an inclusion of the velocity profile developed by (Walters & Blanch, 1983) of the form

$$u_l = u_{l,max}(1 - R^2/(\alpha R_T)^2) \quad (2.92)$$

where αR_T is the transition point, $u_{l,max}$ is the velocity at the centre of the column. Thus, the mean shear rate is given by the expression

$$\frac{5.3\, u_{l,max}}{R_T} = \bar{\gamma}(R) = \frac{d\overline{u_l}}{dR} \quad (2.93)$$

The maximum liquid circulation, $u_{l,max}$, for the turbulent flow is given by the expression

$$u_{l,max} = \left(\frac{1 - 0.75\varepsilon_g}{1 - \varepsilon_g}\right)\left(\frac{\varepsilon_g g D_T^2}{48 V_t}\right) \quad (2.94)$$

where $V_t = \frac{0.0536 D_T^{1.77}}{\rho_l}$, D_T, ε_g and ρ_l are respectively the turbulent kinematic viscosity $[m^2 s^{-1}]$, diameter of the tank $[m]$, gas holdup fraction and liquid density $[kgm^{-3}]$.

2.9.6. Collision efficiency

The bubble coalescence efficiency or probability of bubble coalescence (P_c) is a function contact time (t_{ij}) between bubbles and the time (τ_{ij}) required for bubbles to coalesce. (Coulaloglou & Tavlarides, 1977) expressed the bubble collision probability as

$$P_{cij} = \exp\left(- {}^{t_{ij}}/_{\tau_{ij}} \right) \tag{2.95}$$

The coalescence time as modelled by (Oolman & Blanch, 1986b) is stated in Eq.(2.96) , while the contact time as found by (Levich, 1962) is expressed in Eq.(2.97) .

$$t_{ij} = \left\{ \frac{r_{ij}^3 \rho_l}{16\sigma} \right\}^{1/2} ln \frac{h_o}{h_f} \tag{2.96}$$

$$\tau_{ij} = \frac{r_b^{2/3}}{\epsilon^{1/3}} \tag{2.97}$$

Here h_o is the initial film thickness that has been estimated to be $1 \times 10^{-4} m$ (Kirkpatrick & Lockett, 1974); h_f is the critical film thickness where rupture occurs, which was calculated to be $1 \times 10^{-8} m$ by (Kim & Lee, 1987).

The total coalescence rate was obtained by the cumulative sum of bubble coalescence rate due to each of the three mechanisms: turbulence, buoyancy and laminar shear rate. The total coalescence rate between any two bubbles is given by the total collision frequency multiplied by the coalescence efficiency between them as in

$$\Gamma_{ij} = (\theta_{ij}^T + \theta_{ij}^B + \theta_{ij}^{LS}) \exp\left(- {}^{t_{ij}}/_{\tau_{ij}}\right) \tag{2.98}$$

The overall coalescence rate for all bubble population is thus given by

$$\Gamma_T = {}^1\!/_2 \sum_i \sum_j (\theta_{ij}^T + \theta_{ij}^B + \theta_{ij}^{LS}) \exp\left(-{}^{t_{ij}}\!/_{\tau_{ij}}\right) \tag{2.99}$$

where the constant ${}^1\!/_2$ is included to prevent counting coalescence events between bubble pairs twice.

2.9.7. Particle Fission

To derive an expression for the probability that there is a particle in state $(x, x + dx)$ at $(t, t + dt)$ due to particle fission (breakage) denoted by $f_1(x, t + dt)dx$, the following notation about the particle state probabilities at certain time need be made:

1) the probability that a particle of state x' at time t would break in the time interval $(t, t + dt)$ is assumed to be given by $\Gamma(x')dt$;

2) the probability of two or more particles breaking in the time interval $(t, t + dt)$ is $0(dt^2)$ since the breakage of a given particle is independent of all other particles;

3) assuming also that the probability of a daughter particle arising from a particle of state x' has its state between $(x, x + dx)$ is given by $P(x, x')dx$.

Furthermore, in deriving an expression for $f_1(x, t + dt)dx$, it is noticed that a particle may wind up in state $(x, x + dx)$ from time t to time $t + dt$ through either of two mutually exclusive ways:

1) A particle may be in adjacent interval $(x - dx', x)$ at time t, where $dx' = \dot{X}(x - dx')dt$, and grow into $(x, x + dx)$ without breaking during the time interval $(t, t + dt)$. The probability of this first case occurring is

$$f_1(x - dx', x)dx'[\,1 - \Gamma(x - dx')dt] \tag{2.100}$$

2) The particle might be in state $(x, x + dx)$ from a breakage of another larger particle during the time interval $(t, t + dt)$. The probability of this event occurring is

$$\int_x^\infty 2P(x, x'')\,\Gamma(x'')dt f_1(x'', t)dx''dx \tag{2.101}$$

The constant 2 appears in Eq.(2.101) because either of the two daughters from binary breakage of a parent may be in $(x, x + dx)$ at time $t + dt$. The integral term $P(x, x'')dx$ represents that a daughter particle of state interval $(x, x + dx)$ results from state x'' at time $t + dt$. The term $\Gamma(x'')dt$ stands for the particle being in state x'' and breakup in time interval $t + dt$, while $f_1(x'', t)dx''$ denotes the probability of the particle being in state interval $(x'', x'' + dx'')$ at time t.

The definition of $f_1(x, t + dt)$ leads to the development of Eq.(2.102) which describes the advection transport of a bubble property $f_1(x, t + dt)$ due to the phenomenon of bubble breakage leading to birth and death of bubbles.

$$\frac{\delta f_1}{\delta t} + \frac{\delta [f_1 \dot{X}]}{\delta x} = -\Gamma(x) f_1 + 2 \int_x^{\infty} P(x, x'')\, \Gamma(x'') f_1(x'', t) dx'' \qquad (2.102)$$

2.9.8. Bubble breakage rate model development based on the framework

In the following discussion, reference is made to the derived coalescence source term of Eq.(2.81) to explain the breakage rate source term. Gas bubbles evolving vertically upwards expand due to changes in gas density or due to mass transfer. When this occurs, the phenomenon of gas expansion contributes to external source terms in addition to the phenomena of bubble coalescence and break-up. Notably, the phenomena of coalescence and break-up contribute to the PBM source terms in the case where bubble coalescence leads to the birth of bubble in larger class bins and break-up phenomena lead to the birth of bubbles in smaller class bins. The event of bubble coalescence and break-up accounts for the PBM sink terms on the occasion when bubbles in a certain class die due to its coalescence with bubbles in other classes or bubbles in a class breaks up to produce bubbles in smaller classes. In a case when there is no sedimentation of gas bubbles during the processes of their evolution, the advection – dispersion equation of bubble number density could be written as in Eq.(2.103) .

In Eq.(2.103) , $m(v)$ is the mean number of daughter bubbles formed from the break-up of a mother bubble of size v; $f(v', v)$ is the probability density function of daughter bubbles generated from the rupture of a mother bubble of size v; $g(v')$ is the break-up frequency of bubbles of size v'.

$$\frac{\partial n(v',z,t)}{\partial t} + \nabla\left(u_g n(v',z,t)\right) = \left(\frac{1}{\rho_g}\frac{D\rho_g}{D_t} + \frac{\dot{n}a_p}{\alpha_g\rho_g/\mu_g}\right)\partial(v'f)/\partial v + \int_{v'}^{\infty} m(v)f(v';v)\,g(v)n(v,t) - g(v')n(v',t) + \frac{1}{2}\int_0^v n(v,t)\,n(v'-v,t)q(v,v'-v,t)dv - n(v',t)\int_0^{\infty} n(v,t)q(v,v',t)\,dv \quad (2.103)$$

The probability density function (p.d.f) of daughter bubbles, v', generated from the rupture of a mother bubble of size $v, f(v', v)$, is a p.d.f with reference to v' parameterised by v. It is not a joint p.d.f describing the distribution of both v' and v (Martinez, et al., 2010). Moreover, this p.d.f needs to satisfy the normalisation condition of the form $\int_0^{\infty} pdf\ f(x)dx = 1$. Thus, since $f(v', v) = 0$ for $v' > v$, the normalisation equation will take the form of $\int_0^v f(v', v)dv = 1$.

In a multiphase system of a cloud of bubble dispersion in a homogeneous and isotropic turbulent flow moving with the fluid and in the absence of gas expansion phenomenon and dissolution effects, the rate of change of bubble number density can be written as in Eq.(2.104) .

$$\frac{\partial n(v',z,t)}{\partial t} + \nabla\left(u_g n(v',z,t)\right) = \int_{v'}^{\infty} m(v)f(v';v)\,g(v)n(v,t)dv - g(v')n(v',t) + \frac{1}{2}\int_0^v n(v,t)\,n(v'-v,t)q(v,v'-v,t)dv - n(v',t)\int_0^{\infty} n(v,t)q(v,v',t)\,dv \quad (2.104)$$

The rate of change of $n(v', z, t)$ of Eq.(2.104) will take the form of Eq.(2.105) in a very dilute system, where the rate of bubble coalescence is zero and there is a phenomenon of bubble

breakage only. Eq.(2.104) will take the form of Eq.(2.106) in a flow regime having a Weber number less than the critical Weber number of 2.3 (i.e. no breakage process) but where the phenomenon of bubble coalescence takes place.

$$\frac{\partial n(v',z,t)}{\partial t} + \nabla\left(u_g n(v',z,t)\right) = \int_{v'}^{\infty} m(v) f(v';v)\, g(v) n(v,t) dv - g(v') n(v',t) \tag{2.105}$$

$$\frac{\partial n(v',z,t)}{\partial t} + \nabla\left(u_g n(v',z,t)\right) = \frac{1}{2}\int_{0}^{v} n(v,t)\, n(v'-v,t) q(v,v'-v,t) dv - n(v',t)\int_{0}^{\infty} n(v,t) q(v,v',t)\, dv \tag{2.106}$$

The PBM for $n(v',z,t)$ as stated in Eq.(2.105) and Eq.(2.106) describes the unsteady state multiphase fluid systems, i.e. the bubble number density $n(v',z,t)$ changes with time. If given a steady, quasi – one-dimensional flow where radial dispersion is negligible, the PBM of Eq.(2.104) , Eq.(2.105) and Eq.(2.106) will take the form of Eq.(2.109) , Eq.(2.107) and Eq.(2.108) respectively leaving out the first terms representing the unsteady state term of the system.

$$u_g(v',z)\frac{d\left(n(v',z)\right)}{dz} = \int_{v'}^{\infty} m(v) f(v';v)\, g(v) n(v) dv - g(v') n(v') \tag{2.107}$$

$$u_g(v',z)\frac{d\left(n(v',z)\right)}{dz} = \frac{1}{2}\int_{0}^{v} n(v)\, n(v'-v) q(v,v'-v) dv - n(v')\int_{0}^{\infty} n(v) q(v,v')\, dv \tag{2.108}$$

$$
\begin{aligned}
u_g(v',z)\frac{d\big(n(v',z)\big)}{dz} & \\
&= \frac{1}{2}\int_0^v n(v,t)\, n(v'-v) q(v, v'-v) dv \\
&- n(v') \int_0^\infty n(v) q(v, v')\, dv \\
&+ \int_{v'}^\infty m(v) f(v'; v)\, g(v) n(v) dv - g(v') n(v')
\end{aligned}
\tag{2.109}
$$

When focussing on a PBM having the breakage rate model as Eq.(2.107) and Eq.(2.109) , two closure problems of break-up frequency and probability density function of daughter bubbles need be solved. The development of the breakage frequency in the work of (Martinez, et al., 2010) is based on an assumption that bubbles are injected into a turbulent water flow which is locally homogeneous, isotropic and nearly equilibrium.

Additional assumptions are that the initial bubble size v or D_o (bubble size represented with volume or diameter) lie in the inertial sub-range, $\eta < D_o < L_x$. The symbols η and L_x are respectively the Kolmogorov microscale of viscous dissipation of the underlying turbulence and size of large energy containing eddies. It was also assumed that the bubble void fraction is always very small and that there is no two-way coupling between the two phases; i.e. the presence of air does not affect the evolution of turbulence in the water.

Accordingly, for a bubble to break, a requisite condition was that the surface of the bubble has to deform by the turbulent stresses in form of the deformation energy produced by the surrounding water. The minimum energy required to deform a bubble of size D was modelled as

$$E_s(D) = \pi\sigma D^2, \tag{2.110}$$

where σ is the surface tension of the liquid phase in the system. The surface restoring pressure defined as the surface energy per unit volume was

$$T_s(D) = \frac{6E_s}{\pi D^3} = \frac{6\sigma}{D} \tag{2.111}$$

The average deformation energy per unit volume produced by the turbulent stresses as a result of velocity fluctuations existing in the liquid between two points separated a distance D was

$$\tau_t(D) = {}^1\!/_2\,\rho\overline{\Delta u^2}(D) \tag{2.112}$$

Thus, in a turbulent fluid system where bubbles are subjected to two opposing energies of surface tension restoring energy $T_s(D)$ and turbulent stress deformation energy $\tau_t(D)$, bubbles break when $\tau_t(D) > T_s(D)$. If the combination of forces on a bubble is such that $\tau_t(D) = T_s(D)$, the diameter of the bubble is said to be a critical diameter. Bubbles with diameter $D < D_c$ are stable against breakage. However, should a bubble diameter be greater that the critical diameter, i.e. $D > D_c$, the bubble surface energy will be smaller than the deformation energy, thus, the bubble will break.

The quantity $\overline{\Delta u^2}(D)$ in Eq.(2.112) has been determined to be equal to $\beta(\epsilon D)^{2/3}$ in the work of (Kolmogorov, 1949). Kolmogorov used the (Batchelor, 1953) computation of the mean value of the square of the difference of velocities at two neighbouring points under isotropic and homogeneous turbulent conditions as in Eq.(2.113)

$$\overline{|u(x+r,t) - u(x,t)|^2} = 6u^2 - 2R_{ii}(r,t) \tag{2.113}$$

Eq.(2.113) takes the form of Eq.(2.115) when the energy spectrum, $E(k,t)$, is defined as

$$E(k,t) = \alpha\epsilon^{2/3}k^{-5/3} \tag{2.114}$$

where $\alpha = 1.7$ is a universal constant.

$$\overline{|u(x+r,t) - u(x,t)|^2} = {}^9\!/_5\,\Gamma({}^1\!/_3)\alpha(\epsilon r)^{2/3} \tag{2.115}$$

Substituting $r = D$ into Eq.(2.115) yields value of velocity fluctuations for the computation of turbulent stresses, where ${}^9\!/_5\,\Gamma({}^1\!/_3)\alpha = 8.2 = \beta$.

The critical diameter is thus determined from the point where the two graphs of turbulent stresses and surface energy restoring forces as a function bubble diameter intercept as in Eq.(2.117) derived from Eq.(2.116) .

$${}^1\!/_2\,\rho\beta(\epsilon D)^{2/3} = \frac{6\sigma}{D} \tag{2.116}$$

$$D_c = \left(\frac{12\sigma}{\rho\beta}\right)^{3/5}\epsilon^{-2/5} \tag{2.117}$$

Classifying the bubble sizes in terms of volume instead of diameter, the critical bubble volume is of the form of Eq.(2.118) .

$$V_c = \left(\frac{12\sigma}{\rho\beta}\right)^{9/5} \epsilon^{-6/5} \left(\frac{6}{\pi}\right)^{-1} \tag{2.118}$$

The D_{min} is a function of bubble diameter D and it is calculated by equating the surface energy between points spaced at a distance D_{min} to the deformation energy, i.e.

$$1/2\, \rho\beta\epsilon^{2/3} D_{min}^{2/3} = \frac{6\sigma}{D} \tag{2.119}$$

$$D_{min} = \left(\frac{12\sigma}{\rho\beta D}\right)^{3/2} \epsilon^{-1} \tag{2.120}$$

A bubble with diameter $D < D_c$ on which any two points on the surface of the bubble separated a distance D' such that $D_{min} < D' < D$ will be imparted with sufficient stress energy from the surrounding turbulence which leads to bubble break-up.

Similarly, the corresponding V_{min} to D_{min} as a function bubble volume V will be expressed as

$$V_{min} = \left(\frac{12\sigma}{\rho\beta}\right)^{9/2} \epsilon^{-3} \left(\frac{\pi}{6}\right)^{\frac{5}{2}} V^{\frac{-3}{2}} \tag{2.121}$$

Since a range of diameter length exists between D and D_{min} along which a bubble may break, a daughter bubble size distribution results from a breakage of a bubble.

The development of the bubble breakage frequency is dependent on the postulation that the rate of the breaking-up processes is inversely proportional to the difference between the non-inertial forces and fluid turbulence. The non-inertial force produces motion between bubbles. The postulation is interpreted as saying that the longer the difference between the gradient of the pressure of turbulent fluctuations and the restoring pressure, $\frac{6\sigma}{D}$, the larger the probability that the bubble will break in a certain time. In addition, a model of the break-up frequency is expected to decrease to a zero limit value as the difference between turbulent stress and surface restoring pressure tends to zero.

Thus, the equation that describes the bubble deformation takes the form of (Martinez, et al., 2010)

$$a_b = \frac{u_b}{t_b} = \frac{\sum F_e}{Mass} = {}^1\!/_2 \frac{\overline{\Delta u^2(D)}}{D} - \frac{6\sigma}{\rho D^2} \tag{2.122}$$

where a_b, u_b and t_b are the characteristic acceleration of deformation, characteristic velocity of deformation, the time taken for a bubble to break-up and F_e is the effective force acting on the surface of a bubble of size D.

Since $u_b \propto {}^D\!/_{t_b}$, Eq.(2.122) can be re-written as

$$\frac{D}{t_b^2} = {}^1\!/_2 \frac{\overline{\Delta u^2(D)}}{D} - \frac{6\sigma}{\rho D^2} \tag{2.123}$$

Thus, the bubble break-up time from Eq.(2.123) is

$$t_b \propto \frac{D}{\sqrt{\overline{\Delta u^2(D)} - \frac{12\sigma}{\rho D}}} \tag{2.124}$$

The break-up frequency is then given by

$$g(\epsilon, D) = \frac{1}{t_b} = \frac{K_g \sqrt{\beta(\epsilon D)^{2/3} - \frac{12\sigma}{\rho D}}}{D} \tag{2.125}$$

where the constant $\beta = 8.2$ as given by (Batchelor, 1953) and $K_g = 0.25$ as determined experimentally by (Martinez, et al., 2010).

The break-up frequency model developed by (Martinez, et al., 2010) as stated in Eq.(2.125) has been validated experimentally and a good agreement was found. The break-up model was further used by (Martinez, et al., 2010) to develop the probability density function (p.d.f) of daughter bubbles based on a weighted probability model such that it satisfies the closure property expected of the model. It was considered in the development of the p.d.f of daughter bubbles that when a parent bubble of size D_o breaks it yields two complimentary masses with respect to their diameters, which are D_1 and D_2.

The following were noted in the development of p.d.f of daughter bubbles:

1) Since the values of pressure deformation forces, τ_t, are not uniform with the distance D, the bubble splitting phenomenon is not a purely random process;

2) The probability for splitting as a function of size $D_1 < D_{min} = \left(\frac{12\sigma}{\beta\rho D_o}\right)^{\frac{3}{2}}\epsilon^{-1}$ from a bubble of size D_o should be zero;

3) If the bubble size splitting from the parent bubble lies within the range $D_{min} < D_1 < D_o$, the probability of splitting was calculated to be function of the difference in the stresses between the surface restoring pressure stress and turbulent deformation stresses, which depends on D_1,i.e.

$$\Delta\tau_{t1} = \frac{1}{2}\rho\beta(\epsilon D_1)^{\frac{2}{3}} - \frac{6\sigma}{D_0} \tag{2.126}$$

The probability of splitting of bubble size of complimentary fraction of D_1, i.e. D_2 breaking away from the parent D_0 was also modelled in a similar way as in D_1 to obtain

$$\Delta\tau_{t2} = \frac{1}{2}\rho\beta(\epsilon D_2)^{\frac{2}{3}} - \frac{6\sigma}{D_0} \tag{2.127}$$

From this individual probability of splitting of fraction of parent bubble D_0, it was postulated in (Martinez, et al., 2010) that the probability of the formation of a pair of bubbles of sizes D_1 and D_2 originating from the deformation of a mother bubble of size D_0 was weighted by the product of the two product stresses as in Eq.(2.126) and Eq.(2.127) to obtain Eq.(2.128) .

$$P\left({}^{D_1}/_{D_0}\right) \propto \left[\frac{1}{2}\rho\beta(\epsilon D_1)^{2/3} - \frac{6\sigma}{D_0}\right]\left[\frac{1}{2}\rho\beta(\epsilon D_2)^{2/3} - \frac{6\sigma}{D_0}\right] \tag{2.128}$$

Eq.(2.128) was modified by a mass balance expression of the form: $V_0 = V_2 + V_1$;

$V_2 = V_0 - V_1$; $D_1 = V_1^{\frac{1}{3}}$. Thus,

$$D_2 = (D_0^3 - D_1^3)^{1/3};\ D_2 = D_0\left(1 - \left(\frac{D_1}{D_0}\right)^3\right)^{1/3} \tag{2.129}$$

When Eq.(2.129) is substituted into Eq.(2.128) , we have

$$P\left({}^{D_1}/_{D_0}\right) \propto \left[\frac{1}{2}\rho\beta(\epsilon D_1)^{2/3} - \frac{6\sigma}{D_0}\right]\left[\frac{1}{2}\rho\beta\left(\epsilon D_0\left(1 - \left(\frac{D_1}{D_0}\right)^3\right)^{1/3}\right)^{2/3} - \frac{6\sigma}{D_0}\right] \tag{2.130}$$

Eq.(2.130) can be simplified to

$$P\left({}^{D_1}/_{D_0}\right) \propto \left({}^{1}/_{2}\,\rho\beta(\epsilon D_0)^{2/3}\right)^2 \left(\left(\frac{D_1}{D_0}\right)^{2/3} - \frac{12\sigma}{\rho\beta\epsilon^{2/3}D_0^{5/3}}\right)\times$$
$$\left(\left(1-\left(\frac{D_1}{D_0}\right)^3\right)^{2/9} - \frac{12\sigma}{\rho\beta\epsilon^{2/3}D_0^{5/3}}\right) \tag{2.131}$$

Since

$$\frac{D_c}{D_0} = \left(\frac{12\sigma}{\rho\beta}\right)^{3/5} \epsilon^{\frac{-2}{5}} \left(\frac{1}{D_0}\right);$$
$$\delta^{5/3} = \left(\frac{D_c}{D_0}\right)^{5/3} = \frac{12\sigma}{\rho\beta}\epsilon^{-2/3}\frac{1}{D_0^{5/3}} \tag{2.132}$$

Eq.(2.133) results from Eq.(2.131)

$$P\left({}^{D_1}/_{D_0}\right) \propto \left(\frac{1}{2}\rho\beta(\epsilon D_0)^{2/3}\right)^2 \left[(D^*)^{2/3} - \delta^{5/3}\right]\times$$
$$\left[(1-(D^*)^3)^{2/9} - \delta^{5/3}\right] \tag{2.133}$$

where

$$D^* = {}^{D_1}/_{D_0};\ \delta = {}^{D_c}/_{D_0}\ ;\ D_c = \left(\frac{12\sigma}{\beta\rho}\right)^{3/5}\epsilon^{-2/5} \tag{2.134}$$

The p.d.f of pairs of daughter bubbles stated in Eq.(2.133) results if bubble size D_1 that breaks from a mother bubble size D_0 lies in a bubble size range $D_{min} \leq D_1 \leq D_{max}$, where

$D_{min} = \left(\frac{12\sigma}{\beta\rho D_0}\right)^{3/2}\epsilon^{-1}$ and $D_{max} = D_0\left(1-\left(\frac{D_{min}}{D_0}\right)^3\right)^{1/3}$; provided that $D_{min} > \eta$, otherwise $D_{min} = \eta$, where η is kolmogorov microscale of viscous dissipation.

When the p.d.f of daughter bubble fractions of a parent bubble, $D^* = {}^{D_1}/_{D_0}$, is normalised as in

$$\int_{D_{min}}^{D_{max}} P\left({}^{D_1}/_{D_0}\right) d\left({}^{D_1}/_{D_0}\right) = 1 \tag{2.135}$$

The p.d.f of the ratio diameter, $D^* = {}^{D_1}/_{D_0}$, is thus

$$f^*(D^*) = \frac{D^{*2}\left[{D^*}^{2}/_{3} - \delta^{5}/_{3}\right]\left[\left(1 - D^{*3}\right)^{2}/_{9} - \delta^{5}/_{3}\right]}{\int_{D_{min}}^{D_{max}} D^{*2}\left[{D^*}^{2}/_{3} - \delta^{5}/_{3}\right]\left[\left(1 - D^{*3}\right)^{2}/_{9} - \delta^{5}/_{3}\right] dD^*} \tag{2.136}$$

When Eq.(2.136) is expressed in terms of bubble volume while ensuring volume conservation during bubble breaking process, Eq.(2.137) and Eq.(2.138) result.

$$f_v^*\left(\frac{V_1}{V_0}\right) = f_v^*(V^*) = \frac{P_v(V^*)}{\int_0^1 P_v(V^*)dV^*} \tag{2.137}$$

$$f_v^*(V^*) = \frac{\left[{V^*}^{2}/_{9} - \delta^{5}/_{3}\right]\left[(1 - V^*)^{2}/_{9} - \delta^{5}/_{3}\right]}{\int_{V_{min}}^{V_{max}}\left[{V^*}^{2}/_{9} - \delta^{5}/_{3}\right]\left[(1 - V^*)^{2}/_{9} - \delta^{5}/_{3}\right] dV^*} \tag{2.138}$$

The review of literature shows the ERT technique is more adequate for imaging objects in a body with limited spatial resolution but high temporal resolution as applied in industries, Medicine, Biomedicine and Geophysics. Studied publications on the progression in the development of ERT algorithms indicate efforts at enhancing the spatial resolution of ERT images for robust applications have not yielded satisfactory results till date.

It is known from the reviewed publications that the capacity of the ERT technique could be explored to accurately measure the gas holdup fractions, which is a boundary condition for a PBM. The poor spatial resolution of the ERT images renders the computed values of bubble population parameters (i.e. size and axial distribution of bubbles at steady or unsteady state) from the images directly less accurate.

The review of literature also informs that ERT is a low-capital cost, simple, non-intrusive, non-invasive means of imaging objects based on the conductivity contrasting of suspended objects and the medium. The captured images could also be interpreted to measure changes in density of the mixture phase during gas dispersion into a BCR to achieve a multiphase system. The interpretation of ERT images for density change measurements is possible because the dispersion of gas (non-conductive material) into a conductive liquid phase reduces the conductivity of the medium. This is due to the reduction of density of the conductive phase and increase in density of the non-conductive phase.

It was gathered from the review of literatures that an application of the PBM model only for bubble population parameter measurement in a BCR is based on correlation models in terms of liquid properties, superficial gas velocity, column dimensions and gas holdup. This applications of the PBM are known to be valid at fixed ranges of the bubble population properties. Outside of the ranges, the gas holdup correlation models for the boundary conditions are invalid (Akita & Yoshida, 1974). Since many industrial processes set-up in a column are operated at higher gas flow rates and in a turbulent regime, the use of correlation model results for PBM simulations will be inadequate for hydrodynamic parameter predictions in a column.

However, within the boundary limit for which the correlation models for PBM simulations are valid, it allows the computation of steady and unsteady changes in all bubble population parameters at sufficient high spatial resolution. Besides, a PBM of bubble swarm in a column yields simulation results that require an experimental validation, which ERT technique can be utilised to measure.

Given the highlighted demerits related to the independent applications of either ERT or a PBM to acquire relevant information on bubble population behaviour, a coupling of these models will be undertaken in this work. The purpose of the coupling of ERT and a PBM is to develop an ERT/PBM hybrid algorithm that allows for measurements of bubble population parameters of bubble swarm at higher spatial and temporal resolution based on an accurately estimated boundary conditions.

Chapter 3: Thesis objectives

3.1. Background on thesis objectives

The central objective of this work is to harness the potential of ERT images for the measurement of bubble population parameters required for hydrodynamic parameter predictions in a BCR. The objective is conceived given the recent applications of ERT technique to monitor the trajectory of a spherical conductive target object in a tank. The trajectory movement resembles the bolus left ventricular ejection in a human body.

The effort to harness the capacity of ERT generated images is viewed to enhance the spatial resolution of ERT images. There is a demand for a significant improvement in the spatial resolution of online ERT images captured as bubbles evolve either in a steady or an unsteady state process in a BCR. The images of evolving bubbles will, to a large extent, contribute to the usefulness of ERT technique in chemical, petrochemical and biochemical engineering research. Alternative techniques such as electrical point probe technique, optical probe technique and bubble size analyser are used to measure bubble size distribution in BCR. However, these techniques are known to be less accurate, costly, bulky, cumbersome, invasive, intrusive and complicated.

Subsequent to the usefulness of PBM for bubble population properties measurements, a hybridization of ERT and PBM concept is perceived to provide a new interpretation technique of ERT images. The new interpretation technique is envisaged to allow for a new method of predicting accurate hydrodynamic parameters at a low capital cost, in a non-invasive, non-radioactive manner and by a simple means.

The possibility of hybridizing ERT to PBM is based on the bubble population properties measurable by ERT technique in the process of dynamic gas disengagement (DGD). The bubble population parameters are the average bubble rise velocities, grouped into classes by their sizes, the local and global gas void fractions and the BNDD. These bubble population properties measurable by the ERT technique in the process of DGD are required boundary conditions for solving a PBM. The use of ERT measurements as a boundary condition for PBM will enable a validation of PBM by an experimentally validated ERT data. Thus, the PBM will enable accurate column hydrodynamic parameter predictions since the PBM is

dependent on the bubble population properties, physical properties of the phases, operational conditions of processes and dimensions of the BCR.

3.2. Hypothesis

The results of ERT imaging can be integrated with the DGD Technique through a PBM framework to yield a high accuracy size and spatial distribution of bubbles in a BCR.

3.3. Research approach

The following exercises will be undertaken to develop an interpretation model of ERT reconstruction that provides both higher spatial and temporal resolution through a coupling of ERT with a PBM. It is not the case that ERT can in itself simply be coupled to PBM to test this approach. The ERT technique requires further refinement before the intended hybridization can occur.

The progress in the development of ERT algorithm section (section 2.1) in the literature review outlines the methodology that has been explored in refining the ERT algorithm to enhance its application in varied fields. The algorithms that range from basic to advanced algorithms derived from the implementation of the physics of ERT problem are:

1) Gauss-Newton inverse solver;

2) Temporal inverse solver;

3) Gauss-Newton inverse solver with spatial image elements correlation;

4) Gauss-Newton inverse solver with spatial image element correlation and measured data frames correlation.

The Gauss-Newton (GN) inverse solver with spatial image element correlation in 3D and data frame correlation (i.e. GN with 4D regularization) will be used to image non-conductive objects suspended in a tank that containing a mild saline solution. The accuracy of the GN with 4D regularization to image the movement of the objects accurately in the conductive solution will also be ascertained. If this algorithm produces a satisfactory result, it will be

further utilized to image the gas holdup fractions in the column for varied superficial gas velocities.

The local and global gas holdup fractions in the column are expected to increase with increasing superficial gas velocity. Based on this expected result, the accuracy of the GN with 4D regularization algorithm will be determined by the consistency of the ERT estimate for gas holdup fractions with theoretical results.

Should the GN with 4D regularization algorithm yield less accurate results, the GN algorithm with a temporal correlation of data frames will be tested for its effectiveness. In a case where this algorithm for imaging the gas void fractions in 3D produces inaccurate results, the GN algorithm with spatial image element correlation (i.e. imaging in 3D) will be investigated for accurate measurements.

The GN algorithm in 3D without spatial image element correlation and temporal data frame correlation will be examined if the use of GN 3D algorithm with spatial image element correlation yields inaccurate results. The inaccurate results will be un-interpretable gas void fraction measurements with increasing superficial gas velocity.

The BCR for experimental studies is of height 1.545 m and diameter 0.29 m. The four rings of electrodes (each ring comprises of 16 electrodes) are placed at axial lengths 0.37 m, 0.67 m, 0.93 m and 1.24 m on the boundary of the column. Findings in the literature indicate that for an accurate imaging of constituents' non-conductive substances in a tank, the data measurement should be made on the entire column surface. The column geometric dimensions, sensor electrode positions and the fraction of the area covered by sensor electrodes to the total column surface area are factors that inform the use of either a 2D or 3D imaging algorithm.

Should the results of the 3D images be less accurate by the stated sources of error, the GN algorithm with Tikhonov regularization will be applied to image the gas holdup in 2D.

The available experimental materials are:

1). A pilot scale bubble column reactor of height 1.545m and diameter 0.29m with four layers of electrode rings placed at height 0.37 m, 0.67 m, 0.93 m and 1.24cm, from the column base; 2). A porous tubular sparger (gas distributor) mounted at the base of the column to allow for distribution of gas into the liquid; 3). A rotameter for

measurement of superficial gas velocities ranging from 0.001-0.0573 m/s; 4). An ABB differential pressure transmitter for measurement of local gas void fraction of target column section by the differential pressure (DP) measurement technique. The DP transmitter is of make ABB DPT 265 Diaphragm Seals (DS) with a span limit of 0.4–40 Kpa, output signal of 4–20 mA and product code 264 DSFS5A2B1V1E1B1; 5). An ERT data acquisition system with a maximum of 8 layers measurements.

The following measurements and computations will be made in hybridizing ERT and a PBM:

1. A suitable ERT reconstruction algorithm (either in 3D or 2D) will be identified from the available algorithms through an accurate imaging of suspended non-conductive solid test objects and gas holdup fractions with increasing gas flow rate. The efficient algorithm will be used to calculate the local time and area average of conductivity distribution (TACD) at varied superficial gas velocities.

2. The conductivity of the air-water mixture phase will be determined by connecting the DP transmitter over local column sections for the simultaneous measurements of the gas void fractions and the ERT data. From the ERT images of known data frames, the TACD will be calculated. The conductivity of the continuous, dispersed and TACD (mixture phase conductivity value) will be substituted into Maxwell's relation as reviewed. The obtained gas void fraction results will be correlated to the actual void fraction measured using the DP.

Should the results from Maxwell's relation be inaccurate, the local DP gas holdup values will be plotted against the local ERT TACD depending on the superficial gas velocity. The graph will be a calibration model of the actual local gas void-fraction against the local ERT TACD with respect to superficial gas velocity.

3. The aim of the third step is to measure the bubble population size distribution from analysis of the gradient of time-varying local gas void fraction during DGD process. Since ERT algorithms yield a high temporal resolution, the ERT technique will be applied to accurately measure the time-variant local gas void fraction during DGD process. The local time-variant area-average of conductivity distribution (ACD) will be computed from the time-dependent ERT voltage data during DGD process to obtain a graph of the local ACD with time. From this graph, the graph of the local gas

void-fraction or local gas volume of bubbles with time during DGD process can be computed.

4. Since the imaged dispersion will be through a porous tubular gas distributor, the column will be compartmentalised to four sections for accurate measurement of the DP local gas void fractions. Thus, an analysis of local ERT time-variant ACD will be made to obtain a graph of local gas void fraction with time. Both graphs will then be analysed to determine the mean values of bubble sizes in bubble population classes disengaging locally before complete disengagement from the continuous phase.

From the bubble size distribution results at four compartments, the mean of the local BNDD along the column axis will be computed to obtain the graph of axially averaged BNDD ($\bar{n}_z^{ERT-DGD}(v)$). The detailed description of the method for obtaining $\bar{n}_z^{ERT-DGD}(v)$ will be given in Chapter 5. The results of $\bar{n}_z^{ERT-DGD}(v)$ at varied superficial gas velocities will be shown in Chapter 8, where the hybridization of ERT and PBM will be reported.

5. Given an initially steady state bubble swarming before the DGD process, the known bubble size distribution will be used to compute the stead state local radially averaged BNDD depending on column height ($\bar{n}_v^{ERT-SS}(z)$).

Since there will be four sections, four data points of $\bar{n}_v^{ERT-SS}(z)$ at height 0.37 m, 67cm, 93cm and 124 cm will be computed. These computations of $\bar{n}_v^{ERT-SS}(z)$ will be made to achieve an effective hybridization of a PBM with ERT through a parameterization of the PBM source terms models. The function $\bar{n}_v^{ERT-SS}(z)$ will then form a criterion for accurate parameterization that ensures the function $\bar{n}_v^{PBM-SS}(z)$ by the PBM agrees with $\bar{n}_v^{ERT-SS}(z)$ by the ERT.

In order to accurately predict the hydrodynamic parameters in a BCR, having obtained $\bar{n}_z^{ERT-DGD}(v)$ and $\bar{n}_v^{ERT-SS}(z)$, the steady state BNDD $n(v,z)$ need be determined. The $n(v,z)$ is expected to enable the description of the evolution of bubble population swarming governed by bubble coalescence and breakage phenomena during the axial bubble population transport.

Since a PBM describes the bubble swarming process, ERT measurements yielding $\bar{n}_z^{ERT-DGD}(v)$ and $\bar{n}_v^{ERT-SS}(z)$ will be hybridized to a PBM for the accurate

determination of actual $n(v,z)$. The known $n(v,z)$ by the hybrid technique will allow for the determination of actual bubble size distribution, coalescence and breakage rates leading to bubble birth and death in the reactor.

6. At the highest superficial gas velocity of 0.016 m/s, the hydrodynamic regime in the column was translational and not turbulent. Therefore, a partial mixing of air-water mixture phase was achieved. Results in the reviewed literature show that partial fluid mixing system often encountered in BCR can be described by a tank-in-series model. The tank-in-series model accounts for the presence or absence of backflow between neighbouring cell sections. The 1D axial dispersion model (ADM) is an alternative technique for the description of the partial fluid mixing in reactors as found in the literature.

Thus, the PBM will be formulated in form of 2D problem (i.e. in 1D space and 1D bubble size) where the inlet BNDD, bubble sizes and the gas holdup fraction are known. The inlet BNDD will be assumed using a log-normal distribution leaving the surface of the sparger.

The column height will be sectioned to a known number of discrete axial sections. In the first discrete section, the inlet boundary conditions are the local gas holdup fraction, the global bubble sizes and the assumed log-normal BNDD. The PBM will be solved locally in the first section using the inlet boundary conditions to obtain the first section outlet BNDD. The outlet BNDD at first column section, the local gas holdup at the inlet of the second section and the global bubble sizes will be the inlet boundary conditions for the second discrete column section. According, the PBM will be solved in the second discrete column section and the results used as the boundary condition for the next discrete section and likewise for higher axially placed sections.

7. The DGD process of bubble population will be modelled in the form of inhomogeneous unsteady state advection transport equation. The DGD model will describe the axial transport of varied bubble sizes through the bulk liquid phase before their exit to the atmosphere at the top of the column. The source term models for the DGD process will describe the bubble expansion rate due to mass transfer and change in gas density in the axial direction of the column.

8. The model equation describing the population of bubbles disengaging from the liquid will be solved by the method of characteristics in order to compute axially averaged BNDD, $\bar{n}_z^{M-DGD}(v)$. The obtained $\bar{n}_z^{M-DGD}(v)$ should be similar to the obtained function $\bar{n}_z^{ERT-DGD}(v)$ (objective 4) from analysis of gas holdup fraction estimates computed from ERT data captured during DGD process.

9. The PBM will be solved by the method of class. The total local gas volume at discrete column height (as in objective 6) will be calculated from the resulting PBM solution. The ratio of these local gas volumes to mean values of bubble volumes will yield the graph of radially averaged BNDD depending on column height $\bar{n}_v^{PBM-SS}(z)$.

10. In Chapter 8, the inlet BNDD, at discrete first column section, the coalescence and breakage rates will be parameterised such that $\bar{n}_z^{M-DGD}(v)$ and $\bar{n}_z^{ERT-DGD}(v)$ agree and $\bar{n}_v^{PBM-SS}(z)$ and $\bar{n}_v^{ERT-SS}(z)$ agree too. An alternative technique for measurement of bubble size distribution during bubble swarming in a BCR will be mentioned, also, in Chapter 8.

11. A good agreement of expected results in objective 10 will directly lead to the determination of actual BNDD of bubble sizes at discrete column height $n(v,z)$. The $n(v,z)$ is a required quantity (parameter) for calculating hydrodynamic parameters in the column. The hydrodynamic parameters of processes given the flow regime in the experimental BCR will be determined for performance description of the column and its scale-up design in Chapter 9.

3.4. Key questions

To accomplish the outlined objectives in section 3.3, the following questions will be considered:

1. Given the most suitable ERT imaging algorithm for measurement of changes in the local gas holdup with a gas flow rate in the column, what assumptions or observation about the bubble population evolution within the column sections are being made?

2. How are ERT reconstructed images analysed to obtain a graph of local ACD as a function of time during gas disengagement processes?

3. How is the local time-variant ACD analysed to compute the size distribution of bubbles disengaging from a local column section?

4. How is the local TACD interpreted to compute the local radially averaged BNDD ($\bar{n}_v^{ERT-SS}(z)$) at steady state?

5. How is the model of DGD process developed from the computed $n(v,z)$ and solved to compute $\bar{n}_z^{M-DGD}(v)$?

6. How is the radially averaged BNDD, $\bar{n}_v^{PBM-SS}(z)$, computed from PBM simulations?

7. How are the ERT measurements hybridized to PBM in order to compute $n(v,z)$ as a function of superficial gas velocity and what are the accuracies of the computed $n(v,z)$?

8. What is the minimum spatial resolution of the resulting ERT and a PBM hybrid algorithm for bubble population parameter predictions given the used equipment?

Chapter 4

Experimental measurements of gas holdup fractions of bubble swarm at steady state by the ERT technique

ERT is a low-cost imaging technique for producing images of constituents within a body (such as a bubble column reactor - BCR). The images are generated through a reconstruction of interior body conductivity from analysis of captured periphery voltage signals on the body surface. The ERT measurement technique produces images at a high temporal resolution to the extent that changes in conductivity contrasting in a column can be determined for every 0.001 seconds (i.e. 1000 data frames per second). However, its low spatial resolution has limited its application for measuring bubble properties in a column to gas void fractions of bubble population only.

Recently, the applications of ERT to study hydrodynamic processes in a BCR have been extended by an analysis of ERT images during DGD process. Such analysis of the captured ERT data leads to the determination of bubble size distribution in a BCR as done in the work by (Haibo, et al., 2007). To enhance the usefulness of ERT technique in investigating hydrodynamic parameters in a BCR, an interpretation model of ERT reconstructed images needs be developed. Such interpretation technique is expected to allow for the computation of the following bubble properties: bubble size distribution, BNDD, bubble coalescence and breakage rate and gas void fractions in a column. However, the interpretation technique may not be obtained by the sole analysis of ERT images owing to ill-conditioning of the ERT inverse problem that yields images with low spatial resolution.

A population of bubbles swarming axially in the column is known to vary in size due to temperature, pressure and phenomena of bubble coalescence and breakup. This means bubble sizes and their concentration (BNDD) are dependent on the spatial coordinate system of the column. A model to describe the evolution of bubble properties within the space of a BCR should incorporate the various factors affecting bubble properties. The population balance concept has proved to be an efficient model for predicting bubble sizes in a BCR since it provides a path to include the details of the bubble coalescence and breakage. The bubble interaction phenomena of coalescence and breakage are known to control the bubble size distribution in a BCR. The accurate prediction of the bubble coalescence and breakage rates require the knowledge of the physical properties of the fluid

state and operating conditions in the column. The PBM is similar to other conservative concepts such as mass, heat and momentum since it considers the balance of countable entities such as bubbles, drops and crystals.

Thus, an interpretation of ERT measurements in the light of a hybrid model of ERT and a PBM is anticipated to allow for the computation of the local bubble population properties. These are the bubble sizes, bubble number densities, bubble coalescence and breakage rates and gas void fractions of bubble population. The hybrid model development will involve measuring the bubble population parameters at local column sections through the analysis of ERT signals captured during DGD process. The local gas void fractions of the dispersed phase during the steady state operational mode in the column will be computed from a map of the ERT measurements to the DP measurements.

The PBM will be solved to obtain the local BNDD using the boundary conditions of known inlet bubble size distribution, the inlet gas void fractions and a guess inlet BNDD. The inlet bubble size distribution will be the global bubble size distribution obtained by coupling of the ERT and DGD process and divided into a discrete number of classes.

The PBM source term models of bubble coalescence rate, bubble breakage rate and the inlet BNDD will then be parameterised. The obtained solution of the PBM will then be used an initial condition for a model of DGD process in the column. Thus, the bubble population properties will be parameterised such that when the model of DDG is solved, the obtained axially averaged BNDD agrees with that derived from the analysis of the ERT measurement during DGD. This agreement will be further verified when the parameterised inlet BNDD leads to the local static gas void fraction by the ERT technique validate that by the PBM computation.

The description of the ERT hardware equipment and the ERT implemented measurement sequences for the data capturing are stated in Sections 4.1 and 4.2 respectively. Thereafter, Sections 4.3 provide a detail description of the design of the pilot scale BCR employed for developing the ERT and PBM hybrid model. The presentation of the methods adopted in measuring local gas void fractions by the ERT technique is given in Section 4.4. In Section 4.5, the description of the DP transmitter used for gas void fraction measurements as well as the method of its calibration and results are given. In the subsequent Section 4.6, the results of the correlation of the gas void fractions by the ERT and the DP are shown leading to the discussion and conclusions on the results.

4.1. Hardware equipment for ERT data capturing

A current pulse measuring technique developed by (Randall, et al., 2007) is simpler to implement than the conventional alternating current (AC) excited system. The current pulse measuring technique is capable of high-speed operation, thus, enabling dynamic systems to be investigated. The UCT ERT data acquisition hardware provides for the possibility of capturing data frame rate of up to 1000 frames per second (fps) over a ring of 16 electrodes system and displays the images at 20fps. The current pulse measuring technique has been used for a fast approximation of the conductivity distribution within a measurement plane in real-time. The measurements were possible owing to a 2D reconstruction algorithm embedded in its ''online'' control and the data capture software program (as in Figure 4.3). The system hardware is controlled by a C++ program to provide a real-time visualisation of the conductivity/resistivity distribution in a reference domain of the bubble column or by storing data for post-processing.

A study on performance and requirements of various ERT instruments using adjacent injection strategies was conducted by (Stephenson, et al., 2007). In the study, it was found that a frame rate ranging from 0.5 to 285fps is achievable with the UCT tomography hardware. The UCT hardware system allows for a-four configurations of measurement strategies as illustrated in Figure 4.1. The strategies are such that current injections between any pair of electrodes are possible on either the same or different planes; and voltage measurements between either horizontally or vertically adjacent electrodes but not opposite electrode pairs. The signal-to-noise ratio of the current hardware system (presented in Figure 4.2) has been estimated to range from 65db at 1 fps to 45 db at 285 fps.

With a view to measuring voltage signals at the periphery of a bubble column, a current signal need be stimulated through the periphery ring of electrodes into a mildly saline or conductive solution(Figure 4.5). The mildly saline conductive solution (for example $8000\mu S/cm$) is a homogeneous phase before either a non-conductive solid or liquid or gas phase is dispersed through it. The excitation of the conductive solution is done through a constant current driven into the electrode system (typically from 2mA to 2.5mA) via a multiplexer.

Prior to the dispersion of the non-conductive phase through the conductive bulk solution, the periphery electrodes detect sequences of homogeneous voltage signals in form of 16 ‘U’ shaped curves of approximately equal amplitude as in Figure 4.4. The 16 ‘U’ curves signals

are captured from a ring or a layer of 16 electrode plates. The dispersion of the non-conductive phase through the conductive phase perturbs the homogeneous conductivity distribution, which results in distorted captured voltage signals. The range of conductivity measurable with the hardware is 0.04ms/cm at 41db to 60ms/cm at 37db (Stephenson, et al., 2007). A four-way multiplexer controls a constant current source and sink from a selected electrode pairs generated by the sum of all the multiplexer resistances connected in series and the electrode impedance.

The total impedance is known to vary between 100Ω to 1Ω depending on the electrode size and solution conductivity. The constant current source on the electrode system is usually maximised by lowering the total impedance that reduces the voltage drop due to the multiplexer's module and the contact electrodes with the solution. The reduction of the total impedance is achieved by including a high input differential amplifier in the current pulse ERT system.

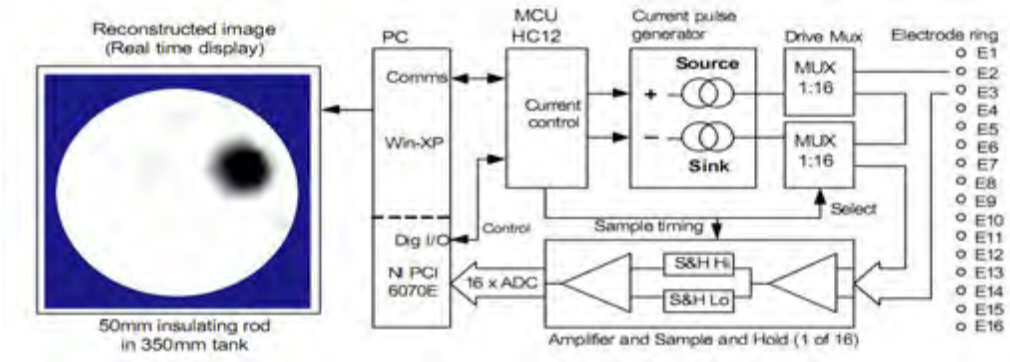

Figure 4.1. Current pulse ERT system for a single ring of 16 electrodes (Randall, et al., 2007).

(a) (b)

Figure 4.2. Data acquisition system: a) Exterior view; b) Plan view.

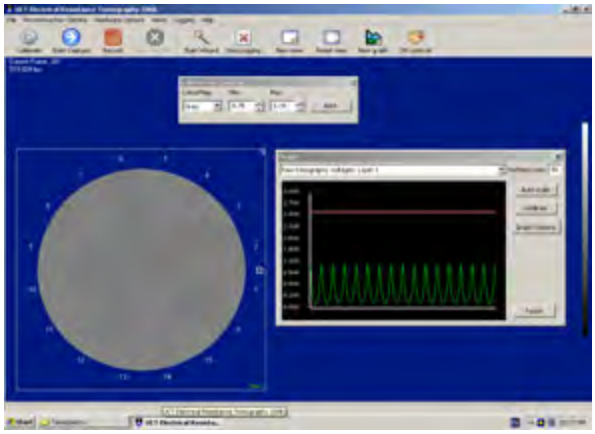

Figure 4.3. On-line reconstruction of resistivity distribution (2D) from capture voltage data in the form of 'U' curves.

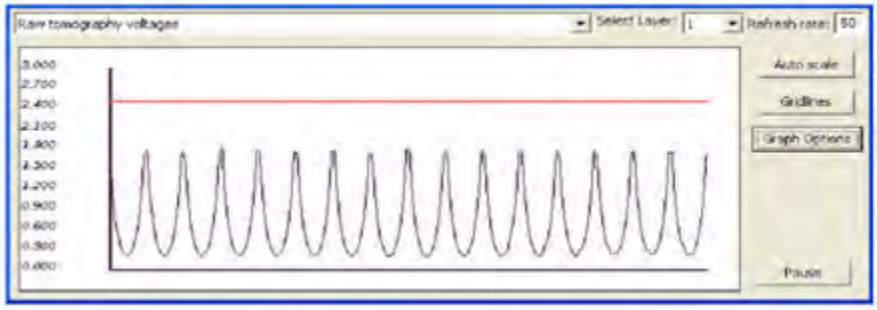

Figure 4.4. The data set for a single frame as displayed by the real time software. Data is for a homogeneous system and therefore symmetrical. Each "U curve" is data recorded during single current injection cycle (Randall, et al., 2007).

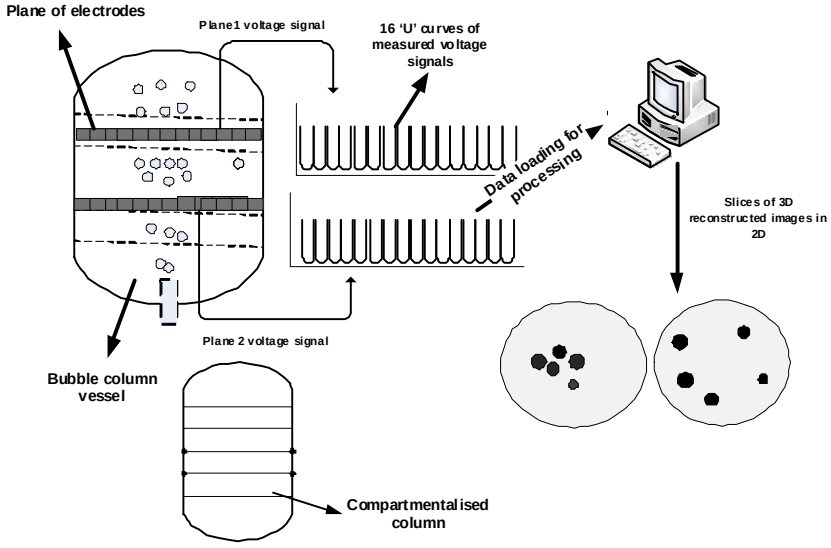

Figure 4.5. Stages of data processing for ERT image reconstruction.

4.2. Implemented measurement sequences for the ERT imaging technique

Four measurement strategies are possible with the UCT hardware instrument. Among these, the case of current stimulation through adjacent electrode pairs and voltage measurement through adjacent electrode pairs in a ring is often referred to as the Sheffield measurement sequences (Figure 4.7). In an electrode ring, every current stimulation (i.e. source (positive) and sink (negative)) through adjacent electrode pairs produces 16 measurable voltage signals, including the current drive pairs as in the format of Figure 4.6. This means after successive sequential current stimulations over all possible 16 pairs of electrodes (independent measurement sequences), 256 (16 x 16) data will be captured.

By these measurement sequences, three out of sixteen voltage measurements are invalid due to interference effects of voltage measurements through current stimulated electrodes. Thus, 208 data of the total 256 date sets (a data frame) will be used for reconstruction of the conductivity distribution in the interior of the section bounded by an electrode ring. Table A1.13 in appendix G illustrates a scheme of selection of valid data sets for a frame of data captured for ERT image reconstruction.

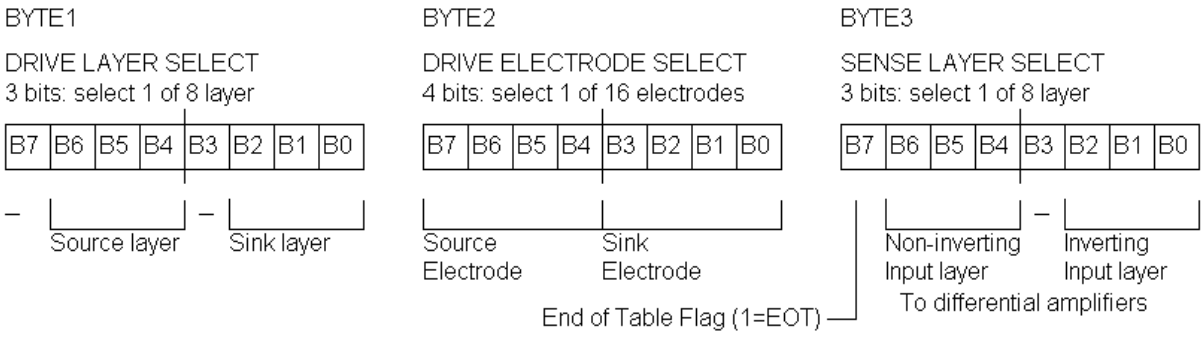

Figure 4.6. Electrode select sequence table format.

The adjacent current injection and adjacent voltage measurement scheme have been implemented in this study because it yields a high number of data sets for image reconstruction. The used measurement scheme is preferred to an opposite current stimulation scheme and adjacent voltage measurement scheme that produces 12 valid data of the 16 data captured for every current stimulation. This implies 16 current stimulation sequences will produce a frame of valid 192 data sets as compared to 208 data sets generated by the utilized scheme. The selection scheme from a frame of data obtained by

opposite current injection and adjacent voltage measurement is presented in Table A1.14 in appendix G.

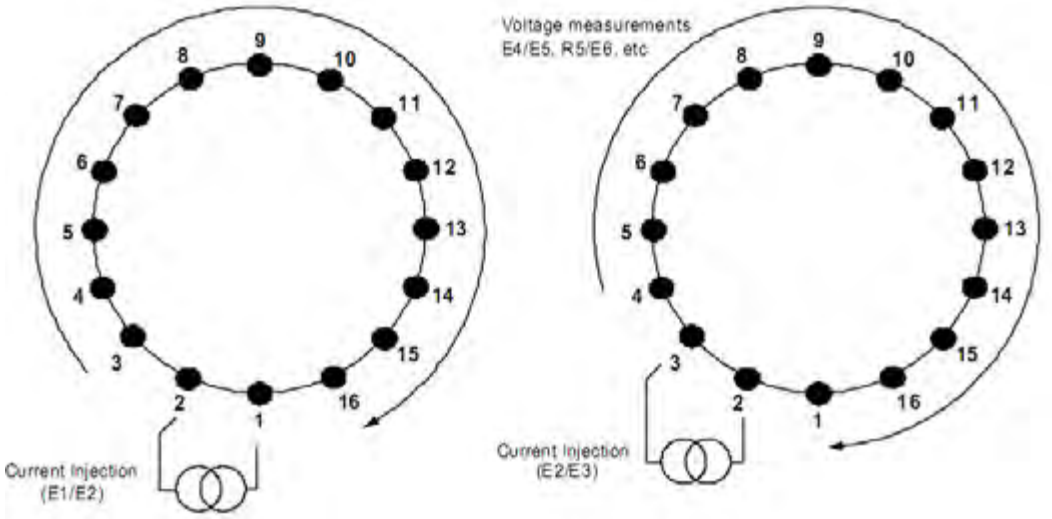

Figure 4.7. Adjacent pairs measuring sequence for a 16 electrode system. The figures show the first two positions of the current injection sequence. The output from the 16 amplifiers is recorded for each of the 16 current injection positions (Randall, et al., 2007).

Table 4.1. Number of adjacent measurement from rings of electrode and number of measurements used for image reconstruction

S/N	Current injection strategy (Sixteen Sequences)	Number of rings	Total number of adjacent measurements	Total number of measurements used for reconstruction
1	Opposite	Two rings	1024	896
2	Adjacent	Two rings	1024	928
3	Opposite	Three rings	2304	2112
4	Adjacent	Three rings	2304	2160
5	Opposite	Four rings	4096	3840
6	Adjacent	Four rings	4096	3904

The degree of ill-posedness of the inverse problem is reduced by obtaining a high ratio of measured data to discretised finite element. Thus, a high number of data set will be required for an accurate 3D reconstruction than a 2D reconstruction (Adler, et al., 2008). When data

are captured over 2, 3 or 4 rings using varied measurement schemes, Table 4.1 shows the total captured data and the number of valid date for an image reconstruction respectively.

The specifications of the computer system available for image reconstruction is as follows: Processor – Intel Core i7-4790 CPU@ 3.60GHz x 8 processor 3.40GHZ; Memory – 15,5GiB; OS type – 64-bit operating system, Disk – 975,4GB. The present computing system was used to discretize a cross-section of the column of diameter 29cm into 2500 elements. However, the time taken to compute the inverse of the Jacobian matrix resulting from 2500 elements is too high. Given this long length of time for reconstruction, the cross-section of target domain (cylindrical cell section of the BCR) was discretized in 2D using 832 finite elements. The discretization of the cross-section was also on the basis of the need to explore the high temporal capacity of ERT reconstructions to enhance its spatial resolution

The high temporal resolution of ERT images is harnessed for improving its spatial resolution in this work by coupling ERT to DGD technique to measure the time-variant disengaging gas void fractions. The results will further be interpreted for determining the characteristic time of the bubble size disengagement.

4.3. Bubble column reactor used for the hybrid model development

Hydrodynamic regimes studied using ERT images in the present work were set-up in a pilot scale bubble column reactor of height 1.545 m and diameter 0.29 m as shown in Figure 4.8. A porous tubular stainless steel gas distributor of height 0.265 m and diameter 0.03m was mounted at the column base for gas dispersion (Nitrogen gas/air) into the liquid (water). The local gas holdup fraction along the column height is expected to vary given the sparger design that produces uniformly distributed bubbles at column sections axially higher from the sparger. At column sections closer to the gas distributor, the lack of uniform distribution of bubbles will yield a decrease in bubble resident time with column height. .

Along the axial length of the column, pressure ports (i.e. pressure legs) were fabricated at height 0.245 m, 0.515 m, 0.745 m, 0.995 m and 1.295m from the base of the column. The axial interval lengths between respective pressure legs were 0.27 m, 0.23 m, 0.25 m and 0.30 m to allow for accurate local gas void fraction measurements at column sections within the pressure legs.

A rotameter for measurements of gas flow rates ranging from 4-230 litres per minute(lpm) was employed in measuring the gas volumetric flow rates into the column. The maximum attainable superficial gas velocity was 0.016 m/s (64lpm) due to the axial spacing of the four electrode layers, aerated water level and the column height. The column height restricts attaining higher superficial gas velocities because the water-head level need be at least 0.2 m above an electrode layer for accurate ERT data.

PVC tubing of various lengths was used to connect cell sections of the BCR to a DP transmitter. The output differential pressure signals measured by the DP at its high and low ports were displayed as analogue signals on a Labview plot platform.

The BCR was fitted with eight rings of electrodes to allow for the possibility of capturing generated voltage signals at the column periphery over multiple layers. Each ring of electrodes is made up of sixteen rectangular electrode plates of height 20 mm and width 10 mm covering approximately 1.32 litres of 17.536 litres volume of the column section. This is a section of height 0.27 m and diameter 0.145 m. The low fraction of the volume covered by periphery 16 electrode plates to the volume of the column section rendered the captured data inadequate for 3D imaging of the dispersion. Moreover, when data were captured on 4 of the 8 rings located at heights 0.37 m, 0.67 m, 0.93 m and 1.24 m of the column for image reconstruction in 3D, the computed gas void fractions were inaccurate. The large error in the gas holdup fractions was due to the low volume ratio of the 2.64 litres covered by the two sensor rings to the 17.536 litres volume of target column section. The target column section was bounded at its base and top by the two sensor rings.

Many of the advanced ERT reconstruction algorithms explored in creating the gas dispersion images in 3D yielded inaccurate results due to a low ratio of measured data(1024) to the finite element of the interior domain(15000 elements). (Pinheiro, et al., 1998) stated that to obtain a 3D image by the ERT technique, it is required to use a full 3D data collection strategy that ensures a created image is made from data collected over the whole body surface.

The ERT image of air dispersion in a mildly saline solution (conductivity of 1000$\mu S/cm$) using an iterative 3D algorithm with an included 4D regularization parameters is shown in Figure 4.8c. The 4D regularization parameter was developed by the correlation of the data frame

measurements (1D) and the domain finite image elements (3D). Figure 4.8b is a reconstruction of the air dispersion using the Newton-Raphson formula with included Tikhonov regularization parameter that results in the Levenberg - Marquardt algorithm.

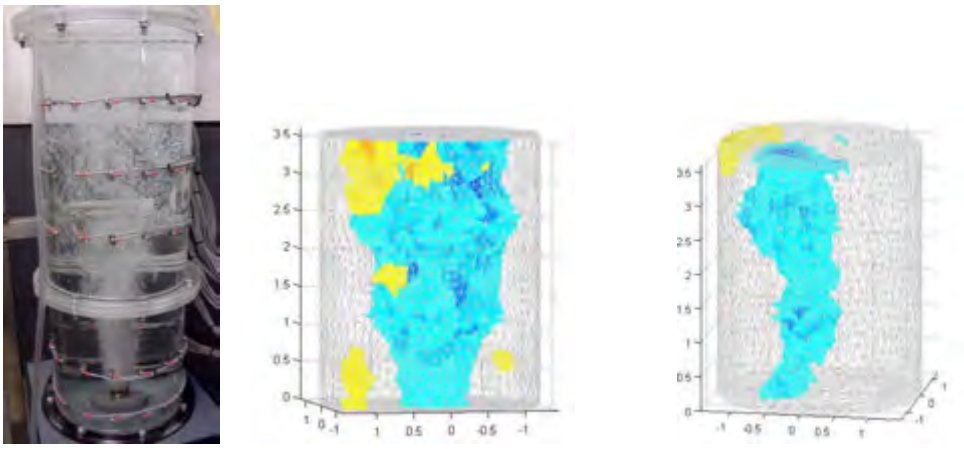

(a) (b) (c)

Figure 4.8. Air dispersion through the UCT BCR during online operation and its ERT image reconstructions: a) Air dispersion through a BCR; b) Image reconstruction using the Gauss-Newton algorithm without 4D regularization; c) Image reconstruction using the Gauss-Newton algorithm with 4D regularization.

4.4. Local gas-holdup computations by the ERT technique

A semi-batch hydrodynamic fluid flow regime with stagnant liquid phase and the superficial gas velocity ranging from 0.002 – 0.016m/s was set-up in the BCR described in Section 4.3. The inlet volumetric gas flow rate was varied such that the air-water multiphase system at a given volumetric flow rate assumed a steady state operational mode. The ERT data for imaging the dispersion on the four electrode rings cross-sectional areas embedded in the four column sections were captured at height 0.37 m, 0.67 m, 0.93 m and 1.24 m. The degree of well-distribution of bubble population increases with column height especially from the second to the third column section. The bubbles were packed close to the gas distributor surface in the first and second column sections because of the use of a porous tubular gas distributor (as in Figure 4.8a). The local gas void fractions at all cross-sectional areas within the column sections should be constant and independent of the column height for a given gas flow rate. This expected results will hold in a well-distributed (approximately uniform distribution) form of bubble population usually produced by sintered porous flat plates gas distributors.

A reconstruction of the dispersed gas phase in 3D could yield accurate values of the mixture phase conductivity (air-water) required for gas void fraction calculations. However, given the available column dimensions and the volume covered by the periphery sensor electrode, a low ratio of measured data to a the number of domain finite elements was obtained. The obtained fewer measurements to discretized domain elements disallowed accurate interpretation of gas void fraction from ERT images in 3D.

As a result, reconstruction of the dispersed phase at the column cross-sections in 2D was investigated for gas holdup calculations depending on superficial gas velocity since the results were interpretable. The reconstructed images in 2D were evaluated to be interpretable for gas holdup computations because the graph of its computed TACD increases with superficial gas velocity. This is an expected result since the gas volume trapped in the liquid phase increases with superficial gas velocity, which was not obtained with the reconstructed dispersion in 3D.

4.4.1. ERT data capturing

The ERT data for image reconstruction of the dispersed phase at the local column cross-sections were captured using the adjacent current injection and adjacent voltage measurement sequences. The data measurement scheme and pattern of selecting valid data for the image reconstruction are presented in Table A1.13. A total number of 208 valid data were sorted out of the total 256 data frame for the 2D image reconstruction. In order to acquire ERT images of the dispersed gas phase at regions in a BCR during aeration, an absolute or a difference ERT algorithm could be employed. The absolute algorithm requires 2 data frames of the offset voltage and inhomogeneous voltage signals. The difference algorithm requires 3 signals of the offset voltage, homogeneous voltage and inhomogeneous voltage signals.

Studies have shown that the difference algorithm is superior as a functional algorithm than the absolute algorithm for imaging the transient conductivity distribution changes within the interior of a BCR. Thus, the difference algorithm was used in this work for image reconstruction of data captured on the sensor electrode layers placed at 0.37 m, 0.67m,

0.93m and 1.24m. The ERT data set was captured at this four electrode layers three times for accuracy because of the axial movement of the DP for local gas void fraction measurements.

At each instant of the local time-variant data capturing for a given gas flow rate, the maximum, the mean and minimum conductivity values of all element within a target region were calculated.

4.4.2. ERT data capturing modelled by the ERT forward model and reconstruction by the ERT inverse model

The development of ERT forward model addresses the forward problem of simulating the periphery voltage signals from the known current stimulations and conductivity distribution in the interior of a body. Let the domain of an interior conductivity distribution $\xi \in C^k$ be denoted by Ω; the induced periphery electric potential be U; and the stimulated periphery current be I_i. The ERT forward problem is formulated as given Ω of the $\xi \in C^k$, the induced U generated due to periphery I_i is expected to satisfy the elliptic partial differential equation of Eq.(4.1)

$$\nabla \cdot \xi \nabla \mathrm{U} = 0 \qquad (4.1)$$

If I_i is the current injected into the l_{th} electrode area E_l with constant impedance Z_l, the complete electrode boundary conditions are

$$V_i = U + Z_i \, \xi \frac{\partial \mathrm{u}}{\partial \mathrm{n}} \qquad (4.2)$$

$$I_i = \int_{E_l} \xi \frac{\partial \mathrm{u}}{\partial \mathrm{n}} \, \partial s \qquad (4.3)$$

where V_l is the constant voltage in electrode E_l, n is the outward unit normal vector and

$$\xi \frac{\partial \mathrm{u}}{\partial \mathrm{n}} = 0 \qquad (4.4)$$

the current density on the boundary inter-electrode gap (Polydorides & Lionheart, 2002). Eq. (4.2) and Eq.(4.3) are the Dirichlet boundary conditions, while Eq.(4.4) specifies the Newman boundary condition. The forward problem in many ERT algorithms is addressed through the use of the finite element method (FEM) developed with a first or second-order shape functions. The ERT images of interior objects are created through solving the forward and inverse problems.

The aim of the inverse conductivity problem is to obtain a stable solution ξ^* which minimizes the residual error

$$f(\xi) = {}^1\!/_2\,(F(\xi) - V)^*\,(F(\xi) - V) = {}^1\!/_2\,\|F(\xi) - V\|_2^2 \qquad (4.5)$$

where $F(\xi)$: $C^n \rightarrow C^m$ is the non-linear forward operator in a problem with n elements and m measurements, and $V \in C^m$ is the vector of voltage measurement for a fixed set of a current pattern. Applying Taylor's expansion to the residual Eq.(4.5), and assuming the second derivative term of the expansion equals λI ($\lambda \in R$), Eq.(4.5) can be re-written as Tikhonov regularized solution of Eq.(4.6). The position scalar and identity matrix respectively are denoted by λ and I. The successive iterative solution is denoted as in Eq.(4.7).

$$h_{LM} = (F'(\xi)^* F'(\xi) + \lambda I)^{-1}\, F'(\xi)^* \big(V - F(\xi)\big) \qquad (4.6)$$

$$\xi_{k+1} = \xi_k + h_{LM} \qquad (4.7)$$

The mathematical formulations of the ERT forward and inverse problem were solved using forward and inverse solver functions contained in the electrical impedance and diffuse optical reconstruction software (EIDORS) library toolbox. EIDORS is an open source software library adaptable to ERT data set captured from an ERT instruments for image reconstruction (Adler, et al., 2008). Included in the EIDORS library of functions are functions developed from a known knowledge of the peculiarity of the University of Cape Town (UCT) ERT data acquisition system. The functions 'eidors_readdata' and 'inv_solve' were explored in solving the forward and the inverse problems respectively as presented in the computer code cited in Appendix B.

In Eq.(4.7), the solution of the inverse problem, ξ_k, is a vector of 832 conductive values corresponding to the number of elements used in discretising the cross-sectional area of the column section. Therefore, for 20 frames of data captured over a known period of time, ξ_k^f, where f ranges from 1 to 20, an array of (832 x 20) conductive values will be calculated.

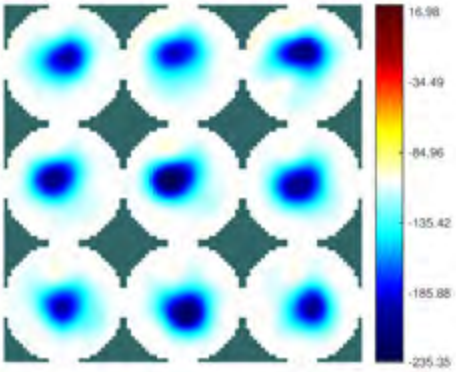

(a)

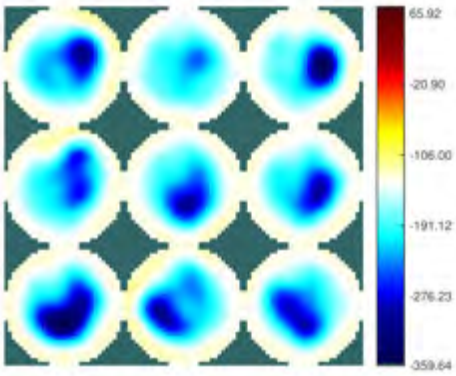

(b)

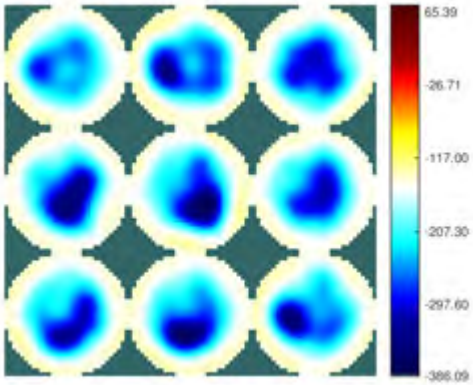

(c)

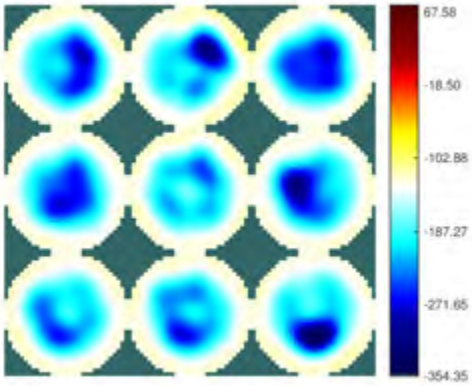

(d)

Figure 4.9. ERT reconstruction of steady state dispersion at a superficial gas velocity of 0.016m/s at local column cross-sectional area of the captured data on the time interval of 0.636 seconds: (a) first section, (b) second section, (c) third section, (d) fourth section.

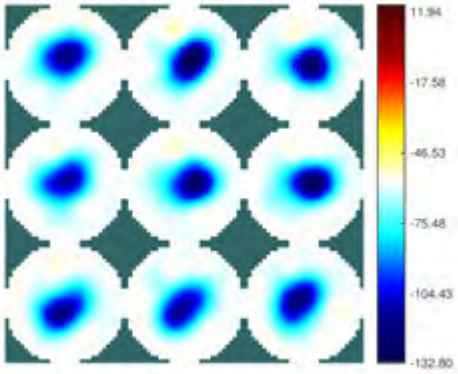

(a)

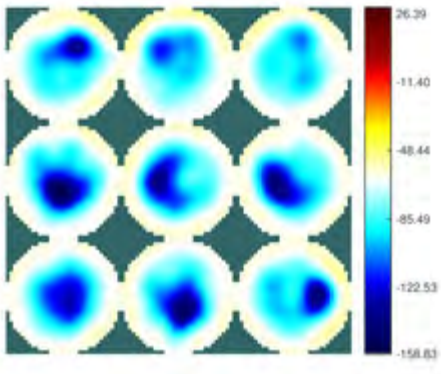

(b)

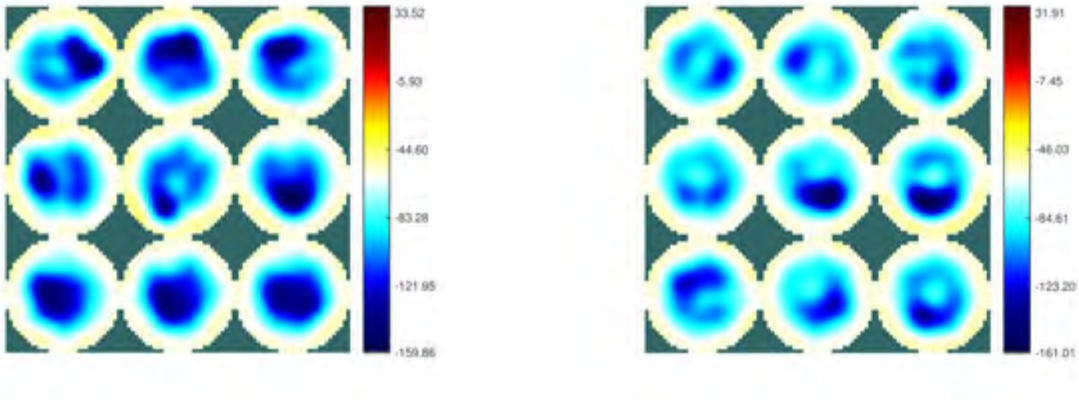

(c) (d)

Figure 4.10. ERT reconstruction of steady state dispersion at the superficial gas velocity of 0.01m/s at a local column cross-sectional area of the captured data on the time-interval of 0.636 seconds: (a) first section, (b) second section, (c) third section, (d) fourth section.

4.4.3. Time and area average of conductivity distribution (TACD) and gas holdup computations from ERT images

The computation of the area average of conductivity (ACD) values on the cross-section of a sensor layer is based on the following model. Let the area of a discrete element be A_i, where $i = 1,2,\dots,N$, and N is the highest index of elements (i.e. for 832 elements, $N = 832$). In a case where the cross section was uniformly discretized, $A_i = A_{i+1} = \dots = A_N$. Let the conductivity value on each element be ξ_i, where $i = 1,2,\dots,N$. The ACD is then

$$\bar{\xi}_A^f = \frac{\sum_{i=1}^{N} \xi_i^f A_i^f}{\sum_{i=1}^{N} A_i^f} \tag{4.8}$$

where $f = 1,2,\dots,m$, f is the index of the data frames.

Since the size of each discrete element is equal,

$$\bar{\xi}_A^f = \frac{\sum_{i=1}^{N} \xi_i^f}{\sum_{i=1}^{N} i} \tag{4.9}$$

The TACD is then

$$\langle \bar{\xi}_A^f \rangle = \frac{\sum_{f=1}^{m} \bar{\xi}_A^f}{\sum_{f=1}^{m} f} \tag{4.10}$$

The mean of the conductivity values on all elements within a target column section over a known time period will be denoted by the TACD as in Eq.(4.10). The maximum and minimum conductivity values on all elements within a target column section over a known time period were calculated using the expression in Eq.(4.11) and Eq.(4.12) respectively.

$$\xi^{max} = \max\left(\max\left(\xi_1^f, \xi_2^f, \xi_3^f, \xi_4^f, \dots, \xi_N^f\right)\right); \tag{4.11}$$

$$\xi^{min} = \min\left(\min\left(\xi_1^f, \xi_2^f, \xi_3^f, \xi_4^f, \dots, \xi_N^f\right)\right); \tag{4.12}$$

In a 2-phase gas-liquid dispersion system, Maxwell's relation (Maxwell, 1873), Eq.(4.13), relates the gas holdup ($\varepsilon_{g,i}$) to the known conductivity of the continuous phase (ξ_1), dispersed phase (ξ_2) and the mixture phase (ξ_{mc}). The ξ_{mc} term in Eq.(4.13) is the TACD of the local mixture phase $\langle\bar{\xi}_A^f\rangle$ computed from the pixel conductivities of the ERT reconstructed images.

$$\varepsilon_{g,i} = \frac{2\xi_1 + \xi_2 - 2\xi_{mc} - {\xi_{mc}\,\xi_2}/{\xi_1}}{\xi_{mc} - {\xi_2}/{\xi_1} + 2(\xi_1 - \xi_2)} \tag{4.13}$$

If the dispersed phase is a non-conductive material $\xi_2 = 0$, Eq.(4.13) is simplified to

$$\varepsilon_{g,i} = \frac{2\xi_1 - 2\xi_{mc}}{2\xi_1 + \xi_{mc}} \tag{4.14}$$

4.4.4. Results of gas void fractions by the analysis of ERT images

The image reconstruction of the dispersion from the ERT data frames captured by the four electrode ring sensors at the gas flow rate of 0.016 m/s and 0.01 m/s are shown in Figure 4.9(a-d) and Figure 4.10 (a-d) respectively. The reconstructed images at lower superficial gas velocities ranging from 0.002 to 0.009m/s investigated in this study are displayed in Figure A1.1 to Figure A1.9 in the appendix. The images in the stated figures are arranged according to the order of data frame progression from the top left towards the top right, and then downwards with a termination at the bottom right image.

The images were obtained from analysis of ERT signals data captured over four electrode layers by the independent 2D measurement scheme. Radial variation in the conductivity distribution of the locally captured images with time could be observed in some images

though the 2-phase fluid system was steady state homogeneous flow. The radial conductivity difference variation can be explained by the local bubble population swirling resulting in radial variation in conductivity difference. Besides, the ERT high temporal signals are sensitive to slight variation in the conductivity field. The observed time-variant radial conductivity variation can also be related to the inverse algorithm technique of imaging generation.

Table A1.1, Table A1.2, Table A1.3 and Table A1.4 show the computed maximum, minimum and TACD values of areas within the first, second, third and fourth electrode layers respectively for 3 repeated measurements. These ERT data were captured for superficial gas velocities ranging from 0.002-0.016 m/s. Table A1.5, Table A1.6, Table A1.7 and Table A1.8 highlight the mean of maximum, minimum and the TACD values of the area conductivity locally in the column averaged over the number of measurements. Figure 4.11 shows the relations between the local mean values of TACD over 3 repeated measurements depending on the superficial gas velocity of data on Table A1.10.

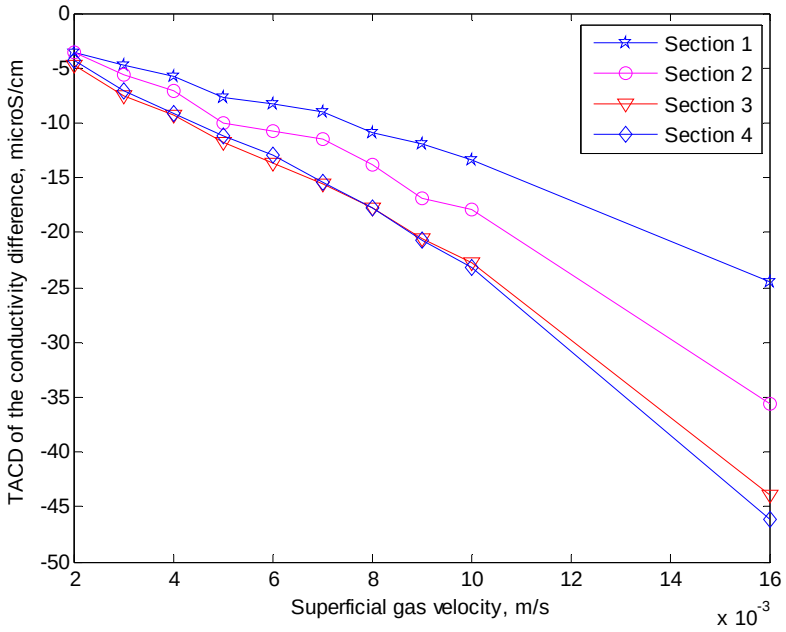

Figure 4.11. The local ERT TACD of the conductivity difference captured at steady state dispersion from 3 repeated measurements as a function superficial gas velocity.

The TACD conductivity difference values are negative because of the used ERT difference algorithm. The difference algorithm creates the dispersion images using the un-aerated and aerated phases conductivity distributions as well as the offset conductivity distribution.

Substituting the obtained TACD conductivity difference values into Maxwell's relation results in un-interpretable and inaccurate negative gas holdup values ($\varepsilon_g s$). Thus, in this work, the correlations for the local ERT TACD conductivity difference and the local DP gas void fraction measurements depending on superficial gas velocity will be developed. As a result, from a known ERT conductivity difference value in the column, the corresponding gas void fraction can be computed.

4.4.5. Conclusions on the local gas holdup computations by the ERT technique

Figure 4.11 shows the graphs of the mean of the local TACD as a function of superficial gas velocity. The graphical results indicate that the mean conductivities on all elements on the cross-sections at the column sections decrease with increasing superficial gas velocity (u_g). This is an expected result since an increasing the non-conductive gas (air) volume at any column section will lead to a decrease in mean conductivity (or increase resistivity) values in the sections.

The column height (1.545 m) and the need for the water-depth to be at least 0.2 m above the ERT electrode layer for accurate ERT data disallowed increasing u_g to achieve ε_g of 0.25. Thus, the considerable error in the ERT reconstruction at ε_g greater than 0.25 (Jia, et al., 2015) was not investigated. The superficial gas velocity of 0.016 m/s that yields the gas void fraction of 0.047 was the maximum achievable given the present column design and the axial lengths of the electrode layers.

Moreover, along the increasing column axis at a given superficial gas velocity, the mean TACD was observed to decrease as shown in Figure 4.11 and Figure 4.9. The difference in the local TACD is due to the variation in the local resident times of bubbles during axial swarming in the column. The bubble resident times were noticed to decrease with increasing column height. In particular, the swirling of bubbles at the third column section increases the bubble population resident times relative to the fourth column section at some superficial gas velocities (Figure 4.11). The TACD was higher at lower superficial gas velocities at Section 4 relative to Section 3 owing to the ratio of height of dispersion to the column diameter that lies in the range 4-6 (Vijayan, et al., 2007) (Rollbusch, et al., 2015). The variation in the bubble population resident times was on the account of the geometry of the tubular gas distributor producing dispersion with the periphery of the first and second column sections almost un-aerated as shown in Figure 4.9(a-b), Figure 4.10(a-b) and (a-b) of

Figure A1.1-Figure A1.9. The bubbles were noticed to be uniformly and well-distributed at Section 3 and 4.

4.5. The differential pressure (DP) transmitter and method of its calibration

The differential pressure is the difference in magnitude between a pressure value and a reference pressure. Both the absolute and gauge pressure values of a fluid state can be thought of as the differential pressure of the fluid with reference to the vacuum or a zero pressure and the atmospheric pressure respectively. By connecting the DP pressure ports to appropriate BCR pressure legs, the DP of the aerated fluid state with reference the un-aerated fluid state can be measured. That is the top and the low-pressure legs of the BCR connected to the DP high and low ports as shown in Figure 4.12.

As depicted in Figure 4.12, the water head should be above the column top pressure leg for accurate DP recordings using the DP transmitter. The DP transmitter senses the DP inform of a change in density of the volume of the aerated fluid system and the un-aerated fluid system. An increase or a decrease in density of fluid in the target column section leads to a respective increase or decrease of the pressure on the column bottom pressure leg. The corresponding output signals of the displayed water-head levels were viewed on a Labview graphical software.

The DP measures the decreasing density as the decreasing DP when the transmitter's high and low ports are connected to the bottom and top pressure legs of the column. However, to ensure the transmitter measures a density decrease as an increase in differential pressure locally, the transmitter's high and low ports were respectively connected to the top and bottom pressure legs. This manner of connection is referred to as 'cross-connection' of the pressure legs in this work and was made in line with the transmitter calibration method. The 'cross-connection' was made to allow for easier processing of positive real numbers instead of negative real numbers as shown in Figure 4.12.

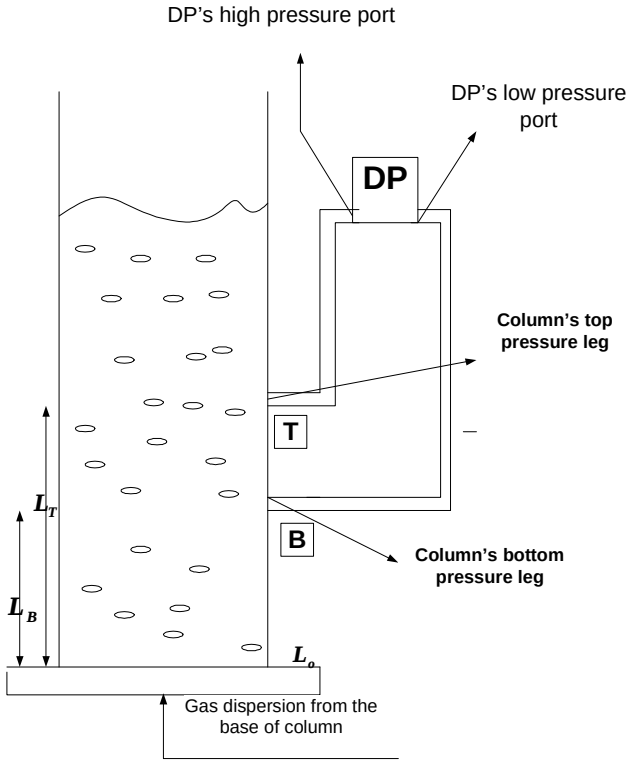

Figure 4.12. Density measurement by the differential pressure (DP) transmitter.

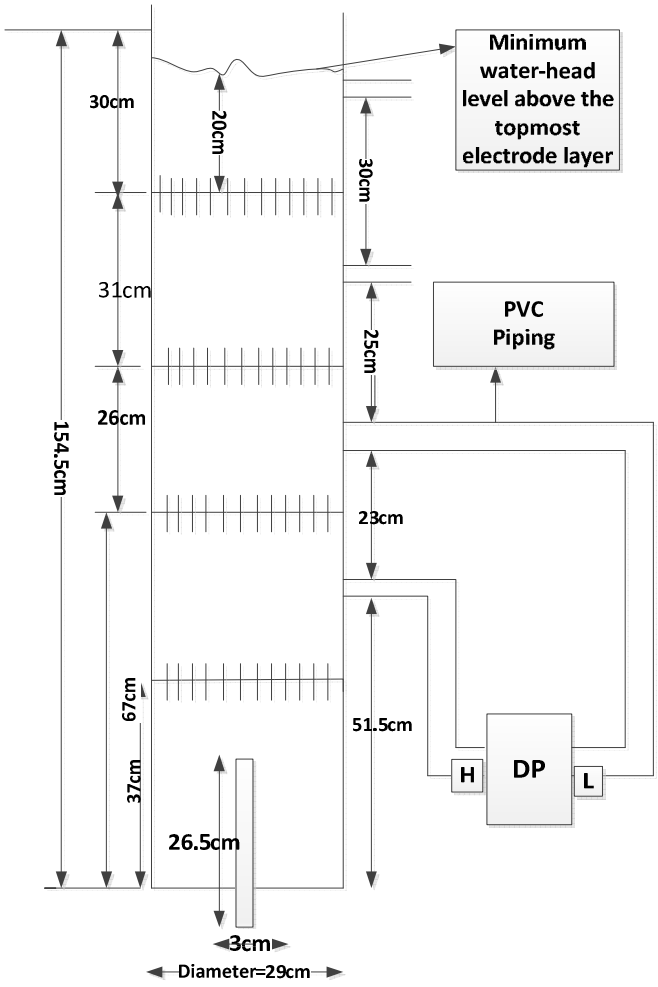

Figure 4.13. A diagram of the bubble column reactor fixed with a tubular porous tube air distributor at its base and electrode layers on its periphery with dimensions used for experimental studies

The BCR used for this work is designed with a dip tubular porous sparger of height 0.265 m and diameter 0.03 m. The base of the second column section was axially spaced from the top of the sparger by 0.22 m in an attempt to image well-distributed bubbles given the sparger geometry. The base of the first column section by the column sectioning was directly on the sparger's top surface to gain an insight of the inlet bubble size distribution. By the column sectioning dimensions (Figure 4.13), the bubble population were distributed at the centre top of the gas distributor at column section 1 and 2. The bubble population was well-distributed radially at section 2 and 3 during the bubble evolution. The heights of the first, second, third and fourth column sections were respectively 0.27 m, 0.23 m, 0.25 m and 0.30 m. The ERT data were captured on the four electrode rings fixed at 0.37 m, 0.67 m, 0.93 m and 1.24 m.

Given the BCR geometric dimensions, the sparger design and coupled electrode rings positions, the BCR was sectioned into four cells for the following reasons:

1. The height of a target BCR section was expected to be more than 0.2 m to achieve a higher accuracy measurement of the pressure drop;

2. The height of the water level above an electrode layer should be more than 0.2 m to limit the distortion of the electric field flux shape generated by current stimulation through boundary electrodes.

Before the calibration of the ERT estimate of gas holdup fractions against the DP measurement technique, the DP transmitter was initially calibrated against a water depth. In the experiment, the corresponding DP signal amplitude h_{DP} for a known water height h_w was initially determined. The background conductivity of the mildly saline bulk solution in the BCR was initially determined to be 410$\mu s/cm$ before aeration. Accordingly, the ERT equipment was set for a 4-layer independent data capturing and the DP ports were connected to appropriate column pressure legs. Thereafter, both the ERT and the DP signals were simultaneously captured before, during and after air sparging into the fluid system. The ERT data and the DP data were captured at these three instances to allow for accurate estimation of the offset values associated with both measurements.

In the first measurement set, the DP ports were connected to the two legs of the column first section and the ERT and DP data collection were captured. At the column first section, the bubble population concentration at the centre top of the gas distributor at higher resident rate hindered accurate interpretation of the DP signal for gas void fraction measurements. The ERT and DP simultaneous data capturing were repeated when the DP transmitter was connected to the column second, third, and fourth sections respectively. The DP signals were interpretable for accurate gas void fraction measurements at Section 2, 3 and 4 because the degree of bubble well-distribution increases with column height. In addition, the bubble population resident time was noticed to decrease with column height with higher bubble swirling at Section 3. Notably, during each data capturing using the DP, the ERT data were measured over four rings to allow for verification of the consistency of the ERT void fraction estimation.

4.5.1. Results of DP transmitter calibration

The derivation of the gas hold-up relation in a 2-phase gas-liquid system in terms of the pressure values before and during aeration as well as the difference of the two values is as follows. The derivation could also be based on the pressure values at the top and bottom pressure legs of the column (Figure 4.12) and the density of the gas-liquid mixture phase.

In a 2-phase semi-batch gas-liquid system, the pressure drop along the column is related by the following expression

$$\frac{dP}{dh} = -\rho_m g \tag{4.15}$$

where P, h, ρ_m and g represent respectively the pressure $[kgm^{-1}s^{-2}]$, the column height $[m]$, the density of the gas-liquid mixture phase $[kgm^{-3}]$ and the acceleration due to gravity $[ms^{-2}]$. The negative sign indicates the direction of pressure increase is opposite to the direction column height increase (Figure 4.12). Integrating Eq.(4.15) along the column height to determine the differential pressure change due to gas dispersion at a column section of height $H = L_T - L_B$, Eq.(4.16) is obtained.

$$\int_{P_B}^{P_T} dP = -\int_{L_B}^{L_T} \rho_m \, g dh \tag{4.16}$$

The top and bottom positions of the pressure legs on the column are respectively denoted by L_T and L_B as in Figure 4.12. Evaluating the integral of Eq.(4.16), Eq.(4.17) results as in

$$(P_B - P_T) = \rho_m g(L_T - L_B) \tag{4.17}$$

The pressure difference between the bottom and top pressure leg is measurable using the DP transmitter. Since the difference in height of the column ($\Delta L_{cell} = L_T - L_B$) could directly be measured on the column, Eq.(4.17) could be re-written as in Eq.(4.18).

$$\Delta P_{cell} = \rho_m g \Delta L_{cell} \tag{4.18}$$

The density ρ_m of the gas-liquid mixture is related to the density of the gas ρ_G and liquid ρ_L as well as gas hold-up ε_g in the column by the expression in Eq.(4.19)

$$\rho_m = \varepsilon_g \rho_G + (1 - \varepsilon_g)\rho_L \tag{4.19}$$

Substituting Eq.(4.18) into Eq.(4.19) and solving for ε_g, the following expression is derived.

$$\varepsilon_g = \frac{-\Delta P}{g\Delta L(\rho_L - \rho_G)} + \frac{\rho_L}{(\rho_L - \rho_G)} \tag{4.20}$$

In a case where $\rho_L \gg \rho_G$, Eq.(4.21) results from Eq.(4.20).

$$\varepsilon_g = 1 - \frac{\Delta P}{g\Delta L\rho_L} \tag{4.21}$$

Simplifying Eq.(4.21) further, Eq.(4.22) and Eq.(4.23) are obtained.

$$\varepsilon_g = \frac{g\Delta L\rho_L - g\Delta L\rho_m}{g\Delta L\rho_L} = \frac{g\Delta V\rho_L - g\Delta V\rho_m}{g\Delta V\rho_L} \tag{4.22}$$

$$\varepsilon_g = \frac{W_L - W_m}{W_L} = \frac{W_g}{W_L} \tag{4.23}$$

where W_L, W_m and W_g are the weights of liquid $[kgms^{-2}]$, mixture of gas-liquid phase and gas phase respectively.

The weight of a substance immersed or suspended in a liquid is the weight of the volume of the liquid it displaces. Thus, the weight of the liquid of density ρ_L displaced by the gas of weight W_g is the weight W_L'. The volume of the liquid displaced or volume occupied by the gas is then V_L' such that $W_g = W_L' = \rho_L V_L' g$. Expressing Eq.(4.23) in terms of volume of fluid states contained in a column during aeration leads to Eq.(4.24)

$$\varepsilon_g = \frac{\rho_L V_L' g}{\rho_L V_L g} = \frac{V_L'}{V_L} \tag{4.24}$$

In Eq.(4.24), the gas hold-up fraction is the ratio of the volume occupied by the gas phase in the aerated fluid state to the total volume occupied by the liquid phase before aeration. The gas void fraction at a column section was calculated in accordance with Eq.(4.24) using the following defined variables.

Let the height of water displaced during the aeration of the homogeneous mildly saline bulk solution be denoted by h_a; and the DP reading corresponding to the height of displaced water head be h_{DP}. By the stated DP calibration correlation, h_a was calculated from the DP reading as in Eq.(4.25).

$$h_a = \frac{h_{DP}}{h_w} \tag{4.25}$$

The h_a values in the BCR at section 2, 3 and 4 as a function of superficial gas velocities ranging from 0.002 to 0.016 m/s are presented in Table 4.2. The DP values were validated by the water-head level measurements using the DP to gauge the water-depth pressure against the atmospheric pressure.

Table 4.2. The height of displaced water head during aeration of the liquid phase, h_a, (cm) for varied superficial gas velocities.

U_g (m/s)	Section 2 h_a^1(cm)	Section 3 h_a^2(cm)	Section 4 h_a^3(cm)
0.002	0.44	0.57	0.91
0.003	0.74	0.88	1.53
0.004	0.85	1.26	2.01
0.005	1.08	1.54	2.39
0.006	1.14	1.72	2.66
0.007	1.34	1.92	3.05
0.008	1.46	2.29	3.37
0.009	1.50	2.35	3.67
0.010	1.70	2.63	4.12
0.016	2.12	4.36	6.58

If the volume of gas (air) in the first column section was calculated as $A_c h_a^1 = V_{gas}^1$; and the volume of the section filled with liquid before aeration, V_{lig}^1, was calculated as $A_c h_{sc}^1 = V_{lig}^1$, the gas void fraction can be calculated as

$$\varepsilon_g^1 = \frac{V_{gas}^1}{V_{lig}^1} = \frac{A_c h_a^1}{A_c h_{sc}^1} = \frac{h_a^1}{h_{sc}^1} \tag{4.26}$$

In Eq.(4.26), h_a and h_{sc} are respectively the heights of column occupied by the gas and liquid. Table A1.9 (appendix) shows the local gas void fraction in percentage (%) as a function of superficial gas velocity (m/s). The stated values are the mean values of the gas void fractions from the DP data sets when the liquid phase was aerated at known superficial gas velocities. The errors associated with the mean values from a data sets in hundreds were calculated by the product of the standard deviation and the t-statistic based on 95% confidence interval. Figure 4.14 shows the graphs of the local gas void fractions as a function of superficial gas velocity at column section 2, 3 and 4 compared to published results.

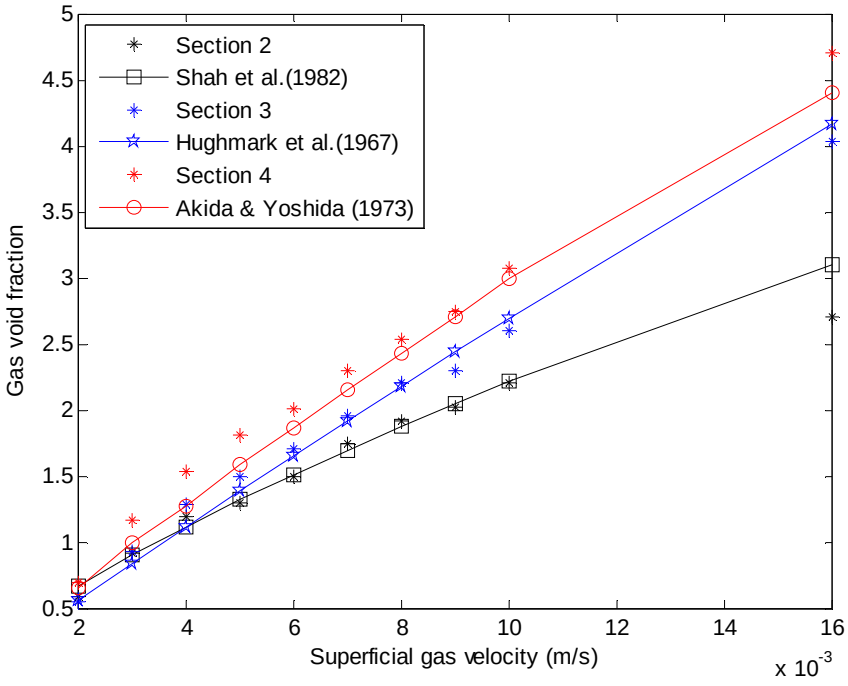

Figure 4.14. Local gas void fraction as a function of superficial gas velocity measured using the DP

The relationship between the gas holdup fraction and the superficial gas velocity is generally of the form of Eq.(4.27) (Shah, et al., 1982). The value of n was reported to depend on the flow regime. For the bubbly flow regime, the value of n was found to vary from 0.7 to 1.2 (Deckwer, et al., 1980).

$$\varepsilon_g = C^1 U_g^n \tag{4.27}$$

Since bubbly flow regimes were studied, the n was chosen as 0.75. The chosen value was intended to allow for the determination of C^1 through a regression analysis of the model with the measured gas void fractions at section 2. A range of values for C^1 from 0.5 to 0.9 was sampled to compute the Chi-squared values, X^2, based on the method of least square regression between the model and the measured data. The X^2 is defined as

$$X^2 = \frac{1}{\sigma^2}\sum_{i=1}^{n}(y_i - f(x_{1i}, \dots, x_{li}; a_1, \dots, a_m))^2 \tag{4.28}$$

where σ is the common standard deviation in the measured data; y_i and f respectively denotes the measured and the model predicted gas void fraction at a given gas flow rate. The graph of the calculated Chi-squared values over sampled constants are shown in Figure 4.15.

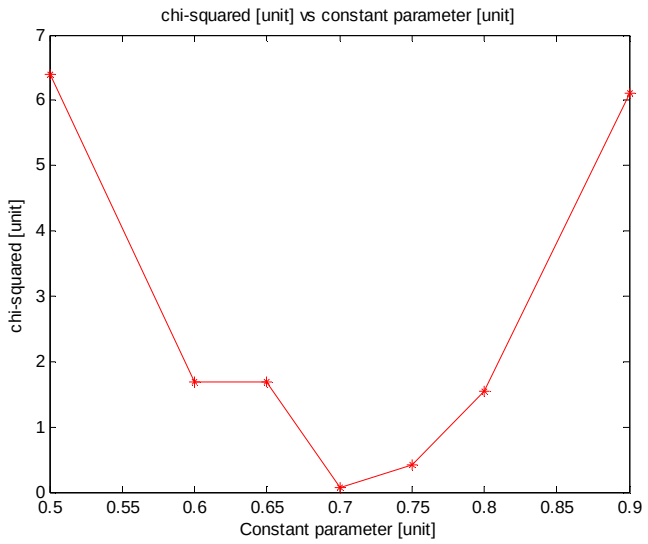

Figure 4.15. Graph of chi-squared against sampled constant for fitting model with experimental data.

Figure 4.15 indicates a constant value outside the sampled range will lead to much disparity between the model and measured data. Figure 4.15 also shows that the constant value of 0.7 minimises the X^2 expression. The confidence interval at 95% of the mean of the sampled constants was calculated using Eq.(4.29)

$$\bar{x} \pm t_{n-1;\alpha/2} S_{\bar{x}} \tag{4.29}$$

where $S_{\bar{x}}$ is the standard error of the mean; $t_{n-1;\alpha/2}$ is the t-statistic corresponding to the t-distribution for $n-1$ degrees of freedom; and α is the chosen level of probability. Thus, the value of C^1 was determined to be 0.7±0.1 at 95% confidence interval (i.e. $\alpha = 0.05$). The results in Table A1.9 are plotted in Figure 4.16 with the graph lines through the data points.

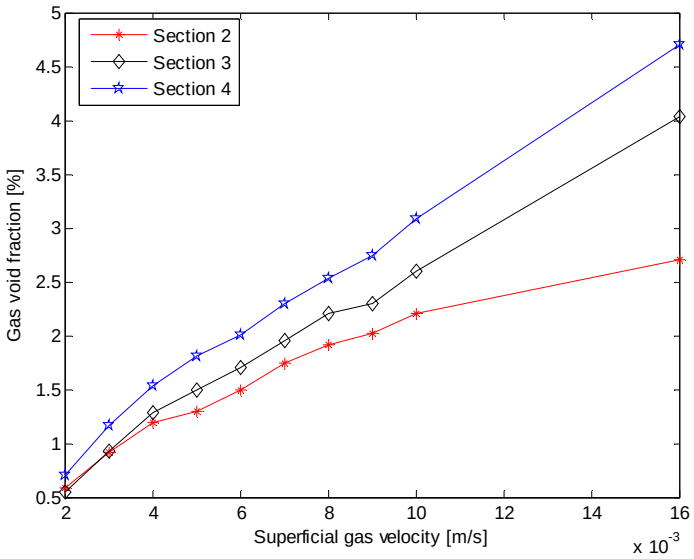

Figure 4.16. Local gas void fraction as a function superficial gas velocity.

The graphs of the gas void fractions along the column axis for varied superficial gas velocities are displayed in Figure 4.17.

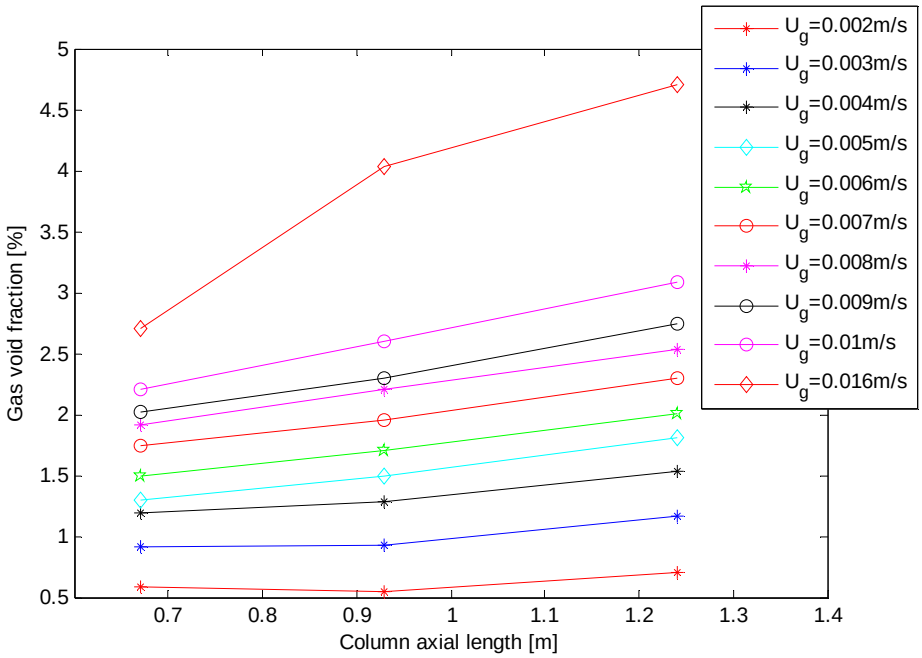

Figure 4.17. Gas void fraction as a function of column axial length for varied superficial gas velocities

The residual mean square, S^2, is a regression analysis quantity used to evaluate the accuracy of which a parameterised model represents the true underlying relationship between dependent and independent variables. The S^2 is defined as

$$S^2 = \frac{S_R}{n-m} \tag{4.30}$$

where the residual sum of squares, S_R, is expressed as

$$S_R = \sum_{i=1}^{n} (y_i - f(x_{1i}, \dots, x_{li}; a_1, \dots, a_m))^2 \tag{4.31}$$

n and m respectively represent the number of observations and parameters. The square root of S^2 is the standard deviation of the disparity between model and measurements. The R-square (S^2) is defined as the difference between unity(one) and the ratio of the residual sum of squares to the total variations accounted for in a measurements (Catherine A., 2001). The $S^2$and R^2 values were calculated between the measured local gas void fractions with gas flow rates against the published empirical correlations by (Hughmark, 1967), (Shah, et al., 1982) and (Akita & Yoshida, 1973). The empirically developed correlations by (Hughmark, 1967), (Shah, et al., 1982) and (Akita & Yoshida, 1973) were reported to be valid within the studied superficial gas velocities and operating conditions as reviewed in Section 2.7.1.

The measured and the calculated local gas void fractions using appropriate correlation were denoted by y_i and $f(x_{1i}, \dots, x_{li}; a_1, \dots, a_m)$ respectively at a given gas flow rate. Table 4.3 shows the calculated S^2, R^2 and the standard deviations by comparing the local gas void fractions for varied gas flow rates with published results.

Table 4.3. The residual mean squares and the standard deviations of the local gas void fractions over studied flow rates against published results.

	Sec. 2	Sec. 3	Sec. 4
Reference results	Shah et al. (1982)	Hughmark (1967)	Akida & Yoshida(1973)
S^2	0.022	0.082	0.038
Standard deviation	0.149	0.012	0.195
Chi_squre	0.440	0.104	0.238
R_square	0.950	0.988	0.974
F-statistic	155.52	684.187	293.978

4.5.2. Discussion and conclusions on the DP calibration

The graphs of the measured gas void fraction with gas superficial velocity at the second, third and fourth sections of the column agree respectively with the empirical correlations by (Shah, et al., 1982), (Hughmark, 1967) and (Akita & Yoshida, 1973) as shown in Figure 4.14. The trends of the local gas holdup fraction depending on superficial gas velocity were reported in the study on dynamic gas disengagement by (Sriram & Mann, 1977). The local gas void fraction for a given gas flow rate is observed to increase along the column axis. The difference in the local gas void fractions is also noticed to increase with an increase in gas flow rate as shown in Figure 4.16 and Figure 4.17.

The disparity in the local gas void fractions can be attributed to the use of a porous tubular gas distributor. For all gas flow rates, the gas distributor generated bubble swarm in a way that the bulk of the bubbles reside in the centre region of the column at the first column section. The periphery zone was almost un-aerated at the first column section as seen in

Figure 4.8(a). The bubbles began to be radially distributed at the second column section and were uniformly well-distributed at the third and fourth column sections. The axial bubble swarming pattern influenced by the porous tubular sparger accounts for the variation in the bubble resident times locally in the column. The bubble resident time in the semi-batch fluid flow was highest in section 1, higher in section 2 and high in section 3 and 4. The decreasing bubble resident time with increasing column height explains the short bubble travel times at lower column sections resulting in lower gas void fractions. Similar observations were made in the study on the influence of sparger type and superficial gas velocity on gas holdup in a bubble column reactor (Behnoosh, et al., 2009).

As the bubble population swarm, the bubble coalescence phenomenon leads to increase in the mean bubble size along the column axis up to height of 1.5 m and steady afterwards (Sattar, et al., 2013) (Laari & Turunen, 2003). Although regions in the column with smaller bubbles should result in higher gas holdup fraction, the decreasing bubble resident time with column height contributes to higher gas holdup fractions at higher column sections.

In the study to establish the effects of gas distributor on gas holdup distribution in a column, the perforated was noticed to produce uniform distribution of gas. The cone and the bubble cap distributors were observed to produce bubbles that move up the column as large bubbles in the region close to the column centre (Sailesh. B, et al., 1997). The periphery regions were observed to be un-aerated, which reflected in the captured dispersion images at the lower column sections (Sailesh. B, et al., 1997). The bubble evolution pattern produced by the cone and bubble cap distributors can be likened to the used gas distributor as shown in Figure 4.8(a). The use of sintered porous plate distributors minimises the bubble fluctuation velocity at the sparger orificies and ensured uniform distribution of bubbles radially and axially in the column. The magnitude of the gas holdup fractions generated by sintered plates were higher than that by perforated plates and the difference increases with increasing superficial gas velocity (Sailesh. B, et al., 1997).

Thus, the increasing level of uniform distribution of bubbles along column axis contributes to higher gas holdup values along the column axis at a given gas flow rate. The non-uniformity of bubble distribution axially in the column also caused the difference in the local gas void fractions to increase with increasing gas flow rate.

Furthermore, by the relationship between gas void fraction and superficial gas velocity, the reported range of the power index n for homogenous regime is $0.7 < n < 1.2$ (Shah, et al., 1982). The range may have resulted from differences in gas holdup fractions generated by varied gas distributor designs. This is in addition to the column geometric dimensions and operational conditions in the column. The gas holdup fraction at higher sections of the column is similar to that produced by a sintered porous or perforated plates, while that at lower sections is close to that generated by cone or bubble cap or tubular spargers.

4.6. Correlation of the gas void fractions by the ERT and the DP methods

The computed equivalent ERT gas holdups from the mean conductivity values using Maxwell's relation do not agree with the actual void fraction computed using the DP transmitter. Because of the discrepancy, the local ERT conductivity difference value is calibrated against the DP local gas void fraction over superficial gas velocities ranging from 0.002 – 0.016 m/s to obtain the graphs in Figure 4.18.

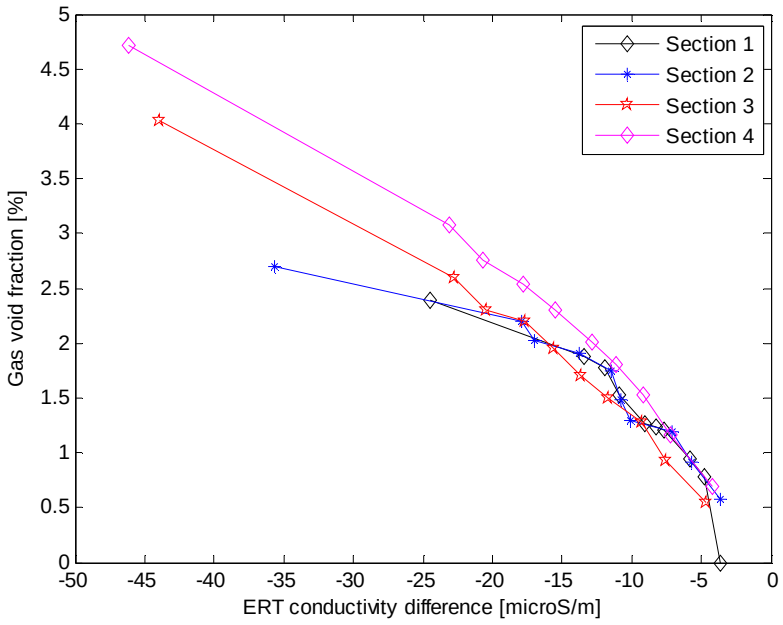

Figure 4.18. The local DP gas void fraction against the local ERT TACD during the steady state gas dispersion for superficial gas velocity ranging from 0.002-0.016 m/s.

Comparing the dependence of the TACD and the gas holdup fraction on superficial gas velocity as shown in Figure 4.11 and Figure 4.16, Figure 4.18 shows TACD decreases

proportionately with increasing gas holdup fraction locally. The decreasing conductivity difference value with increasing gas flow rate was as a result of increasing non-conductive of volume of air locally in the column. Describing the results in Figure 4.18, the increasing gas void fraction leading to proportionate decrease in the TACD along the column height is shown by comparing the local results for a given superficial gas velocity. The graphs are not perfect linear relations owing to the slight deviations of the experimentally measured local gas void fractions from appropriate empirically validated published models.

Moreover, due to the inaccurate measured DP gas void fractions at Section 1, the graph at Section 2 of Figure 4.18 will be assumed to hold at Section 1 given the sparger design. Thus, the gas void fractions Section 1 in Figure 4.18 were determined from the known TACD at Section 1 of Figure 4.11.

4.6.1. Conclusions on the correlation of the ERT data to the DP data for gas void fraction measurements

It was noticed that the gas void fraction increases along the axial length of the column for all the gas flow rates studied. The difference in the gas void fractions along the column axis was also observed to increase with increasing gas flow rate. The disparity in the local gas void fractions for a given gas flow rate is also seen in the local ERT TACD value. Thus, the differences in the graphs in Figure 4.16 are also seen in the graphs of the local gas void fractions against the local ERT gas void fraction estimates in Figure 4.18.

For a given gas flow rate, the local ERT conductivity difference decreases with column height. The conductivity distribution in the column during aeration is influenced largely by the non-uniformity in the bubble population distribution axially in the column. The gross circulation of bubble population at second and third sections accounts for the obtained conductivity differences at Section 3 and 4. Besides, the varying bubble coalescence rates as bubble population swarm axially to the top of the column also affect the conductivity distribution locally in the column.

Moreover, R^2 is close to unity and the large f-statistic values on Table 4.3 are much larger than the corresponding critical f-statistic value. These error analysis results indicate the

trends of the measured gas void fraction with superficial gas velocity are good representations of empirically determined published models.

The new idea of this chapter is the calibration of the ERT TACD results by difference algorithm against the DP transmitter results for the measurements of local gas holdup fractions. The calibration technique yields interpretable estimate of the gas holdup fractions from the obtained negative ERT conductivity difference values than substituting the negative conductivity difference values into Maxwell's relation of Eq.(4.13).

Chapter 5

Experimental measurements of bubble population parameters from captured ERT images in the process of dynamic gas disengagement

In Chapter 4, an experimental approach for the measurements of the local gas void fractions from the calibrated ERT TACD by the DP technique has been described. In order to accurately predict hydrodynamic parameters in a column, the local gas void fractions, the bubble size distribution and the BNDD need be known. Moreover, the gas holdup fractions, the bubble size distribution and the BNDD at the inlet first column section are required boundary conditions for column simulation by a PBM. Among the methods for analysing bubble population properties in a column, the dynamic gas disengagement (DGD) technique has been found to be an effective useful technique (Sriram & Mann, 1977). The area average of conductivity distribution (ACD) captured locally with time in the process of DGD is analysed in this chapter to obtain the bubble size profile and the BNDD in the column.

The DGD technique is fully described in Section 5.1. Older previous methods employed in determining the bubble sizes from the time-dependent gas void fractions during DGD are also described in a subsection of Section 5.1. Thereafter, the new method of interpreting the ERT time-variant ACD captured during DGD for the measurement of bubble sizes is explained in a subsection of Section 5.1. The new method of interpretation yielded the ERT data at discrete time steps when bubble sizes disengaged from the column. The discrete time steps were further analysed to determine the gas volumes of the disengaging bubble size classes locally in the column. A schematic of the sequences of ERT measurements and computations yielding the local BNDD and the axially averaged BNDD as well as the global SMBD is displayed in Section 5.2.

The obtained results of the local bubble population properties and the axial mean of the quantities are presented in tables in the respective section of this chapter. In the sections, the description of the methodologies used to obtain the results is presented alongside the results. The results of the ERT signal analysis allowing the measurement of the bubble population properties are then discussed in Section 5.3 to conclude this chapter.

5.1 Dynamic gas disengagement (DGD) method

The DGD technique is used to compute the gas holdup and the bubble size distribution for calculating the specific interfacial area and the mass transfer coefficient rates of a gas-liquid system. The theoretical basis of the static and dynamic holdups are provided to deepen an understanding of the possibility of exploring these parameters for the computation of bubble population properties.

Considering a column cross-section containing a gas - liquid dispersion of equal-sized bubbles with each bubble rising with velocity U_b as illustrated in Figure 5.1, a mass balance model could be developed. The mass balance in the presence of local superimposed liquid velocity, V_L' (either downwards(-) or upwards(+)) gives the following relationship between the local gas holdup ε' and the local superficial gas velocity U_G' (Sriram & Mann, 1977).

$$\frac{U_G'}{\varepsilon'} - \frac{V_L'}{1-\varepsilon'} = U_b \qquad (5.1)$$

Because the bubble interaction is non-significant at low gas hold-up, an assumption can be made that the bubble rise velocities should equal to the single bubble rise velocity, $U_{b\infty}$, in a large liquid volume. The spatial uniform hold-up, ε, is derivable from Eq.(5.1) to get Eq.(5.2) in a system having low gas hold-up when the liquid motion is negligible.

$$\varepsilon = \frac{U_G}{U_{b\infty}} \qquad (5.2)$$

Eq.(5.2) informs that the hold-up is expected to be linearly proportional to the superficial gas velocity. It has been observed that in an air-water system, the bubble rise velocity is virtually unchanged as the bubble size increases from 3 to 8mm (Sriram & Mann, 1977). Eq.(5.2) has also been found to hold in a non-uniform bubble cloud over this size range. The expression in Eq.(5.2) has been found to be applicable at low gas velocity using spargers that generate small bubbles. The small bubbles were expected to be produced from a uniform gas distribution limiting the gross circulation effects (Sriram & Mann, 1977).

The graphical relation between the gas hold-up and the gas velocity u_g shows an almost proportional increase until a certain value of gas velocity is attained. Further from the critical gas velocity value, the rate of increase of gas hold-up fraction fall-off as shown in Figure 5.2. The rate of increase in hold-up drops at larger gas velocities due to the presence of larger bubbles and/or the onset of circulation pattern.

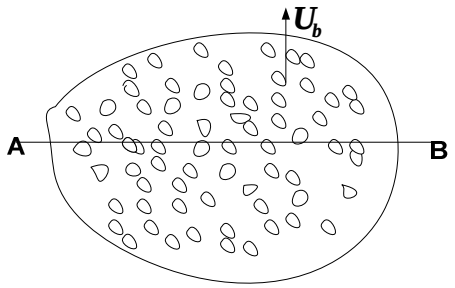

Figure 5.1. The cross-sectional area of bubble swarming in a column (Sriram & Mann, 1977).

Considering a general case where a size distribution of bubbles exists and bubbles of different sizes rise at different velocities, Eq.(5.1) is modified to obtain

$$\frac{U_G'}{\varepsilon'} - \frac{V_L'}{1-\varepsilon'} = \int_0^\infty f(d_b)\, U(d_b) dd_b \qquad (5.3)$$

In Eq.(5.3), $f(d_b)dd_b$ is the volume fraction of bubbles with size between d_b and $d_b + dd_b$ and $U(d_b)$ is the rise velocity of bubbles of size d_b. When Eq.(5.3) is applied to a gas-liquid reactor with no liquid motion and no bubble interactions, the overall static hold-up $\varepsilon(0)$ in a spatial uniform fluid system is of the form

$$\varepsilon(0) = {U_G}\Big/{\int_0^\infty f(d_b)U(d_b)dd_b} \qquad (5.4)$$

The bubble interactions usually arise from bubble coalescence and break-up that cause radial and axial variations in $f(d_b)$. If the value of the overall static hold-up and the rise velocity function $U(d_b)$ are known, a size distribution that satisfies Eq.(5.4) could be found. Theoretically, there are infinite numbers of distribution functional that satisfy the static hold-up condition of Eq.(5.4) since the number of equations are fewer than the numbers of unknowns. The problem of lack of a unique solution to Eq.(5.4) is resolved by observing the dynamic gas hold-up (transient holdup, $\varepsilon(t)$) behaviour that occurs after the gas flow is shut-off.

During the DGD process, larger faster bubbles disengaged more quickly than smaller slower bubbles due to greater buoyancy effects of the liquid on larger bubbles than smaller bubbles. Thus, an accurately sized distribution to Eq.(5.4) will then be expected to satisfy the transient hold-up condition during DGD in addition to the static hold-up.

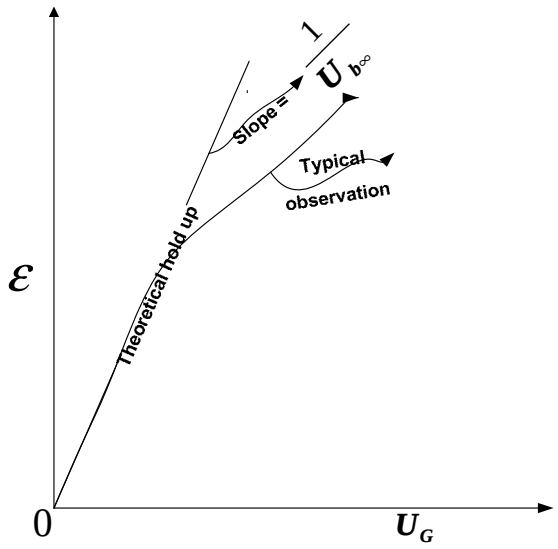

Figure 5.2. A relation between the gas void fraction and the superficial gas velocity.

Figure 5.3a shows the gas-liquid dispersion in a BCR containing bubble population of various sizes before gas was turned off. Figure 5.3b depicts an equivalent manner in which bubbles of different sizes are stratified as soon as the gas was turned off (Sriram & Mann, 1977). The rates of disengagement of bubbles by their sizes are illustrated in Figure 5.3c, where larger bubbles disengaged most quickly and smaller ones least quickly.

In the process of DGD, assuming the height of column section is L, and bubbles of size d_b have velocity $U(d_b)$, this bubble class will be completely disengaged from the section in time, $t = \frac{L}{U(d_b)}$. In a DGD process, it is usually assumed that the bubble size distribution was initial axially homogeneous with no significant bubble interactions. In such a system, the fraction of the volume fraction of bubbles of size d_b in the dispersion after time t from the start of the DGD process will be given by $(1 - t\,{}^{U(d_b)}/_{L})$. Accordingly, if the static hold-up $\varepsilon(0)$ is known, the transient gas hold-up $\varepsilon(t)$ during DGD at time t will be

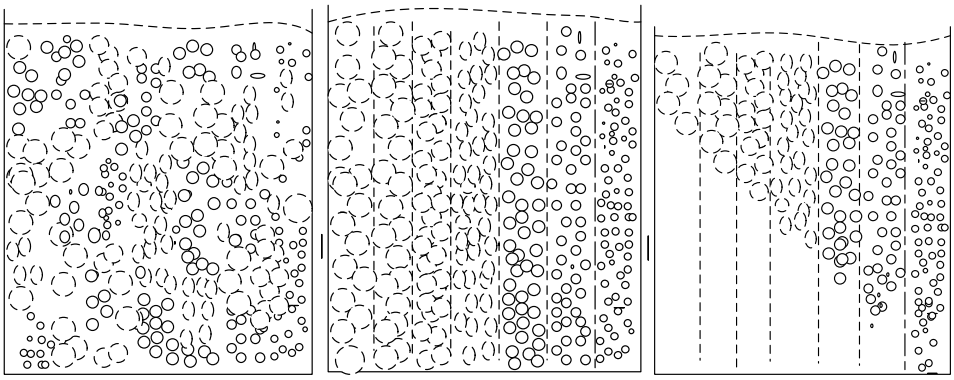

(a) (b) (c)

Figure 5.3. Pictorial representation model of bubble size distribution at various time during DGD process: a) before turning off the air inlet into the column; b) at the instant the air inlet is switched off; c) after an elapsed time t after turning off the air and in the process of DGD (Sriram & Mann, 1977).

$$\varepsilon(t) = \varepsilon(0) \int_0^\infty f(d_b) \left(1 - t^{U(d_b)/L}\right) dd_b \qquad (5.5)$$

with the boundary condition that $\left(1 - t^{U(d_b)/L}\right)$ is zero when $1 < t^{U(d_b)/L}$. The physical meaning of the condition associated with Eq.(5.5) is that bubbles of size d_b have left the dispersion after that time.

Since changing pressure $p(t)$ in the process of DGD can be expressed in term of changing gas void fractions $\varepsilon(t)$ as

$$\varepsilon_g = 1 - \frac{\Delta p}{g \Delta L \rho_L} = \varepsilon(t) = \frac{p(t)}{p_o} \qquad (5.6)$$

Eq.(5.5) can be re-written as in Eq.(5.7).

$$p(t) = p_o \varepsilon(0) \int_0^\infty f(d_b) \left(1 - t^{U(d_b)/L}\right) dd_b \qquad (5.7)$$

Furthermore, the variation in the bubble rise velocities of the different bubble sizes was due to varied densities of bubble sizes and buoyancy force effects of the liquid on the bubbles. The term bubble sizes refer to the mean values of the bubble sizes from the grouping of the bubble population into classes by their sizes and calculating the mean bubble size in every

class. The fact that bubbles of different sizes rise at different rates could be used to determine the bubble size distribution using Eq.(5.7).

5.1.1. The previous method of determining bubble sizes based on the DGD technique

In the work of (Patel, et al., 1989), the height of dispersion during the bubble disengagement was determined by visual observation in the process of DGD. However, the pressure transducer signals were used in the work of (Daly, et al., 1992) to measure the rate of liquid level drop during the bubble disengagement processes. The use of the pressure drop technique during the DGD processes has benefits over the visual inspection of dispersion height since it is applicable for both transparent and opaque bubble column vessel. The data obtained by the pressure drop technique could also be post-processed.

The basic assumptions on the state of the fluid system made by both (Patel, et al., 1989) and (Daly, et al., 1992) during the DGD process are as follow:

1. The dispersion is axially homogeneous (i.e. the bubble size distribution was initially axially homogeneous) at time t = 0;

2. There are no bubble interactions (i.e. bubble coalescence and break-up);

3. There is a constant rate of disengagement processes (i.e. all bubbles disengage independently of each other);

4. The cross-sectional area occupied by bubble rising at velocity, u_{bi}, remains constant throughout the disengagement.

The analysis of the DGD process in the work of (Patel, et al., 1989) differs from that of (Daly, et al., 1992) in the method of obtaining a balance of the fluid condition. Patel's analysis of DGD model is based on a balance of the liquid volume. This means the liquid volume remains constant while the dispersion volume changes during the DGD process. In Daly's analysis model, a balance was made on the dispersion volume below a pressure transducer, which remains constant throughout the entire disengagement process.

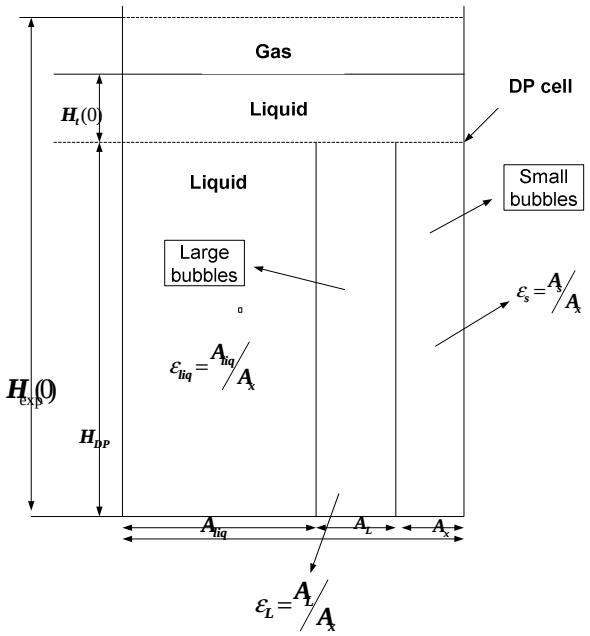
Gas
Liquid
DP cell
$H_t(0)$
Liquid
Small bubbles
Large bubbles
$\varepsilon_s = A_s / A_x$
$\varepsilon_{liq} = A_{liq} / A_x$
$H_{exp}(0)$
H_{DP}
A_{liq}
A_L
A_x
$\varepsilon_L = A_L / A_x$

(a)

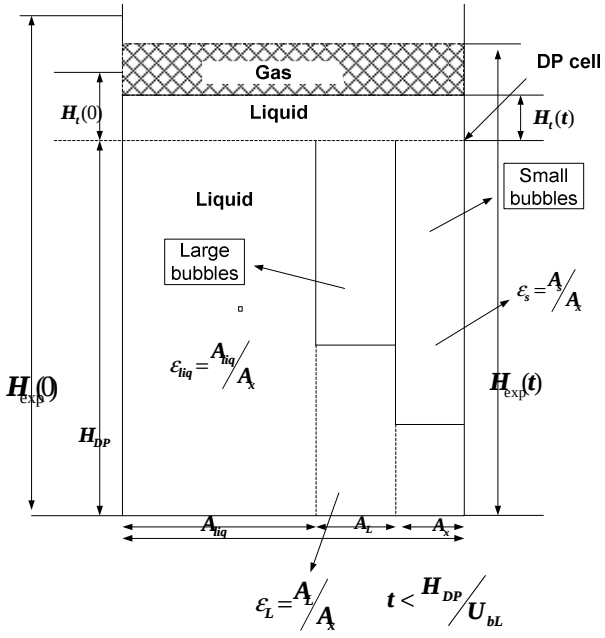
Gas
DP cell
$H_t(0)$
Liquid
$H_t(t)$
Small bubbles
Liquid
Large bubbles
$\varepsilon_s = A_s / A_x$
$\varepsilon_{liq} = A_{liq} / A_x$
$H_{exp}(0)$
$H_{exp}(t)$
H_{DP}
A_{liq}
A_L
A_x
$\varepsilon_L = A_L / A_x$
$t < H_{DP} / U_{bL}$

(b)

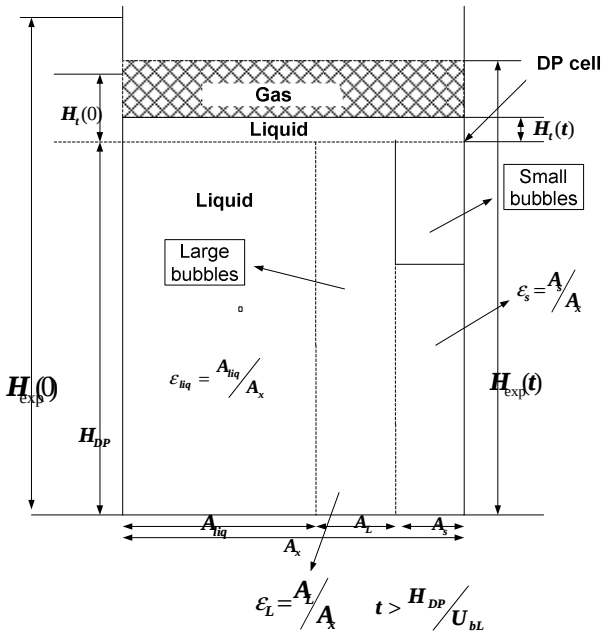

(c)

Figure 5.4. Gas-liquid dispersion at varied times during DGD: a) at initial time t=0; b) during first period of disengagement; c) during the second period of disengagement (small bubble disengagement) (Daly, et al., 1992).

Daly's analysis of the DGD technique for a simple case of bimodal bubble size distribution is presented, which could be generalised for a multimodal bubble size distribution (Daly, et al., 1992). Given an initial state of the 2-phase gas-liquid fluid system of Figure 5.4a, a distinction between large and small bubble sizes can be made under the pressure transducer. The distinction between the large and small bubble sizes above the pressure transducer cannot be made since no information of the dispersed phase is obtained there.

Beginning from the first period of disengagement as in Figure 5.4b, the liquid volume passing below the pressure transducer must be the same as the gas volume composing of small and large bubbles. The two bubble sizes eventually rise above the pressure transducer. This means the liquid volume occupies the spatial volume left by the bubble population. Accordingly, the liquid volume below the pressure transducer at time t can be expressed in terms of the bubble rise velocities and holdup of small and large bubbles as follows:

$$H_t(t)A_x = H_t(0)A_x - t(U_{bs}A_s + U_{bL}A_L);\ \ t < {}^{H_{DP}}/_{U_{bL}} \tag{5.8}$$

where A_L, A_s and A_x are cross-sectional areas occupied by large bubbles, small bubbles and the column respectively; H_{DP}, $H_t(0)$ and $H_t(t)$ are height of transducer (DP cell) above the

distributor, height of the liquid above the transducer at time $t = 0$ and time t respectively; U_{bL} and U_{bs} are rise velocities of the large and the small bubbles respectively.

Dividing every term in Eq.(5.8) by A_x and using the definition of $\varepsilon_{gos} = {A_s}/{A_x}$ and $\varepsilon_{goL} = {A_L}/{A_x}$, Eq.(5.8) can be re-written as in Eq.(5.9)

$$H_t(t) = H_t(0) - t\left(U_{bs}\varepsilon_{gos} + U_{bL}\varepsilon_{goL}\right);\ \ t < {H_{DP}}/{U_{bL}} \tag{5.9}$$

Figure 5.4c is an illustration of the dispersed state of small and large bubbles in the liquid phase during the second period of disengagement. The height of liquid above the pressure transducer during the second period can be expressed as

$$H_t(t) = H_t(t_1) - U_{bs}\varepsilon_{gos}(t - t_1); \qquad t \geq {H_{DP}}/{U_{bL}} \tag{5.10}$$

where $H_t(t_1)$ is the liquid height above the transducer at the beginning of period 2; t_1 is the time at which all large bubbles passed by the transducer (i.e. $t_1 = {H_{DP}}/{U_{bL}}$); $t - t_1$ is the required time for the remaining small bubbles to disengaged from the liquid.

In generalising the bimodal bubble size distribution illustrated in Figure 5.4a – c to obtain the expression for the multimodal size distribution, Eq.(5.11) describes the liquid level drop rate during the disengagement of bubbles of size j.

$$H_t(t) = H_t\left(t_{j-1}\right) - \left(t - t_{j-1}\right)\sum_{i=j}^{N} U_{bi}\varepsilon_{goi}\,; \quad t_{j-1} < t < {H_{DP}}/{U_{bj}} \tag{5.11}$$

In Eq.(5.11), the first period of disengagement is denoted by $j = 1$; the last period of disengagement is represented by $j = N$ and $t_o = 0$ denotes the time before DGD process started.

Furthermore, plotting $H_t(t)$ vs t in the expression of Eq.(5.11) should yield a series of N straight lines with slopes S_j and inflexion points t_j ($j = 1\ to\ N$). Thus, the bubble rise velocities and volume fractions of bubbles in the dispersion at $t = 0$ can be calculated from S_j and t_j using Eq.(5.12) and Eq.(5.13). Eq.(5.13) is obtained by re-expressing Eq.(5.11) with the inclusion of S_j term.

$$U_{bj} < {H_{DP}}/{t_j} \tag{5.12}$$

$$\varepsilon_{goj} = {-(S_j + \sum_{i=j+1}^{N} U_{bi}\varepsilon_{goi})}/{U_{bj}} \qquad (5.13)$$

The S_j in Eq.(5.13) stands for the slope of the disengagement curve corresponding to the disengagement of bubbles during period $t_{j-1} < t < t_j$; and the time the last bubble size j passed above the pressure transducer is denoted by t_j. To obtain the volume fraction of bubbles at various disengagement periods t_j, Eq.(5.13) is solved recursively starting with $j = N$ (for $j = N, \varepsilon_{goN} = {-S_N}/{U_{bN}}$).

These two approaches to analysing the DGD technique have been shown to yield the bubble size distribution in the respective article where the basic assumptions of the fluid system are taken to be valid. The accumulated volume fraction of gas within a known volume of a bubble column reactor of height H could also be represented as

$$\varepsilon_g = \sum_{j=m}^{N} \varepsilon_{g,j} \qquad (m=1\ ,\ \ldots,\ N) \qquad (5.14)$$

where $\varepsilon_{g,j}$ is gas holdup of certain bubble class disengaging from the bulk liquid phase during the period m. The largest bubble class that rises fastest will disengage during the period, $m = 1$, while the smallest bubble class that rises slowest will disengage during the period $m = N$.

In determining the characteristic times t_j of bubble size class disengagements, the output continuous voltage graph that decreases with decreasing liquid depth in a column section could be discretised into equally spaced intervals and averaged. The output voltage graph decreases owing to drop in fluid pressure in a column section as a result of aeration of the liquid phase as measured by the DP technique. For instance, if the output voltage signal graph was discretized into 120 points, these points could be averaged over every 10 data points so as to obtain 12 bubble classes (Daly, et al., 1992).

Following such discretization, if the computed slope between successive points was found to be less than 0.5%, the points between such successive points will be discarded until discrete points were reached where the gradient was greater than 0.5% (Daly, et al., 1992). These discrete points, having slopes greater than or equal to 0.5% will then be used as the next discrete points from the last point where the slope was greater than 0.5%. The set of time intervals between the resulting sets of valid discrete points was taken as the time periods of the disengagement of bubble sizes. The time periods were further used to estimate the

corresponding bubble rise velocities (i.e. the SMB rise velocities) and bubble sizes (diameters and volumes) of varied bubble size classes.

Furthermore, (Fransolet, et al., 2005) developed an algorithm based on the minimization of the pressure signal energy in order to determine the slope breaks separating the classes of bubble sizes. The algorithm involved knowing a prior slope break positions and de-trending the pressure signals within each of the apriori determined classes in order to remove linear trend components. The a-prior slope positions were then adjusted so as to minimise the energy of the de-trended signals.

The stated methods yielded time steps t_j when bubble size classes disengaged from the column. Visual observation of the hydrodynamic process through the present transparent BCR shows a higher variation in bubble sizes. Thus, it is intended in this chapter to continue and improve on the methods of characteristic times of bubble size classes disengagement to obtain higher bubble size resolution.

Given the higher temporal sensitivity of the ERT images to changing gas void fraction, the time-varying ERT data during DGD process can be interpreted to determine t_j accurately. The sensitivity of the ERT data is approximately 500 frames per second with the used ERT equipment. This new method of interpreting the gas void fractions equivalent of the ERT ACD with time $\varepsilon^{ERT}(t)$ during DGD to obtain t_j is explained in the next section.

5.1.2. Development of a novel method of determining bubble sizes by the DGD technique

Bubble sizes were observed to be randomly distributed in the cylindrical space of the BCR during a steady state evolution of bubble population from the base of the column to its top as in Figure 5.3a. However, when the gas disengagement process began, the bubbles were seen to segregate (as in Figure 5.3b). The segregation was such that the mean size of bubble population class that disengage from any of the column section fastest was the largest class. This bubble population class was subsequently followed by the larger bubble size class until the smallest size class disengage from the column section base. During this DGD process, the bubble population rise through the second, third and fourth column sections before their exit to the atmosphere (as shown in Figure 4.13).

The development of the new method of determining bubble size distribution in a column is based on analysis of the transient gas void fraction captured by the ERT sensor electrode layers during DGD process. The new method could be viewed as analysing the time-variant gas void fraction from the start to the end of the DGD process captured by ERT sensors instead of pressure transducers. The ERT technique has a high temporal resolution and sensitive to gas void fraction changes across the column cross-sections than the DP method. Thus, the time t_j^i when bubble size class j disengaged from a layer i along the column axis is expected to be accurately captured by ERT method than DP method.

The time-variant gas void fraction captured by the ERT method is sensitive to the size and axial distribution of bubble sizes (Sriram & Mann, 1977) (Daly, et al., 1992). The DGD process sensitivity to bubble size and axial distribution is illustrated in Figure 5.3(a-c) and Figure 5.4(a-c). Daly related the pressure drop to bubble size and axial distribution by expressing the liquid volume below the pressure transducer at time t in terms of the bubble rise velocities and the holdup of bubble size classes (Eq.(5.11)) (Daly, et al., 1992). The derivation of the balance of dispersion volume below the DP cell for a multimodal bubble size distribution is given in Eq.(5.11). This equation describes the rate of liquid level drop during the disengagement of bubble size j (i.e. $j = 1,2, \dots, \mathrm{N}$). A diagrammatic illustration of the balance of dispersion volume for the case of bimodal bubble classes ($\mathrm{N} = 2$) is given in Figure 5.4(a – c).

Assuming 5 bubble size classes (i.e. $j = 1,2, \dots ,5$) dispersion in the liquid, Eq.(5.11) can be expressed as in Eq.(5.15) to Eq.(5.19). These equation (Eq.(5.15) and Eq.(5.19)) show the dependence of the time-variant pressure drop on bubble sizes and axial distribution during DGD. In Eq.(5.15) to Eq.(5.19), the liquid volume drop with time denotes the pressure drop with time; the bubble rise velocities is represented by the bubble sizes; and the product of differential time $(t - t_j)$ and bubble rise velocities accounts for the axial distribution of bubble sizes. Simplifying Eq.(5.11) that accounts for balance of dispersion volume during the first, second, third, fourth and fifth period (i.e. $j = 1,2, \dots ,5$) of disengagement, Eq.(5.15) to Eq.(5.19) are obtained respectively.

$$H_t(t) = H_t(0) - (t - t_o)\left(U_{b1}\varepsilon_{go1} + U_{b2}\varepsilon_{go2} + U_{b3}\varepsilon_{go3} + U_{b4}\varepsilon_{go4} + U_{b5}\varepsilon_{go5}\right) \tag{5.15}$$

$$H_t(t) = H_t(t_1) - (t - t_1)\left(U_{b2}\varepsilon_{go2} + U_{b3}\varepsilon_{go3} + U_{b4}\varepsilon_{go4} + U_{b5}\varepsilon_{go5}\right) \quad (5.16)$$

$$H_t(t) = H_t(t_2) - (t - t_2)\left(U_{b3}\varepsilon_{go3} + U_{b4}\varepsilon_{go4} + U_{b5}\varepsilon_{go5}\right) \quad (5.17)$$

$$H_t(t) = H_t(t_3) - (t - t_3)\left(U_{b4}\varepsilon_{go4} + U_{b5}\varepsilon_{go5}\right) \quad (5.18)$$

$$H_t(t) = H_t(t_4) - (t - t_4)\left(U_{b5}\varepsilon_{go5}\right) \quad (5.19)$$

Furthermore, the disparity in the time when the mean bubble size of disengaging bubble population left a known column cross-sectional area was explored in this work to calculate bubble size classes. Knowing the time taken for the migration of a change in the gas void fraction from a plane to a higher plane allows for the computation of the disengaging bubble size average rise velocity. The average rise velocity is thus calculated as the ratio of axial length travelled by the ERT gas void fraction change to difference in its arrival time at a plane and a higher plane.

The disengaging gas volume locally at the time a bubble size class travel along the axial length of the column was determined using a DP transmitter connected over column sections. The DP was connected over the second, third and fourth column sections as shown in Figure 4.13 for the measurements of the local disengaging gas volume. The disengaging gas volume at know characteristic bubble disengagement times locally could alternatively be determined from the known local ERT ACD value. This is by substituting the ERT data into a correlation model for gas void fraction between the ERT data and the DP data for varied gas flow rates.

With the DP transmitter connected at a local column section, the local ERT data at four layers and the DP data were captured during the entire DGD period. These simultaneous local measurements using the DP transmitter and the ERT ring sensors was repeated following the DP axial movements from a column section to another. Given the stated assumptions on the fluid state during DGD process, the disengagement process locally was expected to be same approximately for a given gas flow rate when the gas inlet was turned-off repeatedly 3 times. The obtained DP gas void fraction data by the axial movement after each instant of gas turning-off can, thus, be analysed to determine the gas volume locally during the DGD process.

Beginning from the instant the gas in-let was turned off, gas volume (or gas void fraction) locally was noticed to decrease progressively with time until it was zero following complete

disengagement. The graphs of the time-dependent gas volume during DGD processes at superficial gas velocities of 0.01 m/s and 0.016 m/s are shown in

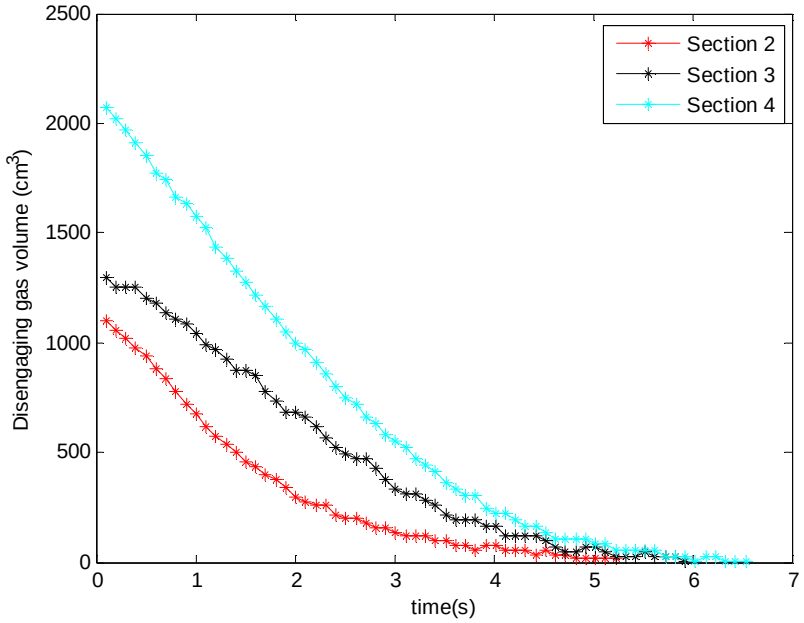

Figure 5.5. The local disengaging gas volume with time at the superficial gas velocity of 0.01 m/s

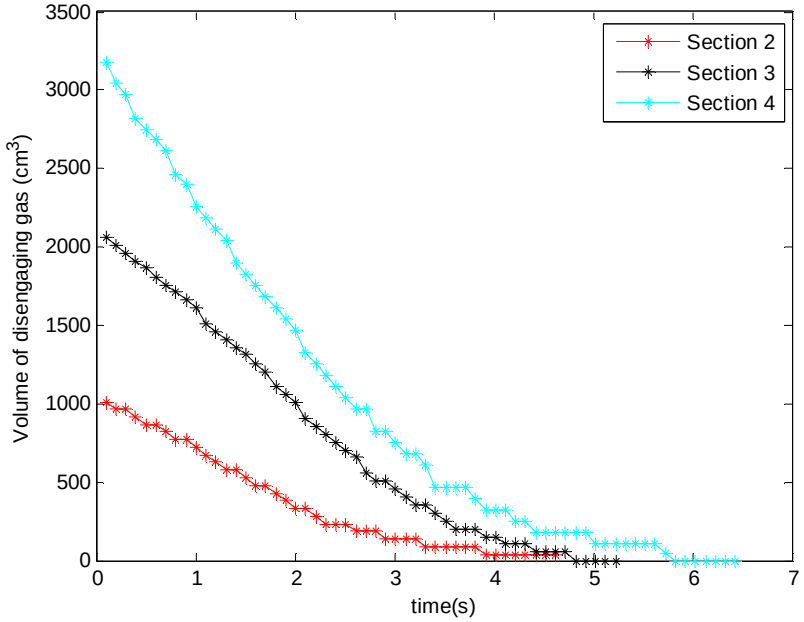

Figure 5.6. The local disengaging gas volume with time at the superficial gas velocity of 0.016 m/s.

5.2. Characteristic times of bubble sizes disengagement during DGD process

The method of calculating the characteristic times of disengagement of bubble sizes is based on the manner of axial transport of local time-variant ERT estimates of gas void fraction during DGD process. The form of axial transport of the change in gas void fraction was captured by the ERT sensor as increasing ACD locally in the column. Due to the higher temporal resolution of the ERT data over the DP data, the ERT data was analysed for the calculation of the characteristic times of disengaging bubble sizes. The increasing ERT ACD change along the column sections was tracked to determine the travel times and the lag times of the gas void fraction in column sections.

The ERT data analysis also included the computation of the time taken for the axial migration of the ERT TACD estimate for the gas void fraction changes. The analysis then allowed for calculating the lag times of the gas void fraction changes across the column planes in order to calculate the accumulated time periods for the disengagement of bubble size classes. The ERT voltage data used for image reconstruction were averaged over every two data frames captured within 0.0106 seconds corresponding to a discrete gas holdup value.

The simultaneous capturing of ERT data over four layers during DGD process motivated its interpretation for the calculation of the characteristic disengagement times of bubble size classes. This approach was explored instead of the interpretation of the local gas void fraction using the DP transmitter. The local characteristic disengagement times of bubble size classes could not be determined from the DP transmitter data since 3 or 4 DPs transmitters were not available for simultaneous capturing of local gas void fraction changes.

However, the use of 3 DP transmitters to capture the gas volume change at the 3 column sections simultaneously during the DGD process may not yield expected accurate data. This is because the DP measures changes in gas void fractions (or gas volume) at the column sections due to the density changes of the dispersed phase in the continuous phase. The density of the dispersed phase at a column section depends on the gas volume and volume of the column section. Thus, gas void fraction changes within the column sectional volume will be less sensitive to disengaging bubble size classes locally compared to the changes at column cross-sectional area captured by ERT sensors. Although the gas dispersion was not uniform globally in the column given the axial distribution of gas void fraction obtained in

Chapter 4, the gas dispersion was steady radially and axially at local column section. This was verified by the local ERT 2D images with time at column section and the local DP measurements as well as visual observation of the local dispersion. Thus, the DGD analysis is expected to be valid since the assumption associated to the DGD process approximately hold in the column at steady state.

As an example, the local time-variant ERT images captured at 0.64 seconds time interval during DGD process at superficial gas velocity of 0.016 m/s are shown (b) of Figure 5.7, Figure 5.8, Figure 5.9 and Figure 5.10. The diagrammatic illustration of the local column sections where data were captured are shown in (a) of Figure 5.7, Figure 5.8, Figure 5.9 and Figure 5.10. The images in Figure 5.7a and similar ones are arranged in order of time progression from the top left image towards the top right and then downwards with termination at bottom right. In these figures, the low conductivity region (high resistivity) corresponds to the deep blue colour, while the high conductivity region (low resistivity) corresponds to the white background colour. Table A1.11 shows the local time-dependent ERT TACD (average over two frames) captured during DGD process at superficial gas velocity of 0.016 m/s.

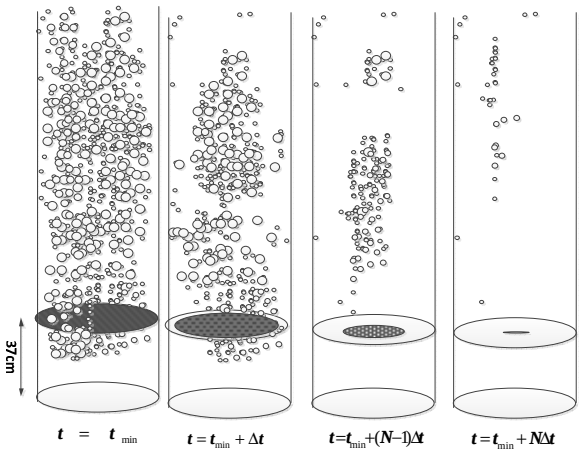

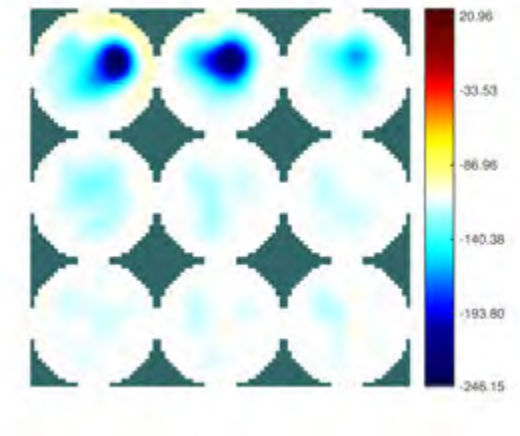

(a) (b)

Figure 5.7 . Diagrammatic illustration of the changing gas holdup with time progression on the first electrode layer during DGD process; (b) ERT images of the air dispersion at gas flow rate of 0.016m/s at 0.64 seconds time interval during the DGD process on the first electrode layer

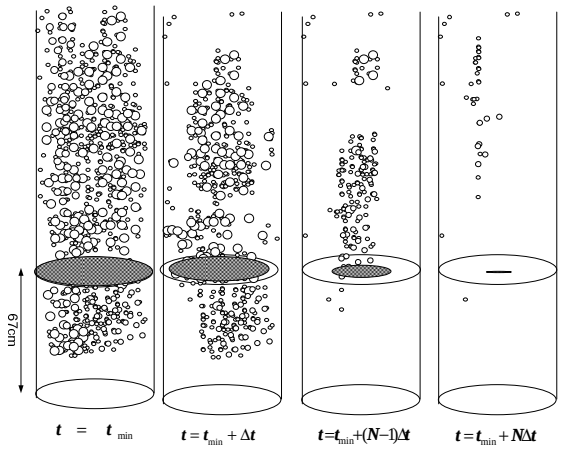

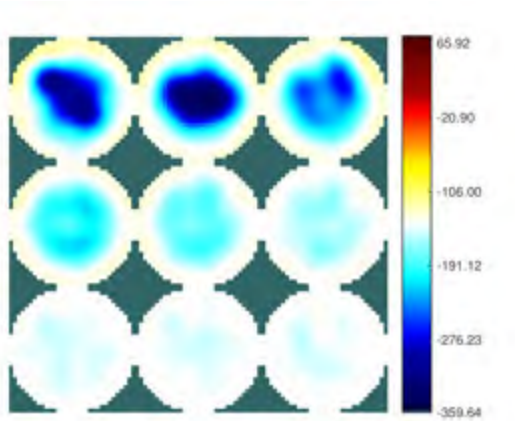

(a) (b)

Figure 5.8. Diagrammatic illustration of the changing gas holdup with time progression on the second electrode layer during DGD process; (b) ERT images of the air dispersion at the gas flow rate of 0.016m/s at 0.64 seconds time interval during the DGD process on the second electrode layer.

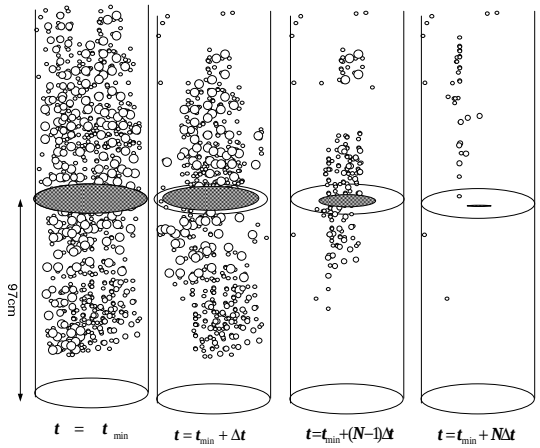

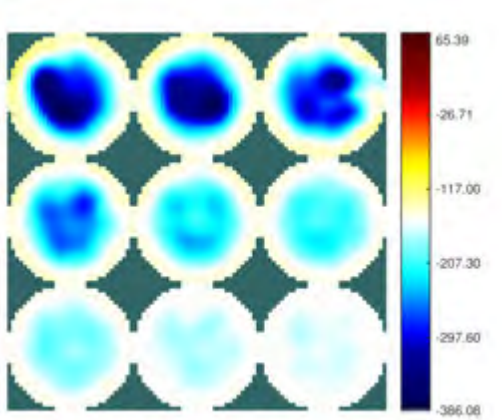

(a) (b)

Figure 5.9. Diagrammatic illustration of the changing gas holdup with time progression on the third electrode layer during DGD process; (b) ERT images of the air dispersion at gas flow rate of 0.016m/s at 0.64 seconds time interval during the DGD process on the third electrode layer

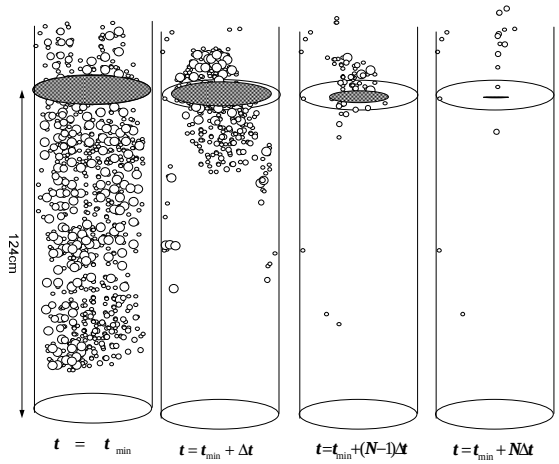

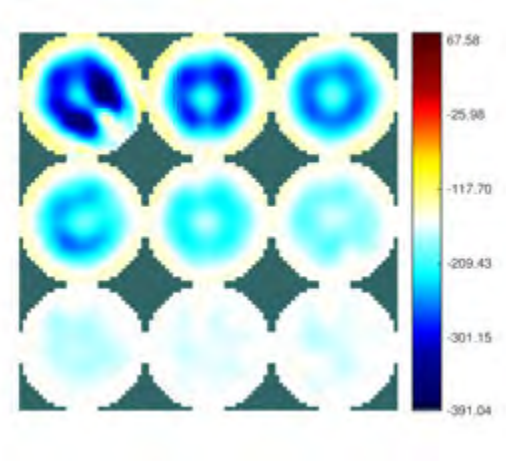

(b) (b)

Figure 5.10. Diagrammatic illustration of the changing gas holdup with time progression on the fourth electrode layer during DGD process; (b) ERT images of the air dispersion at the gas flow rate of 0.016m/s at 0.64 seconds time interval during the DGD process on the fourth electrode layer.

The analysis of the ERT TACD at local sections of the column on Table A1.11 showed a unit increase in values of the TACD after certain period of time during the DGD processes. The time-variant unit increase in the ERT TACD was interpreted to mean the gas volume that composes of a bubble size class disengage from a column section during the characteristic time of the bubble size class disengagement.

The time a unit increase in the TACD (approx. to 2 s.f) is seen on ring 1 leads the time it is observed on ring 2. The time the TACD is seen on ring 2 leads the time it is seen on ring 3. The lead times are illustrated in Figure 5.11 for a bubble size by the time taken for the gray area at a column cross-section to migrate axially during DGD process. The lag time in the migration of a void change could be deduced from the (b) in Figure 5.7 to Figure 5.10. The first four unit changes in the ERT ACD reach electrode layer 2, 3 and 4 relative to electrode layer 1 by the lag times of 0.3604, 0.5936 and 0.8904 seconds respectively.

Focussing on a certain bubble size class, the contribution of the mean bubble sizes in the class disengaging at any time will be dependent on the axial spatial location of the reference mean bubble sizes. Due to buoyancy liquid effects, visual observation of the DGD process shows that the mean bubble sizes disengaging at any time from any section, $\overline{d^l_{t_{min}}}$ of the column having contributions from varied bubble sizes is such that

$$\overline{d^l_{t_{min}+\Delta t}} > \overline{d^l_{t_{min}+2\Delta t}} > \overline{d^l_{t_{min}+3\Delta t}} > \overline{d^l_{t_{min}+4\Delta t}} > \cdots > \overline{d^l_{t_{min}+N\Delta t}}; \quad (5.20)$$

for $i = 1,2,3,4$

By the notation in Eq.(5.20), the duration of DGD process t ranges from $t = [t^i_{min}, t^i_{max}]$. The term Δt is an increment in time from t_{min} when a unit increase in the ERT TACD lasted at a reference layer including the lag (delayed travel) time from an initial time at gas inlet stoppage (t_{min}). The term $2\Delta t$ is the increment in time when 2 unit increase in the TACD lasted including its lag time to a reference layer from its value at t_{min}. Likewise, the term $N\Delta t$ is the increment in time when N unit increase in the TACD lasted including its lag time to a reference layer from its value at t_{min}.

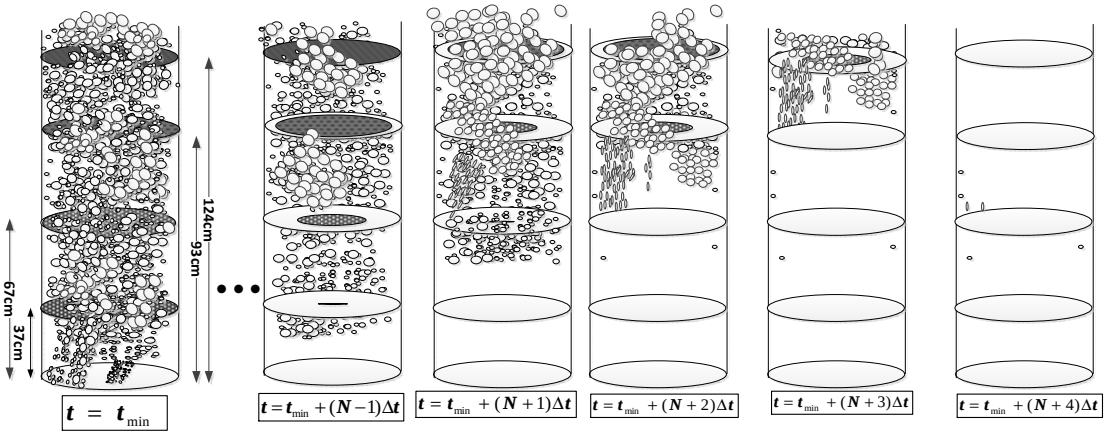

Figure 5.11. Diagrammatic illustration of changing local ERT estimate of gas void fractions with time during DGD. The sequences of obtained data are shown in Table 5.1. The gray areas at cross-sections of the ring sensors are proportional to the degree of conductivity at column cross-sections.

Table 5.1. The ERT void fraction estimates at column sections at varied time during DGD process illustrated in Figure 5.11

$z(cm)$	t_{min}	$t_{min+\Delta t}$	$t_{min+2\Delta t}$	$t_{min+3\Delta t}$	$t_{min+4\Delta t}$	$t_{min+5\Delta t}$	… .	$t_{min+N\Delta t}$	$t_{min+(N+1)\Delta t}$
37	$\varepsilon^1_{t_{min}}$	$\varepsilon^1_{t_{min+\Delta t}}$	$\varepsilon^1_{t_{min+2\Delta t}}$	$\varepsilon^1_{t_{min+3\Delta t}}$	$\varepsilon^1_{t_{min+4\Delta t}}$	$\varepsilon^1_{t_{min+5\Delta t}}$	…	$\varepsilon^1_{t_{min+N\Delta t}}$	0
67	$\varepsilon^2_{t_{min}}$	$\varepsilon^1_{t_{min}}$	$\varepsilon^1_{t_{min+\Delta t}}$	$\varepsilon^1_{t_{min+2\Delta t}}$	$\varepsilon^1_{t_{min+3\Delta t}}$	$\varepsilon^1_{t_{min+4\Delta t}}$		$\varepsilon^1_{t_{min+(N-1)\Delta t}}$	$\varepsilon^1_{t_{min+N\Delta t}}$
93	$\varepsilon^3_{t_{min}}$	$\varepsilon^2_{t_{min}}$	$\varepsilon^1_{t_{min}}$	$\varepsilon^1_{t_{min+\Delta t}}$	$\varepsilon^1_{t_{min+2\Delta t}}$	$\varepsilon^1_{t_{min+3\Delta t}}$	…	$\varepsilon^1_{t_{min+(N-2)\Delta t}}$	$\varepsilon^1_{t_{min+(N-1)\Delta t}}$
124	$\varepsilon^4_{t_{min}}$	$\varepsilon^3_{t_{min}}$	$\varepsilon^2_{t_{min}}$	$\varepsilon^1_{t_{min}}$	$\varepsilon^1_{t_{min+\Delta t}}$	$\varepsilon^1_{t_{min+2\Delta t}}$	…	$\varepsilon^1_{t_{min+(N-3)\Delta t}}$	$\varepsilon^1_{t_{min+(N-2)\Delta t}}$

$\boldsymbol{z(cm)}$	$\boldsymbol{t_{min+(N+2)\Delta t}}$	$\boldsymbol{t_{min+(N+3)\Delta t}}$	$\boldsymbol{t_{min+(N+4)\Delta t}}$
37	0	0	0
67	0	0	0
93	$\varepsilon^1_{t_{min+N\Delta t}}$	0	0
124	$\varepsilon^1_{t_{min+(N-1)\Delta t}}$	$\varepsilon^1_{t_{min+N\Delta t}}$	0

Table 5.1 shows the migration of changes in gas void fractions captured by the ERT images as a unit increase in the ERT TACD at with time (as shown in Table A1.11) during local bubble sizes disengagement. The manner of the changing gas void fractions in Table 5.1 illustrated with Figure 5.11 describes the progression of the changing TACD with time during DGD process as shown in Figure 5.7 to Figure 5.10.

Comparing the changes in gas void fractions at time t_{min} to time $t_{min+\Delta t}$ on Table 5.1, the gas void fraction $\varepsilon^1_{t_{min}}$ at layer 1 at time t_{min} has migrated to layer 2 in time $t_{min+\Delta t}$. The gas void fraction $\varepsilon^2_{t_{min}}$ at level 2 at time t_{min} has migrated to layer 3 in time $t_{min+\Delta t}$. The lag or travel time t^{i+1}_{lag} for a change in gas void fraction $\varepsilon^i_{t_{min}}$ from layer i to layer $i+1$ is of the form of Eq.(5.21), where t^{i+1}_{last} and t^{i}_{last} are the times when $\varepsilon^i_{t_{min}}$ lasted at level i and $i+1$ respectively.

$$\left(t_{min+\Delta t} + t_{\text{last}}^{i+1}\right) - \left(t_{min} + t_{\text{last}}^{i}\right) = t_{lag}^{i+1} \tag{5.21}$$

Similar migration of changes in gas void fractions from one column section to the other was noticed comparing the change in gas void fractions in column sections at time $t_{min+j\Delta t}$ with time $t_{min+(j+1)\Delta t}$. Here $j = 1, \ldots, N$ means the number of periods of disengagements and N is the last period of disengagement.

The lag time for the migration of a gas void change to reach higher electrode layers with reference to the base layer 1 was noticed for every unit increase in the local TACD. It was expected that the lag time would increase as the larger bubbles disengaged from the column section, resulting in an overall decrease in the average bubble size. Models of lag times taking note of differences in the lag times associated with the characteristic times of disengagement of bubble sizes were tested but the computed local BNDD could not be interpreted. Thus, it was assumed in present work that the successive lower bubble population sizes disengaged from the liquid at the same lag time as the first bubble size class with respect to the electrode sensor layers.

Furthermore, the characteristic time for the disengagement of bubbles in a class locally was calculated from half the sum of the total time a unit change in the ACD lasted and the lag time to reach the reference column section. This was done since the ACD were calculated from the electrode layers embedded in the column sections. Thus, the disengagement period j of bubbles in class size j from column section i was calculated using the expression of Eq.(5.22).

$$t_j^i = t_{min+(j-1)\Delta t}^i + \left(\frac{t_{min+j\Delta t}^i - t_{min+(j-1)\Delta t}^i}{2}\right); \tag{5.22}$$

$$i = 1,2,3,4 \text{ and } j = 1,2, \ldots, N+1$$

The term $t_{min+j\Delta t}^i$ denotes the time period the gas void fraction associated to a bubble size j lasted at column section i. The t_{lag}^i represents the lag or travel time from the first ring before the first gas void fraction change (i.e. bubble size $j = 1$) is captured by the ERT electrode ring embedded in column section i. The term t_{min}^i (i.e. t_{lag}^i at $i = 1,2, \ldots$) denotes the initial time of the DGD process from when a unit change in the ERT ACD is sensed on layer i. The lag times t_{lag}^2 and t_{lag}^3 can be interpreted as the times the first change in gas

void fraction was detected at layer 2 and 3 respectively relative to layer 1. Thus, in Eq.(5.22), for $j = 1, t_{min}^{1} = 0$, $t_{min}^{2} = t_{lag}^{2} = 0.3604$, $t_{min}^{3} = t_{lag}^{3} = 0.5936$ and $t_{min}^{4} = t_{lag}^{4} = 0.8904$. It was observed that a total number of N bubble size classes disengaged from respective section of the column. The smallest bubble size class N was noticed to disengage from section 1, 2, 3 and 4 after time $t_{min+(N+1)\Delta t}$, $t_{min+(N+2)\Delta t}$, $t_{min+(N+3)\Delta t}$ and $t_{min+(N+4)\Delta t}$ respectively.

5.3. Results: Stages of interpretation of ERT measurements coupled to the DGD process for the computation of bubble population parameters

The developed new method of interpreting the ERT ACD during DGD is applied in this section to estimate the axially averaged BNDD ($\bar{n}_z^{ERT}(r_j)$). In the following variables that will be defined, the index i denotes the discrete axial length of column (z), which ranges from $i = 1,2,3,4$. The index j represents the bubble size class that ranges from $j = 1,2,3,\dots,N$, where N is the last smallest bubble size class. The stages of processing the gas void fractions in terms of the time-dependent ERT ACD data and the disengaging gas volume locally during DGD are as follows:

In the following paragraphs an example of the method calculating the characteristic disengagement times of bubbles leading to the determination of BNDD in the column is provided. The computed local ACD by the difference reconstruction algorithm are stated in Table A1.11 for gas flow rates at 0.016 m/s. The calculated ACD area values are negative because of the use of the difference reconstruction algorithm. The time taken to capture each ERT data frame to calculate the ERT ACD values during DGD was 0.0106 seconds. The ERT ACD values increase with time during the DGD process from the moment of turning-off the gas inlet.

Let the initial local times before the DGD process began be denoted by t_{min}^{i} at section $i = 1,2,3,4$. The t_{min}^{i} were calculated by the number count of the ERT ACD values before a unit change increase that denotes the disengagement of the first bubble size was observed. The t_{min}^{i} were calculated at section 1, 2, 3 and 4 by counting and tracking the ERT ACD from when the gas was turned-off to the end of the span of the ACD values of -12, -20, -26 and -28 respectively of the data in Table A1.11. The characteristic times of the first bubble size class disengagement locally were calculated by the ERT data frame count of the span of the

ERT ACD values yielding -11, -19, -25 and -27 at section 1, 2,3 and 4 respectively. The obtained counts were 17, 6, 7 and 6 frames, which were interpreted to mean the times when a change in gas void fraction of the first bubble size lasted at the column section.

The counted number of data frames were divided by 2 and multiplied by the time taken to capture a frame (i.e. 0.106 sec.) and then added to the initial DGD start time to obtain the time for the first bubble size class disengagement (i.e. Eq.(5.22)). The characteristic disengagement time of the first bubble size class from the ERT ACD should be verified by accurate determination of the time the DGD process actually start. The characteristic disengagement of the last bubble size class can be determined from the time the last unit ERT ACD is observed in the column. The counted number of frames were divided by 2 since the electrode rings were placed at inter-levels between the column sections. The initial times in terms of the number or span of data frames were 23, 27, 43 and 43 frames respectively at layer 1, 2, 3 and 4. Thus, using Eq.(5.23) Eq.(5.24), Eq.(5.25) and Eq.(5.26) respectively the first bubble size disengaged at section 1, 2,3 and 4 to obtain the result in Table 5.2.

$$1.3780sec = \left(43 + \frac{6}{2}\right) \times 0.0106 + 0.8904 \tag{5.23}$$

$$1.0865sec = \left(43 + \frac{7}{2}\right) \times 0.0106 + 0.5936 \tag{5.24}$$

$$0.6784sec = \left(27 + \frac{6}{2}\right) \times 0.0106 + 0.3604 \tag{5.25}$$

$$0.3339sec = \left(23 + \frac{17}{2}\right) \times 0.0106 \tag{5.26}$$

The axial lengths travelled by the bubble population to reach the first, second, third and fourth electrode layers are respectively 0.24 m, 0.54 m, 0.80 m and 1.11 m. The average local bubble rise velocities of the first bubble size class was calculated from the ratio of the axial lengths to the local characteristic disengagement times. The measured average rise velocities of bubble size classes are shown in Table 5.3.

In estimating the bubble size classes from the observed discrete time steps when the ERT ACD increases by a unit value during DGD, the DGD process duration period need be determined accurately. The actual commencement time of the DGD process should be accurately determined owing to the short period of swirling of the dispersion in the

continuous phase after the gas inlet is turned-off. The time the DGD ends should also be ascertained due to the ill-conditioning of the ERT inverse problem that was solved to obtain the conductivity values during DGD process.

The sensitivity of the periphery ERT electrode layers to disturbance of the homogeneous conductive liquid phase by the dispersed phase increases from the centre towards the boundary of the column. Thus, the change in gas holdup values at much later times during the DGD may not be accurately interpreted to compute bubble size classes at those times. Besides, calculations have shown that five bubble classes are sufficient to accurately determine SMBD (Daly, et al., 1992).

The correlation of Eq.(5.27) that relates the average bubble rise velocity and its SMBD was used to determine the SMBD of bubble size classes at a known height of the column (Fukuma, et al., 1987). The calculated results are shown on Table 5.3.

$$d_{32,i,j} = {}^{0.59u_{i,j}^{b}}\Big/_{g} \tag{5.27}$$

The graph of the local time-variant gas void fraction measured using the DP was analysed to determine the disengaging gas volume locally during the DGD process (Figure 5.6). The local time-variant disengaging gas volume can alternatively be calculated by substituting the ERT TACD during DGD process into the appropriate local graph in Figure 4.18.

The local disengaging gas volumes associated to the disengaging bubble size classes were determined from the graphs in Figure 5.6 using the characteristic disengagement times of bubble size classes. The disengaging local gas volume at column section i during the rising of bubble size class j at a time $t_{i,j}^{DGD}$ was computed by deducting a succeeding later volume ($vol^{g}{}_{i,j+1}$) from a previous volume value ($vol^{g}{}_{i,j}$) as in Eq.(5.28).

$$\Delta vol^{g}{}_{i,j} = vol^{g}{}_{i,j} - vol^{g}{}_{i,j+1} \tag{5.28}$$

$$vol_{32,i,j}^{b} = \frac{\pi d_{32,i,j}}{6} \tag{5.29}$$

The calculated local volume equivalents of SMBDs and the measured differential disengaging gas volume at $t_{i,j}^{DGD}$ are stated in Table 5.4 at u_g of 0.016 m/s and Table A1.17 at u_g of 0.01 m/s.

The ratio of the volume difference $\Delta vol^{g}{}_{i,j}$ to the volume of its associated SMBD (Eq.(5.29)) of the bubble size class j $(vol^{b}_{32,i,j})$ at the respective time $t^{DGD}_{i,j}$ gives the BND value $n^{ERT}_{z,i}(r_j)$ of the bubble size class locally (Eq.(5.31)). Eq.(5.31) was derived from Eq.(5.30). This method of computation was adopted for calculating the BND values locally for other bubble size classes.

$$n(r_i) = \frac{\emptyset R^2 H}{4/3\,\overline{r^3}} f(r_i) \tag{5.30}$$

$$n^{ERT}_{z,i}(r_j) = \frac{\Delta vol^{g}{}_{i,j}}{vol^{b}_{32,i,j}} \tag{5.31}$$

where $n(r_i)$ is volume of gas in a bubble population class divided by mean volume size of bubbles in the class and $f(r_i)$ is the fraction of bubbles with radius r_i. The calculated local BNDD depending on bubble size class at superficial gas velocity of 0.016 m/s are reported in Table A1.12. The graphs of the data in Table A1.12 are shown in Figure 5.12(a-d).

Table 5.2. The calculated characteristic times for the disengagement of bubble size classes locally in the column at the superficial gas velocity of 0.016 m/s.

Layer 1 $(t^{DGD}_{4,j})(s)$	Layer 2$(t^{DGD}_{3,j})(s)$	Layer 3$(t^{DGD}_{2,j})(s)$	Layer 4$(t^{DGD}_{1,j})(s)$
0.3339	0.6784	1.0865	1.3780
0.5247	0.7632	1.1766	1.4999
0.6784	0.8798	1.2402	1.6483
0.7632	1.0229	1.3568	1.8179
0.848	1.166	1.537	1.9716
0.9434	1.3303	1.7225	2.0882
1.0494	1.5052	1.9186	2.2313
1.1978	1.6536	2.0882	2.4592
1.4045	1.7755	2.2578	2.7613
	1.8762	2.4486	3.0051
	1.9822	2.5917	3.2489
			3.5033

Table 5.3. Bubble rise velocities and diameters of bubble size classes at column sections at the superficial gas velocity of 0.016 m/s

Lay. 1 (u_1^b) (cm/s)	*Lay. 2* (u_2^b) (cm/s)	*Lay. 3* (u_3^b) (cm/s)	*Lay. 4* (u_4^b) (cm/s)	*Lay.1* $(d_{32,1}^b)$ (cm)	*Lay. 2* $(d_{32,2}^b)$ (cm)	*Lay. 3* $(d_{32,3}^b)$ (cm)	*Lay. 4* $(d_{32,4}^b)$ (cm)
71.88	79.60	73.63	80.55	3.11	3.81	3.26	3.91
45.74	70.75	67.99	74.00	1.26	3.01	2.78	3.30
35.38	61.38	64.51	67.34	0.75	2.27	2.51	2.73
31.45	52.79	58.96	61.06	0.60	1.68	2.09	2.24
28.30	46.31	52.05	56.30	0.48	1.29	1.63	1.91
25.44	40.59	46.44	53.16	0.39	0.99	1.30	1.70
22.87	35.88	41.70	49.75	0.31	0.77	1.05	1.49
20.04	32.66	38.31	45.14	0.24	0.64	0.88	1.23
	30.41	35.43	40.20		0.56	0.76	0.97
	28.78	32.67	36.94		0.50	0.64	0.82
			34.17				0.70

The ratio of the sum of $\Delta vol^g{}_{i,j}$ over local column sections to the sum of local BNDD ($n_{z,i}^{ERT}(r_j)$) over local column sections was calculated to obtain the mean volume for a bubble size class j ($\overline{vol}_{32,j}^b$) as stated in Table A1.12 using Eq.(5.32).

$$\overline{vol}_{32,j}^b = \frac{\sum_{i=1}^{3} \Delta vol^g{}_{i,j}}{\sum_{i=1}^{3} n_{z,i}^{ERT}(r_j)} \qquad (5.32)$$

Table 5.4. The local volumes of SMBDs and the differential disengaging gas volume during DGD at the superficial gas velocity of 0.016 m/s.

Lay. 1 (vol_{32}^b) (cm^3)	*Lay. 2* (vol_{32}^b) (cm^3)	*Lay. 3* (vol_{32}^b) (cm^3)	*Lay. 4* (vol_{32}^b) (cm^3)	*Lay. 1* (Δvol^g) (cm^3)	*Lay. 2* (Δvol^g) (cm^3)	*Lay. 3* (Δvol^g) (cm^3)	*Lay. 4* (Δvol^g) (cm^3)
15.758	29.066	18.209	31.216	81.64	43.05	54.42	105.1
1.046	14.337	11.290	18.771	36.95	21.19	31.19	110.7
0.224	6.109	8.232	10.657	40.62	56.04	57.18	118.2
0.111	2.473	4.802	5.922	22.85	68.12	89.82	107.1
0.059	1.127	2.272	3.639	16.80	66.76	101.33	141.4
0.031	0.511	1.147	2.578	52.06	50.99	139.02	116.9
0.016	0.244	0.601	1.732	71.61	49.42	126.02	162.2
0.007	0.139	0.361	0.966	50.44	31.71	94.10	177.6
0.003	0.090	0.226	0.482		47.66	98.45	136.6
	0.065	0.139	0.290		50.17	70.17	106.5
			0.182				187.8

The axially averaged SMBD ($\overline{d_{32,J}^{ERT}}$) over local sections corresponding to the $\overline{vol}_{32,j}^{b}$ was computed using Eq.(5.33) to obtain the results stated in Table A1.12 at u_g of 0.016 m/s and Table A1.16 at u_g of 0.01 m/s.

$$\overline{d_{32,J}^{ERT}} = \left(\overline{vol}_{32,j}^{b} \times 6/\pi\right)^{\frac{1}{3}} \tag{5.33}$$

The mean of the local BNDD ($\bar{n}_z^{ERT}(r_j)$) over local column sections was computed from the ratio of sum of $\Delta vol^{g}{}_{i,j}$ over column sections to the sum of $vol_{32,,i,j}^{b}$ over the column sections to obtain the results in Table A1.12 using Eq.(5.34). The graph of the axially averaged BNDD (global BNDD) depending on logarithm of bubble volume for varied $u_g s$ ranging from 0.005m/s to 0.016 m/s are presented in Figure 5.13(a-g).

$$\bar{n}_z^{ERT}(r_j) = \frac{\sum_{i=1}^{3} \Delta vol^{g}{}_{i,j}}{\sum_{i=1}^{3} vol_{32,,i,j}^{b}} \tag{5.34}$$

The mean of the axially averaged SMBD ($\overline{\overline{d_{32,z}(\bar{r})}}$) over all bubble size classes was computed from the ratio of sum of the product of $\bar{n}_z^{ERT}(r_j)$ and $\overline{d_{32,J}^{ERT}}$ to sum of $\bar{n}_z^{ERT}(r_j)$ over all bubble size classes as in Eq.(5.35). The obtain value for the $\overline{\overline{d_{32,z}(\bar{r})}}$ was 0.564 cm at superficial gas velocity of 0.016 m/s.

$$\overline{\overline{d_{32,z}(\bar{r})}} = \frac{\sum_{j=1}^{N} \bar{n}_z^{ERT}(r_j)\bar{d}_{32,j}}{\sum_{j=1}^{N} \bar{n}_z^{ERT}(r_j)} \tag{5.35}$$

The graphs of the local and global BNDD as a function of bubble volume (Figure 5.12 and Figure 5.13) are parameterised log-normal distribution of the form of Eq.(5.36). The determined parameters for the log-normal distributions by the method of linear least square regression explained in Section 4.5.1 of Chapter 4 are stated in Table 5.6 for each graph in Figure 5.12 and Figure 5.13.

$$n(v) = \frac{A}{vC\sigma\sqrt{2\pi}} \exp\left(-\frac{(\ln(v) - B\mu)^2}{2(C\sigma)^2}\right) + D \tag{5.36}$$

Table 5.5. The global SMBD(cm) obtained by the coupling of ERT measurements to the DGD for varied superficial gas velocities

U_g (m/s)/ S/N	SMBD(cm) at 0.01m/s	SMBD(cm) at 0.009m/s	SMBD(cm) at 0.008m/s	SMBD(cm) at 0.007m/s	SMBD(cm) at 0.006m/s	SMBD(cm) a t 0.005m/s
1	2.4250	2.1473	1.5849	1.6923	0.9452	1.3619
2	2.1998	2.0104	1.4708	1.2137	0.1530	0.8694
3	1.6193	1.4750	1.1672	0.9792	0.0321	0.5610
4	1.4553	1.1292	0.8394	0.7785	0.0078	0.5032
5	1.2625	0.9820	0.6284	0.6620	0.0029	0.3289
6	0.9869	0.7520	0.4856	0.5221	0.0011	0.2446
7	0.8314	0.5729	0.3252	0.4966	0.0005	0.1583
8	0.6654	0.4375	0.2570	0.3482	0.0002	
9	0.5432	0.3328	0.2158	0.2401		
10	0.5138	0.2182	0.1608			
11	0.4042					

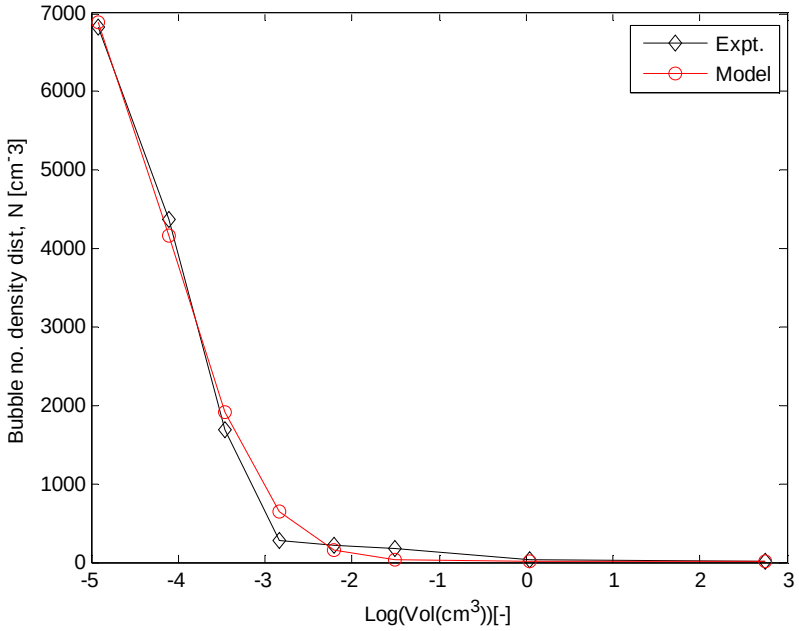
Expt.
Model
Bubble no. density dist, N [cm^-3]
Log(Vol(cm^3))[-]
7000
6000
5000
4000
3000
2000
1000
0
-5
-4
-3
-2
-1
0
1
2
3

(a)

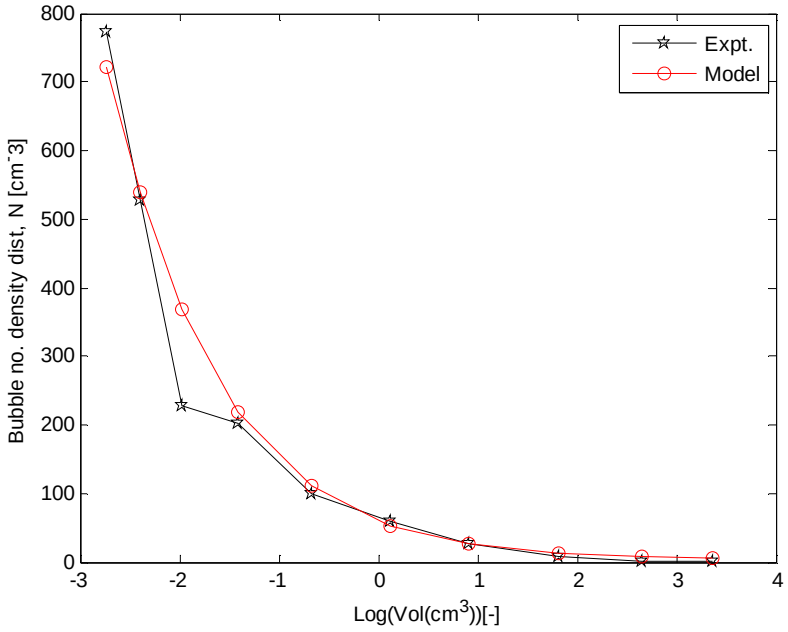
Expt.
Model
Bubble no. density dist, N [cm^-3]
Log(Vol(cm^3))[-]
800
700
600
500
400
300
200
100
0
-3
-2
-1
0
1
2
3
4

(b)

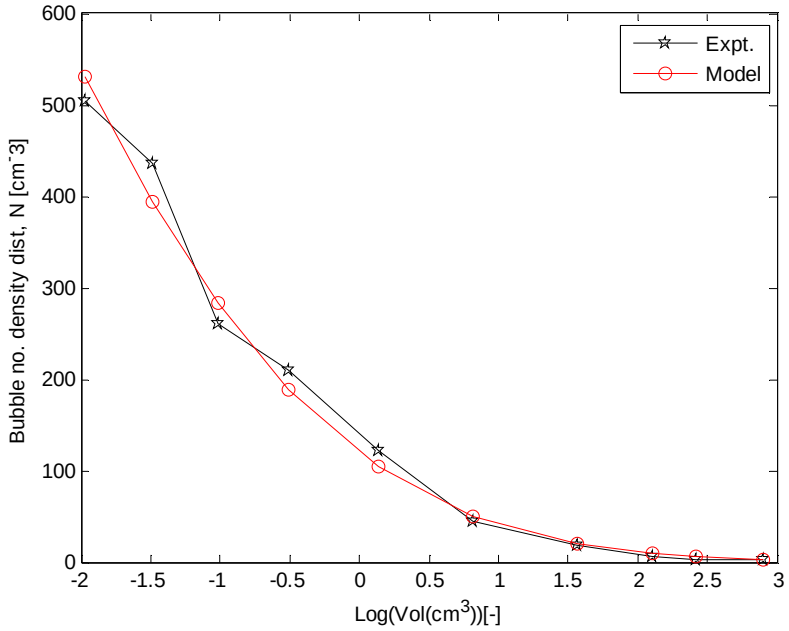

(c)

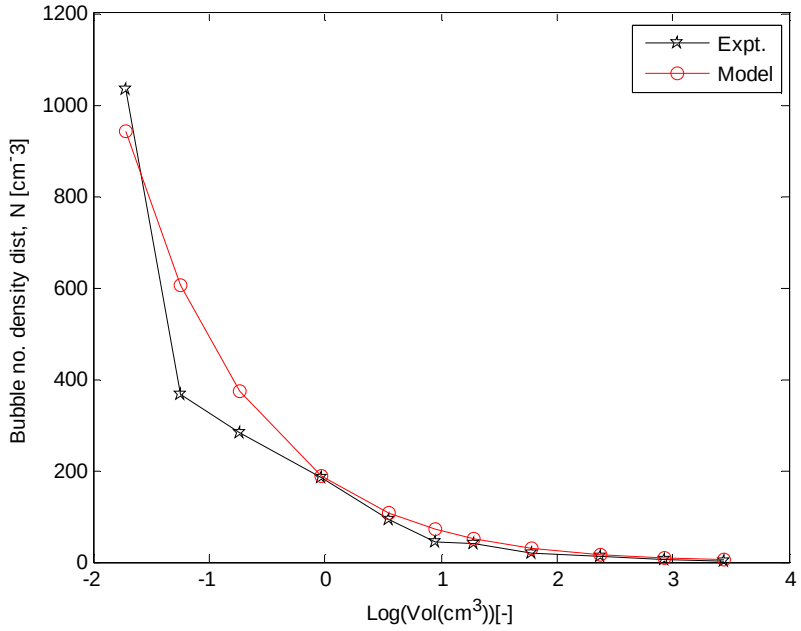

(d)

Figure 5.12. The local BNDD as a function of logarithm of bubble volume for superficial gas velocity of 0.016 m/s: (a) at Section 1, (b) at Section 2, (c) at Section 3, (d) at Section 4.

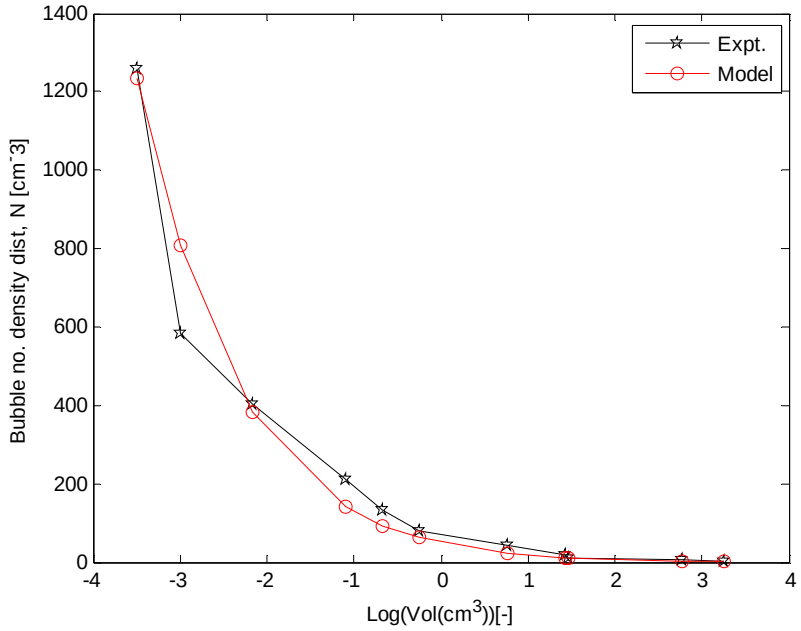
Expt.
Model
Bubble no. density dist, N [cm^-3]
Log(Vol(cm^3))[-]
1400
1200
1000
800
600
400
200
0
-4
-3
-2
-1
0
1
2
3
4

(a)

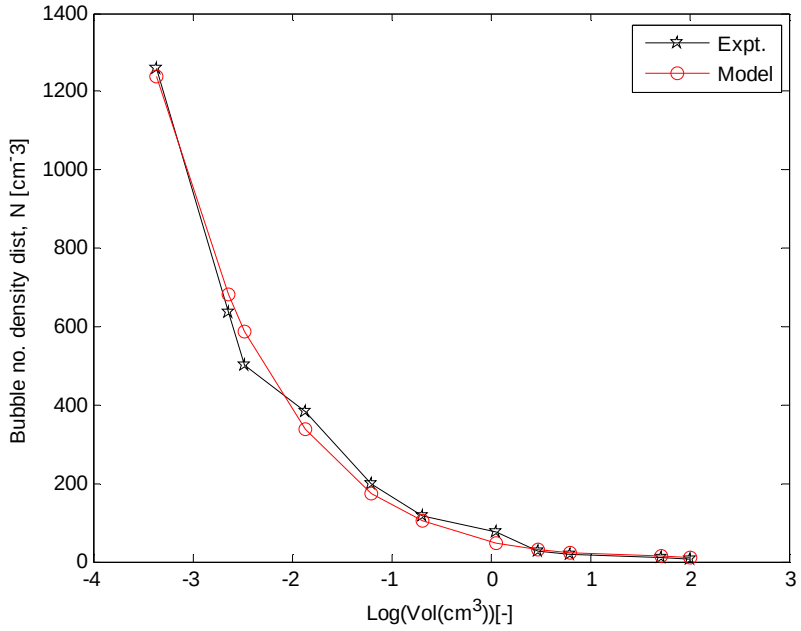
Expt.
Model
Bubble no. density dist, N [cm^-3]
Log(Vol(cm^3))[-]
1400
1200
1000
800
600
400
200
0
-4
-3
-2
-1
0
1
2
3

(b)

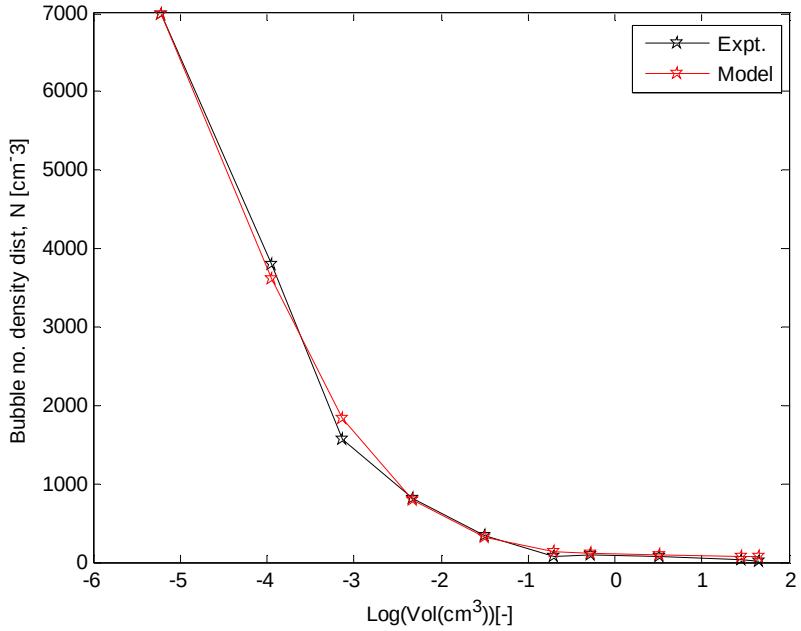
Expt.
Model
Bubble no. density dist, N [cm^-3]
Log(Vol(cm^3))[-]
7000
6000
5000
4000
3000
2000
1000
0
-6
-5
-4
-3
-2
-1
0
1
2

(c)

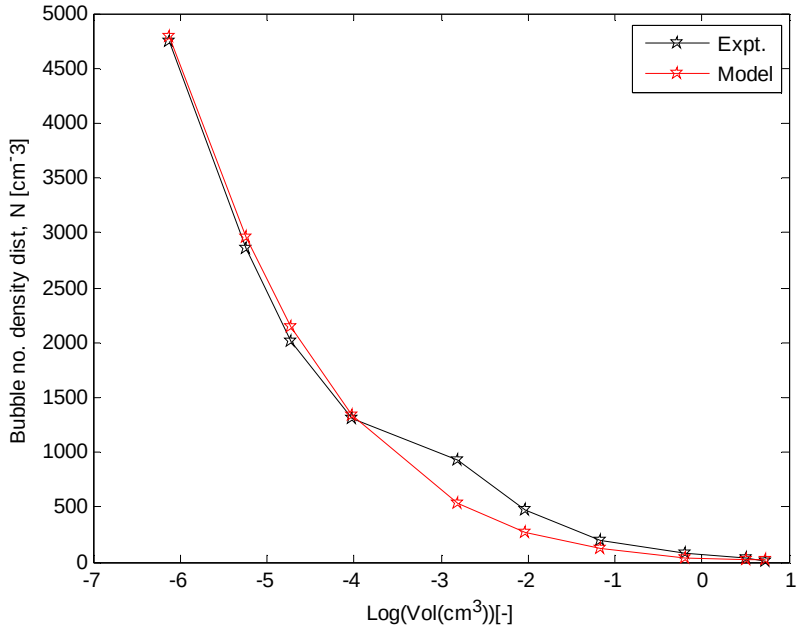
Expt.
Model
Bubble no. density dist, N [cm^-3]
Log(Vol(cm^3))[-]
5000
4500
4000
3500
3000
2500
2000
1500
1000
500
0
-7
-6
-5
-4
-3
-2
-1
0
1

(d)

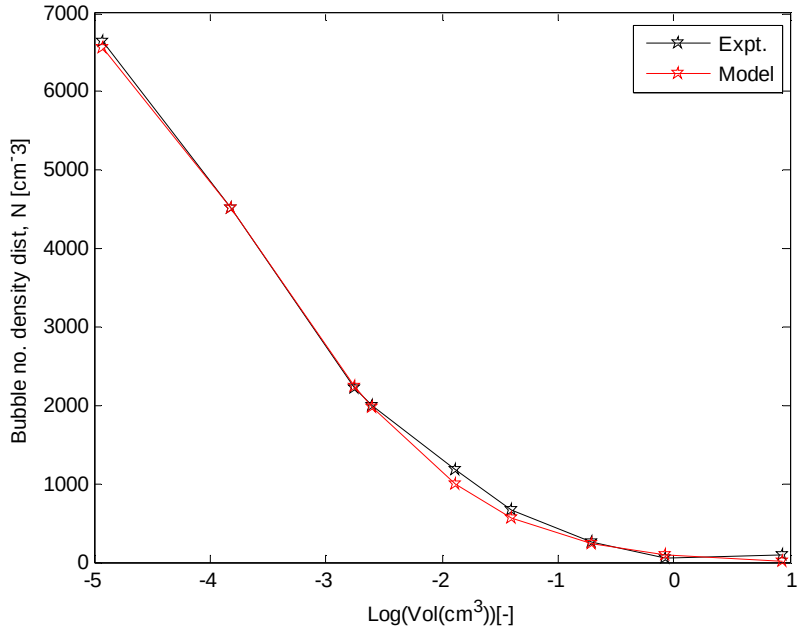
Expt.
Model
Bubble no. density dist, N [cm^-3]
Log(Vol(cm^3))[-]
7000
6000
5000
4000
3000
2000
1000
0
-5
-4
-3
-2
-1
0
1

(e)

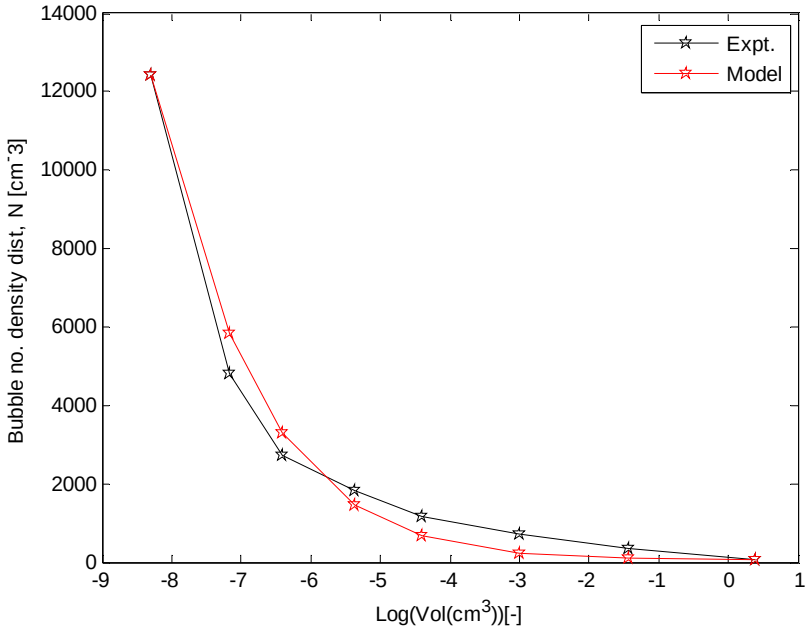
Expt.
Model
Bubble no. density dist, N [cm^-3]
Log(Vol(cm^3))[-]
14000
12000
10000
8000
6000
4000
2000
0
-9
-8
-7
-6
-5
-4
-3
-2
-1
0
1

(f)

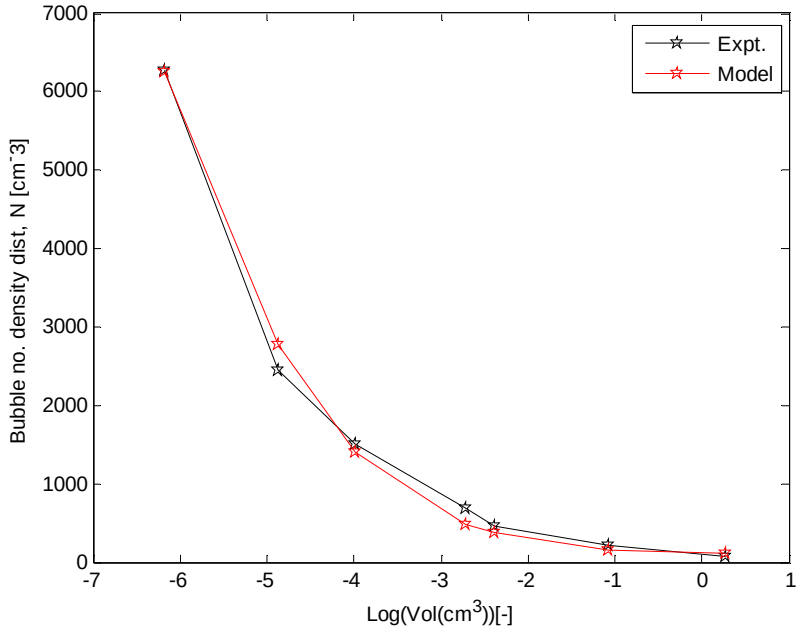

(g)

Figure 5.13. The global BNDD as a function of logarithm of bubble volume at varied superficial gas velocities: (a) at 0.016 m/s, (b) at 0.01 m/s, (c) at 0.009 m/s, (d) at 0.008 m/s, (e) at 0.007 m/s, (f) at 0.006 m/s, (g) at 0.005 m/s.

Table 5.6. The constant values for the log-normal fits of the local and global BNDD at varied gas flow rates and the statistical error values

$U_g(ms^{-1})$	Section	A	B	C	D	X^2	R^2	f-statistic
0.016	1	190±1.0	2.00±0.02	0.45±0.02	5	0.04	0.99	433.20
0.016	2	650±1.0	2.10±0.02	2.20±0.02	5	0.33	0.96	104.31
0.016	3	670±1.0	0.45±0.02	1.30±0.02	0	0.11	0.99	291.10
0.016	4	2650±1.0	0.53±0.02	3.40±0.02	0	0.80	0.92	51.74
0.016	Global	580±1.0	1.20±0.02	2.15±0.02	0	0.34	0.96	109.52
0.010	Global	370±1.0	2.50±0.02	1.60±0.02	8	0.09	0.99	443.88
0.009	Global	340±1.0	2.30±0.02	0.79±0.02	80	0.02	1.00	1498.10
0.008	Global	300±1.0	0.40±0.02	1.30±0.02	0	0.10	1.00	310.80
0.007	Global	700±1.0	1.11±0.02	1.00±0.02	0	0.01	1.00	2149.40
0.006	Global	70±1.0	0.75±0.02	1.25±0.02	74	0.12	0.98	139.10
0.005	Global	175±1.0	1.00±0.02	1.20±0.02	100	0.03	1.00	380.40

The schematic below summarises the necessary bubble population parameters that were computed in coupling ERT data to the DGD process for the determination of the global BNDD ($\bar{n}_z^{ERT}(r_j)$) for varied superficial gas velocities. The numbering of the connecting lines in the flow chart below corresponds to the processing stage numbering of the ERT estimates of gas void fractions in term of the ACD.

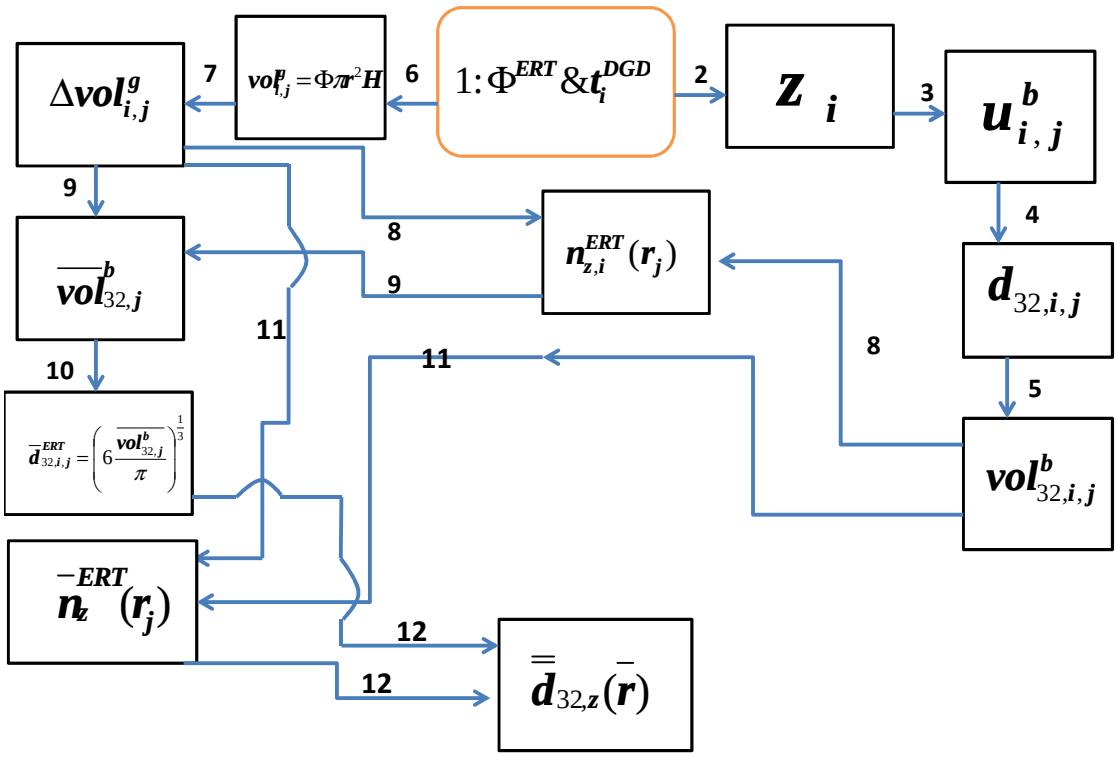

Figure 5.14. A flow chart of bubble population parameter computations leading to the determination of axially averaged BNDD as a function of bubble size and the global mean of bubble sizes in the column.

Keys: The connecting lines are labelled from 2 to 12, where the start is the brown box labelled 1.

5.4. Discussion and Conclusions

In the work of (Daly, et al., 1992), bubble sizes were determined by the discretization of the graph of pressure signals with time measured in a column during DGD process. The bubble sizes were calculated by dividing the plot of the gas void fraction of bubbles against time during DGD process into 5 regions (Haibo, et al., 2007). These methods of determining the bubble sizes by the DGD technique yielded fewer bubble sizes and inaccurately calculated

SMBD. Thus, the methods were reviewed in this work by an adoption of a new technique for determining the characteristic disengagement times of bubble size classes.

The new technique entails simultaneously measurement of the time-variant ERT ACD and the time-dependent gas void fraction locally in the column using a DP transmitter during DGD process. The ERT and the DP results were used to interpret the ERT ACD values in terms of the local gas volume in the column at known times. The discrete times when the local ERT ACD changed by a unit increase during DGD were interpreted for the calculation of characteristic disengagement times of bubble size classes.

The variation in the time intervals for the unit changes in ACD for varied superficial gas velocities results in proportionate characteristic times for bubble size class disengagements. It was noticed that the time intervals for bubble size class disengagements decrease with increase in superficial gas velocity by the method of the ERT ACD interpretation. The determined number of bubbles within a class size and the number of bubble size classes were found to increase with an increase in superficial gas velocity. This is as a result of an increase in the rate of bubble coalescence with an increase in gas flow rate that produces bubbles in larger classes before the commencement of the DGD process (Ribeiro & Lage, 2004), (Hashemi, et al., 2016) (Majumder, et al., 2006).

The decreasing conductivity distribution locally and globally with an increase in the superficial gas velocity is an evidence to the bubble size characterization and the higher coalescence rates. In addition, the mean bubble size of the largest bubble size class was observed to increase with gas flow rate increase as shown in Figure 5.13(a-g), similar to the trend in results by (Majumder, et al., 2006).

The determined log-normal bubble size distribution models are consistent with findings of (Akita & Fumitake, 1974), (Ribeiro & Lage, 2004), (Majumder, et al., 2006) (Riquelme, et al., 2016). It was reported in their experimental work that the bubble size distributions in a column at the superficial gas velocities studied are log-normal distributions. The photographic technique was utilized to capture bubbles in a direct–contact evaporator system and during the absorption of air in varied liquids in the work. The bubble size distribution obtained indicates that the inlet bubble size distribution at the base of the first column section was a log-normal distribution.

This distribution of bubble population was then influenced significantly by laminar fluid effects during bubble disengagement to yield varied parameterized log-normal distributions at higher column sections. The range of bubble sizes also confirms the results obtained in the work by (Akita & Yoshida, 1974) (Bhavaraju, et al., 1978). The smallest bubble size at the first column section and the smallest globally for varied superficial gas velocities are consistent with the bubble size distribution leaving the gas distributor orifices (Bhavaraju, et al., 1978) (Leonard, et al., 2015).

In order to calculate the bubble sizes leaving the orifices on the surface of the tubular porous gas sparger in relation to the locally captured bubble sizes, Eq.(5.37) can be used (Bhavaraju, et al., 1978). The Eq.(5.37) is valid if the volumetric gas flow rate per orifice Q_N is less than the translational volumetric gas flow rate Q_T of the flow regime (i.e. $Q_N < Q_T$).

$$d_{Bo} = \left[\frac{6\sigma d_o}{g(\rho_L - \rho_G)}\right]^{1/3} \tag{5.37}$$

The Q_T was defined as in Eq.(5.38) and Eq.(5.39) depending on the bubble Reynolds number R_{eB}

$$Q_T = \frac{\pi g(\rho_L - \rho_G)}{108\mu_L}\left[\frac{6\sigma d_o}{g(\rho_L - \rho_G)}\right]^{4/3} \text{ for } R_{eB} < 1 \tag{5.38}$$

$$Q_T = 0.38 g^{1/2}\left[\frac{6\sigma d_o}{g(\rho_L - \rho_G)}\right]^{5/6} \quad for\ R_{eB} \gg 1 \tag{5.39}$$

The theoretical correlation of Eq.(5.37) was validated by considerable experimental evidence (Van, et al., 1950) (Datta, et al., 1950). The limits of the regime where Eq.(5.37) is valid as derived by (Van, et al., 1950) are

$$Q_N \leq \frac{0.31}{\mu_L}\left[\frac{(\sigma d_o)^4}{g(\rho_L - \rho_G)}\right]^{1/3} \quad for\ R_{eB} \leq 1 \tag{5.40}$$

$$Q_N \leq 1.66\left[\frac{(\sigma d_o)^5}{\rho^3 g^2(\rho_L - \rho_G)^2}\right]^{1/6} \quad for\ R_{eB} \gg 1 \tag{5.41}$$

In Eq.(5.37), d_o and d_{Bo} are the orifice diameter and the bubble diameter at very low gas rates respectively. The relations in Eq.(5.37) and Eq.(5.38) show the bubble volume is proportional to the gas flow rate (Francesca, et al., 2014). For superficial gas velocities ranging from 0.005 – 0.04 m/s, the hydrodynamic flow regimes lie in Taylor's regime range defined by $R_{eB} \gg 1$. The used tubular gas distributor is of height 0.265 m and radius 0.015 m with each orifice having diameter 250micrometer (250×10^{-6}m). Substituting the values of the fluid physical conditions of density and surface tension as well as the orifice diameter into Eq.(5.39) and Eq.(5.41), Q_T equals $2.79 \times 10^{-7} m^3/s$ and the upper bound limit of Eq.(5.41) is $2.74 \times 10^{-6} m^3/s$.

The total curve surface area of the tubular gas distributor is $249.79cm^2$. The number of orifices on the surface of the gas distributor was calculated from the ratio of the total curve surface area of the distributor to the area of each orifice to obtain 5.09×10^9. Assuming that the maximum inter-orifice spacing is the area covered by 20 orifices, the fewest number of orifices on the gas distributor will be 2.54×10^8. This number of orifices supports the assertion that the porous sparger has an advantage over perforated distributors or other gas distributors since its produces millions of small bubbles contacting offering a higher interfacial area for effective mass transfer rates (Mott, 2006).

Using the calculated number of orifice, 2.54×10^8, the volumetric gas flow rate per orifice Q_N at a superficial gas velocity of 0.016m/s is $4.20 \times 10^{-12} m^3/s$. Since $Q_N < Q_T$ and Q_N is less than the upper bound of Eq.(5.41) for $R_{eB} \gg 1$, Eq.(5.37) was used to calculate the bubble diameter leaving each orifice of the sparger to obtain $2.2mm$.

For superficial gas velocity of 0.016 m/s, the smallest bubble size at Section 1 and globally are 2.4 mm and 3.9 mm respectively. The smallest bubble size at first layer is consistent with the predicted bubble size of 2.2mm leaving the orifices given the orifice diameter and operational conditions in the column (Bhavaraju, et al., 1978).

The liquid phase region above the gas distributor can be divided into two regions (Bhavaraju, et al., 1978). In region 1 that is directly above the gas distributor, the bubble population properties are determined by the bubble formation process at the orifice. The size of bubbles produced by a porous sparger depends on the orifice size distribution and generally follows a unimodal or bimodal distribution (Nikolaos, et al., 2007). The region 1 is also characterised by non-uniform distribution of bubbles across the cross-section of the vessel in which there are multiple orifices (Bhavaraju, et al., 1978). The bubbles originating from the sparger orifices are different in size from the bubbles rising through the main part of the column under normal operating conditions (Akita & Yoshida, 1974).

In region 2 that is directly above region 1, the bubble properties are determined by the bulk liquid motion, which cause bubble breakup and coalescence (Bhavaraju, et al., 1978) (Akita & Yoshida, 1974). In this region, under normal operating conditions in practice, the sizes of

the majority of bubbles depend mainly on a balance between the bubble coalescence and breakup rates (Akita & Yoshida, 1974).

The mean SMBD at the plane of the first electrode ring given the gas void fractions at varied superficial gas velocities were calculated using Eq.(5.42) and Eq.(5.43) (Akita & Yoshida, 1974) to obtain the result in Table 5.7.

$$a_p = {}^1\!/_3 \left(\frac{g\rho_L}{\sigma}\right)^{0.5} \left(\frac{g}{v_L^2}\right)^{0.1} {D_C}^{0.3} \varepsilon_G^{1.13} \tag{5.42}$$

$$d_{vs} = \frac{6\varepsilon_g}{a_p} \tag{5.43}$$

Table 5.7. Calculated SMBD at the base of the first column section based on the gas void fractions and interfacial area for varied superficial gas velocities

U_g (m/s)	SMBD (mm)	Interfacial area (1/m)	ε_g (%)
0.005	6.2	12.54	1.30
0.006	6.1	14.63	1.49
0.007	6.0	17.54	1.75
0.008	5.9	19.37	1.91
0.009	5.9	20.63	2.02
0.010	5.8	22.72	2.20
0.016	5.7	28.64	2.70

The mean bubble sizes at the base of the first column section on Table 5.7 falls within the range of bubble sizes captured by the coupled ERT measurements to the DGD process of Table 5.5 and Table 5.3. The experimental studies by (Laari & Turunen, 2003) as well as the validated simulation studies by (Sattar, et al., 2013) of an air-water 2-phase flow show the SMBD increases with increase in column height to 1.5m. The studied superficial gas velocities by the authors are 0.01, 0.02, 0.06 and 0.08 m/s. Further from the 1.5m height of a column designed with a porous gas distributor, the SMBD was noticed to be approximately steady with column height.

The smallest bubble sizes for varied gas flow rates studied are also shown in Table 5.5. Relating the bubble diameter at the gas distributor surface to the range of global bubble

sizes for each gas flow rates (i.e. Table 5.5), the bubble population underwent varied magnitude of collision frequencies at different liquid regions during their axial evolution. This means the bubble collision frequencies resulting in bubble coalescence rates at the liquid region 1 differs from that at the liquid region 2 (Sailesh. B, et al., 1997). The bubble sizes are approximately uniformly distributed at the liquid region 2. The collision frequencies produced by millions of bubbles at different liquid regions will be determined by the PBM simulation in the following chapter. This is possible since a comparison of the calculated or measured bubble size distribution or the calculated or measured SMBD allows for determining the coalescence and breakup parameters in the column (Laari & Turunen, 2003).

From the log-normal distributions of bubble sizes at column sections, the axially averaged BNDD was computed to allow for determining the global bubble size distribution in the column. Accordingly, the mean of the entire bubble population sizes was calculated to obtain $0.584\ cm$ for the superficial gas velocity of 0.016 m/s. Moreover, the obtained local and global BNDD validate the effectiveness of the DGD technique for the analysis of bubble population parameters: the time-variant gas void fraction, SMBD and BNDD of bubble size classes in a BCR.

Thus, the ERT data captured during DGD has provided data for interpretation of ERT reconstruction of air dispersion to yielding information on bubble population properties in a non-invasive, a simple and at a low capital cost means. These bubble parameters could only be measured alternatively by measurement techniques that yield a high spatial resolution. However, the alternative techniques may be intrusive, bulky and expensive, such bubble size analysers, conductivity probe technique and optical probes. Based on the validity of the results, the developed new technique forms a contribution to the methods of interpreting ERT images captured during DGD process for bubble population properties computation in a column.

Chapter 6

Bubble Population Parameter Measurements by the Method of Modelling of the Bubble Population Swarming in a Steady State Process

The interpretation of the local ERT TACD to yield local gas void fractions of bubble population swarming at steady state in a column has been reported in Chapter 4. However, the local gas void fractions parameter of bubble population are not sufficient to characterise column operations. Other more representative parameters include the local bubble size profile (BSF), the BNDD of bubble sizes, bubble population coalescence and breakage rates. The representative parameters that yield detailed spatial information of bubble population are useful for computing column hydrodynamic parameters. Typical BCR hydrodynamic parameters for column scale-up and design are the volumetric gas-liquid mass transfer rates, gas-liquid interfacial area, the intensity of mixing of the multiphase system and local SMBD.

The ERT images captured during DGD process were analysed in Chapter 5 to determine bubble size profile and BNDD in the column. The BNDD resulting from analysis of the time-variant ERT images of DGD process is useful for validating an advanced interpretation of ERT images of a steady-state multiphase process at higher spatial resolution.

Since the central objective of this study is to predict the steady-state hydrodynamic parameters of a 2-phase gas-liquid flow, ERT images of steady-state dispersion are anticipated to allow for the achievement of the objective. Without the coupling of the ERT data to a physical system model, ERT measurements may not be interpretable to predict hydrodynamic parameters owing to its low spatial resolution. However, the ERT technique allows for imaging the dispersion at high temporal resolution. This capability of the ERT technique will be harnessed to enhance the interpretation of ERT images for predicting steady-state hydrodynamic parameters in a column.

Achieving the stated objective will be investigated through hybridizing ERT measurements to PBM for the calculation of the parameters of evolving bubble population at steady state in a column. The bubble coalescence and breakage phenomena describe the bubble population interactions influencing their properties during axial swarming in a column.

6.1. General mathematical framework of a PBM

The particle population in a certain state can change in a closed system due to particle fission or particle agglomeration. The following definitions are made in describing changes in particle states arising from particle interactions as explained in Section 2.9.1 and 2.9.7 of Chapter 2. Let the individual particle state be described by a scalar variable x, while lies on the positive real line. The variables may be size variables such as diameter, volume or mass. Let the probability of growth owing to mass transfer from the surrounding continuous phase be at a rate $\dot{X}$, depending on x. Let the probability that there is a particle in state $(x, x+dx)$ at time $(t, t+dt)$ due to particle fission be denoted by $f_1(x, t+dt)dx$.

In order to derive an expression for $f_1(x, t+dt)dx$, particles may be found in a state $(x, x+dx)$ at a time interval $(t, t+dt)$ through either of two mutually exclusive ways explained in detail in Section 2.9.7 of Chapter 2 obtain Eq.(6.1).

$$\frac{\delta f_1}{\delta t} + \frac{\delta[f_1 \dot{X}]}{\delta x} = -\Gamma(x) f_1 + 2\int_x^{\infty} P(x, x'')\,\Gamma(x'') f_1(x'', t) dx'' \tag{6.1}$$

Eq.(6.1) is the PBM framework for the unsteady-state advection transport of f_1 under the influence of bubble breakage phenomenon leading to bubble birth and death.

In modelling the agglomeration phenomenon leading to changes in the particle state in a system, let the particle probability in a state $(x, x+dx)$ at a time interval $(t, t+dt)$ due to agglomeration events be given by $f_1(x, t+dt)dx$. Eq.(6.2) describes the unsteady-state advection transport of f_1 under the influence of bubble agglomeration phenomenon leading to bubble birth and death. Eq.(6.2) is obtained by simplifying the re-defined f_1 as in Section 2.9.1 of Chapter 2.

$$\begin{aligned}\frac{\partial f}{\partial t} + \frac{\partial[f_1 \dot{X}(x)]}{\partial x} = \frac{1}{2}\int_0^x f_1(x-y, t) f_1(y; t), q(x-y, y) dy \\ - f_1(x; t)\int_0^{\infty} f_1(\xi; t) q(x, \xi) d\xi\end{aligned} \tag{6.2}$$

When Eq.(6.2) is combined with Eq.(6.1) accounting for events leading to particle being in state $(x, x+dx)$ at time $(t, t+dt)$ by agglomeration and fission phenomena, Eq.(6.3) is obtained.

$$\frac{\partial f}{\partial t}+\frac{\partial[f_1\dot{X}(x)]}{\partial x}=\frac{1}{2}\int_0^x f_1(x-y,t)f_1(y;t),q(x-y,y)dy - f_1(x;t)\int_0^\infty f_1(\xi;t)q(x,\xi)d\xi + 2\int_x^\infty P(x,x'')\,\Gamma(x'')f_1(x'',t)dx'' - \Gamma(x)f_1 \tag{6.3}$$

which is the framework of the general PBM of particles in a state in a continuous system.

6.2. Adaptation of the general PBM to a PBM suitable for description of a BCR

The general PBM framework is used to describe a balance of BNDD depending on bubble size class (state of countable entities) of bubbles (particles) in a liquid medium, water (continuous system). The discretised variable is the bubble size of a bubble population having different number densities. The column is compartmentalised along its axial length into discrete sections such that the outlet BNDD obtained from a PBM solution in a local section is the inlet BNDD at a higher axially placed local column section.

Using this PBM framework, the BNDD varies in space and time due to combined phenomena of bubble coalescence (particle agglomeration) and bubble breakage (particle fission). Let the BNDD varying in space and time t be represented by $n(v,X,t)$. Thus, total number of bubbles in a bubble size class within the range $[v,v+dv]$ occupying spatial range $[X,X+dX]$ within a time interval $[t,t+dt]$ will be of the form $n(v,X,t)dv,dX,dt$.

The bubble population in the class $[v,v+dv]$ can change within the time interval $[t,t+dt]$ when bubbles in bubble classes larger than $[v,v+dv]$ break within the time $[t,t+dt]$ to yield bubbles in class $[v,v+dv]$ within time $[t,t+dt]$. This means bubble breakage events leading to bubble birth. Bubbles in bubble class $[v,v+dv]$ can also breakup within the time $[t,t+dt]$ to yield bubbles in lower bubble classes, i.e. bubble breakage leading to bubble death in the class.

The bubble breakage phenomenon is as a result of the collision of bubbles with turbulent eddies in the liquid phase. Let the mean number of daughter bubbles formed from the break-up of a mother bubble of size v be denoted by $m(v)[unit]$. Let the probability density function of daughter bubbles, v', generated from the rupture of a mother bubble of size v be denoted by $f(v',v)[m^{-3}]$. Let the break-up frequency of bubbles of size v' be denoted by $g(v')[s^{-1}]$ and let the BNDD be denoted by $n(v,X,t)\ [m^{-3}]$. Thus, the bubble breakage rate is expressed as a product of $m(v)$, $f(v',v)$, $g(v')$ and $n(v,X,t)$. The breakage rate

leading to change in BND value of bubbles in a class $[v, v+dv]$ with time $[t, t+dt]$ as a result of bubble breakage leading to bubble birth and death are stated in Eq.(6.4) and Eq.(6.5) respectively.

$$+\int_{v'}^{\infty} m(v) f(v'; v)\, g(v) n(v, X, t) dv \tag{6.4}$$

$$g(v') n(v', X, t) \tag{6.5}$$

Similarly, the equivalent phenomenon to particle agglomeration changing particle population in a continuous system is bubble coalescence events causing changes in BND value of bubble classes. The bubble population in a class range $[v, v+dv]$ can change within the time interval $[t, t+dt]$ owing to bubble coalescence phenomenon. During these events, bubbles in lower bubble classes to $[v, v+dv]$ coalesce to produce bubbles in bubble class $[v, v+dv]$ within time $[t, t+dt]$. This implies bubble coalescence events leading to bubble birth. The bubble population of class $[v, v+dv]$ can also change within the time interval $[t, t+dt]$ due to bubble coalescence events in the class $[v, v+dv]$ with bubbles in other classes than $[v, v+dv]$ within time $[t, t+dt]$. When these events occur, the bubble coalescence events lead to bubble death.

The specific bubble coalescence rate is defined as the product of bubble collision frequency and coalescence probability. The bubble coalescence rate between bubble size $[v, v+dv]$ and size $[v'-v, v'-v+d(v'-v)]$ leading to either bubble birth or death in a bubble class $[v, v+dv]$ within a time interval $[t, t+dt]$ can, thus, be expressed as Eq.(6.6) and Eq.(6.7) respectively.

$$\frac{1}{2}\int_{0}^{v'} n(v, X, t)\, n(v'-v, X, t) q(v, v'-v, t) dv \tag{6.6}$$

$$n(v', X, t) \int_{0}^{\infty} n(v, X, t) q(v, v', t)\, dv \tag{6.7}$$

Combining the phenomena of bubble coalescence and breakage affecting the bubble population in a class $[v', v'+dv']$ within time $[t, t+dt]$ results in Eq.(6.8) similar to Eq.(6.3) in the case of particles system.

$$\frac{\partial n(v',X,t)}{\partial t} + \nabla\left(u_g n(v',X,t)\right) = + \int_{v'}^{\infty} m(v) f(v';v)\, g(v) n(v,X,t) dv - g(v') n(v',X,t) + \frac{1}{2}\int_{0}^{v'} n(v,X,t)\, n(v'-v,X,t) q(v,v'-v,t) dv - n(v',X,t) \int_{0}^{\infty} n(v,X,t) q(v,v',t)\, dv \tag{6.8}$$

The first term on the left-hand side (LHS) of Eq.(6.8) is the unsteady state term that models the changes in $n(v,X,t)$ with time. The second term on the LHS models the advection transport of $n(v,X,t)$ depending on bubble sizes, v', changing in space. The first and second terms on the right-hand side (RHS) denote the breakage phenomenon of bubbles leading to bubble birth and death respectively. The third and fourth terms on the RHS stand for models of bubble coalescence phenomenon leading to bubble birth and death respectively.

The experimentally validated coalescence rate developed by (Prince & Blanch, 1990) expressed in the form of the product of bubble coalescence probability and the sum of bubble collision frequencies due to turbulence effects, buoyancy effects and laminar effects as in Eq.(6.9) was explored in this work

$$q(v,v'-v) = \left({}^{4}/_{3}\left(r_{bi}+r_{bj}\right)^{3}\left(\frac{d\bar{u}_l}{dR}\right) + AS_{ij}\left(u_{ri} - u_{rj}\right) + 0.35\pi B\left(d_{bi}+d_{bj}\right)^{2}\varepsilon^{1/3}\left(d_{bi}{}^{2/3} + d_{bj}{}^{2/3}\right)^{1/2}\right)\exp\left(-{}^{t_{ij}}/_{\tau_{ij}}\right) \tag{6.9}$$

where the bubble rise velocity $u_r[ms^{-1}]$ and cross-sectional area of collision $S_{ij}[m^2]$ in Eq.(6.9) are

$$u_r = \left(\frac{2.14\sigma}{\rho_l d_b} + 0.505 g d_b\right)^{1/2}; S_{ij} = \frac{\pi}{4}(d_{bi}+d_{bj})^2 \tag{6.10}$$

The bubble collision time $t_{ij}[s]$ as well as the bubble coalescence time $\tau_{ij}[s]$ as in Eq.(6.9) are defined respectively as in Eq.(6.11)

$$t_{ij} = \left\{\frac{r_{ij}^3 \rho_l}{16\sigma}\right\}^{1/2} ln\frac{h_o}{h_f} \; ; \; \tau_{ij} = \frac{r_b^{2/3}}{\epsilon^{1/3}} \tag{6.11}$$

$$r_{ij} = \frac{1}{2}\left(\frac{1}{r_{bi}} + \frac{1}{r_{bj}}\right)^{-1} \tag{6.12}$$

In addition, the bubble breakage rate model developed by (Martinez, et al., 2010) was explored in this work for bubble breakage rates modelling. The development of the bubble breakage rate was based on the balance between surface restoring force due to surface tension and turbulence stress force by eddies on bubble surface. The development lead to the obtained expression for breakage frequency $g(v)[s^{-1}]$ of Eq.(6.13), daughter bubble size distribution $f(v';v)[unit]$ of Eq.(6.14), and function of daughter bubbles formed from a parent bubble $m(v)[unit]$ of Eq.(6.15). The explored breakage rate model is based on the assumption that upon breakage, a bubble split into two daughter ones, which is the basis for Eq.(6.15).

$$g(v) = \frac{E\sqrt{\beta\epsilon^{\frac{2}{3}}\left(\frac{6v}{\pi}\right)^{2/9} - \frac{12\sigma}{\rho}\left(\frac{\pi}{6v}\right)^{1/3}}}{\left(\frac{6v}{\pi}\right)^{1/3}} \tag{6.13}$$

$$f(v';v) = \frac{\left[V^{*2/9} - \delta^{5/3}\right]\left[(1-V^*)^{2/9} - \delta^{5/3}\right]}{\int_{V_{min}}^{V_{max}}\left[V^{*2/9} - \delta^{5/3}\right]\left[(1-V^*)^{2/9} - \delta^{5/3}\right]dV^*} \tag{6.14}$$

$$m(v) = 2 \tag{6.15}$$

During the ERT data capturing for imaging the steady-state dispersion, bubble population in size classes were noticed to change as bubble swarm axially due to significant coalescence and insignificant breakage phenomena. The size distribution of the bubble population was not noticed to vary along the radius significantly comparing captured images at sub-sections in a column section. The sub-section or minor section images at a major or column section were obtained from multiple 2D slices of 3D images at major local sections (i.e. any of the four column sections). The radial variation of the captured images along the major sections is on the account of the axial variation of the gas void fraction at uniform laboratory temperature of 25 degree Celsius. The axial variation of the gas void fraction was as a result

of the use of a porous tubular gas distributor mounted at the centre of the base of the column.

The computed local ERT ACD that was approximately the same at minor discrete sections within any of the four major local sections was steady with time for all gas flow rates. The dark area region covered by bubbles on each sensor layer was approximately the same at minor sections of any of the four major sections. This shows there were negligible radial changes in the axial dispersion at a major column section.

Thus, a steady quasi-one-dimensional PBM as in Eq.(6.16) was used to simulate the balance of BNDD based on the balance of gas volume in bubble classes, which change during the advection transport of bubble population axially in the column.

$$\begin{aligned}\frac{u_g \partial n(v', z_i)}{\partial z} = & \int_{v'}^{\infty} m(v) f(v'; v)\, g(v) n(v, z_{i-1}) dv \\ & - g(v') n(v', z_{i-1}) \\ & + \frac{1}{2} \int_{0}^{v'} n(v, z)\, n(v' - v, z_{i-1}) q(v, v' - v, z_{i-1}) dv \\ & - n(v', z_{i-1}) \int_{0}^{\infty} n(v, z_{i-1}) q(v, v', z_{i-1})\, dv\end{aligned} \tag{6.16}$$

Eq.(6.16) is a non-linear system of N equations (for N bubble size classes) given that the dispersion processes were in an isothermal state. The axis-variant gas void fraction depending on superficial gas velocity obtained in Chapter 4 will be used as the inlet boundary conditions at the base of major column sections.

6.3. Method of PBM solution and results

In solving Eq.(6.16), the minimum and maximum of the range of mean bubble sizes of varied bubble classes determined by ERT measurements coupled to the DGD process were divided into 30 classes. An assumed inlet BNDD leaving the surface of sparger was used for the inlet bubble size distribution. The PBM was solved by the method of class allowing to solve for the changes in bubble population in each bubble class as a result of bubble coalescence and breakage phenomena.

The column was compartmentalised into discrete sections to solve for changes in bubble population in each bubble class along the column axis. Each section height was within an interval $[z, z+dz]$. The PBM was solved while ensuring a balance of the gas volume at discrete column sections during bubble axial swarming under coalescence and breakage events. The 2D PBM was solved by axial column sectioning such that the outlet BNDD at the first discrete column section was used as the inlet at the second section. Similar PBM boundary condition definition approach was used at higher axially placed column sections. This sectioning approach is consistent with the adopted technique by (Luo, 1993).

The bubble sizes, BNDD and gas void fractions at the inlet base plane of the first column section need be known as required boundary conditions to solve the PBM. The boundary condition is useful for calculating the changes in BNDD depending on bubble sizes and axial spatial position of bubbles in the column. The local gas holdup fractions of Chapter 4 and the range of the minimum and maximum global bubble sizes of Chapter 5 for the superficial gas velocity of 0.016 m/s were used a boundary condition. The range of the bubble sizes was divided into 30 classes and a log-normal distribution of the bubble sizes was used as the inlet BNDD at the gas flow of 0.016 m/s. The inlet BNDD was assumed by multiplying the standard deviation parameter of the BNDD by 0.15 to ensure the distribution is less skewed to the left of the bubble size range.

The parameters, A, B and C, of the specific coalescence rate $q(v, v'-v)[m^3 s^{-1}]$ were not parameterised (I.e. $A=1; B=1; C=1$) and mean of the logarithm of bubble volumes, μ_b, was multiplied by 1.03 (i.e. $\mu_b = 1.03\mu$). The integrand terms of the coalescence and breakage rate models were computed using the trapezoidal method with fine grid steps to ensure accurate computations. By the formulation of Eq.(6.16) and given the boundary conditions, the BNDD at other discrete axial column height were calculated using MATLAB ODE45. The MATLAB ODE45 is suitable for solving PDEs given the dependency of the source term models on the BNDD.

$$\frac{u_g \partial n(v', z_i)}{\partial z} = \int_{v'}^{\infty} m(v) f(v'; v)\, g(v) n(v, z_{i-1}) dv - g(v') n(v', z_{i-1}) \tag{6.17}$$

$$\frac{u_g \partial n(v', z_i)}{\partial z} = \frac{1}{2}\int_0^{v'} n(v, z)\, n(v' - v, z_{i-1}) q(v, v' - v, z_{i-1}) dv - n(v', z_{i-1}) \int_0^{\infty} n(v, z_{i-1}) q(v, v', z_{i-1})\, dv \quad (6.18)$$

The sensitivity of the BNDD $n(v', z)$ as in Eq.(6.16) to each phenomenon of bubble coalescence and breakage rates was tested assuming the following conditions in the column: 1) A less turbulent fluid flow regime having a Weber number less than the critical Weber number of 2.3 before breakage processes begin (Laari & Turunen, 2003) (Prince & Blanch, 1990). At this critical Weber number, the breakage rate process is zero as in Eq.(6.18). The Eq.(6.18) was solved at the superficial gas velocity of 0.016 m/s while ensuring the balance of the gas void fraction axial distribution as obtained in Chapter 4 to obtain the results of Figure 6.1, Figure 6.2 and Figure 6.3.

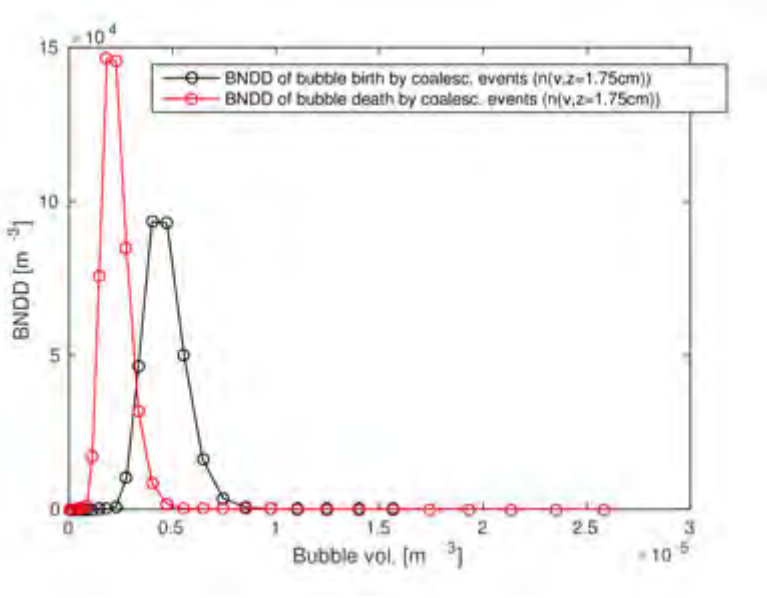

Figure 6.1. Bubble coalescence rate as PBM source term resulting in BNDD of bubble birth and death at a discrete axial column length (approx. Inlet region) at the superficial gas velocity of 0.016 m/s and gas void fraction of 2.7%.

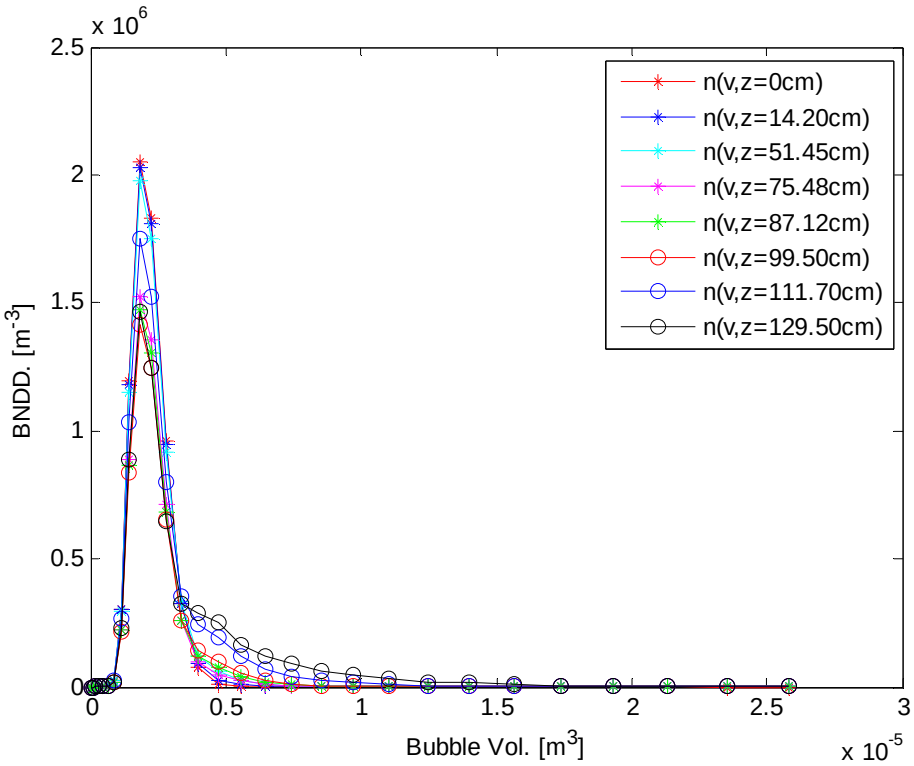

Figure 6.2. The BNDD at column axial lengths from PBM solution having coalescence source term only with the conservation of the axial distribution of gas void fraction.

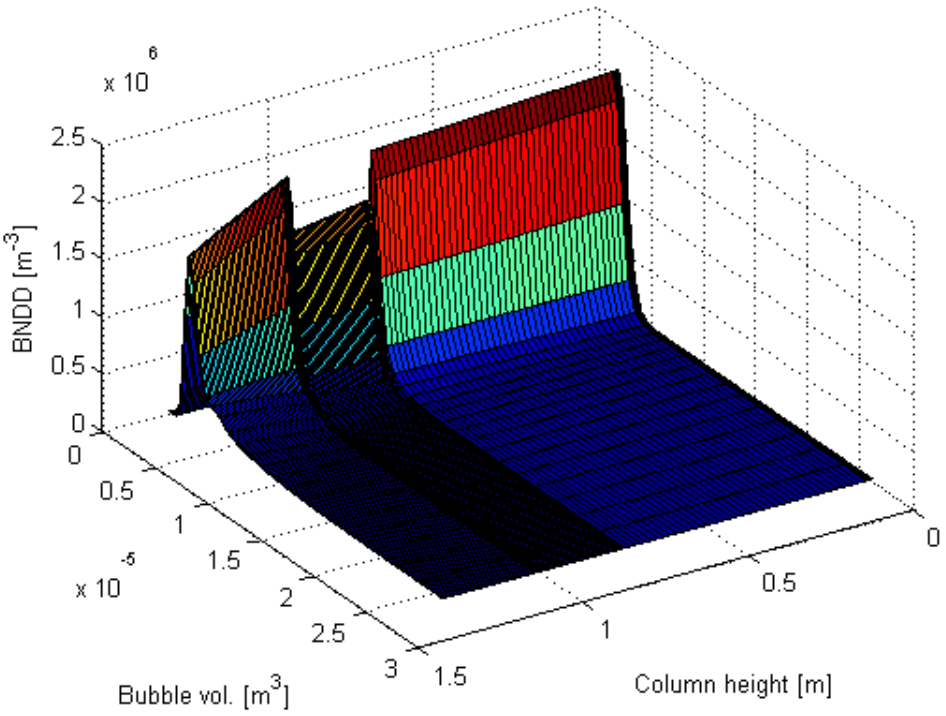

Figure 6.3. The BNDD at column axial lengths from PBM solution having coalescence source term only with the conservation of the axial distribution of gas void fraction in 3D.

Notably, in the PBM solution of Figure 6.3, the elemental column height at the first and second column sections was 1.25 cm. At the third and fourth sections, the values were 0.65 cm and 0.75 cm respectively. The low elemental volume at Section 3 relative to Section 4 accounts significantly for the low magnitude of BNDD at Section 3 compared to Section 4 as shown in Figure 6.3. The local gas void fractions are conserved for the PBM results of Figure 6.3.

At first and second sections, the local BNDD is lower to that at the fourth section and higher than that at the third section due to the differences in the local void fractions and elemental section volumes. The disparity of the local BNDD at the elemental volume of Section 3 and 4 results owing to the closeness of the local gas void fractions at Section 3 and 4.

The coalescence rate is the product of coalescence frequency and coalescence probability. The coalescence rate model developed by (Prince & Blanch, 1990) was used as the source terms model of Eq.(6.18). Using the coalescence rate models without correction, it was noticed that the gas void fraction (or total volume of gas) at the discrete axial length of the column, where BNDD was computed, was not conserved. Thus, the coalescence rate model leading to bubble birth was corrected as in Eq.(6.19) in order to ensure the total volume of gas was conserved at all discrete height of column where $n(v,z)$ was sought.

The correction model to the bubble birth coalescence rate from the computed bubble birth and death coalescence rate models by (Prince & Blanch, 1990) to ensure volume conservation are as follow: Let the coalescence rate leading to birth of bubbles be represented by $\overline{CB}$ (vector space); the coalescence rate resulting in death of bubbles be denoted by $\overline{CD}$ (vector space) and volume of bubble sizes be represented by $\bar{V}$ (vector space), then

$$\overline{CB} = \frac{\left(\frac{\bar{V}\cdot\overline{CB}}{\int_{Vmin}^{Vmax}\overline{CB}dv}\cdot\left(\int_{Vmin}^{Vmax}\overline{CD}dv - \int_{Vmin}^{Vmax}\overline{CB}dv\right) + \bar{V}\cdot\overline{CB}\right)}{V} \tag{6.19}$$

At the superficial gas velocity of 0.01 m/s, the gas void fractions (total volume of gas) at the discrete height of the column without and with correction are shown in Table A1.15 in the appendix. The gas void fractions in Table A1.15 are represented with the following notations: ε_i^{Cor}- Gas void fraction using corrected model, ε_i^{Unc}- Gas void fraction using

uncorrected model, $\Delta\varepsilon_i^{Cor}$- Difference in the gas void fractions for the corrected model and $\Delta\varepsilon_i^{Cor}$- Difference in gas void fraction for the uncorrected model.

In Figure 6.1, the graph with legend 'bubble death by coalesce. events' $[m^{-3}]$ is the product of coalescence rate resulting in bubble death $[m^{-3}s^{-1}]$ and elemental time step $[t, t+dt]$ $[s^{-1}]$ contributing to the BNDD at $z = 1.19cm$. The legend 'bubble birth by coalesce. events' $[m^{-3}]$ is the product of coalescence rate resulting in bubble birth $[m^{-3}s^{-1}]$ and elemental time step $[t, t+dt]$ $[s^{-1}]$, contributing to the BNDD at $z = 1.19cm$.

Figure 6.2 and Figure 6.3 show the $n(v,z)$ resulting from solving Eq.(6.18) at discrete column height within the range $[0, 1.295\ m]$ at stated heights in the legend. The measured gas void fraction axial distribution as obtained in Chapter 4 at the superficial gas velocity of 0.016 m/s was used as the boundary conditions appropriately.

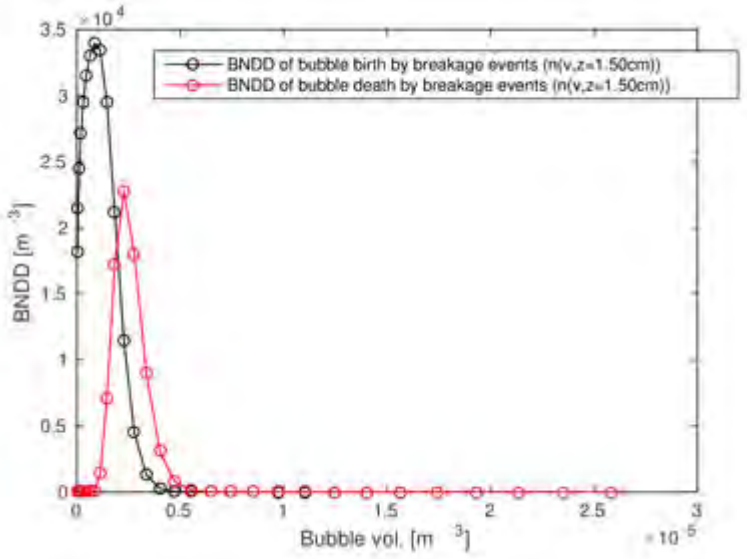

Figure 6.4. Bubble breakage rate as PBM source term resulting in BNDD of bubble birth and death at a discrete axial column length (approx. Inlet region) at superficial gas velocity of 0.016 m/s and gas void fraction of 2.7%.

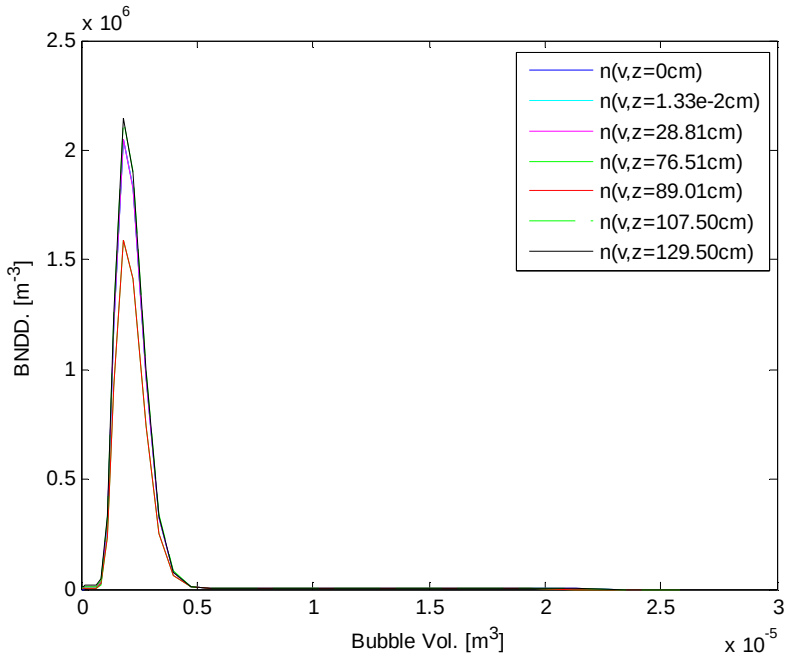

Figure 6.5. The BNDD at column axial lengths from PBM solution having breakage source term only with the conservation of the axial distribution of gas void fraction.

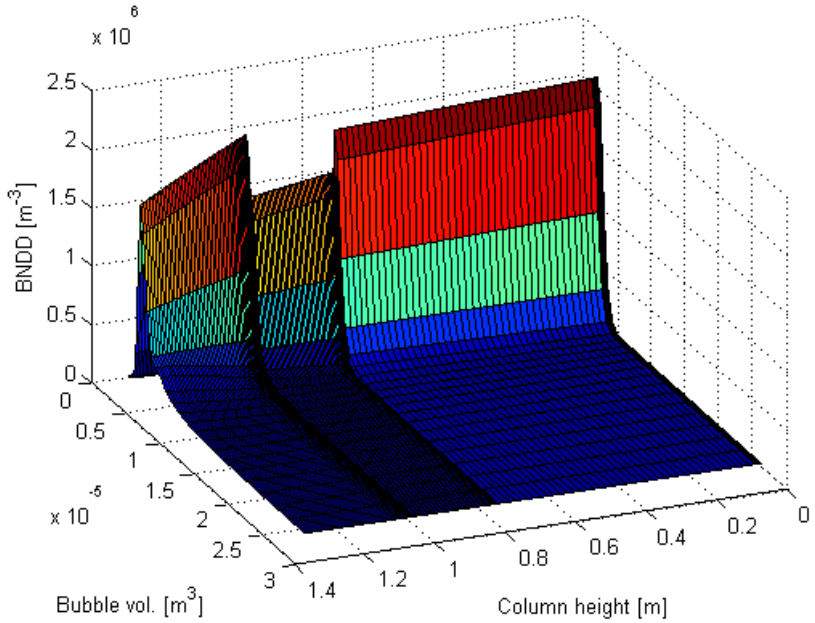

Figure 6.6. The BNDD at column axial lengths from PBM solution having breakage source term only with the conservation of the axial distribution of gas void fraction in 3D.

2) In a very dilute system, the rate of bubble coalescence is zero by the description of Eq.(6.17). Using the same inlet BNDD, bubble sizes and gas void fraction to obtain the results in Figure 6.1, the PBM of Eq.(6.17) having breakage rate source and sink terms models only was solved. The breakage rate model is a product of breakage frequency $g(v)$, probability

density function of daughter bubbles $f(v';v)$, BNDD $n(v,z)$ and function of daughter bubbles formed from the breakage of a mother bubble $m(v)$. The $g(v)$ as in Eq.(6.13) was multiplied by constant 0.76 $(E = 0.76)$ proposed by (Mitre, et al., 2010) and integrated in solving the PBM of Eq.(6.17) to obtain results shown in Figure 6.4, Figure 6.5 and Figure 6.6.

The graphs with the legend 'bubble birth by breakage events' and 'bubble death by breakage events' $[m^{-3}]$ in Figure 6.4 are the product of breakage rate resulting in bubble birth and death $[m^{-3}s^{-1}]$ and elemental time step $[t, t+dt]$ $[s^{-1}]$ contributing to the BNDD at $z = 1.87cm$. Figure 6.5 and Figure 6.6 show the resulting BNDD due to the phenomenon of bubble breakage leading to bubble birth and death at stated column heights denoted in the legend. The gas void fraction at discrete column heights was conserved for the solutions in Figure 6.5 and Figure 6.6. Thus, there was no need for correcting the breakage rate leading to bubble birth and death.

Thereafter, the effects of the combination of coalescence and breakage rates models on the BNDD at specific column heights was examined by solving the PBM of Eq.(6.16). The same specific coalescence rate and breakage frequency models that yielded the solution of Figure 6.1 and Figure 6.4 were used to solve the PBM of Eq.(6.16). The obtained solutions to the PBM of Eq.(6.16) are shown Figure 6.7(a-b).

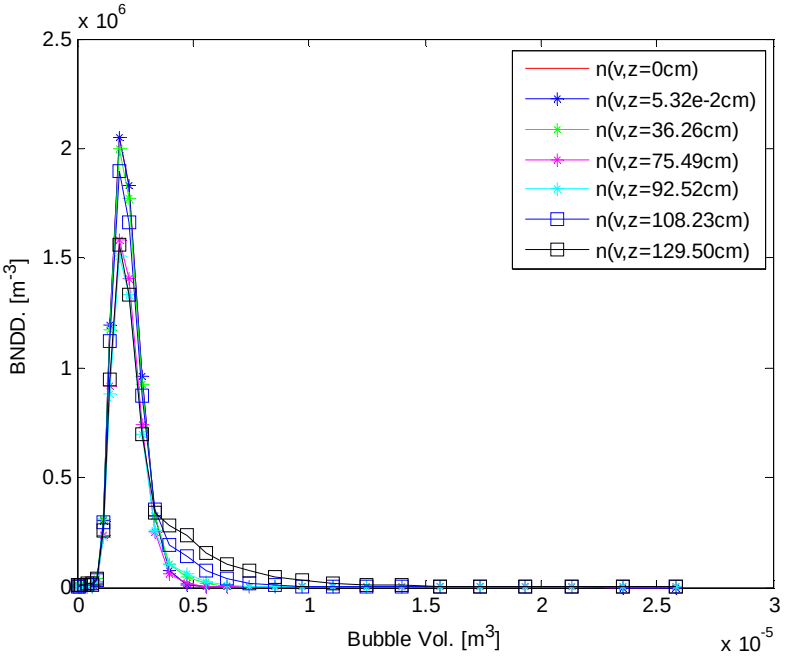

(a)

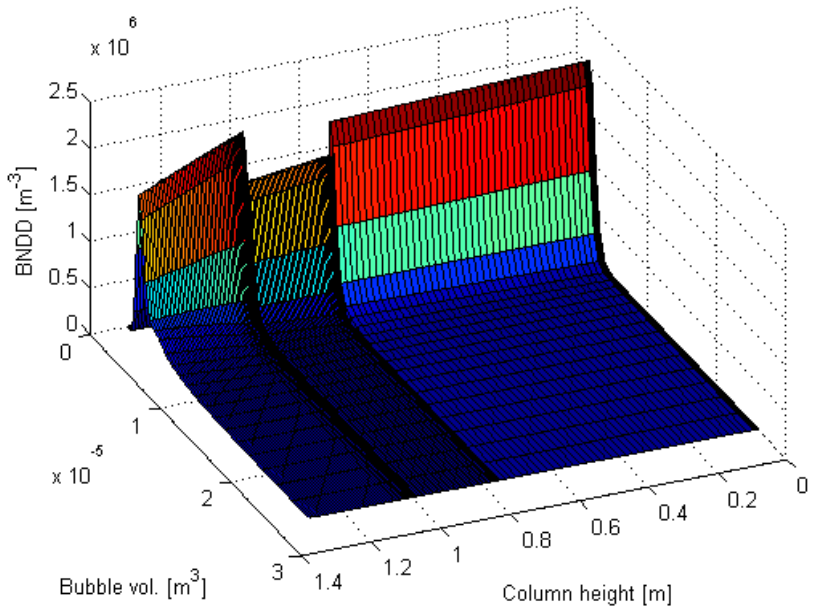

(b)

Figure 6.7. The BNDD along column height resulting from solving a PBM with the source and sink terms of breakage and coalescence rate models: (a) the BNDD at discrete column height in 2D; (b) the BNDD at discrete column height in 3D.

Given the fluid state physical properties, the geometric column dimensions and operational conditions in the column at a superficial gas velocity of 0.016 m/s, the Reynolds number of the air-water fluid flow system was found to 4640. This Reynolds number indicates that the fluid flow regime was turbulent where the axial bubble swarming was influenced significantly by the bubble coalescence and insignificantly by breakage rates phenomena. At the superficial gas velocity of 0.01, 0.009 and 0.008 m/s, the Reynolds numbers are 2900, 2610 and 2320 respectively indicating the fluid flow regimes are translational.

The fluid flow regime at superficial gas velocities lower than 0.008 m/s is laminar flow since the Reynolds numbers are less than the critical Reynolds number of 2300. Thus, the bubble evolution process at superficial gas velocities less than or equal to 0.01 m/s was controlled by bubble coalescence events majorly and by negligible bubble breakage events (Mitre, et al., 2010). The computer codes for solving the PBM as well as the PBM source and sink terms models of bubble coalescence and breakage leading to either bubble birth or death are in Appendices C1 to C6 respectively.

6.4. Discussion and conclusions

In deriving a PBM that allows for the computation of the BNDD $n(v,z)$, a number of breakage rate models and coalescence rate models were explored. A balance of gas volume at discrete column sectional volume was not obtained with many of the models except for the coalescence rate model developed by (Prince & Blanch, 1990) and breakage rate model developed by (Martinez, et al., 2010). In particular, the breakage rate model by (Martinez, et al., 2010) was suitable because its development included the contributory factor of probability density function of daughter size distribution.

The Weber number at the highest superficial gas velocity of 0.016 m/s was 1.02, which is less than the critical Weber number of 2.3 when the phenomenon of bubble breakage is observed in fluid systems. At the highest superficial gas velocity, the fluid flow regime was turbulent, while at the value of 0.01, 0.009 and 0.008 m/s, the fluid flow regime was translational. The fluid flow regime was laminar at the superficial gas velocity less than 0.008 m/s with respect to the operational conditions and column geometric dimensions. Thus, the changing BNDD during axial bubble swarming was influenced majorly by bubble coalescence events at all the superficial gas velocities studied.

In this work, the change in $n(v,z)$ was noticed to occur at steady-state and in the axial direction of the column as verified by the local ERT 2D images of dispersion. Accordingly, a 2D advection-dispersion of BNDD governed by the phenomena of bubble coalescence and breakage within the framework of PBM was developed to compute the $n(v,z)$ in the axial direction of the column.

The bubble size, BNDD and gas void fractions determined from ERT measurements coupled to DGD process were used as the required boundary conditions for the PBM. The motivation for using these bubble population parameters from ERT measurements as boundary conditions was to allow for the computation of $n(v,z)$, the coalescence and breakage rate. The coalescence and breakage rates contributing to the changing $n(v,z)$ with column height cannot be determined from analysis of ERT signals.

The mathematical formulation of image reconstruction by the ERT technique is a model of electric potential flux in the body interior due to stimulated periphery current signals. The ERT spatial resolution is adequate for imaging the local gas void fraction but low for imaging the countable entities to account for BNDD in the column. Thus, the use ERT measurements

as boundary conditions for a PBM simulation of bubble swarm, thus, contribute to a new approach of applying a PBM to determine the extent of bubble coalescence and breakage rates as bubble interact during axial swarming.

The solution of the PBM for the case of coalescence rate, being the PBM source and sink terms, accounting only for $n(v,z)$ at a specific height in the column are shown in Figure 6.2 and Figure 6.3. The solutions show the BNDD in lower bubble classes decreases, while that of bubbles in larger classes increases during axial bubble swarming without parameterized specific coalescence rate. Figure 6.4 and Figure 6.5 show the resulting $n(v,z)$ when the source and sink terms of the PBM were due to bubble breakage events leading to bubble birth and death. The results in Figure 6.4 shows the BND in the lower bubble classes increases while that of bubbles in the larger classes decreases during axial bubble evolution in the column. A presentation of the resulting $n(v,z)$ when the PBM was governed by a combination of bubble breakage rate and coalescence rates in the column is given in Figure 6.7.

It could be seen in Figure 6.7a that the breakage rate contribution at much lower bubble classes was dominant, which leads to increase in $n(v,z)$ in the column. In the lower bubble classes, the coalescence rate contribution prevailed over breakage rate since the number density of bubbles in the range of these classes decreases in the axial direction of the column. Further from the lower classes range to the larger and much larger classes range, the coalescence rate was also noticed to dominate breakage rate since the BNDD at these classes increases. The noticed increase in BNDD at the bubble classes was at a magnitude less than a case where the source and sink terms were due to coalescence rate alone.

The computed $n(v,z)$ in the column through an integration of ERT measurements to a PBM based on the use of ERT determined bubble properties as the boundary condition for the PBM will be validated. The validation technique involves parameterising the inlet $n(v,z=0)$, bubble coalescence rate, breakage rate and bubble expansion rate in the process of DGD, such that an agreement is found for two axially averaged BNDDs. The first axially averaged BNDD will be determined from ERT measurements captured during DGD while the second will be calculated from the model of DGD process of $n(v,z)$ obtained at steady state in the column. Furthermore, a good agreement of the axially averaged BNDDs $n(v,z)$ by ERT and a PBM will be said to have been found when the $n(v,z)$ averaged over bubble sizes by ERT measurements agrees with $n(v,z)$ averaged over bubble sizes by PBM at steady states.

Chapter 7

Bubble population balance modelling by dynamic gas disengagement process (DGD)

The use of the ERT technique to estimate the local gas void fractions of a steady state dispersion in a semi-batch operation mode has been explained in Chapter 4. Although the ERT data could capture changes in gas void fractions, it could not be interpreted to determine other bubble population parameters (BNDD) and the magnitude of bubble coalescence and breakage rates. The limitation in the use of the ERT data is linked to its low spatial resolution. In Chapter 5, the ERT data captured during a DGD process were analysed to compute the local BNDD $n^{ERT-DGD}(v,z)$ and an axially averaged distribution for $n^{ERT-DGD}(v,z)$, i.e. $\overline{n^{ERT-DGD}(v)}$. The simulation of the bubble population evolution in a column through the computation of the local BNDD based on the Population Balance Model of BNDD has been described in Chapter 6.

Accurate determination of the bubble population properties, the coalescence and breakage rates are required in calculating the hydrodynamic parameters of an axial bubble evolution in a column. In order to interpret ERT measurements for the determination of bubble population properties, the ERT measurements need be hybridized with models of the physical properties. The PBM enables the computation of bubble population parameters (BNDD) through a balance of physical properties of the dispersed and continuous phase. Thus, the hybrid of the PBM with ERT measurements is expected to allow for an advanced interpretation of ERT measurements for hydrodynamic parameter predictions in a column.

A steady-state PBM will be hybridized to ERT measurements in this work because the dispersed phase was distributed at low superficial gas velocities ranging from 0.005m/s – 0.016 m/s. At this flow rate range, the bubbles were visually noticed to swarm axially at steady state. The hybridization will be developed by solving a steady-state PBM to obtain $n(v,z)$ in the column. From the $n(v,z)$, the local gas void fractions $\varepsilon^{PBM-SS}(z)$ will be computed. The $\varepsilon^{PBM-SS}(z)$ will be calculated similar to the local gas void fractions calculated from the ERT gas void fraction estimates of the steady-state dispersion as in $\varepsilon^{ERT-SS}(z)$.

The PBM results are a conservative system of equations that yields all possible information about bubbles in the column, however, it is model-based. The ERT technique allows for

experimental measurements of the local gas void fractions of the dispersed phase only given its low spatial resolution. The solution of the PBM can, thus, be averaged radially to calculate the local gas void fractions along the column axis. This gas void fractions from the PBM results can also be validated with the experimentally validated ERT gas void fractions. Similarly, using the solution of a steady state PBM as an initial condition for a model of DGD process, the solution of the DGD model yields the BNDD in the column based on volume averaging. The volume averaging means the BNDD is averaged along the column axis. The resulting axially averaged BNDD will be verified by evaluating its consistency with the axially averaged BNDD determined through the coupling of ERT measurements to the DGD process as done in Chapter 5.

The four bubble population parameters that should agree before the BNDD solution can be said to have been found are as follows: the local gas void fractions by the PBM and the ERT measurements at steady state as well as the BNDD determined by the model of DGD and by the ERT measurements during DGD. Let the local gas void fractions determined from the ERT measurements and the PBM simulation based on radial averaging be represented in terms of BNDD averaged over bubble sizes respectively by ($\bar{n}_v^{ERT-SS}(z)$) and ($\bar{n}_v^{PBM-SS}(z)$). Also, Let the bubble sizes resulting from the DGD process modelling and from the ERT data during DGD process based on volume averaging be denoted respectively by ($\bar{n}_z^{M-DGD}(v)$) and ($\bar{n}_z^{ERT-DGD}(v)$). An accurate BNDD will then be determined from the solution of the PBM provided that the $\bar{n}_v^{ERT-SS}(z)$ agrees with the $\bar{n}_v^{PBM-SS}(z)$ and that the $\bar{n}_z^{ERT-DGD}(v)$ agrees with the $\bar{n}_z^{M-DGD}(v)$.

Further analysis of the resolved $n(v,z)$ combined with the determined coalescence and breakage rates that yielded $n(v,z)$ will be utilized to compute the hydrodynamic parameters in the column. Thus, in order to compute $\bar{n}_z^{M-DGD}(v)$, a derivation of the model for the DGD process, the method of its solution and the interpretation technique of the solution are presented in this chapter.

7.1. Derivation of the mathematical model for the transport of bubble population in the process of DGD

Dynamic gas disengagement process refers to a process where bubbles rise through the liquid phase at varied velocities followed by bubble detachment from the liquid at varied times after turning off the gas inlet into a column. The bubble rise velocity of a bubble class

depends on the mean bubble sizes of the class and the axial positions of the bubble population class. The observed manner of bubble disengagement from the liquid phase is illustrated in the diagram of Figure 7.1. Modelling the advection of gas described in Figure 7.1 allows for the computation of the transient hold-up after the bubble swarming at steady state and during the DGD process.

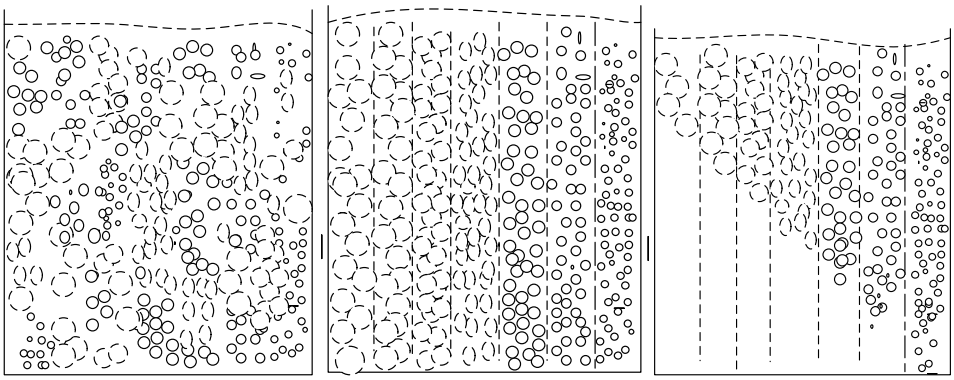

(a) (b) (c)

Figure 7.1. Diagrammatic illustration of the disengagement model of bubble size distribution at various times during a DGD process: a) before turning off the air inlet into the column; b) at the instant the air inlet is switched off; c) after an elapsed time t after turning off the air and in the process of DGD (Sriram & Mann, 1977).

The derivation of the model for the process of DGD is based on the following basic assumptions on the state of the fluid system made by both (Patel, et al., 1989) and (Daly, et al., 1992) during DGD process:

1. that dispersion is axially homogeneous (i.e. the bubble size distribution was initially axially homogeneous) at time t = 0;

2. that there are no bubble interactions (i.e. bubble coalescence and break-up);

3. that there is a constant rate of disengagement (i.e. all bubbles disengage independently of each other);

4. that the cross-sectional area occupied by bubble rising at velocity, u_{bj}, remains constant throughout the disengagement.

The derivation is, thus, as follows: Let the population of entire bubbles in the column be grouped into bins or classes j, such that $j = 1,2,3, \dots, N$, and N is the index of largest bubble class. Let the population of bubbles in a certain class j be denoted by the bubble number

density, $n_j[m^{-3}]$. The n_j is measured in per unit volume since it is the fraction of the gas volume in a class j of the total gas volume divided by the mean bubble volumes in the class per the bubble class volume. The BNDD is $n(v,z)$ to indicate that it varies with bubble size v and axial length z of the column.

Let the density of the gas phase and volume of the mean bubble size in a class j be denoted respectively by $\rho_{g,j}[kgm^{-3}]$ and $v_{g,j}[m^3]$. Moreover, let the density (concentration) of the volume fraction of gas bubbles in a class j and the volume of the column section be denoted respectively by $C[kgm^{-3}]$ and $V[m^3]$. The gas density C of a bubble size can also be expressed as $C = {}^{\rho_g}/_{\gamma_g}\ [kmol/m^3]$, where the gas density and the molar mass of the gas phase are respectively $\rho_g[kgm^{-3}]$ and $\gamma_g[kg(kmol)^{-1}]$.

Thus, the concentration of the volume fraction of gas bubbles in a class j can, thus, be expressed as

$$C = \frac{v_{g,j} n_j \rho_g}{V} \tag{7.1}$$

The advection transport of the BNDD of bubble sizes will be described by a mass balance taking place within a section or a control volume of the column as in Figure 7.2.

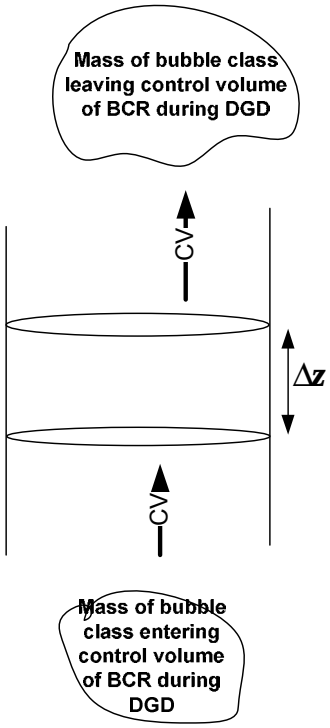

Figure 7.2. An illustration of the change in mass of bubble population volume of a bubble class per unit time within a section of a BCR.

Eq.(7.1) implies that the mass of the gas volume fraction of bubbles in the reference class j is $C_j V = Q = v_{g,j} n_j \rho_g$. The mass balance within the target section as in Figure 7.2 is achieved by accounting for the change in the mass per unit time in the column. The change in mass per unit time will be equal to the difference of the mass entering and leaving added to the rate of mass generation by physical or chemical processes within the time. Moreover, the rate of change in mass of a bubble class gas volume can be expressed in terms of the difference in flux of the mass of the bubble class volume fraction flowing per unit area per unit time through the section denoted by $J_1$and $J_2[kg(m^{-2}s^{-1})]$ added to the mass generation rates, $R_j[kmol/(m^3 s)]$ as in Eq.(7.2).

$$\frac{\partial(C_j V)}{\partial t} = AJ_1 - AJ_2 + R_j V = V\frac{\partial C_j}{\partial t} = A(J_1 - J_2) + R_j V \qquad (7.2)$$

Eq.(7.2) can be re-expressed as Eq.(7.3) where $V = A\Delta z$

$$\frac{\partial C_j}{\partial t} = \frac{A}{V}(J_1 - J_2) + R_j = \frac{\partial C_j}{\partial t} = \frac{1}{\Delta z}(J_1 - J_2) + R_j \qquad (7.3)$$

Given that the flux J is changing in z-direction with gradient of $W_0 \, {\partial J}/{\partial Z}$, then

$$W_0 \, {\partial J}/{\partial Z} = \frac{J_2 - J_1}{\Delta Z} \rightarrow J_2 = J_1 + W_0 \, {\partial J}/{\partial z}\,\Delta z \qquad (7.4)$$

The parameter W_0 is included because mean bubbles in bubble classes may not actually rise vertically along the column axis within all control volume during a DGD process. Some of the bubbles perform fluctuation movements along their rising path (Marco & Mewes, 1999). This can occur owing to the measured axial variation of the gas void fractions for the studied superficial gas velocities in Chapter 4. During the DGD initial condition of steady-state bubble evolution, the degree of well-distribution and radial uniformity of bubble population increases from the column base with column height. This does not agree absolutely with the expected assumption of the steady-state DGD initial condition illustrated in Figure 7.1a. The bubble population was well-distributed at the third and fourth column sections while being concentrated at the centre top of the sparger at the first and second column sections given the sparger geometry.

Besides, the W_0 will be a correction factor in the model since the stratification form of Figure 7.1c and the four DGD assumptions may not hold absolutely during experimental measurements. The W_0 can be interpreted to mean the component factor of the bubble class rise velocity along the column axis during DGD process. Substituting Eq.(7.4) into Eq.(7.2) results in Eq.(7.5)

$$\frac{\partial C_j}{\partial t} = \frac{1}{\Delta z}\left(J_1 - J_1 - W_0 \, {}^{\partial J}/_{\partial Z}\,\Delta z\right) + R_j = -W_0 \, {}^{\partial J}/_{\partial Z} + R_j \qquad (7.5)$$

Therefore

$$\frac{\partial C_j}{\partial t} = -W_0 \, {}^{\partial J}/_{\partial Z} + R_j \qquad (7.6)$$

Furthermore, the mass of the volume fraction of the bubble class moving across the control volume in a unit time per unit area can be calculated by the expression

$$\frac{Q}{A\Delta t} = \frac{CV}{A\Delta t} = \frac{CA\Delta Z}{A\Delta t} = \frac{C\Delta Z}{\Delta t} = J \qquad (7.7)$$

In the limit as Δt tends to zero,

$$\lim_{\Delta t \to 0} \frac{C\Delta Z}{\Delta t} = C\frac{\partial Z}{\partial t} = Cu_{g,j} \qquad (7.8)$$

When Eq.(7.8) is substituted into Eq.(7.6), Eq.(7.9) is obtained

$$\frac{\partial C_j}{\partial t} = -W_0 \, {}^{\partial (C_j u_{g,j})}/_{\partial Z} + R_j = -W_0 u_{g,j} \, {}^{\partial C_j}/_{\partial Z} + R_j \qquad (7.9)$$

where $u_{g,j}$ is the bubble rise velocity of bubble population in class j. The parameter W_0 will be determined experimentally for the actual gradient of changing flux within a control elemental volume during DGD process.

Assuming the gas phase obeys the idea gas behaviour during dispersion, the gas pressure decreases axially upwards in the column. The decreasing gas pressure leads to decreasing gas density along the column axis. Thus, the bubble volume changes owing to the change in gas density along the bubble path in the column. The bubbles volume increases (gas expansion) during their axial transport in the direction of decreasing liquid pressure or density in the column. Notably, the changes in the bubble volume may also result from temperature variations along column axis (Marco & Mewes, 1999).

At the steady state condition of the flow and before an accumulated time, the bubble volume changes in the flow due to gas expansion arising from varying liquid density and mass transfer between the bubbles and liquid. At such steady state, Eq.(7.9) can be rewritten as Eq.(7.10) to derive the source terms for the DGD process.

$$W_0 u_{g,j} \, {}^{\partial C_j}/_{\partial z} = R_j \tag{7.10}$$

During the steady state bubble flow regime, the total molar flow rate $\dot{Q}[kmol/s]$ of bubble class j changes with respect to bubble volume due to gas expansion as in Eq.(7.11) within an elemental volume of column section, dV.

$${}^{\partial \dot{Q}}/_{\partial v} = R_j \tag{7.11}$$

The $\dot{Q}$ is characterised by gas expansion due to changes in gas density and mass transfer between bubbles and the liquid. Thus, the total molar mass flow $\dot{Q}$ can be expressed in terms of cumulative sum of the contributory phenomena to mass such as gas expansion and mass transfer as in Eq.(7.12) (Marco & Mewes, 1999).

$$\partial \left({}^{\partial}/_{\partial t} \left(\frac{\rho_g}{\gamma_g} vf \right) + \dot{n} a_g vf \right) \Big/_{\partial v} = \left({}^{\partial}/_{\partial t} \left(\frac{\rho_g}{\gamma_g} \right) + \dot{n} a_g \right) \frac{\partial (vf)}{\partial v} = R_j \tag{7.12}$$

In Eq.(7.12), $\gamma_g[kg/kmol]$, $f[unit]$, $\dot{n}[kmol/(m^2 s)]$ and $a_g[m^{-1}]$ are respectively the molar mass of gas phase, the probability density distribution of bubble sizes, molar flux transferred out of the bubbles and the interfacial area per volume. Thus, the non-steady gas disengagement process model of Eq.(7.9) becomes Eq.(7.13) with the inclusion of the source reaction rate terms.

$$\begin{aligned} &{}^{\partial C_j(z,t)}/_{\partial t} + W_0 u_{b,j}(z,t) \, {}^{\partial C_j(z,t)}/_{\partial z} \\ &\qquad = {}^{\partial \left({}^{\partial}/_{\partial t} \left(\rho_g vf(v) \right) + \gamma_g \dot{n} a_g vf(v) \right)}/_{\partial v} \end{aligned} \tag{7.13}$$

Notably, every term in Eq.(7.13) has a unit of $kg(m^3 s)^{-1}$ by dimensional analysis. The relative changes in bubble sizes per unit time is calculated by multiplying all bubble volumes by the same function factor. The function is expected to take into account the effect of a relative change in bubble volume on the size distribution (Marco & Mewes, 1999). The

relative change in every bubble volume due to mass transfer from the interaction of the liquid and bubbles is denoted by the second term of the source in Eq.(7.13). The molar flux $\dot{n}$ is positive ($\dot{n} > 0$) if the mass transfer is directed out of the bubble into the liquid (Marco & Mewes, 1999). The included W_0 factor will also allow for parameterising the changing flux with an elemental control volume on the account of the used source terms model by (Marco & Mewes, 1999) (Lehr & Mewes, 2001). This source term model was not verified experimentally in this work but assumed to hold during a DGD process.

Eq.(7.13) describes the rate of change of bubble volume fraction density in a bubble class moving across a control volume in a unit time per unit area of the column under the influence of gas expansion due to changes in gas and mass transfer. The first term of Eq.(7.13) accounts for the change in density of volume fraction of bubble size j along column axis with time. The second term of Eq.(7.13) denotes the change in density of volume fraction of bubble size j along the axis of the column. Eq.(7.13) describes the disengagement of bubbles using the solution of the PBM simulation of steady state bubble evolution in the column as its initial condition.

7.2. Method of solving the derived mathematical model for the transport of bubble population in the process of DGD

Eq.(7.13) is re-written as in Eq.(7.14) to indicate the concentration of the gas volume of a bubble size class is a function of column axis z and bubble size class (in volume v). The bubble size class is denoted with index j while time with t. The source terms of Eq.(7.14) describes the phenomenon of gas expansion that occurs along the axial direction of the column in the process of DGD.

$$\partial C_j(z,t)/_{\partial t} + W_0 u_{b,j}(z,t)\, \partial C_j(z,t)/_{\partial z} = \left(\partial(\rho_g)/_{\partial t} + \gamma_g \dot{n} a_p\right) \partial\left(v' f_j(z,t)\right)/_{\partial v} \qquad (7.14)$$

for $j = 1,2,3, \ldots N$, and N is the index of largest bubble class in the column.

The first and the second terms of the left hand side of Eq.(7.14) are respectively the unsteady state term and the axial transport term of the gas volume concentration of a bubble class describing its change with time. The velocity, $u_{b,j}[{}^{m}/_{S}]$, with which the bubble size class j travels along z is a function of the axial length of the column z and time t, since different bubble sizes rise with varied rise velocities. The velocity relation is expected to hold since it is assumed that no bubble interactions such as coalescence and breakup phenomena occur in the process of DGD. The velocity function corresponding to a bubble class j is denoted by $u_{b,j}(z,t)$.

The terms on the right hand side of Eq.(7.14) model the expansion of bubble sizes due to changes in gas density and mass transfer during DGD processes (Lehr & Mewes, 2001). The symbol v' represents the volume of the reference bubble class $[m^3]$.

The molar flux of the interaction between the bubbles and the liquid can be expressed as $\dot{n} = K_L C_o$, where K_L is the mass transfer rates of the gas to liquid and C_o is the gas concentration or the solubility of gas in the liquid. At the superficial gas velocity of 0.016 m/s, Eq.(7.15) was used to determine the SMBD in the column (Akita & Fumitake, 1974).

$$\frac{d_{VS}}{D} = 26\left({gD^2\rho_L}/{\gamma}\right)^{-0.5}\left({gD^3}/{v_L^2}\right)^{-0.12}\left({U_G}/{\sqrt{gD}}\right)^{-0.12} \tag{7.15}$$

The average mass transfer rate corresponding to the SMBD was calculated using Eq.(7.16).

$$K_L = 0.5 g^{5/8} D_L^{1/2} \rho_L^{3/8} \gamma^{-3/8} d_{vs}^{1/2} \tag{7.16}$$

The solubility C_o of air in water at 25°C and 1 atmospheric pressure is $0.023 kg(m^3)^{-1}$. Thus, the term $\dot{n}\gamma_g$ was calculated to be $7.84 \times 10^{-6} kg/(m^2 s)$. From the known local gas void fraction at Section 1 and 2 given the superficial gas velocity (Chapter 4), the specific gas-liquid interfacial area was calculated by Eq.(7.17) to obtain 30.57 m^{-1}.

$$a_p = {6\varepsilon_g}/{d_{vs}} \tag{7.17}$$

The changing gas density of a bubble size class per time was calculated based on the axial pressure drop per time using the ideal gas equation of Eq.(7.18).

$$\Delta\rho = {}^{\Delta P}/_{RT} \tag{7.18}$$

The symbols $\Delta\rho$, ΔP, R and T denote respectively the axial density change, the axial pressure change, the individual gas constant and the ambient temperature.

By the PBM simulation, the average height of the elemental column section volume was calculated as Δz. Given a bubble class rise velocity $u_{b,j}$ at an elemental time $\Delta t_o \approx 1 \times 10^{-4} s$, the bubble class will transport axially by $\Delta z_o = u_{b,j}\Delta t_o$. Thus, the time-variant bubble class density was calculated using Eq.(7.19) based on the elemental axial pressure change.

$$\Delta\rho_g = {}^{\rho_l g \Delta z_o}/_{RT} \tag{7.19}$$

The stratification of the bubble population and their detachment from the liquid phase at varied times depending on their sizes illustrated in Figure 7.1a – c is described by Eq.(7.14). Eq.(7.14) is a set of N PDEs, where N is the number index of largest bubble class (i.e. $j = 1, 2, 3, \dots N$). Every PDE in Eq.(7.14) corresponding to a transport model of bubbles in a class j is transformed to an ODE by method of characteristics as explained in Appendix E, in order to develop an analytical solution to Eq.(7.14).

The characteristic equations that result from Eq.(7.14) as explained in Appendix E are

$$\frac{dz}{W_0 u_{b,v}} = \frac{dt}{1} = \frac{dC_j}{p} \tag{7.20}$$

Where $p = \left({}^{\partial(\rho_g)}/_{\partial t} + \dot{\gamma_g} n a_p \right) {}^{\partial\left(v' f_j(z,t)\right)}/_{\partial v}$.

Splitting Eq.(7.20) into two equations, Eq.(7.21) is derived.

$$\frac{dz}{dt} = W_0 u_{b,j};\ dz = W_0 u_{b,j} dt \tag{7.21}$$

Integrating Eq.(7.21) leads to

$$z = W_0 u_{b,j}(t - t_o);\ z = W_0 u_{b,j} t - K; K = W_0 u_{b,j} t_o \tag{7.22}$$

The second equation from Eq.(7.20) is then

$$\frac{dC_j}{P} = \frac{dz}{W_0 u_{b,j}}; dC_j = \frac{Pdz}{W_0 u_{b,j}}; C_j(t,z) = \frac{Pz}{W_0 u_{b,j}} + g(n); \tag{7.23}$$

Since K in Eq.(7.22) and n in Eq.(7.23) are constants, then,

$$K = z - W_0 u_{b,j} t = n \tag{7.24}$$

The requirement for the solution $C_j(t,z)$ to satisfy the initial condition is ensured by substituting Eq.(7.25) into Eq.(7.23) to get Eq.(7.26) – Eq.(7.27).

$$C_j(t_o,z) = C_j(0,z) = f(t=0,z) = f(z) = \frac{Pz}{W_0 u_{b,j}} + g(n);$$
$$g(n) = f(z) - \frac{Pz}{W_0 u_{b,j}} \tag{7.25}$$

$$\begin{aligned} C_j(t,z) = \frac{Pz}{W_0 u_{b,j}} + g(n) &= \frac{Pz}{W_0 u_{b,j}} + g\left(z - W_0 u_{b,j} t\right) \\ &= \frac{Pz}{W_0 u_{b,j}} + f\left(z - W_0 u_{b,j} t\right) - \frac{P(z - W_0 u_{b,j} t)}{W_0 u_{b,j}} \end{aligned} \tag{7.26}$$

$$C_j(t,z) = f\left(z - W_0 u_{b,j} t\right) + Pt \;\; for\; j = 1,2,3,\ldots N \tag{7.27}$$

The analytical solution for the respective equation in the set of Eq.(7.14) for $j = 1,2,3,\ldots N$ is Eq.(7.27). The solution of Eq.(7.27) is the density of gas in a bubble class j varying along the column axis and time that satisfies the developed model of DGD process. From the solution of Eq.(7.27), the gas volume in the bubble classes at any axial length and time during the process of DGD can be calculated.

7.3. Interpretation technique for the analytical solution of the derived mathematical model for the transport of bubble population in the process of DGD

The initial condition implies the bubble class gas concentration before the DGD process started (i.e. $C(t=0,\ v,z)$). In addition to the initial condition requirement (Eq.(7.25)) that the solution of Eq.(7.14) need satisfy, it also has to satisfy a boundary condition. The statement of the boundary condition is that if the expression $\left(z - W_0 u_{b,j} t\right) < 0$ holds, then $f\left(z - W_0 u_{b,j} t\right) = 0$ to indicate the concentration of gas volume of bubble size j at time t is zero at axial length z. This means the concentration of the gas volume is disengaged from the base of the column $z = 0$ up to a certain height z of the column.

Thus, the initial condition of concentration of gas bubbles in a bubble class C_j is expressible in term of the corresponding gas void fraction $\varepsilon_{g,j}$ occupied by bubbles in the bubble class j as in Eq.(7.28). In Eq.(7.28), the total gas volume over all bubble sizes in a target section of the column is denoted by the term $\pi R^2 H$.

$$C_j = \frac{v_{b,j} n_j \rho_g}{V};\ \frac{C_j V}{\rho_g \pi R^2 H} = \frac{v_{b,j} n_j \rho_g}{\rho_g \pi R^2 H} = \frac{v_{b,j} n_j}{\pi R^2 H} = \ \varepsilon_{g,j} \qquad (7.28)$$

The gas volume in a bubble class disengaging from a local column section, which is of interest, is computable from Eq.(7.28) by multiplying $\varepsilon_{g,j}$ by $\pi R^2 H$. The symbols R and H denote respectively the radius and height of a reference column section.

Let the gas void fraction made up of bubbles in a bubble class j disengaging from a local section i of the column at time t be denoted by $\varepsilon_{i,j}(t)$. Likewise, let the volume equivalent of the void fraction $\varepsilon_{i,j}(t)$ be represented with the symbol $v_{g,i,j}(t)$ for $i = 1,2,3,4; j = 1,2,3 \ldots N$, since the ERT data were analysed over four column sections for bubble population grouped into N classes.

The actual inlet bubble size distribution (BSD) leaving the surface of the gas distributor is determined by the empirical correlation of Eq.(7.29) (Azad & Sultana, 2006) (Akita & Yoshida, 1974).

$$\frac{d_{vs}}{d_o} = 1.88 \left(u_o \Big/ \sqrt{g d_o} \right)^{1/3} \qquad (7.29)$$

In Eq.(7.29), d_{vs} is the volume-surface mean diameter of initial bubbles leaving the sparger; u_o is the gas velocity through the gas distributor orifice with diameter d_o. At the superficial gas velocity of 0.016 m/s, the d_{vs} is 0.32 mm. After leaving the surface of the sparger and during the bubble axial evolution, the bubbles interact by coalescence resulting in a different BSD at discrete column heights.

For the case of superficial gas velocity of 0.016 m/s, the maximum and minimum of axially averaged bubble size profile determined by the ERT method coupled with the DGD process were 3.67 cm and 0.39 cm respectively. The obtained local and axially averaged BNDD were log-normal density distributions as explained in Chapter 5. The range of bubble sizes were grouped into 30 classes to ensure high resolution of BNDD.

The mean and standard deviation of the bubble size classes for the inlet log-normal BNDD were parameterised with constants 1 and 0.15 respectively as in Figure 6.7 of Chapter 6. The PBM solution of Figure 6.7 was used as the initial condition $C(t = 0,\ v, z)$ with the assumed parameter $W_0 = 1$ during DGD process in solving Eq.(7.14).

The solutions of Eq.(7.14) given the stated boundary and initial conditions were coded in MATLAB (found in section D of the appendices) to compute the transient hold-up $\varepsilon_{i,j}(t)$ with time in the column. The results can also be interpreted to mean the local gas volume corresponding to a bubble class $v_{g,i,j}(t)$ disengaging from the column sections with time. Figure 7.3 shows the time-variant local disengaging gas volume during the DGD process from the solution of Eq.(7.14) at superficial gas velocity of 0.016 m/s at different $w_o$parameter values. The solution of the DGD process model using different W_0 parameters are plotted on the same graph with the measured time-variant disengaging gas volume locally in Figure 7.3(a-b). In the legends of the graphs, 'M-DGD' and 'Expt. DGD ' denotes solutions by the DGD process modelling and by experimental measurements respectively.

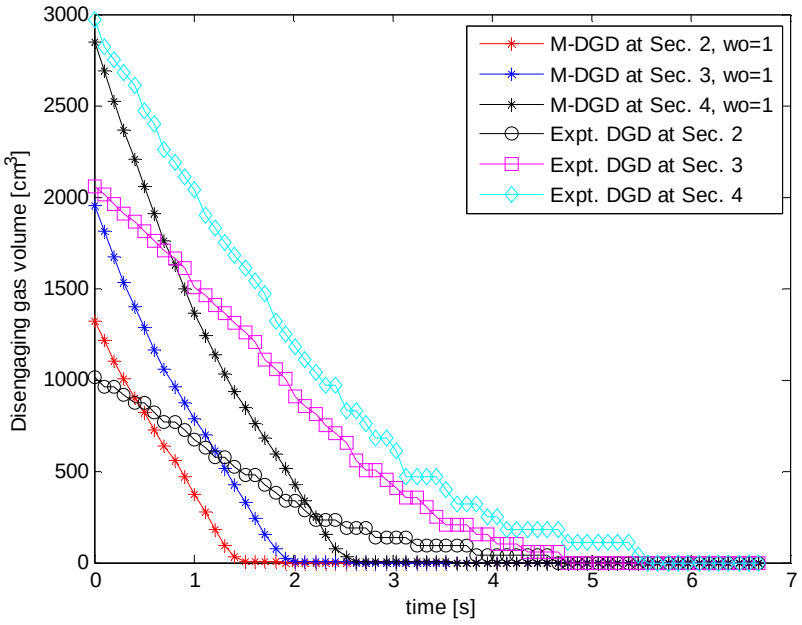

(a)

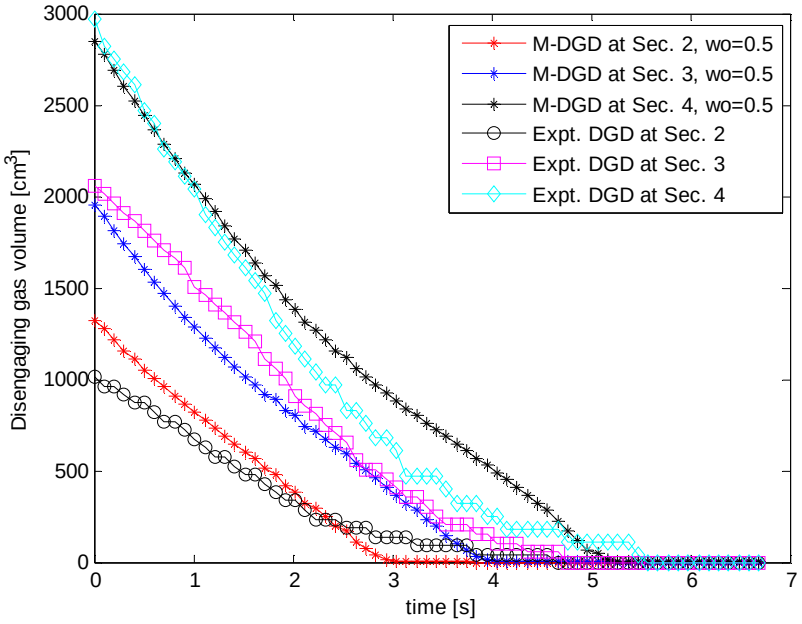

(b)

Figure 7.3. The time-dependent disengaging local gas volume computed from the solution of the DGD process model at different $\boldsymbol{w_0}$ parameters compared to the experimental data at superficial gas velocity of 0.016 m/s: (a) $\boldsymbol{w_0} = \mathbf{1}$, (b) $\boldsymbol{w_0} = \mathbf{0.5}$.

From Figure 7.3 results, the gas volume of a particular bubble size class disengaging locally can be computed if the characteristic local disengagement time of a bubble size class is known. For example, beginning from the time t_0, $t = 0$, when the air inlet into the column was turned-off, the first bubble size was observed to disengage from the liquid at time t_1. The second bubble class was noticed to disengage at time t_2. The gas volume at a column section i for the first bubble size class will be

$$v_{g,i,1} = v_i(t_0) - v_i(t_1). \tag{7.30}$$

At the same section i, gas volume composing of bubbles in the second class will be

$$v_{g,i,2} = v_i(t_1) - v_i(t_2) \tag{7.31}$$

where $v_i(t)$ is the graph of the gas volume in column section i with time t and $v_{g,i,j}$ is the gas volume for bubble class j at column section i. Similar differential gas volumes at other time intervals locally will be calculated to compute the gas volume composing of bubbles in lower classes. The ratio of the gas volume $v_{g,i,1}$ to the mean volume of bubble volumes in a size class disengaging at a time t will be calculated to compute the BND value of the class.

Using the characteristic disengagement times of bubble class sizes stated in Table 5.2 at $U_g = 0.016m/s$, the local and global BNDD were calculated as outlined in Figure 5.14 of Chapter 5 to obtain results in Figure 7.4 (a-d). The parameters for the log-normal fits to the global (G) BNDD using varied values of W_o and the statistical errors of the fits are stated in Table 7.1.

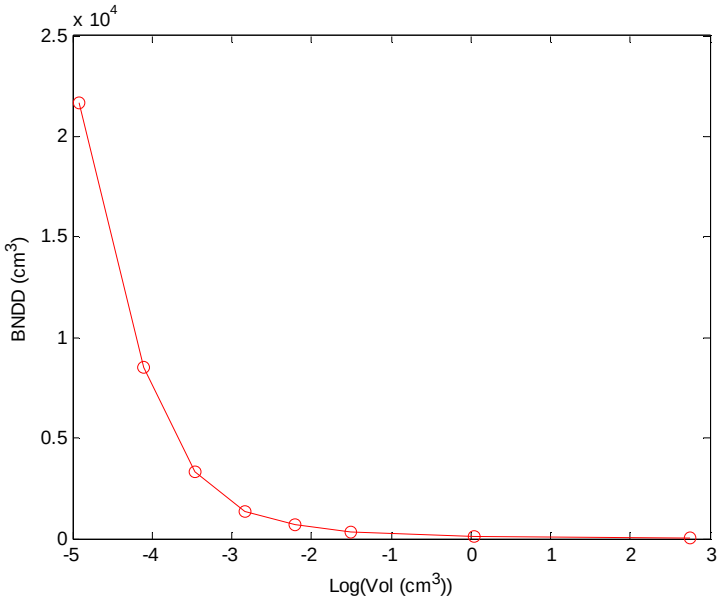

(a)

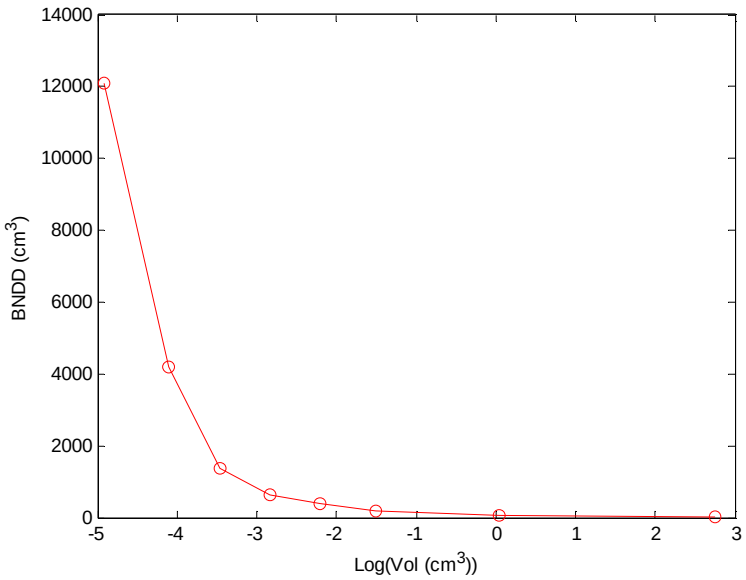

(b)

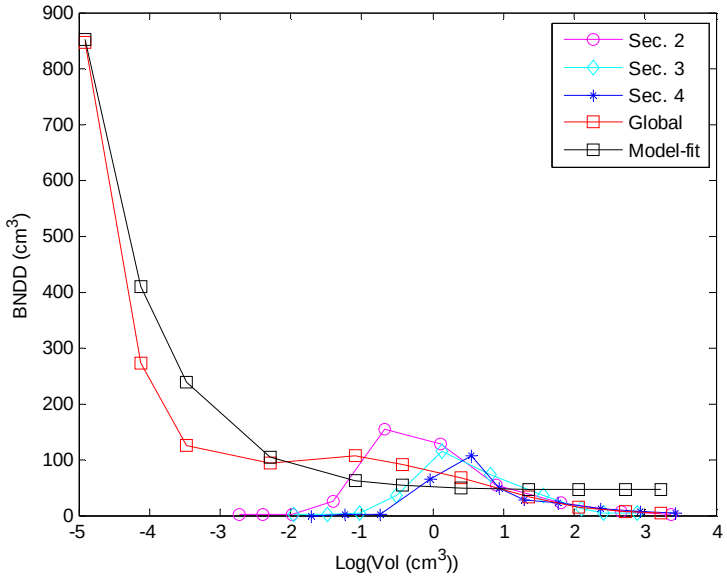

(c)

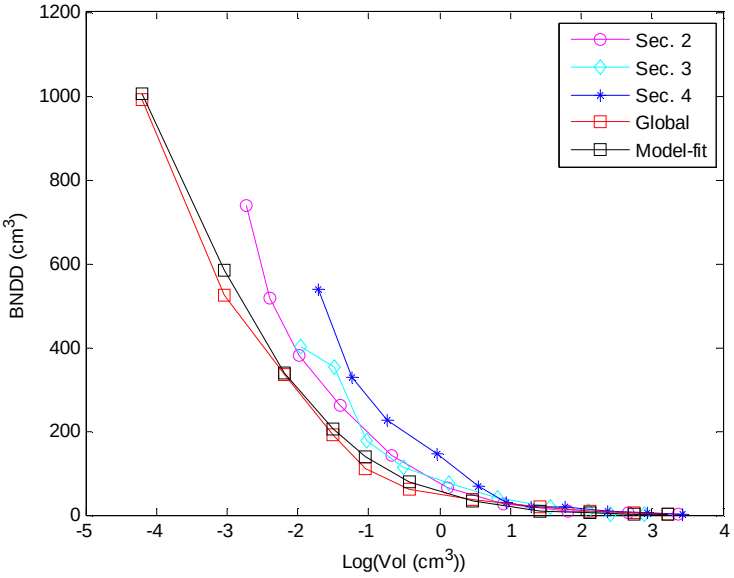

(d)

Figure 7.4. The BNDD against logarithm of bubble volume with varied parameter of W: (a) at Section 1 with $W_o = 1$, (b) at Section 1 with $w_o = 0.5$ (c) at Section 2, 3, 4 and globally with $W_o = 1$, (d) at Section 2, 3, 4 and globally with $W_o = 0.5$ at superficial gas velocity of 0.016 m/s.

Table 7.1. The constant values for the log-normal fits of the global BNDD by the DGD process model and the statistical error values.

$U_g(ms^{-1})$	Section	A	B	C	D	X^2	R^2	f-statistic	w_o
0.016	G	470±1.0	0.50±0.02	11.00±0.02	45	0.664	0.93	63.00	1
0.016	G	330±1.0	0.91±0.02	1.04±0.02	0	0.06	0.99	795.06	0.5

The resulting log-normal model for BNDD supports the findings of (Akita & Yoshida, 1974) and those of (Riquelme, et al., 2016), (Majumder, et al., 2006) and (Lage, 1996) who analysed bubble behaviour in bubble columns to obtain log-normal distributions. A log-normal distribution was also obtained by (Haibo, et al., 2007) in the analysis of bubble size distribution in the column in the process of DGD.

7.4. Discussion and conclusions

In Chapter 5, the characteristic disengagement times of bubble size classes locally and globally were computed from analysis of ERT ACD captured at column cross-sections during DGD process. The time profile results were interpreted to determine local BNDD in the process of DGD and globally in the column during steady state bubble evolution.

Chapter 7 focuses on modelling the process of DGD in the column using the solution of PBM at steady state as an initial condition. It was essential to model the DGD process so that the solution of the PBM can be related to bubble population properties measured by the ERT technique in Chapter 4 and 5. The relationship between the BNDD from solution of DGD model to the BNDD obtained from the ERT data captured during DGD will allow for accurate hybridizing ERT measurements and PBM.

A reference to the relationship between the static holdup ε_g, dynamic holdup, the BNDD, the superficial gas u_G and liquid velocities V_L explained in Section 5.1 of chapter 5 is made in this discussion. The purpose of the reference is to emphasise the importance of an analytic solution of a model of DGD process in combining a 2D PBM with two 1D ERT experimental data. An hybrid of ERT measurements and a PBM is, thus, envisaged to lead to accurate determination of the BNDD of bubble evolution at steady state in the column.

The relationship between ε_g, local u_G, local V_L and the rise velocity $U(d_b)$ of bubble sizes, d_b, was given in Eq.(5.3). In a special case where the liquid motion was zero and no bubble interaction that could influence bubble sizes such as phenomena of bubble coalescence and breakage processes, Eq.(5.4) was derived from Eq.(5.3). Eq.(5.4) is an ill-conditioned form since knowing the static gas holdup $\varepsilon(0)$ and the bubble rise velocity function $u(d_b)$ does not lead to a unique solution of $f(d_b)dd_b$ in the column at steady state.

Thus, the ill-conditioning state of Eq.(5.3) was reduced by observing the dynamic gas holdup behaviour that occurs starting from the initial static holdup condition when the gas inlet into the column was turned-off. Based on the resulting set of equations (as in Eq.(5.5)), an accurate solution, $f(d_b)dd_b$, satisfying the static holdup equation will also be expected to satisfy the other transient holdup equations. The derived models in Eq.(5.4) and Eq.(5.5) ensure the solution of the distribution of gas volume of bubble sizes $f(d_b)dd_b$ at steady state is unique. The uniqueness of result is validated through the requirement that it meets the conditions of static and transient gas void fraction in the column.

This concept of validating the distribution of gas volume of bubble sizes (or BNDD) at steady state based on the static and transient gas holdup fraction conditions motivated the need for capturing ERT data during DGD process as well as modelling the DGD process. From the known values of static and dynamic gas hold values, the inlet BNDD $(n(v, z = 0))$, expected coalescence and breakage rate at steady state condition can accurately be parameterised. The parameterisation will be achieved through the agreement of the static and dynamic gas holdup by the PBM with that from the ERT measurements.

The purpose of the parameterization will be to reconcile the resulting $n(v, z)$ from the 2D PBM simulation with the 1D ERT data steady state gas void fractions and the 1D ERT transient gas void fraction. This calculation is expected to lead to the determination of distribution of bubble sizes in the column. In hybridizing the 2D PBM and the two 1D ERT measurements, the resulting $n(v, z)$ from the PBM simulation that satisfies the static and transient holdup conditions will be sought.

The obtained $n(v, z)$ from the PBM simulation can be validated if it satisfies the static holdup by verifying that the radially averaged $n(v, z)$ over bubble sizes agree with that from the ERT static gas holdup measurements. In validating $n(v, z)$ if it meets the transient or dynamic gas holdup condition, a model of DGD process was developed in this chapter.

The inclusion of W_o parameter in the developed DGD process model by the plug flow approach is important owing to the assumptions associated with the plug flow model development that may not hold during experiments. The first key assumption is that the fluid is perfectly mixed in the radial direction but not in the axial direction. Secondly, that fluid flow is of constant density with no pressure drop during the flow.

Since perfect fluid mixing was not attained radially coupled with the pressure drop of the fluid contained in an elemental control volume in the plug flow during DGD process, the gradient of flux need be accurately modelled.

The method of solving the DGD process model for the concentration of gas volume of bubble size class to obtain an accurate analytical solution was described in Section 7.2. Furthermore, the technique of interpreting the solution of the DGD process model was explained in Section 7.3. The technique yields the transient gas void fraction values during DGD process. The transient gas void fractions can be validated with ERT data.

Without parameterising the gradient of flux term (i.e. $W_o = 1.0$), the time-variant disengaging gas volume was noticed to be different significantly from the experimental data at $u_g = 0.016\, m/s$ as shown in Figure 7.3a. By multiplying the gradient of flux term by 0.5 (i.e. $W_o = 0.5$), the time-variant local disengaging gas volume differs slightly from the experimental data as shown in Figure 7.3b. The results in Figure 7.3(a-b) were obtained using the coalescence rate model by (Prince & Blanch, 1990) and breakage rate by (Martinez, et al., 2010) without parameterisation in computing the DGD model initial condition. The explored bubble expansion model by (Marco & Mewes, 1999) for the DGD model source term was also not parameterised.

The Weber number for the steady state fluid flow regime at highest $u_g = 0.016\, m/s$ was 1.02, which is less than the critical Weber number of 2.3 before bubble breakage events are observed. Thus, the breakage events will be assumed to be negligible in the steady state bubble evolution process. The collision frequency will be parameterised in computing the initial condition for the DGD process model in the next chapter. In addition, the gradient of the flux term of the plug flow during the DGD process will be parameterised to ensure the time-varying disengaging gas volume by the DGD process model agree with the experimental data. When such results agree, the resulting local and global BNDD by the two approaches will also agree.

The solution of the DGD model combined with the technique of interpreting the solution allows for computing the local BNDD as well as axially averaged BNDD (global bubble size distribution) in the column. The resulting local BNDD and axially averaged BNDD were found to be parameterised log-normal distributions, which agree with the distribution of the inlet BNDD. The inlet BNDD was the boundary condition for the PBM simulation of the process in the column at steady state.

The $n(v,z)$ from the steady state PBM are log-normal distributions, which agree with the computed distribution of $n(v,z=z_1,z_2,z_3,z_4)$ by the DGD process modelling except for the difference in parameters. Based on these results, the DGD model could be said to be adequate for describing the DGD process. The newly developed model, thus, contribute to a new approach of modelling the advection transport of bubble size distribution in the process of DGD in a column.

Chapter 8

Hybridization of ERT measurements and a PBM for computation of bubble population properties in the column

The axial distribution of gas void fraction at steady state and global bubble size distribution in the column were determined from analysis of ERT images as described in Chapter 4 and Chapter 5 respectively. The ERT images of dispersion could not be analysed for determining the size and axial distribution of bubble population during bubble swarm at steady state because of its low spatial resolution. To address the stated limitation of the use of the ERT images, a PBM that allows for the computation of all possible bubble population properties in the column was solved in Chapter 6. Subsequently, the PBM solution was used as an initial condition for a model of DGD process in Chapter 7. The aim of the present chapter is to develop a method of hybridizing the 2D PBM with the experimentally measured local gas void fractions at steady state and in the process of DGD using the ERT technique.

The ERT generated images of dispersion at steady state yield spatial distribution of gas void fractions of the region occupied by bubbles but not the bubble size distribution. The ERT images of dispersion during a DGD process does not only yield the spatial distribution of gas void fractions but also the bubble size distribution globally. Thus, the hybrid model of the ERT and PBM will be achieved through a correlation of the ERT measurements at steady state and during the DGD process to that by the PBM. A correlation of such is envisaged to allow for the predictions of the BNDD in the column.

The measurement of the BNDD at steady state can be accomplished by other techniques that yield high spatial resolution at the expense of complicated, low accuracy, bulky, intrusive and expensive methods. A typical example of an alternative technique is the Electrical Point Probe Technique (Burgess & Calderbank, 1975) and (Steinemann & Buchholz, 1984). The description of the probe positions in the column and its measurement techniques, as well as the limitations of the technique, are stated in Section 2.8 of Chapter. The technique was reported in the work by (Burgess & Calderbank, 1975) and later upgraded in the study by (Steinemann & Buchholz, 1984).

The prediction of bubble population properties using the hybrid of the PBM and the ERT measurements based on common bubble population parameters both techniques could

measure is being explored. This approach is expected to be more reliable than the results from the use of the Electrical Point Probe Technique.

The method of hybridizing ERT measurements and a PBM for bubble swarming axially in the column will be described in Section 8.1. The hybrid of the ERT measurements and the PBM in Section 8.1 is intended for the determination of the BNDD, $n(v,z)$, as bubbles swarm axially at steady state in the column. The accuracies of the resolved BNDDs $n(v,z)$ by the hybrid of ERT and a PBM for superficial gas velocities of 0.016 and 0.01 m/s based on equipment available for studies are stated in Section 8.2. The effects of the superficial gas velocity on calculated $n(v,z)$ based on the ERT and the PBM hybrid method at steady state are reported in Section 8.3 of this chapter. In section 8.4, the discussion and conclusions on the developed hybrid model of the ERT and the PBM for determining the $n(v,z)$ in a BCR at steady state are stated. The effects of superficial gas velocity on the resolved $n(v,z)$ are also given in Section 8.4.

8.1. Hybridization of ERT measurements and a PBM for determining the BNDD in a column

The objective of this section is to find the BNDD, $n(v,z)$, which describes the bubble swarm phenomenon through the liquid phase at superficial gas velocities of 0.016 and 0.01 m/s at steady state. An accurate hybrid predicted $n(v,z)$ for a given flow rate is expected to be verified by the experimentally measured ERT static and transient local gas void fraction as explained in Chapter 7.

Figure 8.1 is a symbolic flow chart that illustrates the sequences of bubble population parameters to be measured by the ERT and computed by the PBM in hybridizing the ERT and a PBM. The ERT and a PBM hybrid model is intended to yield $n(v,z)$ in the column at steady state. An explanation of the symbolic flow chart is provided in the following paragraphs.

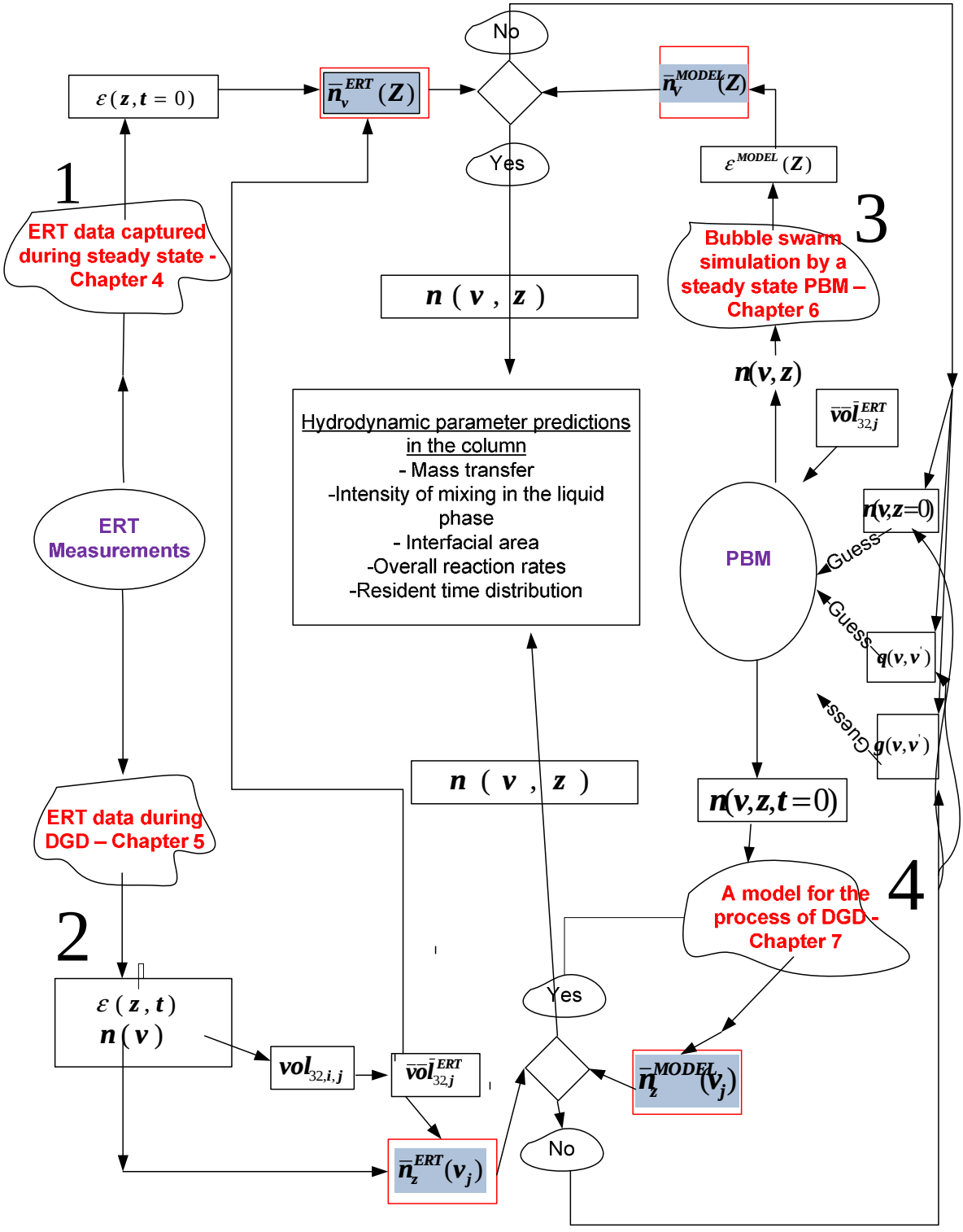

Figure 8.1. Schematic of flow of computation in hybridizing ERT measurements and a PBM for hydrodynamic parameter predictions in the column.

In the context of hybridization of the ERT and the PBM, the static and the dynamic holdup values were calculated from calibrated ERT TACD using the DP technique. The static gas holdup values were calculated from the calibrated local ERT TACD during bubble swarming at steady state. The dynamic holdup values were computed from the calibrated transient ERT TACD during DGD process in the column. The dynamic gas holdup values measured during DGD process were further analysed as in Chapter 5 to compute the global bubble size classes and their number densities BNDD $n(v,z)$ depending on column height.

The information of bubble size classes at discrete column heights allows for the determination of the mean bubble size class at a known height z using Eq.(8.1). The mean bubble size class, the static local gas holdup fractions and column sectional volume V_C were used to calculate the average of the local BNDD over bubble sizes at steady state using Eq.(8.2). This is steady state calculation labelled 1 in Figure 8.1. The obtained local gas void fractions $\varepsilon(z)$ of Chapter 4 are stated in Table 8.1. Figure 8.2 is a diagrammatic illustration of the representation of the average of the BNDD over bubble sizes at column sections (i.e. radial averaging of BNDD).

Table 8.1. The local gas void fractions at superficial gas velocities of 0.016 and 0.01 m/s.

Column section	Section 1 & 2	Section 3	Section 4
$\varepsilon(z)$(%) at 0.01 m/s	0.0220	0.0206	0.0308
$\varepsilon(z)$(%) at 0.016 m/s	0.0270	0.0403	0.0470

$$\overline{v^{ERT}(z)} = \sum_{j=1}^{N} v_j(z) \Big/ \sum_{j=1}^{N} j \tag{8.1}$$

$$\bar{n}_v^{ERT-SS}(z) = \frac{V_C \varepsilon(z)}{v^{ERT}(z)} \tag{8.2}$$

The calculations represent a radial averaging of a 2D BNDD to obtain a 1D BNDD as a function of column height as in Eq.(8.2) (i.e. $\bar{n}_v^{ERT-SS}(z)$) at steady state.

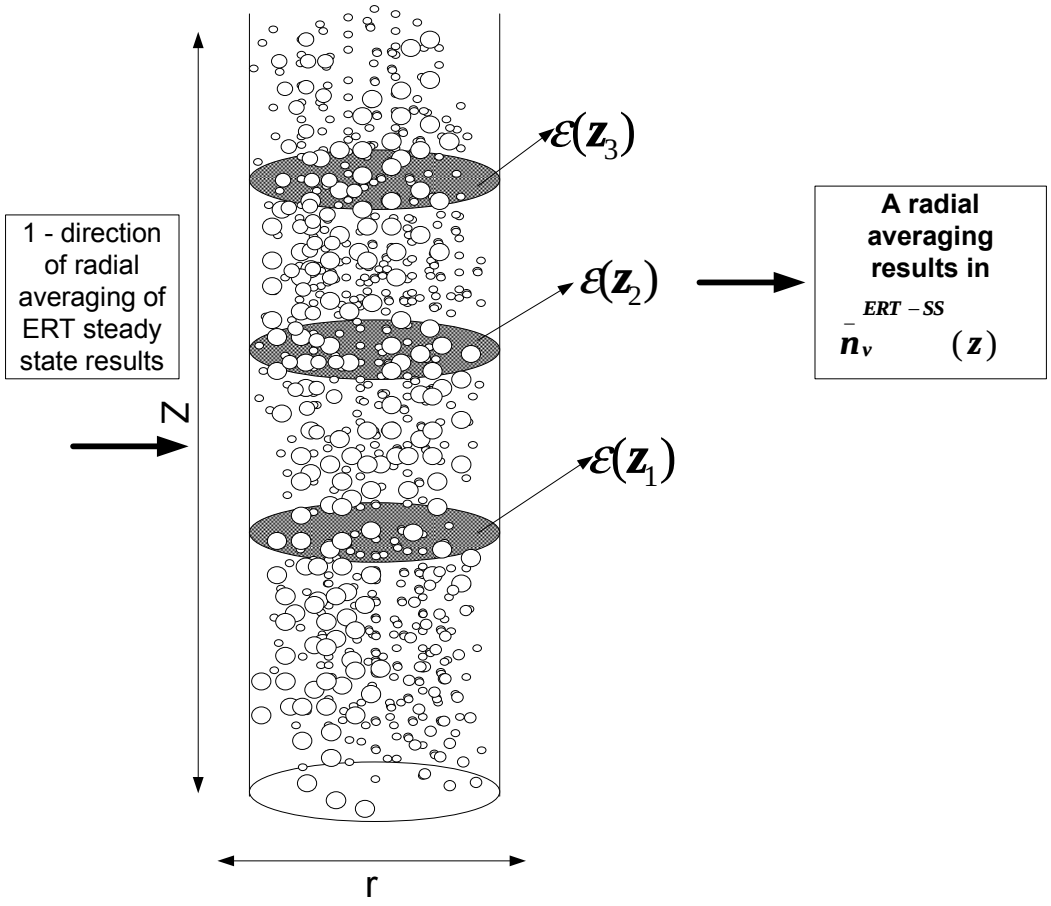

Figure 8.2. The axial distribution of static gas holdup fractions in the column determined by the ERT technique experimentally – numbered 1 in the algorithm of Figure 8.1.

From the determined $n(v,z)$ during the DGD process (denoted by $n^{ERT-DGD}(v,z)$), the $n^{ERT-DGD}(v,z)$ was averaged along the column axis as in Eq.(8.3) to obtain $\bar{n}_z^{ERT-DGD}(v)$. This is the computation labelled 2 in Figure 8.1. The $\bar{n}_z^{ERT-DGD}(v)$ can be interpreted as an axial averaging of the 2D BNDD to obtain a 1D BNDD as a function of bubble size $\bar{n}_z^{ERT-DGD}(v)$ as illustrated in the diagram of Figure 8.3.

$$\bar{n}_z^{ERT-DGD}(v) = \int_0^L n^{ERT-DGD}(v,z)dz \Big/ \int_0^L dz \tag{8.3}$$

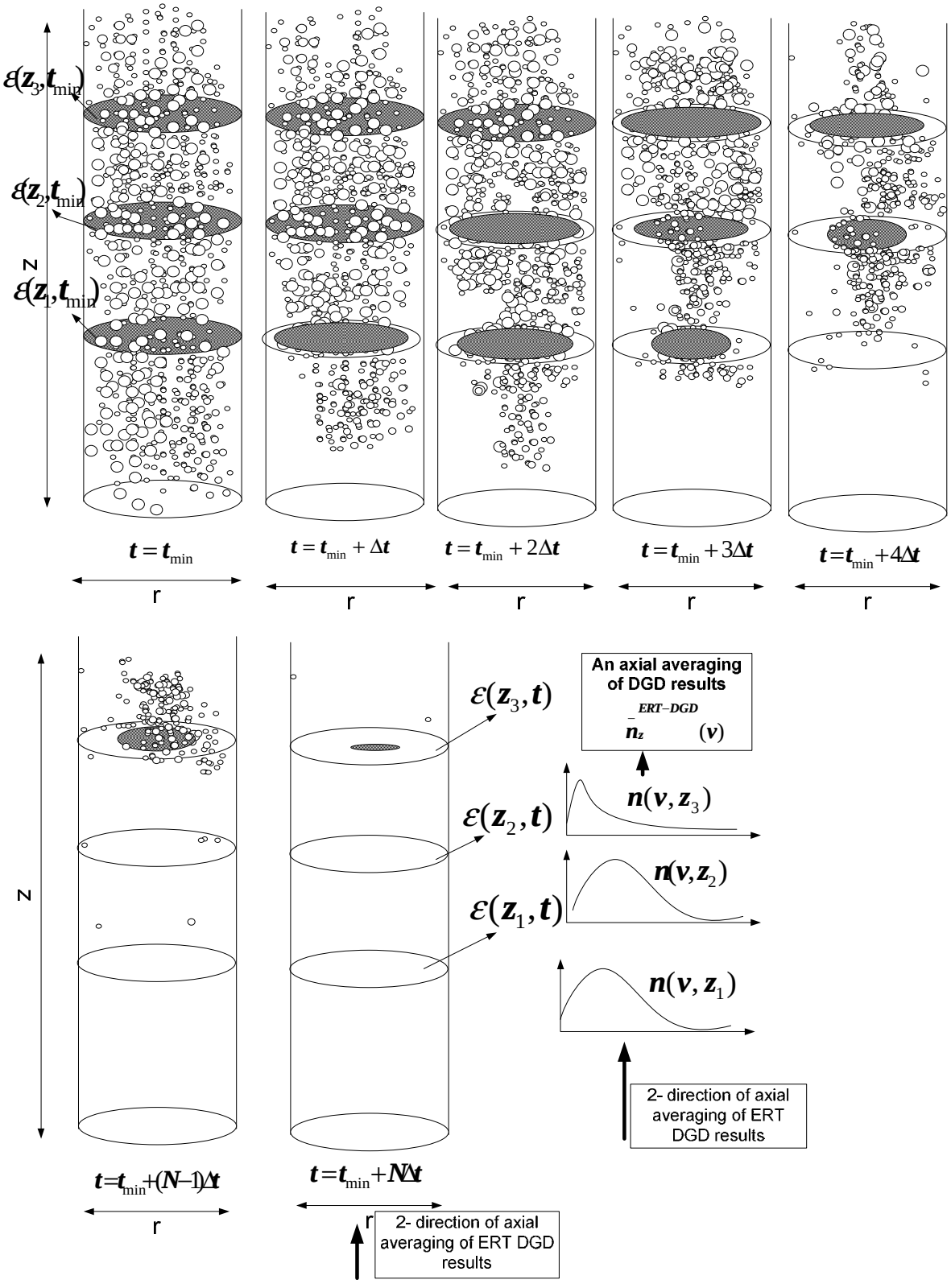

Figure 8.3. The dynamic gas holdup during the DGD process that yielded the size distribution of bubbles – numbered 2 in the algorithm of Figure 8.1.

The resolved global bubble size classes in the column through a coupling of the ERT and DGD process allowed for the determination of the minimum and maximum range of bubble sizes depending on u_g. From the known upper and lower bound of bubble size classes, the bubble population were group into 30 classes for higher size resolution. The inlet BNDD $n(v, z = 0)$, which is the PBM boundary condition was modelled using a guess log-normal distribution to assume the bubble size distribution leaving the sparger surface. The mean and standard deviation of the natural logarithm of bubble volumes will be parameterised to obtain the actual inlet BNDD.

Accordingly, a 2D steady-state PBM was solved to simulate the bubble swarm phenomenon under the influence of significant bubble coalescence and negligible breakage rates as source term models. The 2D steady-state PBM was solved since at all gas flow rates studied the bubble swarming events were visually observed to be steady with respect to time. In addition, the local gas void fractions by the ERT technique were also noticed to change insignificantly with respect to time for a given gas flow rate. The solution of the 2D steady-state PBM is the BNDD, denoted by $n^{PBM-SS}(v, z)$, which describes the bubble population of a bubble class within the range $[v, v + dv]$ at height $[z, z + dz]$.

From $n^{PBM-SS}(v, z)$, an average of the BNDD over bubble size, v, (denoted by $\bar{n}_v^{PBM-SS}(z)$) was calculated as in Eq.(8.4) based on the result of Eq.(8.1) at local sections of the column. The calculation of $\bar{n}_v^{PBM-SS}(z)$ is similar to that of $\bar{n}_v^{ERT-SS}(z)$ as illustrated in the diagram of Figure 8.4 labelled 3 in Figure 8.1. The obtained PBM solution $n^{PBM-SS}(v, z)$ was then used as the initial condition for the developed model for the process of DGD in the column.

$$\bar{n}_v^{PBM-SS}(z) = \frac{\int_{v_{min}}^{v_{max}} v n^{PBM}(v, z) dv}{\overline{v^{ERT}(z)}} \tag{8.4}$$

The solution of the DGD model process was analysed, as in Chapter 7, to compute the BNDD, denoted by $n^{M-DGD}(v, z)$. The $n^{M-DGD}(v, z)$ was subsequently averaged along the axial direction of the column as in Eq.(8.5) to obtain $\bar{n}_z^{M-DGD}(v)$. The computation of $\bar{n}_z^{M-DGD}(v)$ is similar to $\bar{n}_z^{ERT-DGD}(v)$ as illustrated in the diagram of Figure 8.4 labelled 4 in Figure 8.1.

$$\bar{n}_z^{M-DGD}(v) = \int_0^L n^{M-DGD}(v, z) dz \Big/ \int_0^L dz \tag{8.5}$$

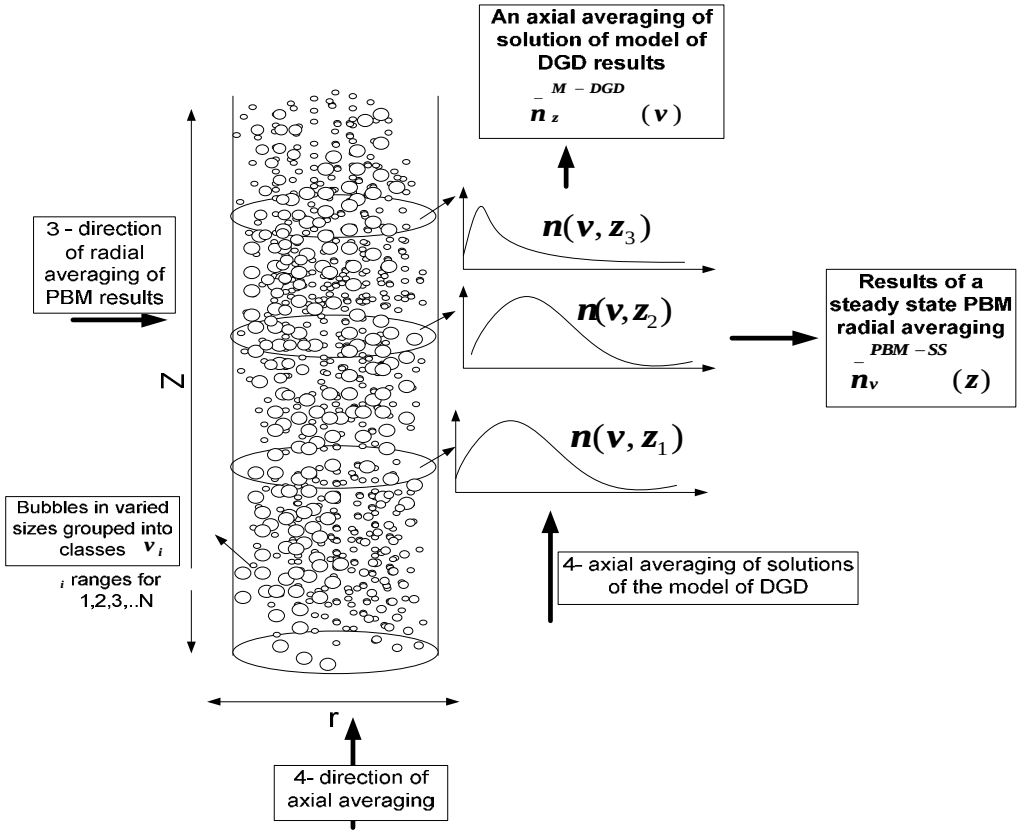

Figure 8.4. The simulation of bubble swarm phenomenon using a 2D steady-state PBM and modelling of the DGD process after gas dispersion was turned-off that yielded BNDD as a function of bubble size and space – numbered 3 and 4 respectively in the algorithm of Figure 8.1.

Accordingly, in order to resolve the actual $n(v,z)$ of the steady state bubble swarm, the inlet BNDD $n(v,z=0)$, the specific coalescence rate $q(v,v')$ and the breakage frequency $g(v,v')$ as well as the gradient of flux term $^{\partial J}/_{\partial z}$ during DGD model were parameterised. The parameterisation was intended to ensure the steady and unsteady ERT measurements agree with PBM and DGD model computations. The ERT measurements agreeing with PBM computations means Eq.(8.2) (label 1 in Figure 8.1) agrees with Eq.(8.4) (label 3 in Figure 8.1); and Eq.(8.3) (label 2 in Figure 8.1) agrees with Eq.(8.5) (label 4 in Figure 8.1).

The solution of the PBM, $n(v,z)$, on parametersing the inlet $n(v,z=0)$, the $q(v,v')$, $g(v,v')$ and $^{\partial J}/_{\partial z}$ that lead to an agreement of Eq.(8.2) and Eq.(8.3) respectively with Eq.(8.4) and Eq.(8.5) was taken as the actual BNDD ($n(v,z)$) in the column for a known u_g.

The turbulent, laminar and buoyancy collision frequencies are contributory bubble collision properties to the specific coalescence rate as described in Chapter 6. The breakage

frequency is a function of the energy dissipation rate due to turbulent eddies and a bubble size. In estimating the bubble breakage frequency, the energy dissipation rate was assumed to be $2m^2s^{-3}$ at the u_g of 0.016 m/s (Martinez, et al., 2010).

The stated constant values of Table 8.2 were parameters for physical quantities to obtain the actual solution $n(v,z)$ of Figure 8.5 for the case of the gas flow rate at 0.016 m/s meeting the required conditions. The parameterization of the bubble breakage frequency was made to indicate the phenomenon of bubble breakage was negligible during bubble swarming at the u_g of 0.016 m/s. The parameters for the quantities were adjusted until the best fits of Figure 8.7 and Figure 8.8 were obtained. The statistical errors associated with the fits and the accuracy of the determined $n(v,z)$ is evaluated in Section 8.2. The required consistency of the model with the conditions of steady and unsteady state ERT estimates of gas void fractions are described in the following paragraphs.

Table 8.2. Parameters for physical quantities to determine the BNDD by the hybrid of ERT and a PBM method at superficial gas velocity of 0.016 m/s

Lb (m^3)	Ub (m^3)	Avg. of bs(unit)	Std. of bs(unit)	BCF (unit)	TCF (unit)	LCF (unit)	BBF (unit)	W_o (unit)
3.00×10^{-8}	25.85×10^{-6}	1.03 ± 10^{-3}	0.15 ± 10^{-3}	1	3	1	1.00×10^{-9}	0.80 ± 10^{-3}

Keys: Lb – Lower bound of bubble sizes (bs), Ub – Upper bound of bs, TCF – turbulent coalescence frequency, LCF – laminar coalescence frequency, BCF – buoyancy coalescence frequency, Avg.- Mean of logarithm of bs, Std. – Standard deviation of logarithm of bs, BBF- Bubble breakage frequency, W_o - scaling factor for the flux gradient at elemental column section volume during DGD.

In the computations labelled 4 in Figure 8.1, the result of Figure 8.5 was used as an initial condition for the model of the DGD process to obtain the solution of the DGD process of Figure 8.6. The solution of the DGD model was the graph of time-variant disengaging gas volume locally in the column. The disengaged gas volumes at characteristic disengagement times of bubble size classes were analysed from the solution of the DGD model similar to the measured time-variant disengaging gas volume of Chapter 5. The obtained results are presented in Table 8.3.

The local and the global BNDD were obtained by the ratio of the characteristic disengaged gas volume to the disengaged mean bubble volume at the characteristic time by the scheme of Figure 5.14. Following this scheme, the local BNDD on Table 8.4 were obtained at $u_g = 0.016$ m/s. The axially averaged BNDD was calculated from the results in column 1 to 4 of Table 8.4 to obtain the result of column 5 of Table 8.4 using Eq.(8.5). The results of the axially averaged BNDD determined from ERT images captured during DGD, Eq.(8.3), are displayed in column 8 of Table 8.4.

The two graphs of axially averaged BNDD by a model of DGD and by experimental measurement during DGD against the logarithm of axially averaged bubble volume are shown in Figure 8.7. In this figure, the legends 'Model DGD data (PBM data)' and Expt. DGD data' denote the averaged of modelled and measured BNDD against the volume of $\bar{d}_{32,j}^{Model}$ and $\bar{d}_{32,j}^{ERT}$ respectively. These are the computations labelled 4 and 2 in Figure 8.1 (i.e. Eq.(8.5) and Eq.(8.3)).

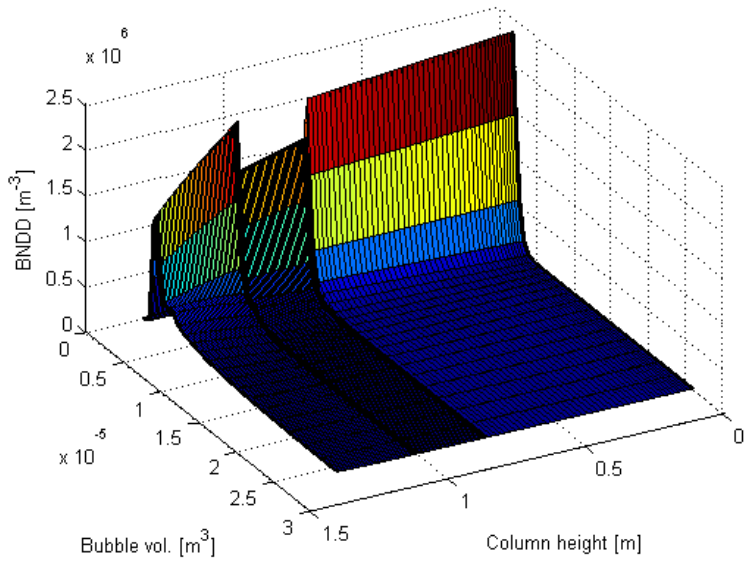

Figure 8.5. A solution of PBM yielding the BNDD depending on bubble volume and column height satisfying the static and dynamic holdup conditions at the superficial gas velocity of 0.016 m/s.

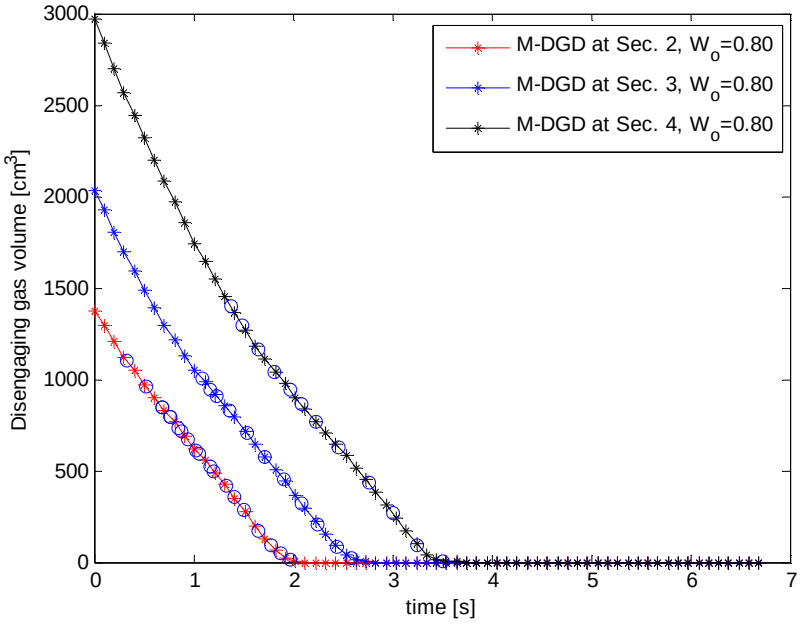

Figure 8.6. The solution of the DGD process model showing the time-variant disengaging gas volume locally at the superficial gas velocity of 0.016 m/s. The characteristic times of disengagement of bubble size classes are indicated by the circle symbols on the graphs.

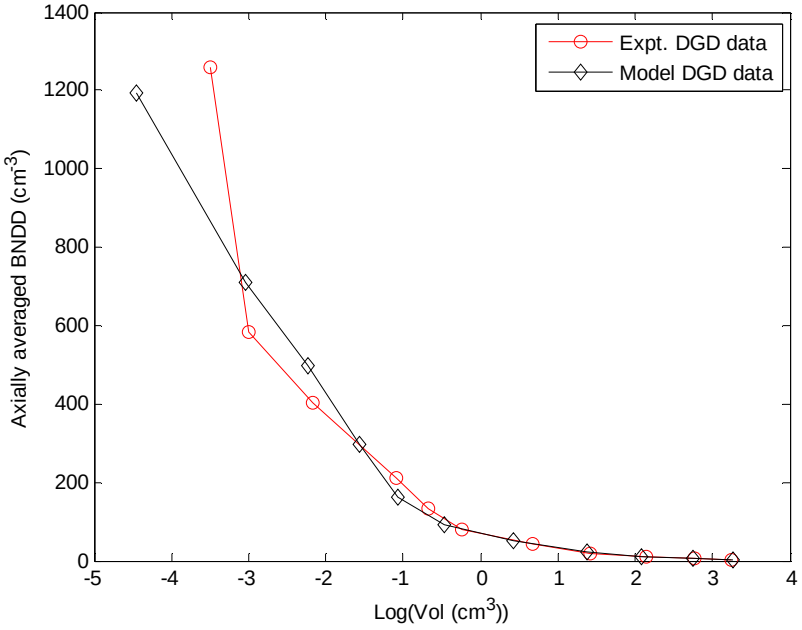

Figure 8.7. Axially averaged BNDD depending on the logarithm of bubble volume during DGD process by the ERT measurement and a model of DGD process at the superficial gas velocity of 0.016 m/s.

Table 8.3. The disengaged gas volumes locally from the solution of DGD process model at local characteristic times of disengagement of bubble size classes.

Sec. 1 (cm^3)	Sec. 2 (cm^3)	Sec. 3 (cm^3)	Sec. 4 (cm^3)	
	56.22	58.29	111.05	
140.82	80.91	39.69	125.90	
	99.74	73.27	122.16	
	93.19	126.28	100.52	
110.35	108.00	127.48	81.34	
53.05	129.41	128.91	90.76	
61.20	109.12	126.05	141.91	
64.61	79.38	114.74	196.24	
74.53	50.73	123.90	163.43	
97.68	32.00	60.27	172.78	
140.04			85.86	

Table 8.4. The local BNDD and axially averaged BNDD as well as the axially averaged SMBD depending on bubble size class obtained from the solution of DGD process model and ERT measurement at the superficial gas velocity of 0.016 m/s.
Key: n^{M-DGD}, G and S mean $n^{Model-DGD}$, Global and Column section respectively

n^{M-DGD} (v,z) (cm^{-3})	n^{M-DGD} (v,z) (cm^{-3})	n^{M-DGD} (v,z) (cm^{-3})	n^{M-DGD} (v,z) (cm^{-3})	$\overline{n^{M-DGD(v)}}$ (cm^{-3})	$\bar{d}_{32,j}^{Model}$ (cm)	$\bar{d}_{32,j}^{ERT}$ (cm)	$\bar{n}^{ERT-DGD}$ (v) (cm^{-3})
S1	S2	S3	S4	G			
	1.9	3.2	3.6	2.9	3.67	3.67	2.6
8.9	5.6	3.5	6.7	6.4	3.10	3.12	4.1
	16.3	8.9	11.5	11.8	2.49	2.53	9.3
	37.7	26.3	17.0	24.2	1.96	1.99	20.1
105.4	95.8	56.1	22.4	52.8	1.43	1.55	42.8
236.8	253.1	112.4	35.2	90.2	1.06	1.14	77.9
553.9	447.9	209.9	81.9	163.1	0.86	0.99	134.2
1100.3	572.8	317.6	203.1	298.4	0.73	0.86	210.0
2406.2	560.9	547.9	339.0	497.3	0.59	0.60	403.4
5973.9	492.7	433.6	595.3	710.5	0.45	0.46	584.5
18938.4			472.4	1194.3	0.28	0.39	1259.7

From the local gas holdup fractions at steady state by the ERT technique and the solution of the 2D steady-state PBM of Figure 8.5, the BNDDs averaged over bubble sizes were calculated using Eq.(8.2) and Eq.(8.4). The results of the $\bar{n}^{PBM-SS}(z)$ and $\bar{n}^{ERT-SS}(z)$ are shown in Figure 8.8.

The results shown in Figure 8.8 were obtained from the procedure shown in Figure 8.1. The step labelled 1 in Figure 8.1 yielded the results represented by the legend " ERT & DP data at steady state" in Figure 8.8. Likewise, the step labelled 3 in Figure 8.1 yielded the result with the legend "steady state PBM data" in Figure 8.8. The results of Figure 8.8 indicate the

determined BNDD ($n(v,z)$) by the hybrid prediction is valid with respect to the axial distribution of gas holdup fraction measured by ERT data calibration against DP data. The accuracy of the result is quantified in the next section.

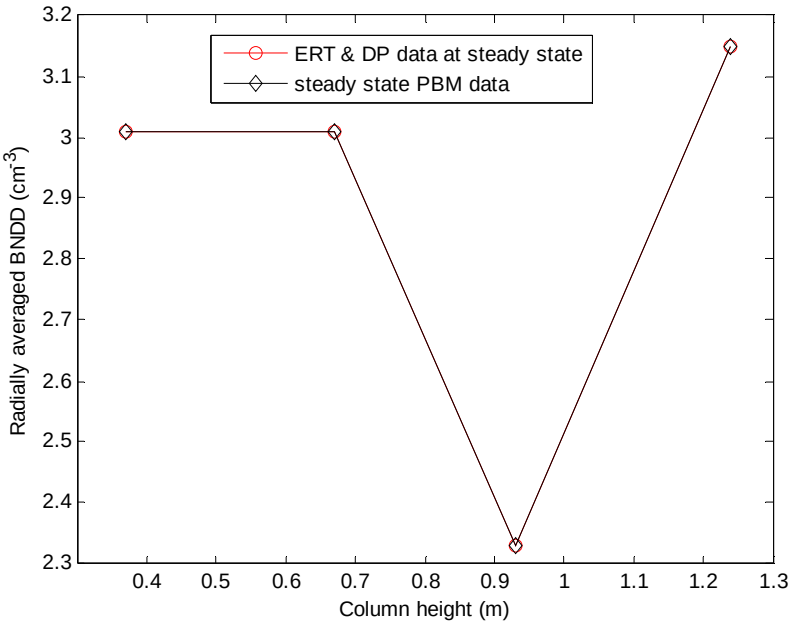

Figure 8.8. BNDD averaged over bubble size (volume) against column height during bubble population swarming at steady state by the ERT measurement and the PBM at the superficial gas velocity of 0.016 m/s.

8.2. Validation of the hybrid predicted BNDD and statistical error analysis

In Figure 8.7, the $\bar{n}^{ERT-DGD}(v)$ using Eq.(8.3) and $\bar{n}^{M-DGD}(v)$ using Eq.(8.5) are plotted. The mean diameters of bubble sizes from the BNDDs by the ERT data measurements and the DGD process model shown in Figure 8.7 are 0.56 cm and 0.52 cm respectively.

The errors between $\bar{n}^{ERT-SS}(z)$ and $\bar{n}^{PBM-SS}(z)$ as well as between $\bar{n}^{ERT-DGD}(v)$ and $\bar{n}^{M-DGD}(v)$ were evaluated by the linear least square regression defined in Chapter 4. The obtained Chi-square (X^2), R-square (R^2)) and f-statistic of the error analysis are stated in Table 8.5.

Table 8.5. The statistical error analysis of the compared ERT steady and dynamic data with PBM and model of DGD process for superficial gas velocity of 0.016 m/s

Statistical error analysis	X^2	R^2	f-statistic	f-critical (alpha level of 5%)
$\bar{n}^{ERT-SS}(z)$ and $\bar{n}^{PBM-SS}(z)$	2.3×10^{-4}	1	13160.00	19.00
$\bar{n}^{ERT-DGD}(v)$ and $\bar{n}^{M-DGD}(v)$	0.26	0.97	170.70	5.12

The least square regression method allows evaluating the extent to which the model results captured the experimental results. The closeness of the R^2 to unity, the larger the f-statistic above the critical value and the lower the X^2 suggest the model results significantly captured the experimental results.

The percentage of the difference of the mean diameters by the experimental and model approaches to the experimental approach is used to estimate the uncertainty (error) of the determined $n(v,z)$. Thus, the uncertainty of the determined $n(v,z)$ at the superficial gas velocity of 0.016 m/s being valid with respect to the ERT dynamic gas holdup during DGD was estimated to be 8.5%. This means the certainty that the determined $n(v,z)$ is valid with respect to dynamic gas holdup captured by ERT technique during DGD process was 91.5%.

The average of the $\bar{n}^{ERT-SS}(z)$ and the $\bar{n}^{PBM-SS}(z)$ of Figure 8.8 in the axial direction of the column were 2.88 (cm^{-3}) and 2.88 (cm^{-3}) respectively. The error in the difference of the two graphs measured by the ratio of the difference of the average of $\bar{n}^{ERT-SS}(z)$ and $\bar{n}^{PBM-SS}(z)$ to the average of $\bar{n}^{ERT-SS}(z)$ along the column height was 0.0%. Thus, the certainty (accuracy) that the determined $n(v,z)$ of Figure 8.5 is valid with respect to the axial distribution of gas holdup measured by ERT technique at steady state was 100.0%.

The value of the uncertainty is related to the use of a tubular sparger and one DP transmitter available for this study that was moved along the column axis for local gas void fraction measurements. The use of a DP transmitter at every column section will address the observed error of the resolved $n(v,z)$ being valid with respect to the ERT measurements.

8.3. Effects of superficial gas velocity on the computed BNDD based on the hybridization of ERT measurements and a PBM

The aims of this section are as follows: 1) evaluate the validity of developed method of hybridizing the ERT measurements and the PBM through a determination of the $n(v,z)$ at lower superficial gas velocities; 2) observe the effects of superficial gas velocity on the determined $n(v,z)$ by the ERT and the PBM hybrid model.

The hybrid predicted $n(v,z)$ for the case of $u_g = 0.016\, m/s$ allowed for estimating the bubble coalescence rate, breakage rate and the inlet BNDD $n(v,z=0)$ as reported in Section 8.1. Similarly, the $n(v,z)$ of the bubble swarming phenomenon given u_g values lower than 0.016 m/s (i.e. 0.005 – 0.01 m/s) were sought by implementing the algorithm of Figure 8.1.

The gas dispersion into the column at $u_g = 0.016\, m/s$ to set-up a semi-batch flow regime at steady state was reduced to 0.01 m/s. Subsequently, the ERT measurements of step 1 and step 2 of Figure 8.1 were made. In the computations of step 3 and 4 of Figure 8.1, the turbulent frequency, the mean and standard deviation of the logarithm of bubble volume classes as well as the flux gradients within elemental volume section were parameterised.

The constants used to multiply quantities were varied over a known range to obtain the mean values of Table 8.6 in order to resolve the $n(v,z)$. Following such parameterisation, the $n(v,z)$ of Figure 8.9 was determined based on the extent of agreement of $\bar{n}^{ERT-SS}(z)$ and $\bar{n}^{PBM-SS}(z)$ of Figure 8.11 as well as $\bar{n}^{ERT-DGD}(v)$ and $\bar{n}^{M-DGD}(v)$ of Figure 8.10. The

statistical error analysis between the average BNDD by ERT technique radially and axially in comparison to that by the PBM and model of DGD process respectively are stated in Table 8.7.

Table 8.6. Parameters for physical quantities to determine the BNDD by the hybrid of ERT and a PBM method at varied superficial gas velocities

U_g m/s	Lb (m^3)	Ub (m^3)	Avg. of bs(unit)	Std. of bs(unit)	BCF (unit)	TCF (unit)	LCF (unit)	BBF (unit)	W_o (unit)
0.01	3.00×10^{-8}	7.47×10^{-6}	1.05 ± 10^{-3}	0.13 ± 10^{-3}	1	3 ± 10^{-3}	1	1.00×10^{-9}	0.80 ± 10^{-3}
0.009	5.44×10^{-9}	5.19×10^{-6}	1.03 ± 10^{-3}	0.13 ± 10^{-3}	1	3 ± 10^{-3}	1	1.00×10^{-9}	0.80 ± 10^{-3}
0.008	2.18×10^{-9}	2.09×10^{-6}	1.05 ± 10^{-3}	0.15 ± 10^{-3}	1	1.8 ± 10^{-3}	1	1.00×10^{-9}	0.80 ± 10^{-3}
0.007	7.25×10^{-9}	2.54×10^{-6}	1.03 ± 10^{-3}	0.15 ± 10^{-3}	1	1.8 ± 10^{-3}	1	1.00×10^{-9}	0.80 ± 10^{-3}
0.006	2.50×10^{-10}	1.48×10^{-6}	1.00 ± 10^{-3}	0.12 ± 10^{-3}	1	1.0 ± 10^{-3}	1	1.00×10^{-9}	1.00 ± 10^{-3}
0.005	2.10×10^{-9}	1.32×10^{-6}	1.00 ± 10^{-3}	1.11 ± 10^{-3}	1	1.0 ± 10^{-3}	1	1.00×10^{-9}	1.00 ± 10^{-3}

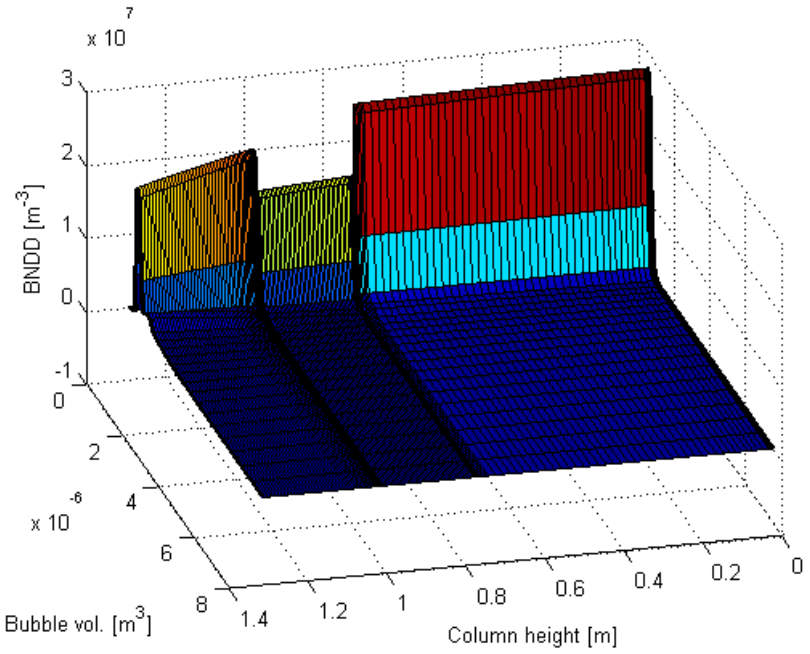

Figure 8.9. Solution of PBM yielding the BNDD depending on bubble volume and column height satisfying the static and dynamic holdup conditions at the superficial gas velocity of 0.01 m/s.

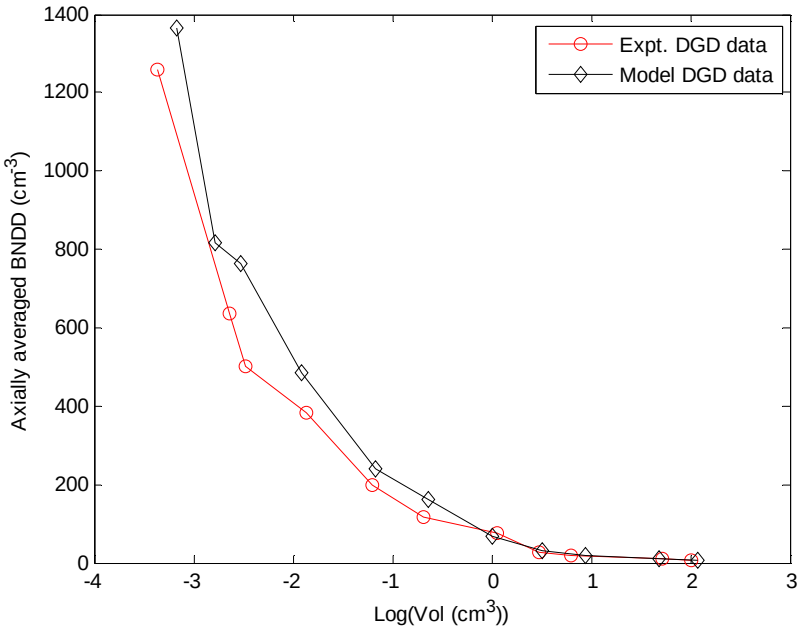

Figure 8.10. Axially averaged BNDD depending on logarithm of bubble volume during DGD process by the ERT measurement and a model of DGD process at the superficial gas velocity of 0.01 m/s.

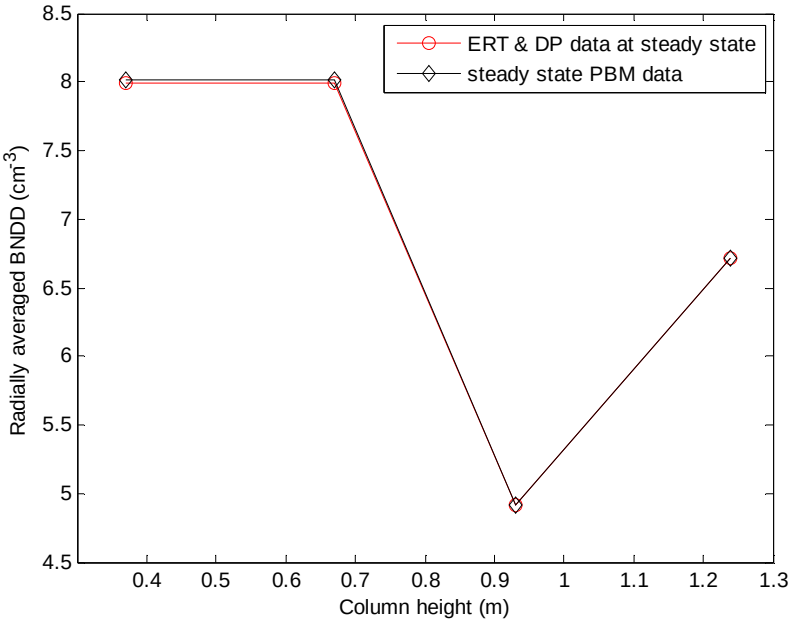

Figure 8.11. BNDD averaged over bubble size (volume) against column height during bubble population swarming at steady state by the ERT measurement and the PBM at superficial gas velocity of 0.01 m/s.

Table 8.7. The statistical error analysis of the compared BNDD from ERT steady and dynamic data with that by PBM and model of DGD process at varied superficial gas velocities

U_g (m/s)	Statistical error analysis	X^2	R^2	f-statistic	f-critical (α evel of 5%)
0.01	$\bar{n}^{ERT-SS}(z)$ and $\bar{n}^{PBM-SS}(z)$	2.7×10^{-4}	1	12611.13	19.00
	$\bar{n}^{ERT-DGD}(v)$ and $\bar{n}^{M-DGD}(v)$	0.85	0.92	48.66	5.12
0.009	$\bar{n}^{ERT-SS}(z)$ and $\bar{n}^{PBM-SS}(z)$	2.6×10^{-4}	1	11399.8	19.00
	$\bar{n}^{ERT-DGD}(v)$ and $\bar{n}^{M-DGD}(v)$	0.29	0.97	199.49	5.32
0.008	$\bar{n}^{ERT-SS}(z)$ and $\bar{n}^{PBM-SS}(z)$	4.0×10^{-4}	1	28389.97	19.00
	$\bar{n}^{ERT-DGD}(v)$ and $\bar{n}^{M-DGD}(v)$	0.30	0.97	117.30	5.32
0.007	$\bar{n}^{ERT-SS}(z)$ and $\bar{n}^{PBM-SS}(z)$	8.5×10^{-5}	1	35375.50	19.00
	$\bar{n}^{ERT-DGD}(v)$ and $\bar{n}^{M-DGD}(v)$	0.32	0.96	84.85	5.59
0.006	$\bar{n}^{ERT-SS}(z)$ and $\bar{n}^{PBM-SS}(z)$	1.72×10^{-4}	1	17443.35	19.00
	$\bar{n}^{ERT-DGD}(v)$ and $\bar{n}^{M-DGD}(v)$	0.58	0.92	33.42	5.99
0.005	$\bar{n}^{ERT-SS}(z)$ and $\bar{n}^{PBM-SS}(z)$	1.08×10^{-3}	1	6948.67	19.00
	$\bar{n}^{ERT-DGD}(v)$ and $\bar{n}^{M-DGD}(v)$	0.21	0.97	82.48	6.61

Table 8.8. The mass transfer rates and the time-variant bubble class density resulting pressure variation leading to bubble expansion during DGD processes for varied superficial gas velocities

u_g (m/s)	ε_g(unit) at Section 1 & 2	$\dot{n}\gamma_g a_p$ $kg/(m^3 s)$	Δt_o (s)	$\Delta\rho_g$ $kg/(m^3 s)$	Inlet mean bubble volume (m^3)
0.016	2.70	2.40×10^{-4}	$1 \times 10^{-4} s$	8.74×10^{-5}	$9.864e-7$
0.010	2.20	1.90×10^{-4}	$1 \times 10^{-4} s$	8.74×10^{-5}	$2.715e-7$
0.009	2.02	1.73×10^{-4}	$1 \times 10^{-4} s$	4.74×10^{-5}	$1.844e-7$
0.008	1.91	1.63×10^{-4}	$1 \times 10^{-4} s$	4.74×10^{-5}	$5.330e-8$
0.007	1.75	1.48×10^{-4}	$1 \times 10^{-4} s$	4.74×10^{-5}	$1.090e-7$
0.006	1.49	1.25×10^{-4}	$0.5 \times 10^{-4} s$	2.74×10^{-5}	$6.070e-8$
0.005	1.30	1.08×10^{-4}	$0.5 \times 10^{-4} s$	2.74×10^{-5}	$7.280e-8$

The gas-liquid mass transfer rates and the time-variant bubble class density due to axial pressure variation resulted in bubble expansion during DGD process. The explained method of calculating the $\dot{n}\gamma_g a_p$ in Section 7.2 of Chapter 7 was used to obtain the $\dot{n}\gamma_g a_p$ for varied u_g as shown in Table 8.8. The $\dot{n}\gamma_g a_p$ values were calculated based on ε_g at Section 1 and 2 because the DGD process starts from the column base.

Since the mass transfer rate decreases with a decrease in u_g, the time-variant bubble class density was also assumed to decrease with a decrease in u_g. Thus, the assumed elemental time step was scaled by half at u_g values of 0.006 and 0.005 m/s. The assumption is expected to be valid since the gas-liquid interfacial area contributing to axial pressure variation decrease with a decrease in u_g.

On reduction of the gas dispersion to achieve a $u_g = 0.009\, m/s$, the BNDD $n(v, z)$ of the bubble evolution was resolved following the scheme of Figure 8.1. The gas dispersion at the

volumetric flow rate of 20lpm produced $u_g = 0.005\, m/s$ in the column. This was the minimum $u_g$value studied since the global gas void fraction was 0.0154. At u_g lower than 0.005 m/s, the accuracy of the measured static and dynamic gas void fractions were low.

For each of the lower superficial gas velocities (i.e. 0.008, 0.007, 0.006 and 0.005 m/s), the ERT measurements were captured during bubble swarm at steady state and in the process of DGD to compute $\bar{n}^{ERT-SS}(z)$ and $\bar{n}^{ERT-DGD}(v)$. Similar approach of developing the boundary condition for the PBM at higher u_g values (i.e. 0.0016 and 0.001 m/s) was repeated for lower flow u_g values.

Table 8.6 highlights the parameter values used in adjusting the inlet bubble size distribution, the turbulent, laminar, buoyancy driven collision rate and the breakage frequency. The parameters in Table 8.6 were adjusted to ensure the determined $n(v,z)$ for a given u_g is valid with respect to the ERT measurements at steady state and during DGD (labelled 1 and 2 in Figure 8.1). Additionally, Table 8.6 displays the parameter values used to scale the gradient of flux within an elemental column section during DGD processes. The scaling was necessary owing to the bubble expansion and fluctuating axial transport of bubbles along the column axis during DGD processes.

The steady state $\bar{n}^{ERT-SS}(z)$ and $\bar{n}^{ERT-DGD}(v)$ were calculated from the experimental ERT static and transient gas void fraction at $u_g = 0.009\, m/s$. The graphs of the $\bar{n}^{ERT-SS}(z)$ and $\bar{n}^{ERT-DGD}(v)$ are shown respectively in Figure 8.12 with the legend 'ERT & DP data at steady state' and Figure 8.14 with the legend 'ERT DGD Data'. The BNDD $n(v,z)$ of Figure 8.13 was the steady-state PBM solution based on the stated parameter of Table 8.6 satisfying the required steady and transient conditions. The function $\bar{n}^{PBM-SS}(z)$ was calculated from the PBM solution and the function $\bar{n}^{M-DGD}(v)$ was calculated from the model of DGD process in line with schemes of Figure 5.14 and Figure 8.1.

The graph of $\bar{n}^{PBM-SS}(z)$ is shown in Figure 8.12 with the legend 'Steady state PBM data', while the graph of $\bar{n}^{M-DGD}(v)$ is shown in Figure 8.14 with the legend 'Model DGD Data'. The statistical error between $\bar{n}^{ERT-SS}(z)$ and $\bar{n}^{PBM-SS}(z)$ as well as between $\bar{n}^{ERT-DGD}(v)$ and $\bar{n}^{M-DGD}(v)$ are stated in Table 8.7 at $u_g = 0.009\, m/s$.

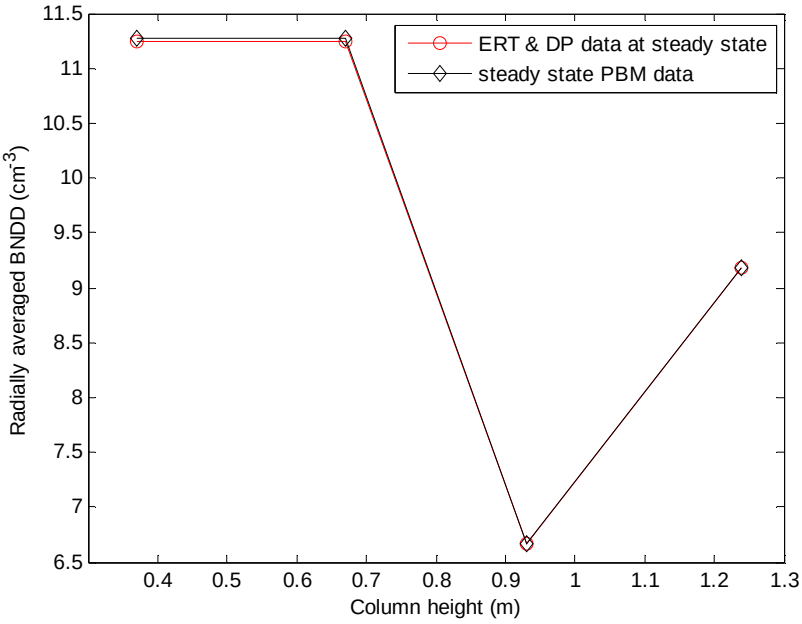

Figure 8.12. BNDD averaged over bubble size (volume) against column height during bubble population swarming at steady state by the ERT measurement and the PBM at superficial gas velocity of 0.009 m/s.

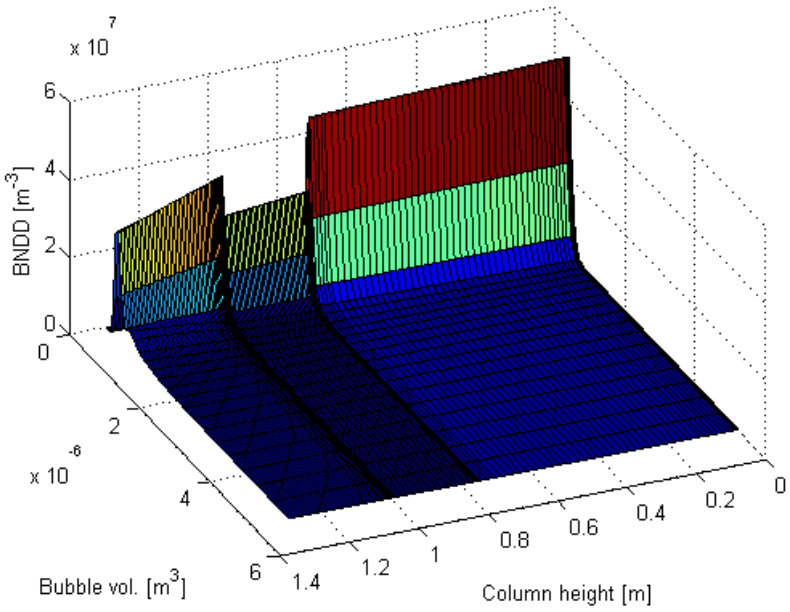

Figure 8.13. The solution of PBM yielding the BNDD depending on bubble volume and column height satisfying the static and dynamic holdup conditions at the superficial gas velocity of 0.009 m/s.

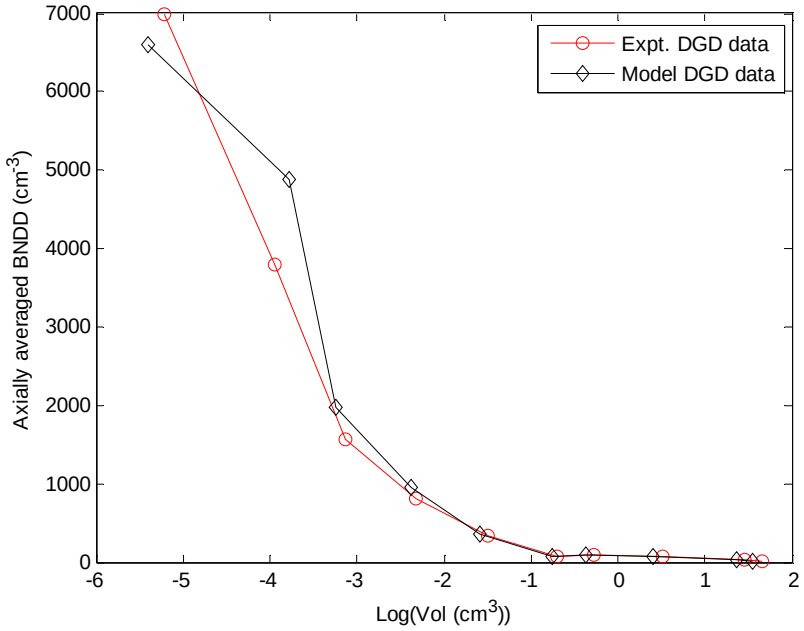

Figure 8.14. Axially averaged BNDD depending on the logarithm of bubble volume during DGD process by the ERT measurement and a model of DGD process at the superficial gas velocity of 0.009 m/s.

Similar experimental static and transient ERT measurements as in $u_g = 0.009\, m/s$ were made at $u_g = 0.008\, m/s$ to obtain the $\bar{n}^{ERT-SS}(z)$ and $\bar{n}^{ERT-DGD}(v)$ of Figure 8.15(a and c) respectively. The graph of $\bar{n}^{ERT-SS}(z)$ is represented with the legend 'ERT & DP Data at steady state' while the graph of $\bar{n}^{ERT-DGD}(v)$ with the legend 'Expt. DGD data'. Figure 8.15b shows the PBM solution at $u_g = 0.008\, m/s$ satisfying the static and transient conditions by the parameters on Table 8.6 and the statistical error analysis of Table 8.7. The computed $\bar{n}^{PBM-SS}(z)$ and $\bar{n}^{M-DGD}(v)$ from the PBM solution are shown in Figure 8.15(a and c) with the legends 'steady state PBM data' and 'Model DGD data'.

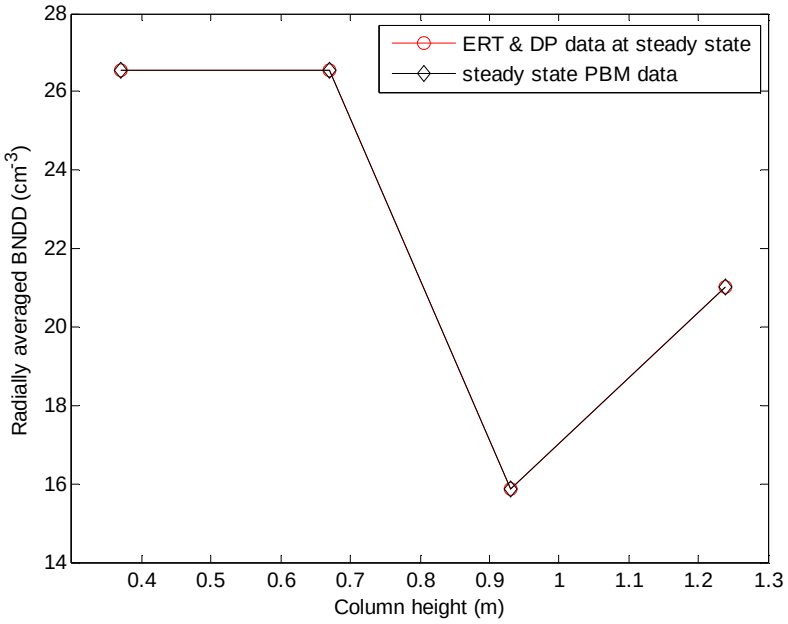
ERT & DP data at steady state
steady state PBM data
Radially averaged BNDD (cm-3)
Column height (m)
28
26
24
22
20
18
16
14
0.4
0.5
0.6
0.7
0.8
0.9
1
1.1
1.2
1.3

(a)

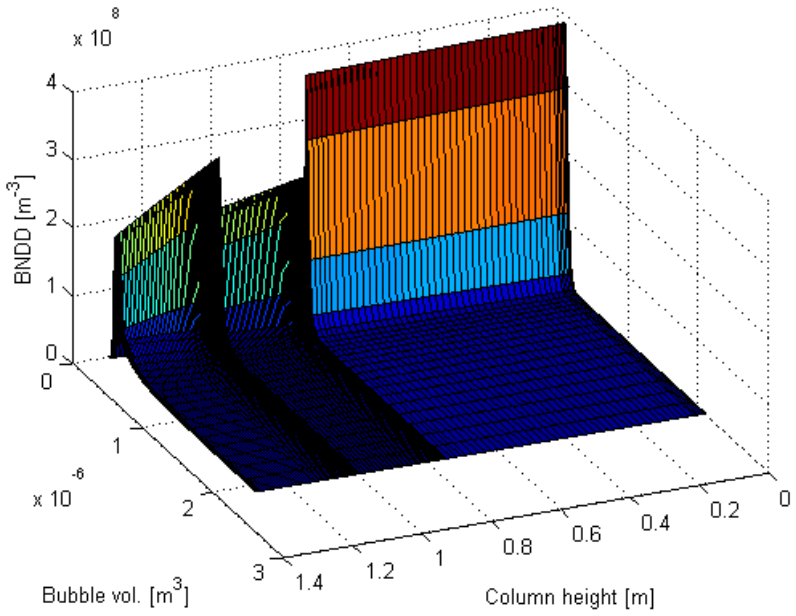
x 10^8
BNDD [m-3]
x 10^-6
Bubble vol. [m3]
Column height [m]
4
3
2
1
0
0
1
2
3
1.4
1.2
1
0.8
0.6
0.4
0.2
0

(b)

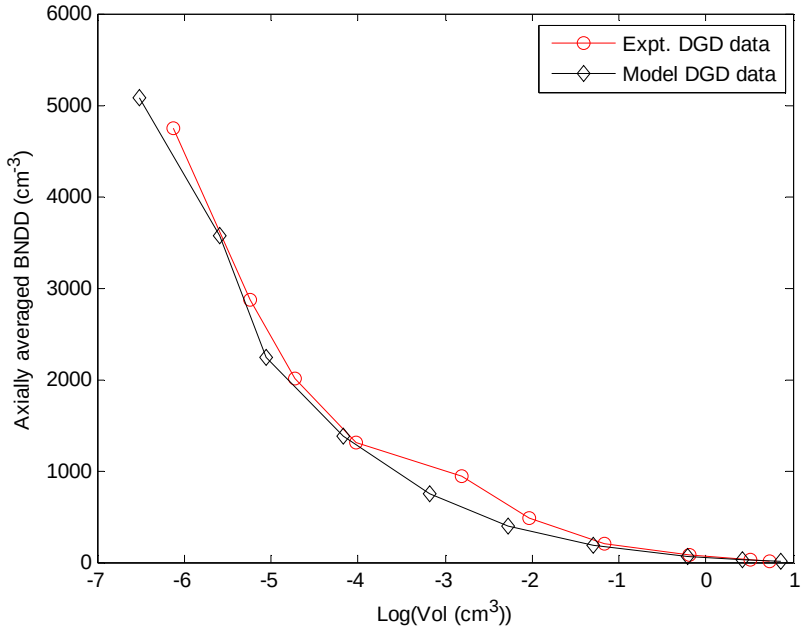

(c)

Figure 8.15. BNDD graphs at superficial gas velocity of 0.008 m/s (a) BNDD averaged over bubble size (volume) against column height by the ERT measurement and the PBM (b) Solution of PBM yielding the BNDD depending on bubble volume and column height satisfying the static and dynamic holdup conditions, (c) Axially averaged BNDD depending on the logarithm of bubble volume during DGD process by the ERT measurement and a model of DGD process.

At superficial gas velocity of 0.007 m/s, the resolved PBM solution based on the extent of agreement of $\bar{n}^{ERT-SS}(z)$ and $\bar{n}^{PBM-SS}(z)$ as well as $\bar{n}^{ERT-DGD}(v)$ and $\bar{n}^{M-DGD}(v)$ are shown in Figure 8.16a. The graphs of $\bar{n}^{ERT-SS}(z)$ and $\bar{n}^{PBM-SS}(z)$ are shown in Figure 8.16b by the similar legend representations at higher u_g values. In addition, the graphs of $\bar{n}^{ERT-DGD}(v)$ and $\bar{n}^{M-DGD}(v)$ at $u_g = 0.007\, m/s$ are displayed in Figure 8.16c. The parameters for the inlet BNDD, coalescence, breakage rates and flux gradient during DGD process are stated in Table 8.6. The statistical error analysis of the radially and axially averaged experimental measured BNDD to that by modelling are reported Table 8.7.

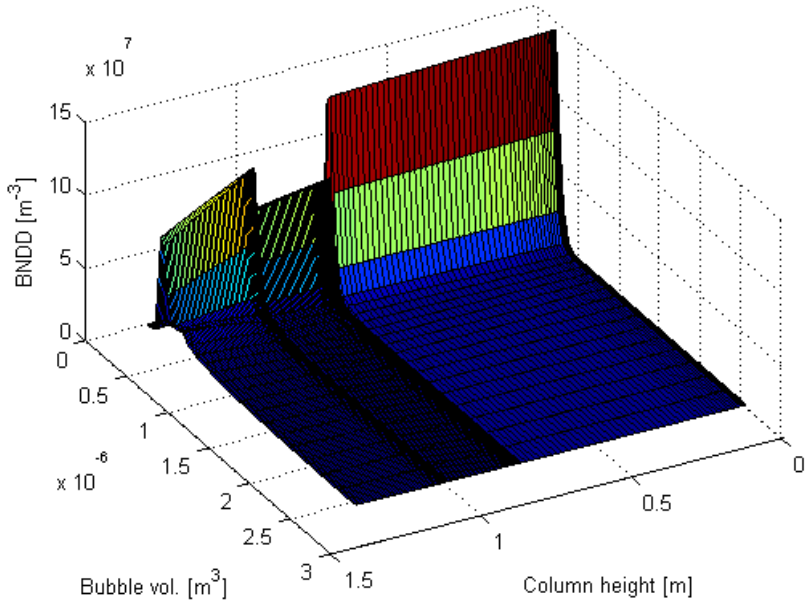
x 10^7
15
10
5
0
BNDD [m^-3]
0
0.5
1
1.5
2
2.5
3
x 10^-6
Bubble vol. [m^3]
0
0.5
1
1.5
Column height [m]

(a)

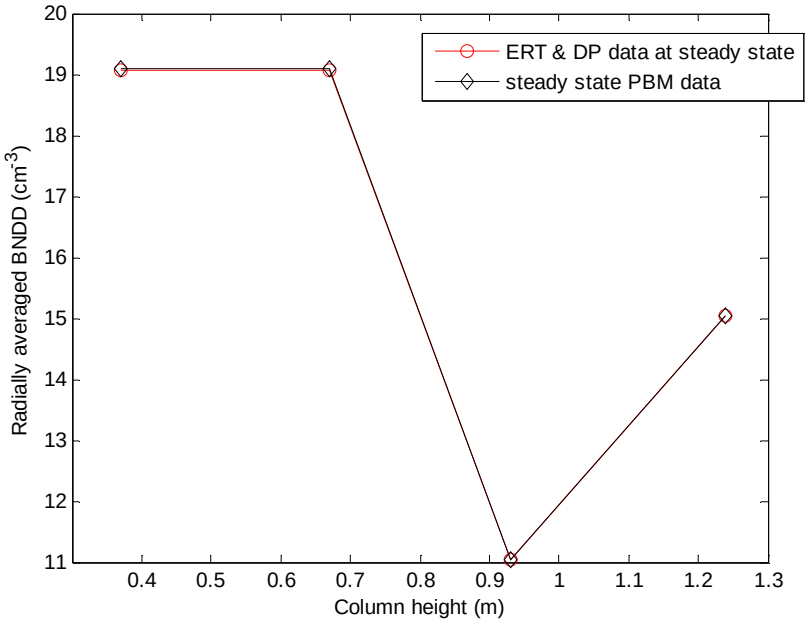
ERT & DP data at steady state
steady state PBM data
Radially averaged BNDD (cm^-3)
20
19
18
17
16
15
14
13
12
11
0.4
0.5
0.6
0.7
0.8
0.9
1
1.1
1.2
1.3
Column height (m)

(b)

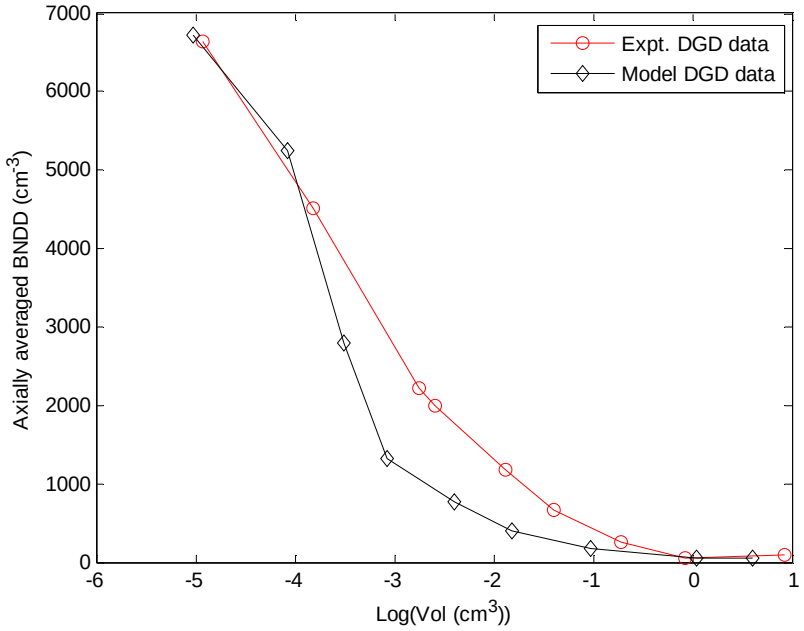

(c)

Figure 8.16. BNDD graphs at the superficial gas velocity of 0.007 m/s (a) Solution of PBM yielding the BNDD depending on bubble volume and column height satisfying the static and dynamic holdup conditions, (b) BNDD averaged over bubble size (volume) against column height by the ERT measurement and the PBM (c) Axially averaged BNDD depending on logarithm of bubble volume during DGD process by the ERT measurement and a model of DGD process.

Similarly, at $u_g = 0.006\, m/s$, the resolve PBM solution producing the functions $\bar{n}^{ERT-SS}(z)$ and $\bar{n}^{ERT-DGD}(v)$ agreeing with the functions $\bar{n}^{PBM-SS}(z)$ and $\bar{n}^{M-DGD}(v)$ respectively are shown in Figure 8.17a. The graphs of $\bar{n}^{ERT-SS}(z)$ and $\bar{n}^{PBM-SS}(z)$ as well as $\bar{n}^{ERT-DGD}(v)$ and $\bar{n}^{M-DGD}(v)$ are shown in Figure 8.17(b and c) respectively. The legend representations are consistent with the used legends at higher u_g values. Moreover, the parameters for the inlet BNDD, coalescence rate, breakage rate and the flux gradient during DGD process are stated in Table 8.6 yielding the statistical error results in Table 8.7.

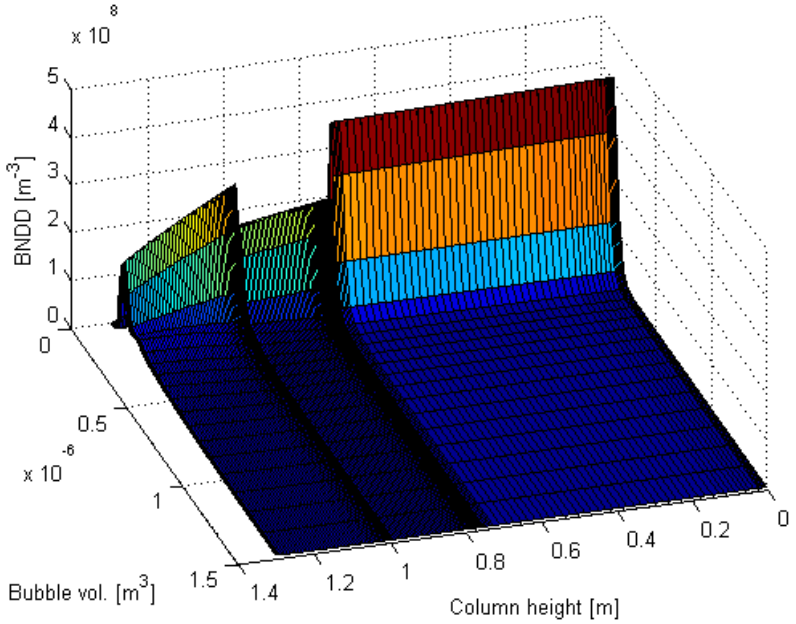
x 10^8
BNDD [m^-3]
5
4
3
2
1
0
0
0.5
x 10^-6
1
1.5
Bubble vol. [m^3]
1.4
1.2
1
0.8
0.6
0.4
0.2
0
Column height [m]

(a)

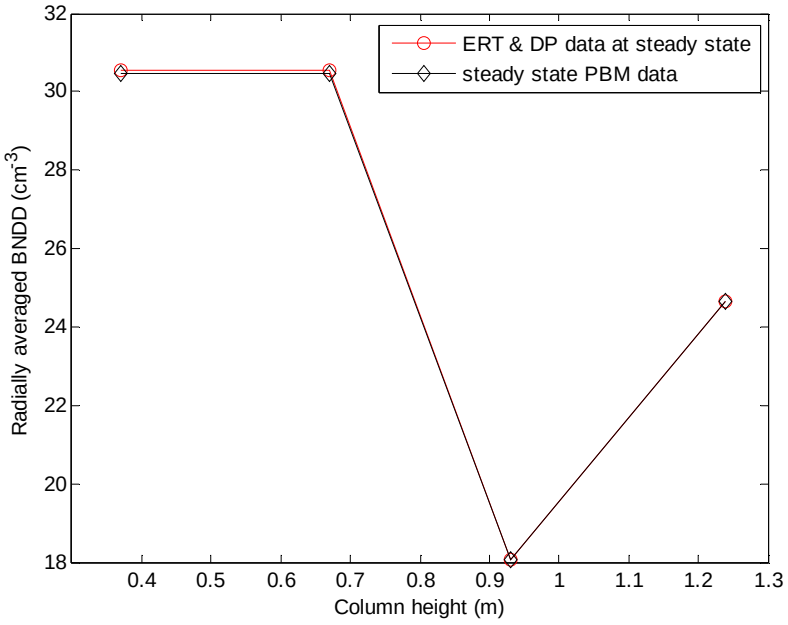
ERT & DP data at steady state
steady state PBM data
Radially averaged BNDD (cm^-3)
32
30
28
26
24
22
20
18
0.4
0.5
0.6
0.7
0.8
0.9
1
1.1
1.2
1.3
Column height (m)

(b)

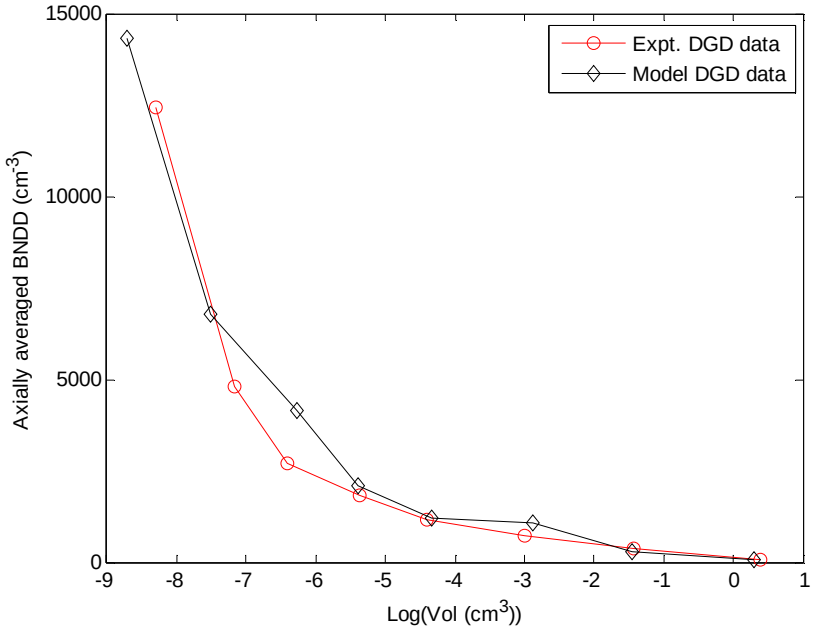

(c)

Figure 8.17. BNDD graphs at the superficial gas velocity of 0.006 m/s (a) Solution of PBM yielding the BNDD depending on bubble volume and column height satisfying the static and dynamic holdup conditions, (b) BNDD averaged over bubble size (volume) against column height by the ERT measurement and the PBM (c) Axially averaged BNDD depending on the logarithm of bubble volume during DGD process by the ERT measurement and a model of DGD process.

The inlet BNDD and the breakage rate were parameterised as stated in Table 8.6 combined with published coalescence rate and flux gradient without parameterisation to resolve the BNDD at $u_g = 0.005\, m/s$ as in Figure 8.18a. Figure 8.18 (b and c) show respectively the extent of agreement of $\bar{n}^{ERT-SS}(z)$ and $\bar{n}^{PBM-SS}(z)$ as well as $\bar{n}^{ERT-DGD}(v)$ and $\bar{n}^{M-DGD}(v)$ based on the statistical error of Table 8.7.

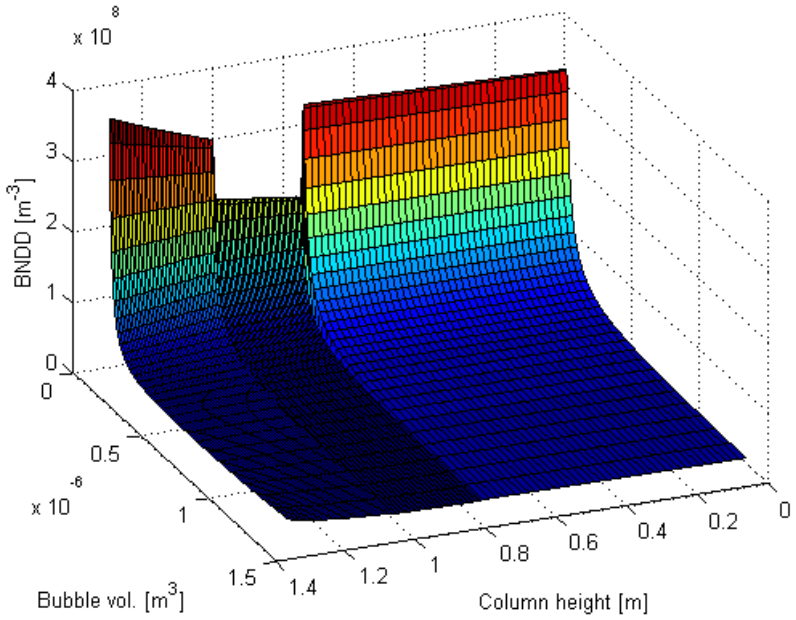
x 10^8
BNDD [m^-3]
4
3
2
1
0
0
0.5
x 10^-6
1
1.5
Bubble vol. [m^3]
1.4
1.2
1
0.8
0.6
0.4
0.2
0
Column height [m]

(a)

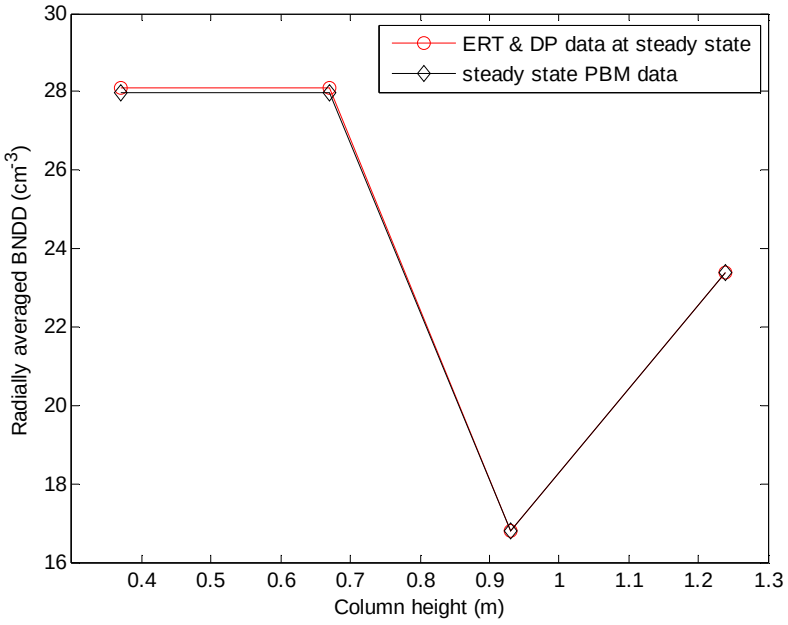
ERT & DP data at steady state
steady state PBM data
Radially averaged BNDD (cm^-3)
30
28
26
24
22
20
18
16
0.4
0.5
0.6
0.7
0.8
0.9
1
1.1
1.2
1.3
Column height (m)

(b)

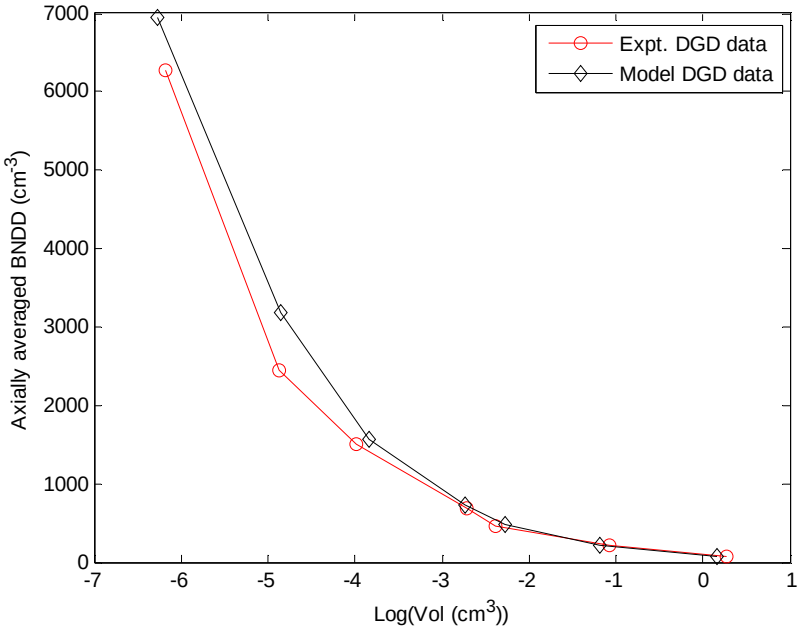

(c)

Figure 8.18. BNDD graphs at the superficial gas velocity of 0.005 m/s (a) Solution of PBM yielding the BNDD depending on bubble volume and column height satisfying the static and dynamic holdup conditions, (b) BNDD averaged over bubble size (volume) against column height by the ERT measurement and the PBM (c) Axially averaged BNDD depending on the logarithm of bubble volume during DGD process by the ERT measurement and a model of DGD process.

The plots in Figure 8.19 - Figure 8.25 show the gas void fractions $\varepsilon(v,z)$ per volume of bubble size class of bubble classes calculated from the hybrid predicted $n(v,z)$ at superficial gas velocities ranging from 0.005 m/s – 0.016 m/s.

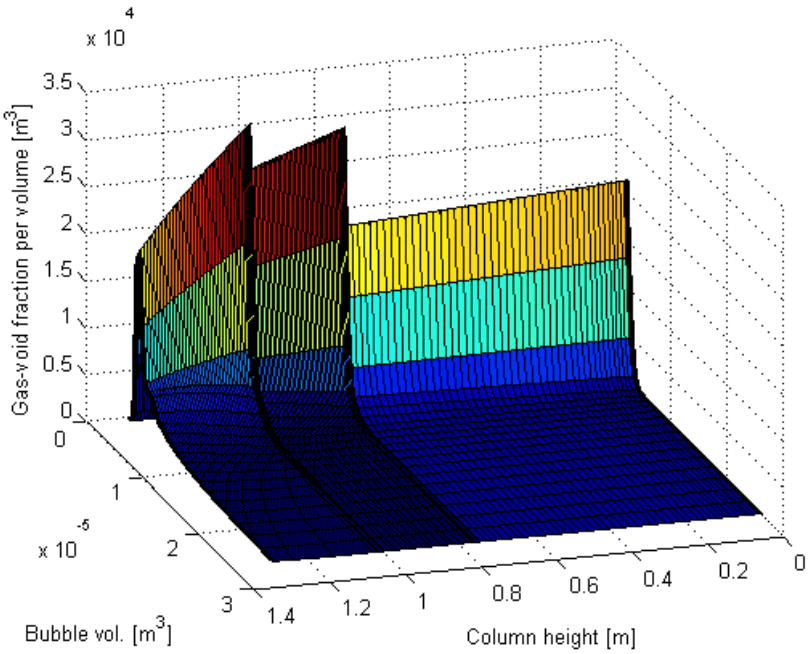

Figure 8.19. The gas void fraction as a function of bubble class volume and column height at the superficial gas velocity of 0.016 m/s.

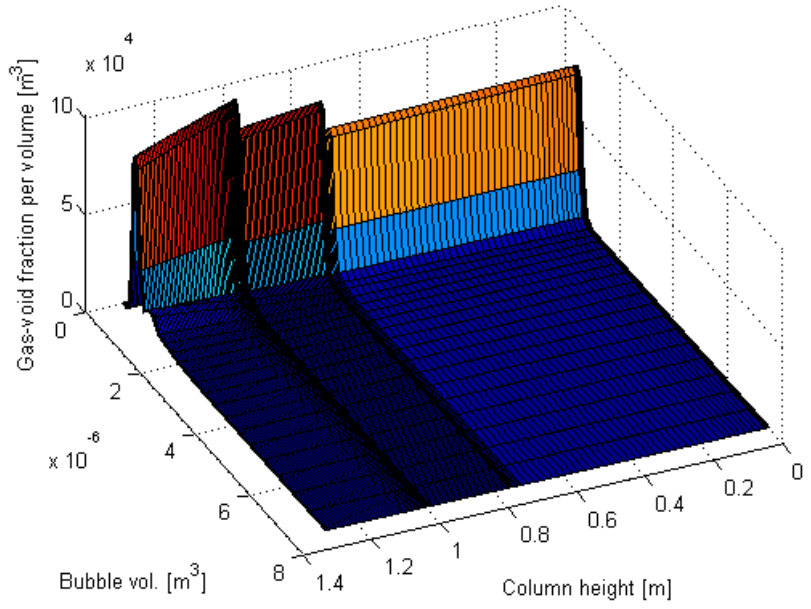

Figure 8.20. The gas void fraction as a function of bubble class volume and column height at the superficial gas velocity of 0.01 m/s.

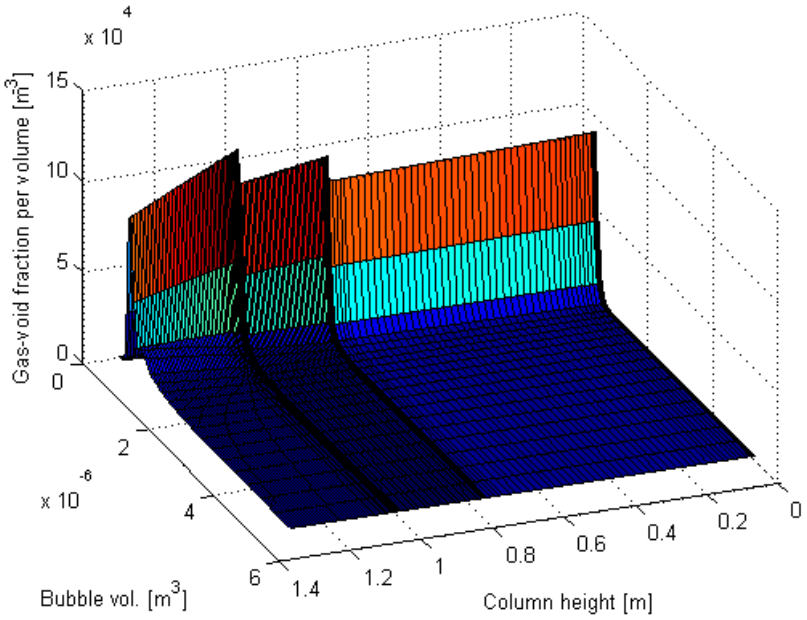

Figure 8.21. The gas void fraction as a function of bubble class volume and column height at the superficial gas velocity of 0.009 m/s.

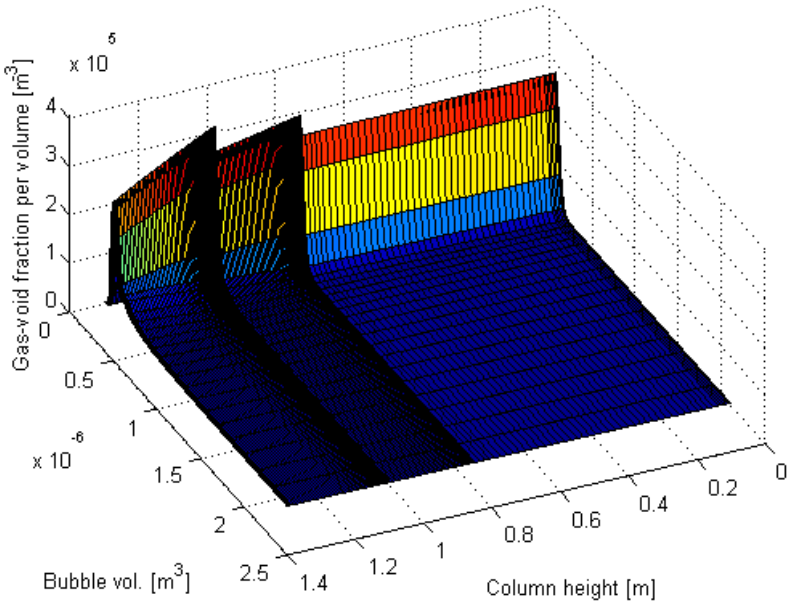

Figure 8.22. The gas void fraction as a function of bubble class volume and column height at the superficial gas velocity of 0.008 m/s.

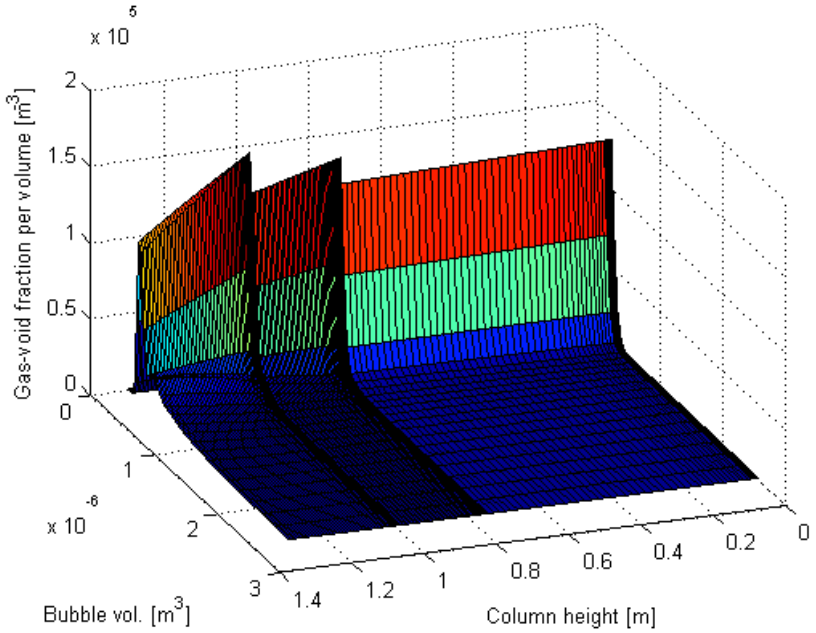

Figure 8.23 The gas void fraction as a function of bubble class volume and column height at the superficial gas velocity of 0.007 m/s.

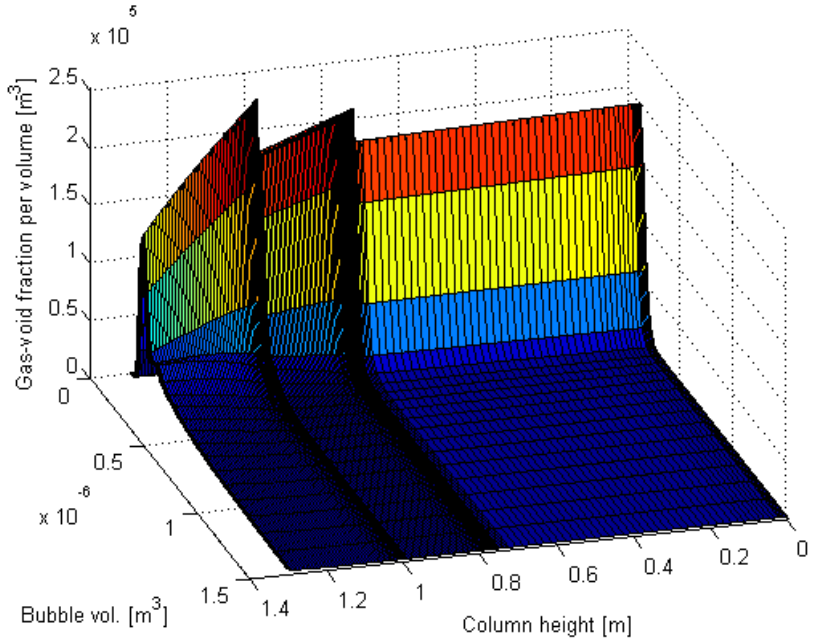

Figure 8.24. The gas void fraction as a function of bubble class volume and column height at the superficial gas velocity of 0.006 m/s.

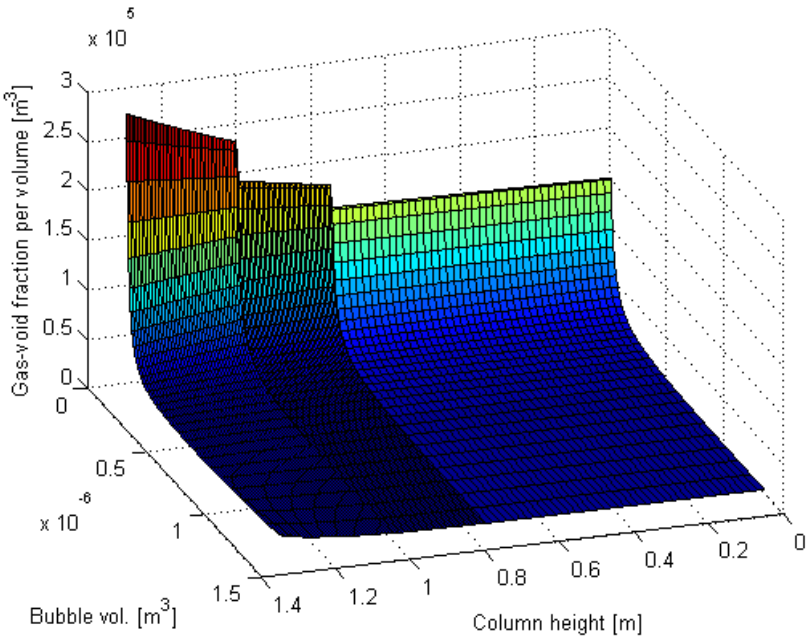

Figure 8.25. The gas void fraction as a function of bubble class volume and column height at the superficial gas velocity of 0.005 m/s.

8.4. Discussion and conclusions

The Electrical Point Probe measurement technique, being an alternative technique for measuring bubble population parameters, is cumbersome, bulky, complicated, expensive and intrusive as described in Chapter 2. However, the ERT technique is portable, low-cost, non-invasive, non-intrusive and simple to set-up. The ERT data captured from the column could be reconstructed either online or off-line post-processing to image the gas dispersion based on conductivity contrasting within a BCR.

The BNDD $n(v,z)$ describing the bubble evolution in the column at steady state was determined such that the calculated dynamic and static gas holdup fractions agree with measured dynamic and static gas holdup fractions respectively by the ERT technique. In determining the $n(v,z)$ at higher superficial gas velocities, the turbulent driven collision frequency was parameterised. The parameter values stated in Table 8.6 were used since the degree of turbulence in the liquid phase increases with increase in superficial gas velocity. Thus, the plots of $n(v,z)$ in Section 8.3 for varied gas flow rates show the turbulence driven coalescence rate increases with superficial gas velocity.

The resolved $n(v,z)$ also indicate the laminar and buoyancy driven collision rates were steady for all the gas flow rates studied since with no parameterization, the BNDDs $n(v,z)$ were predicted at estimated certainty. The parameter values for the flux gradient within an elemental control volume during DGD processes range from 0.8 to 1.0 as stated in Table 8.2 and Table 8.6. The parameter $W_o = 0.8$ at higher u_g values lead to the hybrid predicted BNDDs owing to high bubble population within the control volumes. The high bubble population affects the bubble rise velocity of the mean bubble class more significantly than a situation of less population. Thus, without parameterising the flux gradient or $W_o = 1.0$, the hybrid predicted BNDDs were determined at lower u_g values.

Although at the highest u_g the fluid regime was turbulent, there were insignificant breakage events since the fluid Weber number was less than the critical Weber number for bubble breakage. The use of the fixed low-value parameters stated in Table 8.6 were applicable since the hydrodynamic regime ranged from translational to low turbulence at the highest u_g of 0.016 m/s. The u_g of 0.016 m/s was the highest possible gas flow rate studied owing to the column height available for this work. Further from this gas flow rate, the displaced liquid phase by aeration process spill-off the column. Besides, the water- head level should be at least 0.2 m above an ERT electrode sensor for accurate imaging of the dispersion.

Additionally, the resolved $n(v,z)$ confirms that the breakage rate events in the column for all the flow rates were negligible. The confirmation is based on the insignificant parameter for the breakage rate that yields $n(v,z)$ satisfying the required static and dynamic gas holdup conditions at known accuracy values.

The calculated bubble class void fractions per volume of a bubble class locally from the resolved BNDD based on the ERT/PBM hybrid model are shown in Figure 8.19 - Figure 8.25 for varied superficial gas velocities. The graph of the bubble class void fraction depending on bubble size for a given superficial gas velocity was a scaled surface plot in comparison to the associated BNDD. The graph for a given u_g was obtained from the ratio of the product of BNDD and the mean bubble volume to the volume of the elemental column section.

Moreover, the total gas volume at local column sections calculated from the resolved BNDD in the column increases with increase in superficial gas velocity of gas dispersion. The increase in total local gas volume with increase in superficial gas velocity of dispersion is consistent with existing theories since the gas void fraction at column sections increases

with increase in superficial gas velocity. Notably, the minimum spatial resolution of the ERT and PBM hybrid algorithm for each u_g corresponds to the lower bound of bubble size range that yielded the hybrid predicted BNDD.

The resolved BNDD $n(v,z)$ changes with varying superficial gas velocities as determined by the ERT/PBM hybrid model. As shown in the plots of results of Section 8.3, the resolved $n(v,z)$ was not noticed to increase with increasing superficial gas velocity, though the gas volume at local column sections increases with increasing gas volumetric flow rate. The $n(v,z)$ for varied gas flow rates were obtained because the global mean size class of bubble classes increases with increasing superficial gas velocity locally but not at the same rate as the total volume of gas. This is noticed for the inlet mean bubble volume at higher u_g in Table 8.8 and results in Chapter 5. Thus, the BNDD, which is the ratio of gas volume in a bubble class to the mean bubble volume in the class does not show increasing values with increasing superficial gas velocity.

Chapter 9

Hydrodynamic parameter predictions using the hybrid of ERT and PBM technique in a column

The method of hybrid prediction of BNDD of bubble swarm based on the hybrid algorithm of ERT and PBM has been explained in Chapter 8. The objective of this chapter is to explore the hybrid predicted BNDD $n(v,z)$ for hydrodynamic parameter predictions in a column, which is useful for its performance description and scale-up design.

In designing a BCR to achieve effective product yield, sufficient information on the following hydrodynamic parameters should be known: specific gas-liquid interfacial area, axial solid dispersion coefficients, SMBD, axial dispersion coefficients of the gas and liquid, overall heat transfer coefficient of the multiphase system, mass transfer rates for all species, gas holdup and physicochemical properties of the liquid medium (Kantarci, et al., 2005). The following problem on process design of column operation for its scale-up is considered to show the importance of knowledge of axial and size distribution (or BNDD) of bubbles for a column scale-up design.

1) Air, composing of mostly Nitrogen gas, was distributed into a mildly saline solution of depth 1.39 m contained in a BCR of height 1.545 m and diameter 0.29 m at the ambient temperature of 25℃. The large excess gas was sparged through a porous tubular gas distributor of height 0.265 m and diameter 0.03 m located at the column base. The multiphase dispersion was semi-batch in a steady state such that there was approximately zero dissolved Nitrogen gas throughout the experiment. a) Determine the axial distribution of Nitrogen consumption rate; b) the axial distribution of intensity of the multiphase mixing; 3) the axial gas and liquid dispersion coefficient when the dispersed phase was distributed at varied superficial gas velocities ranging from [0.005 – 0.016 m/s] on the interval of 0.001 m/s?

2a) Suppose the multiphase process in the pilot scale BCR design was to be scale-up based on the geometric symmetry design, what superficial gas flow rate would ensure a volumetric gas-liquid mass transfer rate of 0.3[s^{-1}] and a SMBD of 0.045 m compared to the values for the parameters at a superficial gas velocity of 0.016 m/s with the present pilot scale column?

2b) What are the effects of the determined superficial gas velocity on the mixing time and the gas and liquid axial dispersion coefficients respectively?

In Section 9.1 of this chapter, an account of the application of the hybrid predicted BNDDs for the hydrodynamic parameter predictions in the column is given. An exploration of the hybrid algorithm predictions for column scale-up design is reported in Section 9.2. The results of the use of an alternative experimentally validated simulation model by other researchers for hydrodynamic parameter predictions in a column are presented in Section 9.3. The conclusions on the novel hybrid of ERT and PBM for hydrodynamic parameter predictions in a column with the objectives of performance description and column scale-up design are given in Section 9.4.

9.1. Application of the hybrid of ERT and PBM algorithm for hydrodynamic parameter predictions in a column

The axial distribution of the Nitrogen gas (air) consumption rate of question 1 requires the calculation of the axial distribution of the volumetric gas-liquid mass transfer rates for varied u_gs. This is required because there was approximately zero dissolved Nitrogen gas throughout the experiment, thus, the Nitrogen gas was mostly absorbed by the liquid.

The theoretical framework for the development of the empirical correlation for K_L is presented since the K_L is required for calculating the volumetric mass transfer rates, $K_L a$. Moreover, the local gas holdup fractions $\varepsilon_g(z)$ and the SMBDs d_{vs} need be known for the calculation of $K_L a$ as stated in Eq.(9.3) and Eq.(9.7) respectively. Thus, $\varepsilon_g(z)$ and d_{vs} are calculated prior to the determination of K_L and then $K_L a$ by the following definitions.

The coefficient K_L is actually an average value of K_L since the local value of K_L should vary on the surface of one bubble and depends on the bubble size (Akita & Yoshida, 1974). If the number of bubbles n per unit aerated liquid volume V_C be represented by $^{n}/_{V_C}$ and the diameter of spherical shaped bubble by d, the gas holdup fraction in a unit aerated liquid volume can be expressed as (Akita & Yoshida, 1974) and (Jun, et al., 2015)

$$\varepsilon_g(z) = \frac{\pi}{6V_C} \int_{d_{min}}^{d_{max}} d^3 n(d,z)\, dd \tag{9.1}$$

The volumetric mass transfer rate is the product of K_L and the specific gas-liquid interfacial area a. Thus, the local volumetric mass transfer rate will then be of the form

$$K_L a(z) = \frac{\pi}{V_C} \int_{d_{min}}^{d_{max}} K_L d^2 n(d,z)\, dd \tag{9.2}$$

Dividing Eq.(9.2) by Eq.(9.1), we have

$$K_L a(z) = 6\varepsilon_g(z) \left[\int_{d_{min}}^{d_{max}} K_L d^2 n(d,z) dd \Big/ \int_{d_{min}}^{d_{max}} d^3 n(d,z) dd \right] \tag{9.3}$$

By the definition of the volume-surface mean bubble diameter d_{vs} and the mean value of K_L as in

$$d_{vs}(z) = \int_{d_{min}}^{d_{max}} d^3 n(d,z) dd \Big/ \int_{d_{min}}^{d_{max}} d^2 n(d,z) dd \tag{9.4}$$

$$K_L(z) = \int_{d_{min}}^{d_{max}} K_L d^2 n(d,z) dd \Big/ \int_{d_{min}}^{d_{max}} d^2 n(d,z) dd \tag{9.5}$$

Eq.(9.1) can be combined with Eq.(9.5) to obtain Eq.(9.6).

$$K_L(z) = \left(K_L a(z) \Big/ 6\varepsilon_g(z) \right) d_{vs} \tag{9.6}$$

$$K_L = \left(\frac{4 D_L U_b}{\pi d_{vs}} \right)^{1/2} \tag{9.7}$$

The local average K_L can be computed using Eq.(9.7) (Shimizu, et al., 2000) by the Higbie penetration theory where D_L is the air-water diffusivity. Accordingly, from the knowledge of the local K_L and $K_L a$ from Eq.(9.3), the local specific interfacial area can be calculated using Eq.(9.8).

$$a(z) = {K_L a(z)}/{K_L(z)} \tag{9.8}$$

The enumerated equations will be used accordingly to calculate the hydrodynamic parameters in answering the posed questions.

9.1.1. Gas holdup fraction calculations

The local BNDD $n(v,z)$ in Eq.(9.9) is expressed in terms of column section height $H[m]$, column radius $R[m]$ and radius of mean bubble size $r[m]$ in a bubble class between $[r, r+dr]$. The symbol $f(v)$ denotes the gas volume fraction in a bubble class v of the total gas volume in the column section. The axial distribution of the gas holdup fractions in the column was determined using Eq.(9.10) derived from Eq.(9.9).

$$n(v,z) = \frac{\varepsilon_g(z) R^3 H}{{4}/{3}\,\overline{r^3}} f(v) \tag{9.9}$$

The Eq.(9.10) indicates the size and axial distribution of bubbles, $n(v,z)$, in the column is required for calculating the axial distribution of gas holdup fractions where the mean bubble size in a class is $\overline{v_b} = {4}/{3}\,\overline{r^3}$.

$$\int_{v_{min}}^{v_{max}} \frac{n(v,z)\,\overline{v_b}}{R^3 H}\, dv = \varepsilon_g(z) \tag{9.10}$$

The determined axial and size distribution of bubbles by the hybrid of ERT and PBM predictions, thus, allows for the calculation of the axial distribution of gas holdup fractions. The resolved axial and size distribution of bubbles (BNDD) for varied superficial gas velocities are displayed in Figure 8.5, Figure 8.9, Figure 8.13, Figure 8.15, Figure 8.16, Figure 8.17 and Figure 8.18 of Section 8.3 in Chapter 8.

Using the $n(v,z)$ at known u_g, the Eq.(9.10) was used to compute the axial distribution of gas holdup fractions for varied u_gs. The plot of the axial distribution of gas holdup fraction results in Figure 9.1 for stated u_g values were obtained from the corresponding $n(v,z)$ of Section 8.3 in Chapter 8.

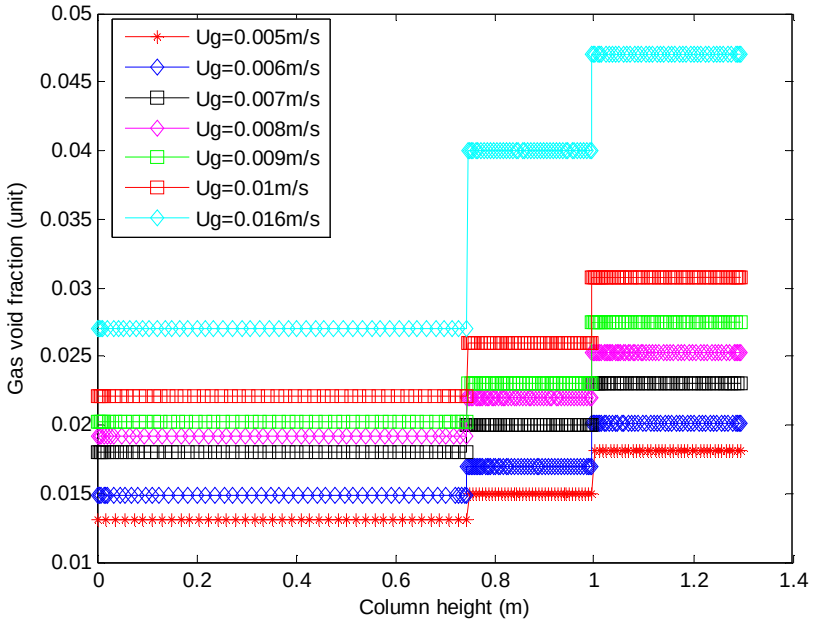

Figure 9.1. Axial distribution of gas holdup in the column at varied superficial gas velocities.

The graphs of Figure 9.1 show an increase in axial distribution of gas holdup fractions with an increase in u_g, which is expected since the gas volume at a local column section increases with increase in superficial gas velocity. The trend of the axial distribution of ε_g at a given u_g is due to the form of the fluid dispersion produced by the tubular gas distributor as discussed in Chapter 4. The bubbles were radially well-distributed at Section 3 and 4 while being dispersed through the column centre and top of the sparger at Section 1 and 2. The decrease in bubble resident time with an increase in column height contributes to the increase in the gas void fraction with column height. As discussed in Chapter 4, the ε_g at Section 1 and 2, Section 3 as well as Section 4 are in agreement with the empirical correlation of (Shah, et al., 1982), (Hughmark, 1967) and (Akita & Yoshida, 1973) respectively. The obtained R-square statistical analysis between the gas void fraction at Section 1 and 2, Section 3 and Section 4 and the published correlations are 95%, 99% and 97% respectively. The results of Figure 9.1 agree with that obtained in the work of (Shimizu, et al., 2000) of Figure 9.10 globally and specifically for the axial distribution of Figure 9.11 at $u_g = 0.01m/s$.

9.1.2. SMBD calculations

In order to calculate the $K_L(z)[mS^{-1}]$ as in Eq.(9.7), the axial distribution of the SMBD $d_{vs}(z)$ should be known. The local $d_{vs}(z)$ was calculated using Eq.(9.4) from the known $n(v,z)$ with respect to u_g. The results of the axial distribution of the SMBD depending on the superficial gas velocity are displayed in Figure 9.2.

$$\overline{d\_vs} = \frac{\sum_{z=z_1}^{z_8} d\_vs(z)}{n(d\_vs(z))} \tag{9.11}$$

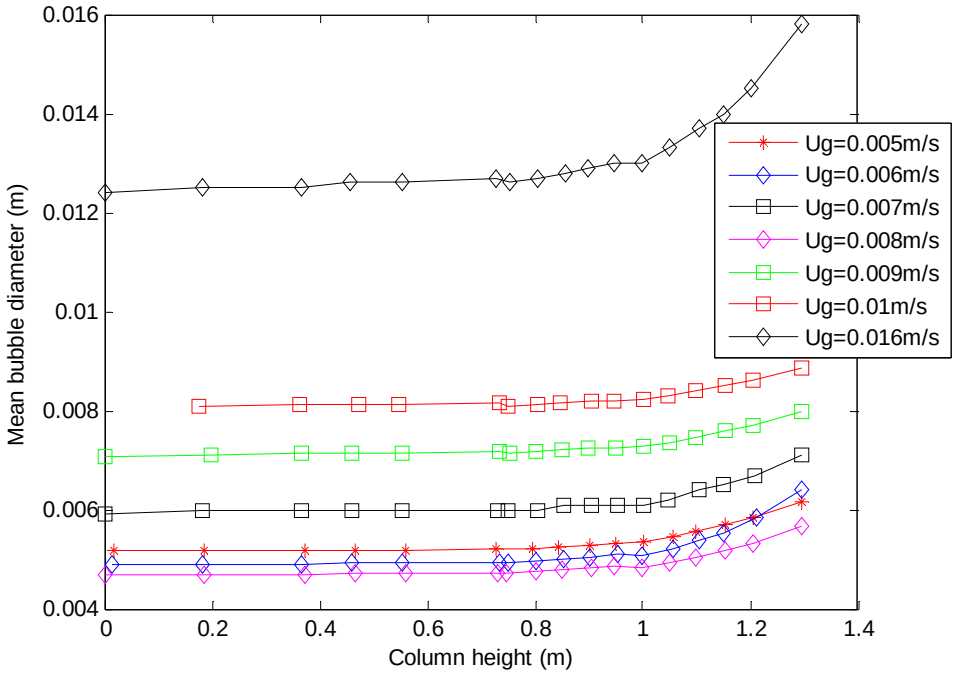

Figure 9.2. The axial distribution of mean bubble diameter in the column at varied superficial gas velocities.

The Eq.(9.11) was derived from Eq.(9.4) to calculate the global SMBD for varied flow rates. At all studied $u_g s$, the axial distributions of the SMBD show the bubble size increases along the column height. This occurred due to significant bubble coalescence rates and insignificant bubble breakage rates during axial bubble swarming in the column. The extent of increase of the d_{vs} along the column height decreases with a decrease in u_g. These results are consistent with the coalescence rate parameters for varied $u_g s$ that yielded the PBM solution and solution of DGD process model agreeing with the experimental measurements.

Similar graphical trend was obtained by (Sattar, et al., 2013), (Laari & Turunen, 2005) and (Laari & Turunen, 2003) in their work where tubular sparger with 2000 holes was used within the range of studied $u_g s$. The obtained graphs shown in Figure 9.2 indicate the axial distribution of SMBD increases with increase in gas flow rate u_g ranging from 0.008-0.016m/s. At lower $u_g s$ of 0.005, 0.006 and 0.007 m/s, the obtained axial distribution of the mean d_{vs} are based on the range of bubble sizes and the inlet BNDD parameter satisfying the experimental measurements.

9.1.3. Liquid-phase mass transfer coefficients

From the calculated d_{vs} for varied $u_g s$, the local $K_L(z)$ were calculated using Eq.(9.7) to obtain Figure 9.3. The resolved hybrid predicted $n(v,z)$ was required for calculating the local $K_L(z)$ since d_{vs} depends on $n(v,z)$ in the column as in Eq.(9.4). The axial distribution of the volumetric mass transfer rates $K_L a(z)$ for varied $u_g s$ based on the interpretation of Eq.(9.3) and Eq.(9.6) were calculated from the product of $K_L(z)$ and the local specific gas-liquid interfacial area $a(z)$. The $a(z)$ for varied $u_g s$ were calculated using Eq.(9.12) (Akita & Yoshida, 1974), (Shah, et al., 1982) owing to its validity at the operational conditions in the column to obtain the graphs in Figure 9.4.

$$a = {}^{1}/_{(3D_C)} \left(\frac{gD_C{}^2\rho_L}{\sigma}\right)^{0.5} \left(\frac{gD_C{}^3}{v_L^2}\right)^{0.1} \varepsilon_g^{1.13} \qquad (9.12)$$

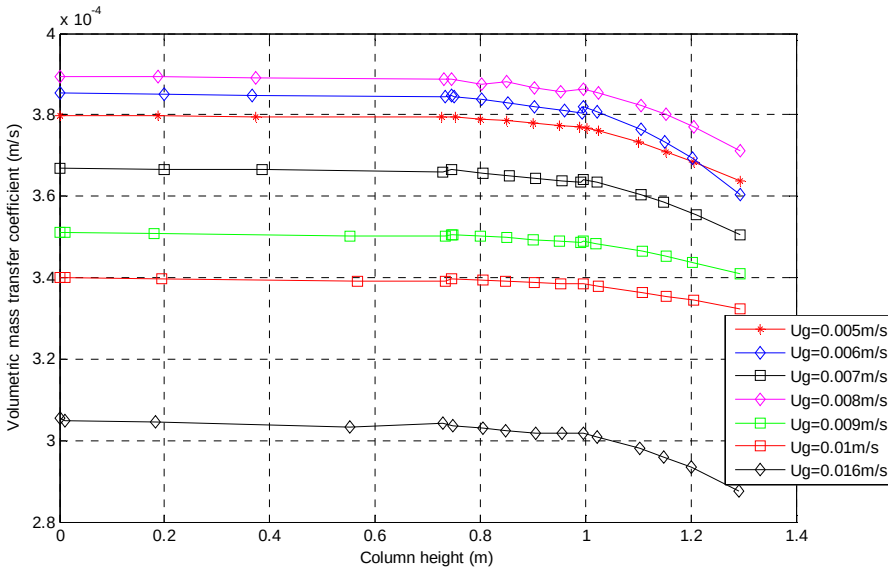

Figure 9.3. The axial distribution of the volumetric mass transfer coefficient at varied superficial gas velocities in the column

The K_L decreases with u_g at larger $u_g s$ (0.008 – 0.016 m/s) because the d_{vs} increases with u_g owing to the balance of the bubble birth and death caused by the significant coalescence events and insignificant breakage events. The trend of the graph of d_{vs} against u_g at lower u_g of Figure 9.2 is also observed in the relation between K_L and u_g at lower $u_g s$ (0.005 – 0.007 m/s). At the lower $u_g s$, the order of increase in d_{vs} was from 0.006, 0.005 to 0.007 as captured by the ERT imaging technique.

Due to the significant coalescence events contributing to an increase in d_{vs} along column height (i.e. Figure 9.2) at a given u_g, the K_L decreases with the column height at a given u_g as shown in Figure 9.3.

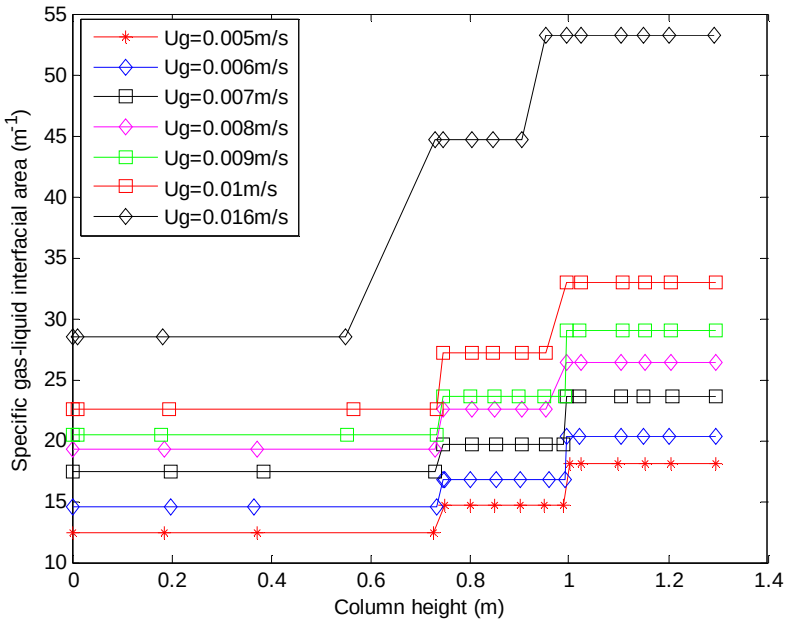

Figure 9.4. The axial distribution of the specific gas-liquid interfacial area at varied superficial gas velocities in the column.

The graphs in Figure 9.4 shows an increase in a with increase in u_g because of the dependence of a on ε_g as in Eq.(9.12). In addition, by the proposed correlation between ε_g and u_g of the form $\varepsilon_g \propto C u_g^n$; $0.7 < n < 1.2$ (Shah, et al., 1982) for bubbly fluid flow regime, the ε_g increases with u_g. The alternative proposed correlation of Eq.(9.13) by (Nagel, et al., 1979) and (Schumpe & Deckwe, 1981) shows an increase of a with increase in ε_g for $n > 0$ as well as an increase of a with increase in u_g.

$$a = k\left(e'/v\right)^{0.4}\varepsilon_g^n;\ a = 48.7\left(u_g/\mu_{eff}\right)^{0.51} \tag{9.13}$$

Given the used tubular gas distributor design that produced uniform and well-distributed bubbles at planes much higher along the column axis, the obtained trend of ε_g along the column height influences the local a as observed in the graphs of Figure 9.4. Since the a varies with ε_g by Eq.(9.12), the validity of the measured ε_g suggests that the calculated a for a given u_g is accurate in line with the experimental results by (Akita & Yoshida, 1974).

Accordingly, the obtained graphs for the gas-liquid volumetric mass transfer rates $K_L a(z)$ for varied $u_g s$ are displayed in Figure 9.5.

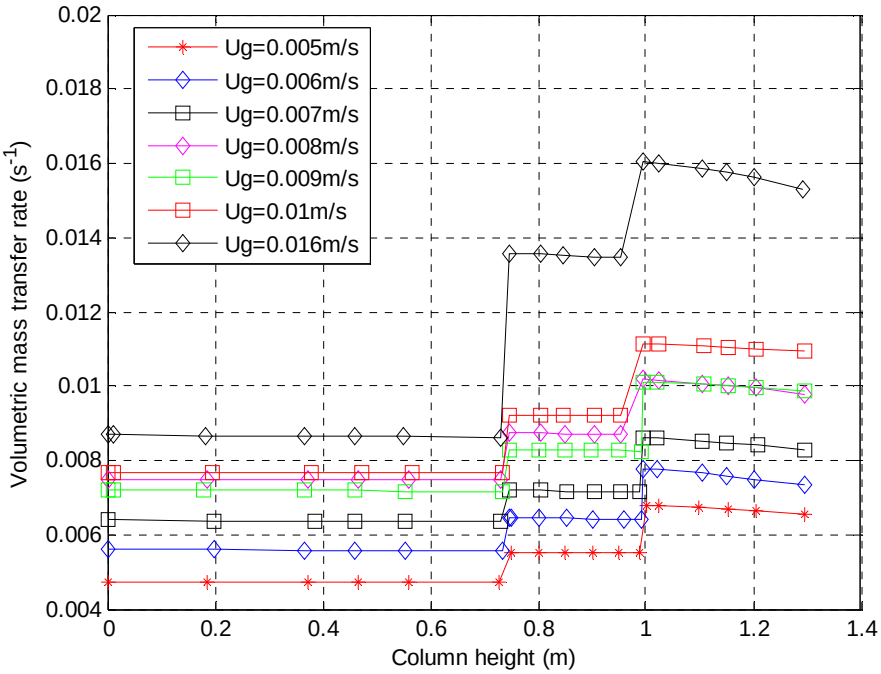

Figure 9.5. The axial distribution of the volumetric gas-liquid mass rates at varied superficial gas velocities in the column.

The product of the trends of the axial distribution of K_L and a are observed in the axial distribution of $K_L a$ over the range of $u_g s$. The $K_L a$ is observed to increase with an increase in the u_g largely except for the measurement at $u_g = 0.008\, m/s$ at lower sections. This occurred due to the K_L at 0.008 m/s being lower than that at lower u_g as shown in Figure 9.3.

The axial distribution of ε_g is not steady owing to the used tubular gas distributor that generated dispersion that increases along the column axis as shown in Figure 9.1. The validation of the local gas holdup fraction against u_g has been discussed in Chapter 4. A sintered porous or perforated flat plate will generate uniformly well-distributed bubble population locally and globally in the column compared to the used sparger.

The graphs in Figure 9.5 were obtained owing to the increasing ε_g with column height at a given u_g that lead to increase in the $K_L a$ from the lower column section to the higher column section. However, at each column section for all the $u_g s$, the $K_L a$ decreases with column height owing to the dominant K_L term. The K_L decreases with column height for all the $u_g s$ studied owing to the increase in the d_{vs} with column height. The d_{vs} was noticed to increase along the column height as a result the balance of the bubble birth and death on the account of bubble coalescence and breakage events during axial bubble swarming.

The results of Figure 9.5 at $u_g = 0.01$m/s and $\varepsilon_g = 0.0308$ at the fourth column section agree with the values obtained in the work of (Shimizu, et al., 2000) though a column with the diameter of 0.2 m was used as in Figure 9.13. The trend of the corresponding gas void fraction of Figure 9.11 also agrees with the measured ε_g at $u_g = 0.01$m/s at the fourth column section. A simulation model for the prediction of gas holdup and volumetric mass transfer rates was developed by (Shimizu, et al., 2000) in their work. Their results were validated with well-established correlation model of (Akita & Yoshida, 1973), (Kawase, et al., 1987), (Shah, et al., 1982) and their experimental measurements as in Figure 9.12.

Furthermore, the global hybrid-predicted $K_L a$ over the range of studied $u_g s$ were validated against the empirical correlation of Eq.(9.14) (Kantarci, et al., 2005) (Shah, et al., 1982) that is valid for u_g ranging from 0.002 – 0.08 m/s.

$$K_L a = b u_g^n \tag{9.14}$$

The correlation was proposed based on the oxygen transfer in tap water in a BCR were the parameter b and n were estimated to be 0.467 and 0.82 respectively at 17.7% mean error. The graph of the global hybrid-predicted $K_L a$ against u_g agrees with the correlation of Eq.(9.14) with $b = 0.42$ and $n = 0.82$ as in Figure 9.6 by the statistical error on Table 9.1. In addition, the hybrid-predicted $K_L a$ against u_g agrees with the correlation of Eq.(9.15) valid in an air-water fluid system with u_g ranging from 0.003-0.4 m/s (Akita & Yoshida, 1973)

(Shah, et al., 1982). The accuracy level of the agreement between the two results is stated in Table 9.1.

$$K_L a = \frac{D_l}{D_c^2} 0.6 \left({}^{v_l}/_{D_l}\right)^{0.5} \left({}^{g D_c^2 \rho_l}/_{\sigma}\right)^{0.62} \left({}^{g D_c^3}/_{v_l^2}\right)^{0.31} \varepsilon_g^{1.1} \qquad (9.15)$$

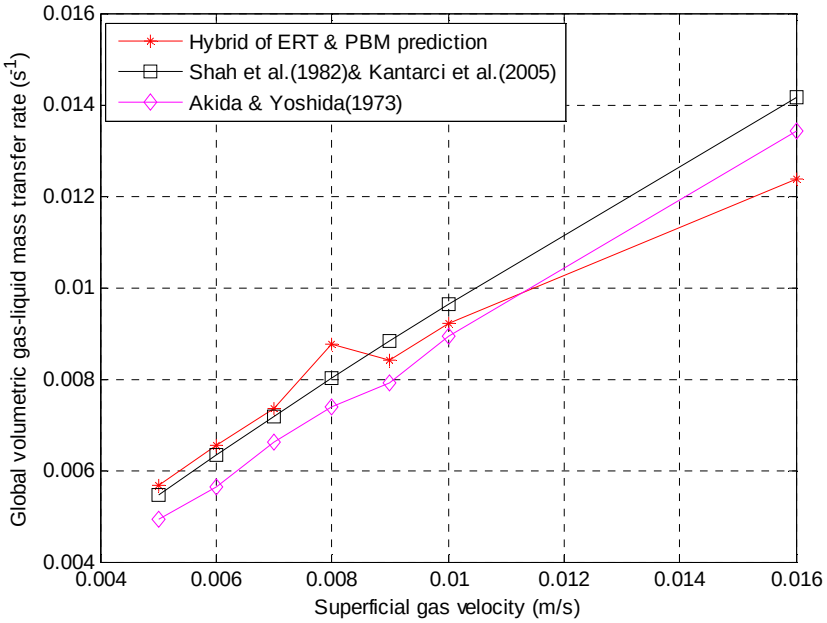

Figure 9.6. The global hybrid-predicted volumetric mass transfer rate against superficial gas velocity compared to empirical correlation results.

Table 9.1. Statistical error results of the comparison of global mass transfer rates as a function of superficial gas velocity by the hybrid technique and empirical correlations

	Mean of $K_L a$ over $u_g s$ (/s)	Chi-square	R-square	f-statistic	f-critical
Empirical correlation by Shah et al.(1982) & Kantarci et al. (2005)	0.00857	0.85786	0.8578	35.9650	5.9874
Hybrid of ERT & PBM prediction	0.00833				
Hybrid of ERT & PBM prediction	0.00833	1.0831	0.8195	27.2371	5.9874
Empirical correlation of Akida & Yoshida (1973)	0.00784				

Moreover, the validity of the global $K_L a$ depending on u_g based on the accuracy level indicates the axial distribution of the d_{vs} of Figure 9.2 depending on u_g is valid. This notion is made since the analysed hybrid predicted $n(v, z)$ to calculate $K_L a$ was used to calculate the d_{vs} for a given u_g.

9.1.4. Intensity of interphase mixing and phase dispersion rates

Furthermore, the intensity of mixing denoted by $\emptyset[unit]$ is computed from the ratio of the mixing time to the mass transfer time (Deckwer & Schumpe, 1993) to address the question 1b. The mixing time model from the correlation of (Camacho, et al., 2004) varies with u_g as in Eq.(9.17) where $\alpha = 0.385$, $k = 0.35$ and $n = 1$ for a Newtonian fluid. Since the mixing time t_m is of Eq.(9.17) and mass transfer time MTT_m equals Eq.(9.16), the intensity of mixing equals Eq.(9.18) (Deckwer, 1986).

$$MTT_m(z) = \left(\frac{1}{K_L a(z)}\right) \tag{9.16}$$

$$t_m = 2^{-2\frac{(1+n)}{3n}} \alpha \frac{{H_L}^2}{k{D_c}^{4/3}(u_g g)^{1/3}} \tag{9.17}$$

$$\emptyset = t_m K_L a(z) \tag{9.18}$$

The graph of the mixing time as a function of u_g for a dispersion height $H_L = 1.29m$ is shown in Figure 9.7. The mass transfer time MTT_m, however, depends on the gas holdup (Laari & Turunen, 2005) values $\varepsilon(z)$ and $d_{vs}\ (z)$ calculated from the resolved $n(v, z)$ by the hybrid of ERT and PBM method. Thus, using Eq.(9.18), the axial distribution of the intensity of mixing $\emptyset(z)$ for varied u_g given the axial distribution of $K_L a$ were calculated as shown in Figure 9.8. Since Figure 9.5 and Figure 9.7 are valid, the results in Figure 9.8 are expected to be valid.

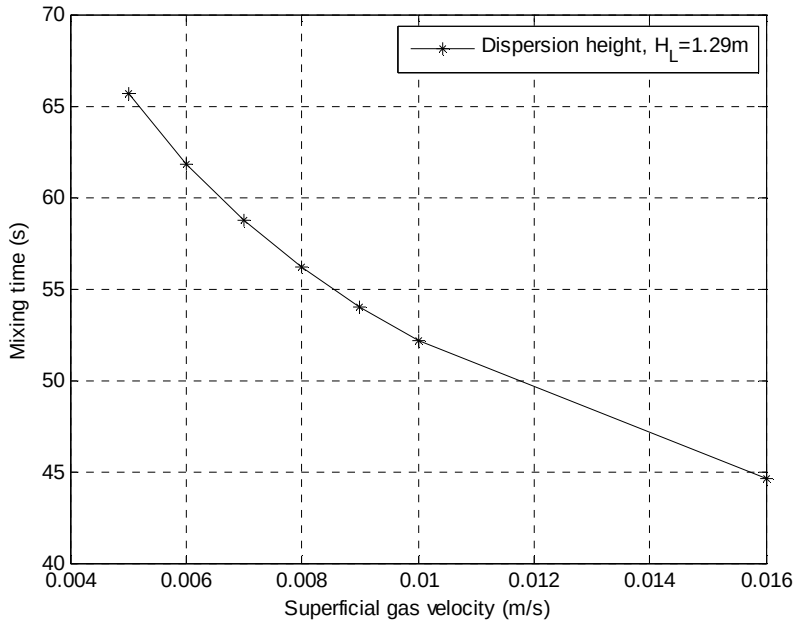

Figure 9.7. The mixing time as a function of superficial gas velocity at the stated dispersion height

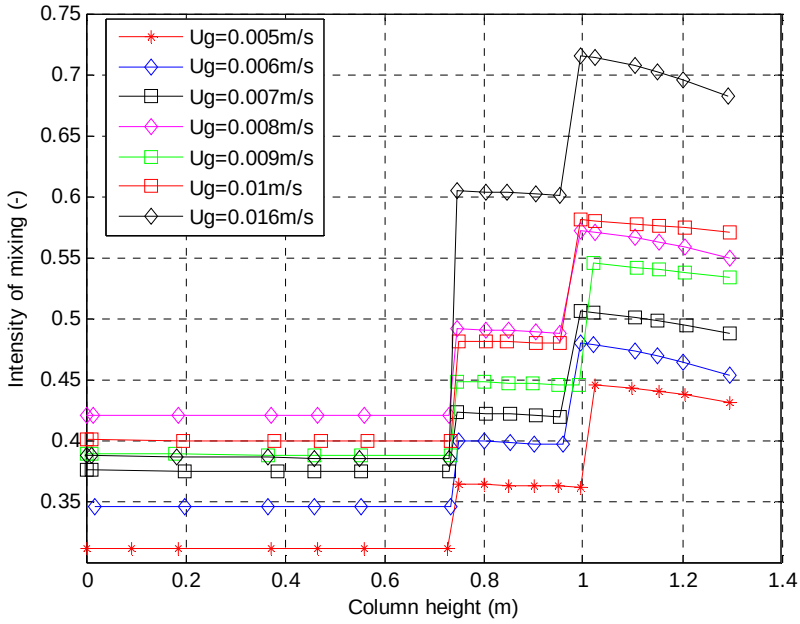

Figure 9.8. Axial distribution of the intensity of mixing in the column at varied superficial gas velocities.

The graphs of the axial distribution of intensity of mixing for varied u_g values of Figure 9.8 show the axial distribution of intensity of mixing increases with increase in u_g except at $u_g = 0.008\, m/s$. The axial distribution of d_{vs} at $u_g = 0.008\, m/s$ accounts for the trend of $\emptyset(z)$ at this u_g. Moreover, the trend of the axial distribution of $\emptyset$ at a given u_g is similar to that of $K_L a$ since the $K_L a$ factor is dominant in the product resulting in $\emptyset$.

In solving question 1c, the axial dispersion rates of gas and liquid phases depending on the column diameter D_C and the u_g of dispersion, were solved using Eq.(9.19) and Eq.(9.20) respectively(Deckwer & Schumpe, 1993) (Camacho, et al., 2004). Figure 9.9 relates the gas and liquid phases dispersion rates to u_g of air in the column.

$$E_L = 0.343 {D_C}^{4/3} (g u_g)^{1/3} \tag{9.19}$$

$$E_G = 20 {D_C}^{3/2} u_g \tag{9.20}$$

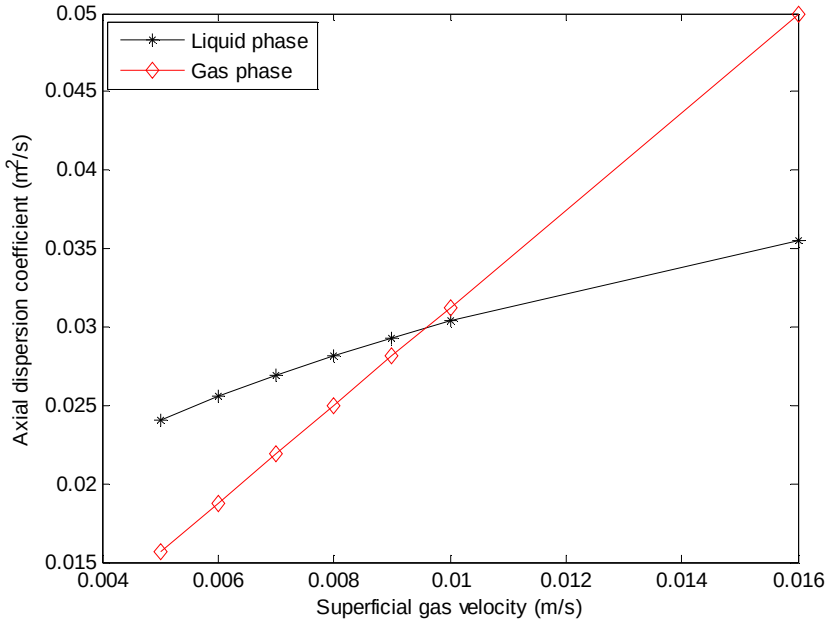

Figure 9.9. Axial dispersion of gas and liquid in the column against superficial gas velocity of dispersion.

The results of Figure 9.9 indicate that $E_G[m^2s^{-1}]$ and E_L increase with U_G, which were expected given the mathematical relationship between E_G and U_G as well as E_L and U_G.

9.2. Exploration of the hybrid predictions of hydrodynamic parameters for column scale-up design

The question 2(a-c) posed at the introductory section of this chapter are addressed in this section. From the results of Figure 9.5 and Figure 9.2, at u_g of 0.016 m/s, the global k_La was 0.0124$[s^{-1}]$, while the global SMBD d_{vs} was 0.0131$[m]$. In question 2a, the column design is expected to be enhanced for an optimal multiphase flow by the geometric scale-up approach (Nauman, 2008) to ensure the value of k_La is 0.3s^{-1} and d_{vs} is 0.045m. The scale-up factors for these quantities were calculated as follows:

Let the scale-up factors for k_La and d_{vs} be denoted respectively by f_{k_La} and $f_{d_{vs}}$, then

$$f_{k_La} = {}^{0.3}/_{0.0124} = 24.19 \tag{9.21}$$

$$f_{d_{vs}} = {0.045}/{0.0131} = 3.44 \tag{9.22}$$

Given Eq.(9.7) and Eq.(9.12), the $k_L a$ can be re-written as in Eq.(9.23)

$$k_L a = {1}/{(3D_C)} \left(\frac{g d_{vs}}{0.59}\right)^{0.25} \left(\frac{4D_L}{\pi d_{vs}}\right)^{1/2} \left(\frac{g {D_C}^2 \rho_L}{\sigma}\right)^{0.5} \left(\frac{g {D_C}^3}{v_L^2}\right)^{0.1} \varepsilon_g^{1.13} \tag{9.23}$$

Since the $K_L a$ in the full-scale plant unit is a factor of 24.19 to the $K_L a$ in a pilot scale unit, the expression of Eq.(9.24) is expected to hold.

$${[K_L a]_{Full-scale\ plant(2)}}\Big/{[K_L a]_{Pilot-scale\ plant(1)}} = 24.19 \tag{9.24}$$

Additionally, since $g[ms^{-2}]$, $\rho_l[kgm^{-3}]$, $D_l[m^2 s^{-1}]$, $\sigma[kgs^{-2}]$ and $v_l[m^2 s^{-1}]$ are constants in the two plant units, Eq.(9.24) can be re-written as

$$\frac{[K_L a]_2}{[K_L a]_1} = \left(\frac{[d_{vs}]_1}{[d_{vs}]_2}\right)^{0.25} \left(\frac{[D_C]_2}{[D_C]_1}\right)^{0.3} \left(\frac{[\varepsilon_g]_2}{[\varepsilon_g]_1}\right)^{1.13} = 24.19 \tag{9.25}$$

Based on the geometry symmetry approach, the column diameter D_C scales by $S^{1/3}$, where S is defined as in Eq.(9.26) or Eq.(9.27) (Nauman, 2008).

$$S = \frac{mass\ flow\ through\ a\ full-scale\ plant}{mass\ flow\ through\ a\ pilot-scale\ plant} = S_{throughput} \tag{9.26}$$

$$S_{volume} = \frac{volume\ of\ fluid\ in\ a\ full-scale\ plant}{volume\ of\ fluid\ in\ a\ pilot-scale\ plant} \tag{9.27}$$

The SMBD, d_{vs}, will also scale by $S^{1/3}$, such that

$$S_{d_{vs}}^{1/3} = 3 \text{ and } S_{K_L a}^{1/3} = 1 \tag{9.28}$$

Substituting the scaling factors for the column diameter and SMBD into Eq.(9.25), the results in Eq.(9.29) to Eq.(9.31) are obtained.

$$(3.44)^{-0.25}(1)^{0.3}(S_\varepsilon)^{1.13} = 23.1 \tag{9.29}$$

$$0.7343(S_\varepsilon)^{1.13} = 24.19 \tag{9.30}$$

$$S_\varepsilon = 22.04 \tag{9.31}$$

The result of Eq.(9.31) implies that the gas holdup should be increased by a factor of 22.04 from the initial values of 3.81% to 83.97% for the full-scale plant unit. In order to achieve the gas holdup of 83.97% in the column, the u_g of 0.016 m/s should be increased to 0.99 m/s based on the correlation between the gas void fraction and the u_g by (Shah, et al., 1982).

With a view to addressing question 2b for the effects of the scale-up approach on the mixing time, Eq.(9.17) is re-written as in Eq.(9.32), where C denotes the constant.

$$t_m = \frac{C}{D^{4/3}(u_g g)^{1/3}} \tag{9.32}$$

By the geometry symmetry scaling approach, Eq.(9.33) holds.

$$\left[t_m D^{4/3}(u_g g)^{1/3}\right]_{pilot\ plant} = C = \left[t_m D^{4/3}(u_g g)^{1/3}\right]_{Full-scale\ palnt} \tag{9.33}$$

The scale-up factor of the mixing time is, then, computed as in Eq.(9.34) to Eq.(9.35).

$$\frac{[t_m]_2}{[t_m]_1} = \left(\frac{[D]_1}{[D]_2}\right)^{\frac{4}{3}} \left(\frac{[u_g]_1}{[u_g]_2}\right)^{\frac{1}{3}} \tag{9.34}$$

$$\frac{[t_m]_2}{[t_m]_1} = (1)^{\frac{4}{3}} \left(\frac{0.016}{0.99}\right)^{\frac{1}{3}} = 0.2528 \tag{9.35}$$

The ratio of column diameter of the full-scale plant to the pilot scale plant (first term on the RHS of Eq.(9.34)) is 1 by the geometric symmetry approach. The results of Eq.(9.35) show the mixing time decreases by a factor of 0.2528 owing to the increase in superficial gas velocity to the value of 0.99 m/s.

The effect of the scale-up approach on the axial liquid dispersion rate (question 2c) was solved by rewriting Eq.(9.19) in terms of variables as in Eq.(9.36) to obtain the results in Eq.(9.39).

$$\frac{[E_L]_1}{\left[u_g^{1/3} D_C^{4/3}\right]_1} = C = \frac{[E_L]_2}{\left[u_g^{1/3} D_C^{4/3}\right]_2} \tag{9.36}$$

$$\frac{\left[u_g^{1/3} {D_C}^{4/3}\right]_2}{\left[u_g^{1/3} {D_C}^{4/3}\right]_1} = \frac{[E_L]_2}{[E_L]_1} \tag{9.37}$$

$$\left(\frac{[u_g]_2}{[u_g]_1}\right)^{1/3} (1)^{4/3} = \frac{[E_L]_2}{[E_L]_1} \tag{9.38}$$

$$\frac{[E_L]_2}{[E_L]_1} = (61.875)^{1/3}(1)^{4/3} = 3.955 \tag{9.39}$$

Furthermore, the effect of the scale-up technique on the axial gas dispersion rate (question 2c) was determined by expressing Eq.(9.20) as in Eq.(9.40)

$$\frac{[E_G]_2}{[U_G]_2} = C = \frac{[E_G]_1}{[U_G]_1} \tag{9.40}$$

$$\frac{[E_G]_2}{[E_G]_1} = \frac{[U_G]_2}{[U_G]_1} = 61.875 \tag{9.41}$$

The Eq.(9.40) is simplified to Eq.(9.41) to calculate the axial gas dispersion rate, which increases by a factor of 61.875.and the liquid dispersion increased by a factor of 3.995.

9.3. Hydrodynamic parameter predictions by experimentally validated simulation method

The hydrodynamic parameters for enhanced designing of a column could either be estimated by experimental measurements or from validated correlation models or simulation models with experimental data. A simulation model was developed by (Shimizu, et al., 2000) based on the phenomena of bubble coalescence and breakup rates for prediction of gas holdup and volumetric mass transfer coefficient in a BCR. The developed simulation model was validated by an experimental study set-up in two columns of dimensions 0.2m and 0.155m in diameter and 1.7m and 0.834m in height respectively.

The results of the simulation model for the measurements of the changes in the global gas holdup with increasing u_g were compared to experimental results as well as well-known correlation models by (Hughmark, 1967) and (Kawase, et al., 1992) as in Figure 9.10.

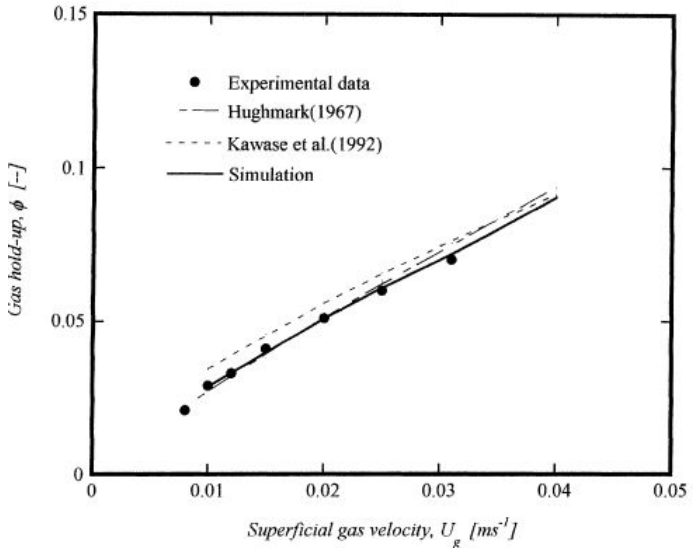

Figure 9.10. Gas hold-up in a 0.2m diameter column against superficial gas velocity.

The results in Figure 9.10 were validated with experimental results of processes set-up in a column with the diameter of 0.2m. The axial distribution of gas holdups in the column at two superficial gas velocities of 0.01 m/s and 0.04 m/s were also calculated from the simulation model as shown in Figure 9.11.

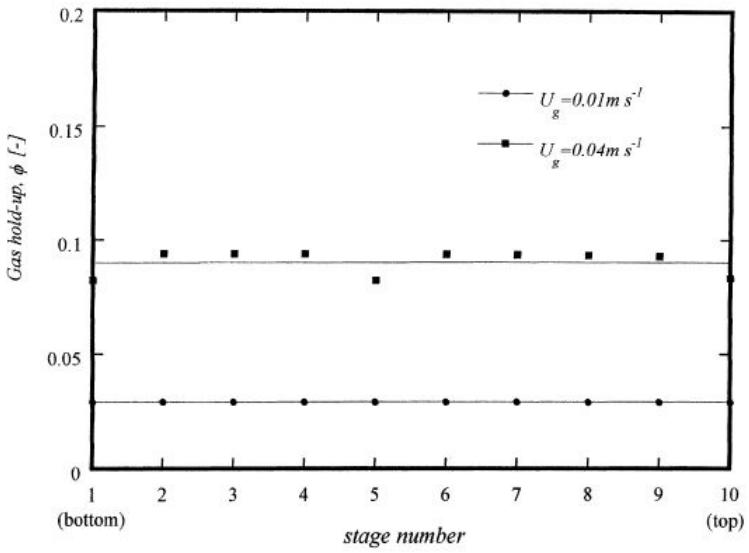

Figure 9.11. Axial distribution of gas hold-up in a bubble column reactor ($\boldsymbol{D_T}$=0.2m).

Furthermore, changes in volumetric mass transfer rates with respect to an increase in u_g were obtained from the simulation model (Shimizu, et al., 2000). The results were compared

to the experimental measurements as well as results from validated correlations as shown in Figure 9.12. For the two $u_g s$ of 0.01 m/s and 0.04 m/s, the axial distribution of the gas-liquid volumetric mass transfer rates in the column were obtained as displayed in Figure 9.13.

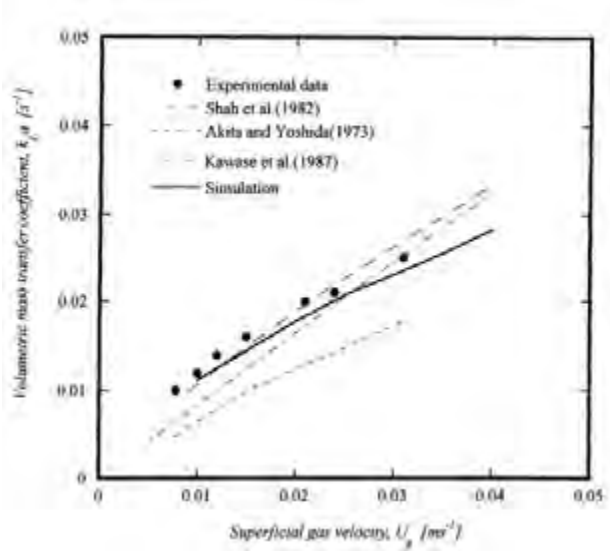

Figure 9.12. Gas-liquid mass transfer rates in a 0.2m diameter bubble column reactor against superficial gas velocity.

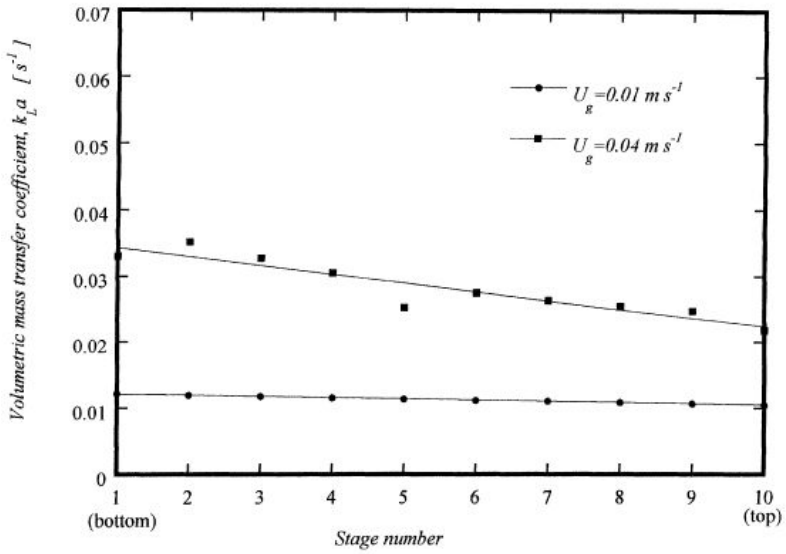

Figure 9.13. Axial distribution of gas-liquid mass transfer rate in a bubble column reactor (D_T=0.2m).

The graphs of Figure 9.12 and Figure 9.13 provide additional experimental results for validating the hybrid predictions of hydrodynamic parameters using the newly developed hybrid algorithm. The results of gas void fractions and axial distribution of gas holdup fractions at u_g of 0.01 m/s as in Figure 9.10 and Figure 9.11 are in agreement with the

hybrid prediction of Figure 9.1 especially at Section 4 at $u_g = 0.01$ m/s . The results of the $K_L a$ of Figure 9.12 and Figure 9.13 for $u_g = 0.01\ m/s$ are, also, in agreement with that by hybrid predictions of Figure 9.5 particularly at $u_g = 0.01\ m/s$ at Section 4 for the same u_g.

9.4. Conclusions on the hybrid predictions of hydrodynamic parameters

The axial and size distribution of bubble swarm is an essential bubble population parameters influencing the design of a BCR for an optimal performance and efficient product yield. From the knowledge of the size and axial distribution of bubble population, all hydrodynamic parameters useful for performance evaluation of a column and for column scale-up design can be estimated.

In addressing the problem of column scale-up design in this chapter, the resolved size and axial distribution of bubble swarm at steady state by the hybrid technique allowed for the prediction of hydrodynamic parameters in the column. The hybrid technique allowed for hydrodynamic parameter predictions through a non-invasive, a non-radioactive, a low-capital-cost, a simple and portable measurement method. The hybrid predicted hydrodynamic parameters agree with published experimental results with associated errors quantified.

Furthermore, the novel hybrid hydrodynamic parameter predictions were explored for scaling the pilot-scale column to a full-scale plant column to achieve a higher volumetric gas-liquid mass transfer rates. The effects of the adjusted parameters in the scale-up on the intensity of multiphase mixing time and the axial liquid and gas dispersion rates were also determined.

Chapter 10

Conclusions

The central goal of this study is to investigate the possibility of harnessing ERT measurements of high temporal resolution but a low spatial resolution for the measurements of bubble population parameters. The knowledge of the bubble population parameters is required for performance description of a column and its scale-up design. The performance description and scale-up design of a column were expected to be achieved through the computation of the hydrodynamic parameters from determined bubble population properties. The measurement of the bubble population parameters can accurately be achieved by a technique that yields both high spatial and temporal resolution. Given these requirements, the ERT measurements without being fused to models of a physical system of a multiphase process will not be suitable for BCR hydrodynamic parameter measurements.

"It was hypothesised in this work that a higher accuracy in interpretation of ERT measurements for accurate hydrodynamic parameter predictions in a column will result from coupling models of a physical system to ERT measurements"

In testing this hypothesis, the images of the steady state axial bubble swarming process was captured by the ERT technique since the ERT low spatial resolution is useful for gas void fraction measurements. The local gas void fractions of the dispersion were simultaneously captured using a differential pressure transmitter by the differential pressure (DP) technique. The differential pressure measurements of the local gas void fractions were validated by the water-head displacement technique. The local DP ε_g for u_g ranging from 0.002-0.016 m/s were compared with published results and good agreements were found with associated errors evaluated as reported in Chapter 4.

The trend of the axial distribution of ε_g for a given u_g was related to the used tubular gas porous sparger design. The bubbles were observed to be uniform and well-distributed at column sections at higher planes well-above the gas distributor region. The bubbles were dispersed through the centre and top of the sparger at the lower column sections closer to the sparger region. The pattern of dispersion leads to variation in bubble population resident times along the column axis during their axial advection transport.

Following the validation of the local ε_g over a range of u_g, the local ERT TACD captured locally were calibrated against the DP data for u_g ranging from 0.002-0.016 m/s. Based on the local calibration graphs, given the ERT TACD, the local gas holdup fraction can be calculated.

In Chapter 5, the high temporal resolution of ERT measurements was harnessed by coupling ERT measurements to DGD process for determination of global bubble size distribution $\bar{n}^{ERT-DGD}(v)$ in the column over a range of u_g. The characteristic times for the disengagement of bubble size classes were determined by calculating the time span or periods for a unit change in the time-variant ERT ACD during a DGD process. The dynamic gas disengagement technique (DGD) describes the phenomenon of bubble population detaching from the liquid phase at varied times due to the difference in bubble sizes rising at varied velocities. By the DGD technique, bubble size classes disengaged according to their sizes with the largest size detaching earliest and the smallest size latest.

The ERT ACD increases with time during a DGD process owing to the decrease in the non-conductive gas volume locally and globally in the column. Thus, for every unit increase in the ERT ACD during a DGD process, the mean disengaging bubble size will be larger than the mean disengaging bubble size at a later unit increase in the ERT ACD. The adopted approach of calculating the characteristic disengagement times of bubble classes yielded a high resolution of bubble classes. The number of captured bubble classes was observed to increase with an increase in u_g. This can be attributed to significant bubble coalescence events that increase with u_g increase yielding bubbles in larger classes. The increase in bubble sizes, thus, increased the length of the disengagement period.

The determined bubble size classes and the obtained log-normal distribution are consistent with empirical correlation results and published distribution as reported in the discussion of Chapter 5.

In Chapter 6, the physical phenomenon of bubble population advection under the influence of bubble coalescence and breakage events controlling the bubble sizes were modelled. The conservative steady state population balance model (PBM) was explored to describe the changing BNDD locally governed by the bubble birth and death by the PBM source terms. The published bubble coalescence model explored was corrected to ensure conservation of gas volume locally. The adopted breakage rate model yielded conservation of gas volume

locally as the bubble population evolve. Because the studied fluid regimes range from homogeneous to transitional regime, there were insignificant breakage events during bubble swarming. Accordingly, the breakage rate was parameterised to ensure insignificant source term contributions in solving the PBM solution. The PBM solutions were subsequently used as initial conditions for DGD processes at varied $u_g s$.

The DGD process described in Chapter 5 was modelled in Chapter 7 to allow for the determination of BNDD depending on bubble size and column height during steady state bubble evolution. The adopted source term models were published correlations in which the component density variation term was calculated by the ideal gas equation while the mass transfer term by the product of K_L and a. Using the PBM solution as the initial condition for the developed DGD process model, the DGD process model was solved to obtain the time-dependent local gas volume during a DGD process.

The solution of the DGD process model was analysed by a developed scheme in Chapter 5 for the calculation of the axially averaged BNDD from the known characteristic times of disengagement of bubble classes. At higher u_g values, the flux gradient within an elemental column section was multiplied by 0.8 to ensure the measured characteristic disengaging gas volumes of classes agree with the modelled results. The parameterisation of the flux gradient was necessary owing to the fluctuating axial transport of bubbles in a bubble class around the column axis during a DGD process. In addition, the utilised gas sparger produced uniform bubble distribution at column section 3 and 4. Thus, the DGD assumptions may not accurately hold at lower column section 1 and 2.

At lower u_g values, the bubble population in classes within an elemental volume was relatively lesser compared to that at higher $u_g s$. It was observed that without parameterising the flux gradient (or multiplied by 1), the measured characteristic disengaging gas volume of bubble classes agree with the modelled results at lower $u_g s$. The resulting local and global BNDDs $\bar{n}^{M-DGD}(v)$ from the analysis of the solution of DGD process model were a log-normal distribution which agrees with results in the literature by alternative techniques.

The size distribution of bubbles in the process of DGD by the ERT measurements and a method of DGD process modelling forms the first criterion for determining the actual axial and size distribution (ANSD) of bubble swarm, $n(v, z)$, in the column. The solution of the

PBM yields the BNDD as a function of column axis and bubble size in the column. The ERT radially averaged BNDD (denoted by $\bar{n}^{ERT-SS}(z)$) was calculated from the gas holdup fraction measurements by the ERT technique and bubble sizes at local sections of the column. The PBM radially averaged BNDD (denoted by $\bar{n}^{PBM-SS}(z)$) was calculated from the ratio of gas volume in a bubble class to the mean bubble volume in the class by analysis of the PBM solution. The $\bar{n}^{ERT-SS}(z)$ and $\bar{n}^{PBM-SS}(z)$ form the second criterion for determining the actual axial and size distribution (ANSD) of bubble swarm, $n(v,z)$, in the column.

The actual ANSD $n(v,z)$ at u_g of 0.016 m/s was determined through parameterisation of inlet BNDD, the bubble coalescence frequency, bubble breakage frequency and the flux gradient during DGD Process. The parameterisation was intended to ensure the $\bar{n}^{M-DGD}(v)$ and $\bar{n}^{ERT-SS}(z)$ agree with the $\bar{n}^{ERT-DGD}(v)$ and $\bar{n}^{PBM-SS}(z)$ respectively. The developed ERT and PBM hybrid algorithm was further validated by utilising it to resolve the ANSD at lower $u_g s$ ranging from 0.01–0.005 m/s. The computed ANSD of bubble swarm at these lower $u_g s$ also allowed for the assessment of the effects of u_g on the determined ANSD of bubbles. The statistical errors between the graphs of $\bar{n}^{ERT-DGD}(v)$ and $\bar{n}^{M-DGD}(v)$ for varied $u_g s$ that do not lie perfectly on each other are stated in Chapter 8.

Furthermore, the resolved ANSD of bubble swarm at steady state by the hybrid algorithm of ERT measurements and a PBM was analysed for the hydrodynamic parameter predictions. The predicted hydrodynamic parameters using empirically validated correlation models were useful for an enhanced design and scale-up of a column. The predicted hydrodynamic parameters values agree with results by empirically validated simulation methods and empirically correlations in literature. The statistical error between the hybrid predicted mass transfer rates and by empirical correlations are stated in Chapter 9. The validity of the hybrid predicted hydrodynamic parameters by a low-capital cost, a non-intrusive, a portable, a non-radio-active technique proves the basis of the hypothesis.

Recommendations

Further work on the developed hybrid of ERT and a PBM algorithm for hydrodynamic parameter predictions in a column using more suitable equipment is encouraged with a view to addressing observed errors in the results. Further extension of the hybrid algorithm of ERT and a PBM will be to include an unsteady state term in the PBM for hybrid prediction of hydrodynamic parameters in an unsteady state system. A hybrid algorithm of such will be efficient for hydrodynamic parameter predictions of an unsteady multiphase flow (for example gas-liquid flow) at higher superficial gas velocities (0.30–0.50 m/s) in a column.

An unsteady state 4D PBM (i.e. 3D space and 1D bubble size) should be solved based on the finite element method (FEM) for adequate fusion with the ERT measurements since the ERT imaging is based on FEM. In addition, the hybrid of ERT and PBM should also be explored for hydrodynamic parameter predictions of 3-phase systems (solid, liquid and gas) in catalysis, crystallisation, bioprocess and mineral processing research studies.

References

Adetunji, 2011. Implementation of an advanced algorithm for enhanced signal analysis in electrical resistance tomography using EODORS toolbox, Cape Town: University of Cape Town.

Adler, A., Borsic, A., Polydorides, N. & Lionheart, W., 2008. *Simple FEMs aren't as good as we thought: experience developing EIDORS V3.3..* Hannover, NH, USA., 9th Conf. Electrical Impedance Tomography,Dartmouth College, Hannover, NH, USA, 16−18 June, 2008..

Akita, F. & Yoshida, k., 1974. Bubble size, interfacial area, and liquid-phase mass transfer coefficient in bubble columns.. *Ind. Eng. Chem. Process Des. Develop.,* 13(1).

Akita, K. & Fumitake, Y., 1974. Bubble size, interfacial area and liquid-phase mass transfer coefficient in bubble columns. *Ind. Eng. Chem., Process Des. Develop.,,* pp. Vol 13, No. 1..

Akita, K. & Yoshida, F., 1973. Gas hold-up and volumetric mass transfer coefficients in bubble columns. *Ind Eng Chem Process Des Dev,* Volume 12, p. 76–80.

Amin, E., Christophe, G. & Jamal, C., 2015. Local hydrodynamics parameters of bubble column reactors operating with non-newtonian liquids: experiments and models developent. *American Institute of Chemical Engineers (AIChE),* p. doi: 10.1002/aic.15130.

Andy, A. & William, R. B. L., 2006 . Uses and abuses of EIDORS: An extensible software base for EIT. *Physiol. Meas. ,* Volume 27, pp. S25-S42.

Anon., n.d.

Azad, M. A. K. & Sultana, R. S., 2006. A numerical model for bubble size distribution in turbulent gas-liquid dispersion.. *Journal of Chemical Engineering,,* 24(1).

Baird, M. & Rice, R., 1975. Axial dispersion in large scale unbaffled columns. . *Chem. Eng. J. ,* Volume 9, pp. 171-174.

Barber, B., Brown, B. & Freeston, I., 1983. Imaging spatial distributions of resistivity using applied potential tomography. *Electronics Let,* Volume 19, pp. 933-935.

Batchelor, G. K., 1953. *The theory of homogeneous turbulence.* Cambridge: Cambridge University press.

Beck, M. S. & Plaskowski, A., 1987. *Cross correlation flowmeters : Their design and application.* Bristol: Hilger.

Behkish, A., 2004. *Hydrodynamic and mass transfer parameters in large - scale slurry bubble column reactors.,* Pittsburgh: PhD, University of Pittsburgh.

Behkish, A., Men, Z., Inga, R. & Mors, i. B., 2002. (2002). Mass transfer characteristics in a large-scale slurry bubble column reactor with organic liquid mixtures. *Chem Eng Sci ,* Volume 57, p. 3307–24.

Behnoosh, M., Ensieh. G, B. & Jafar. S, M., 2009. Experinmental study of gas hold-up and bubble behaviour in gas-liquid bubble column. *Petroleum and Coal,* Volume 51, pp. 27-32.

Bhavaraju, S., Russell, T. & Blanch, H., 1978. The design of gas sparged devices for viscuous liquid systems. *AIChE Journal,* 24(3), pp. 454-466.

Bolton, G. T., Hooper, C. W., Mann, R. & Stitt, E. H., 2004. Flow distribution and velocity measurement in a radial flow fixed bed reactor using electrical resistance tomography. *Chem. Eng. Sci,* Volume 59, pp. 1989-1997.

Bouaifi, M., Hebrard, G., Bastoul, D. & Roustan, M., 2001. A comparative study of gas holdup, bubble size, interfacial area and mass transfer coeffi-cients in stirred gas–liquid reactors and bubble columns.. *Chem Eng Process ,* Volume 40, p. 97–111.

Buchholz, R., Zakrzewski, W. & schugerl, K., 1981. Technique for determining the properties of bubbles in bubble columns. *Int Chem. Eng. ,* Volume 21, pp. 180-187 .

Burgess, J. & Calderbank, P., 1975. The measurement of bubble parameters in two-phase dispersion - the development of an improved probe technique. *Chem. Eng. Sci.,* Volume 30, pp. 743-750 .

Camacho, R. F. et al., 2004. Mixing in bubble columns: a new approach for characterizing dispersion coefficients. *Chemical Engineering Science ,* Volume 59 , p. 4369–4376.

Catherine A., P., 2001. *Statistics for analysis of experimental data,* Princeton, USA: AEESP, Champaign, IL.

Cheney, M. et al., 1990. NOSER: an algorithm for solving the inverse conductivity problem. *Int J Imaging Syst Technol ,* Volume 2, p. 66–75.

Chen, W. et al., 2003. General-ized dynamic modeling of local heat transfer in bubble columns. *Chem Eng J,* Volume 96, p. 37–44.

Clift, R., Grace, J. R. & Weber, M. E., 1978. *Bubble drops and particles.* New York: Academic press.

Clift, R., Grace, J. R. & Weber, M. E., 1978. Bubbles, drops and particles. *Academic press, London. .*

Coulaloglou, C. A. & Tavlarides, L. L., 1977. Description of Interaction Processes in Agitated Liquid-Liquid Dispersions. *Chem. Eng. Sci,* Volume 32, p. 1289.

Daly, J. G., Patel, S. A. & Bukur, D. B., 1992. Measurement of gas holdups and sauter mean bubble diameter in bubble column reactors by dynamic gas disengagement method. *Chem Eng. Sci,* Volume 47, pp. 3647-3654.

Datta, R., Napier, D. & Newitt, D., 1950. The properties and bahaviour of gas bubbles formed at a circular orifice. *Trans. Inst. Chem. Engrs.,* 2(14).

Davidson, J. L. et al., 2004. Three dimensional electrical impedance tomography applied to a metal-walled filtration test platform. *Meas. Sci. Technol.,* Volume 15 , p. 2263..

Deckwer, W. .., Nguyen-tien, K., Godbole, B. & T, S. Y., 1983. On the applicability of the axial dispersion model in bubble columns. *AIChE J,* Volume 29, pp. 915-922.

Deckwer, W., 1986. *Design and simulation of bubble column reactors in chemical reactor design and technology.* Ed. H. I. de Lasa ed. Dordrecht and Boston: Martinus Nijholt Publishers.

Deckwer, W., Burckhart, R. & Zoll, G., 1974. Mixing and mass transfer in tall bubble columns. *Chem. Eng. Sci. ,* Volume 29, pp. 2177-2188.

Deckwer, W. D., Adler, I. & Zaidi, A., 1978. A comprehensive study on C02 - Interphase mass transfer in vertical cocurrent and countercurrent gas flow. *Canadian Journal of Chemical Engineering,* 56(43).

Deckwer, W. D. & Schumpe, A., 1993. Improved tools for bubble column reactor design and scale-up. *Chemical Engineering Science.,* 48(5), pp. 889-991.

Deckwer, W., Louisi, Y., Zaidi, A. & Ralek, M., 1980. Hydrodynamic properties of the Fisher–Tropsch slurry process. *Ind Eng Chem Process Des Dev,* Volume 19, p. 699–708.

Degaleesan, S., Dudukovic, M. & Pan, Y., 2001. Experimental study of gas-induced liquid-flow structures in bubble columns. *AIChE J ,* Volume 47, p. 1913–31.

Essadki, H., Nikov, I. & Delmas, H., 1997. Electrochemical probe for bubble size prediction in a bubble column. *Exp Therm Fluid Sci.,* Volume 14, p. 243–50.

Fan, L., A, M. & Chern, S., 1985. Hydrodynamic characteristics of a gas–liquid–solid fluidized bed containing a binary mixture of particles. *AIChE J ,* Volume 31, p. 1801–10.

Fan, L. S. & Tsuchiya, K., 1990. Bubble wake dynamics in liquids and liquid-solid suspensions. *Butterworth- Heinemann, Boston .*

Field, R. W. & Davidson, J. F., 1980. Axial dispersion in bubble columns. *Trans. Inst. Chem. Engrs,* Volume 52, pp. 1-9.

Francesca, S., Antonio, B., Franco, G. & Alberto, B., 2014. Bubble formation at variously inclined nozzles. *Chemical Engineering Technology,* Volume 37, pp. 1507-1514.

Fransolet, E., Crine, M., Marchot, P. & Toye, D., 2005. Analysis of gas holdup in bubble columns with non-Newtonian fluid using electrical resistance tomography and dynamic gas disengagement technique.. *Chem Eng. Sci. ,* Volume 60 , pp. 6118-6123.

Friendlander, S. K., 1977. *Smoke, dust and haze.* New York : John Wiley and Son.

Fukuma, M., Muroyama, K. & A, Y., 1987. Properties of bubble swarm in a slurry bubble column. *J. Chem Eng. Japan,* Volume 20, pp. 28-33.

Gauss, C. F., 1965. *Disquisitiones Arithmeticae. tr. Arthur A. Clarke..* Yale : University Press. ISBN 0-300-09473-6.

Goble, J., Cheney, M. & Isaacson, D., 1992. Electrical impedance tomography in three dimensions. *Journal of computational electromagnetic,* pp. 128-147.

Grund, G., 1988. *Hydrodynamische Parameter und Stoffaustauscheigenschaften in Blasens$iulen mit organischen Medien,* Germany: PhD thesis, Universittit Oldenburg.

Haibo, J., Mi, W. & Williams, R., 2007. Analysis of bubble behaviour in bubble columns using electrical resistance tomography. *Chemical engineering journal ,* Volume 130 , pp. 179-185.

Halliday, D. & Resnick, R., 1970. *Fundermentals of Physics.* s.l.:John Wiley and Sons Inc.

Hashemi, N., En-Mozaffari, F., Upreti, S. & Hwang, D. K., 2016. Experimental investigatiion of the bubble behaviour in an aerated coaxial mixing vessel through electrical resistance tomography (ERT). *Chemical Engineering Journal,* Volume 289, pp. 402-412.

Helene, C., Anne-Marie, B. & Henri, D., 2006. Axial and radial investigation of hydrodynamics in a bubble column: influence of fluid flow rates and sparger type. *International Journal of Chemical Reactor Engineering,* Volume 4.

Helga, R., Benjamin, J. & Chow, A. A., 2009 . *EIT measurement of heart and lung perfusion.* University of Manchester, UK, 10th Int. Conf. Biomed. Appl. Electrical Impedance Tomography, 16th-19th June 2009 .

Hesketh, R. P., Etchells, A. W. & Russell, T. W. F., 1991. Experimental Observations of Bubble Breakage in Turbulent Flow. *Ind. Eng. Chem. Res,* 30(845).

Hikita, H. et al., 1981. Heat transfer coefficient in bubble column. *Ind Eng Chem Process Des Dev ,* Volume 20, p. 540–5.

Hikita, H. et al., 1980. Gas holdup in bubble column. *Chem Eng J ,* Volume 20, p. 59–67.

Hughmark, G. A., 1967. *Ind. Eng. Chem. Process Des. Dev.,* Volume 6, p. 218–220.

Hyndman, C. L., Larachi, F. & Guy, C., 1997. Understanding gas-phase hydro-dynamics in bubble columns: a convective model based on kinetic theory. *Chem Eng Sci.,* Volume 52, p. 63–77.

Jari, K., Timo, N. & Lasse, M. H., 2011 . Application of three-dimensional electrical resistance tomography to characterize gas holdup distribution in laboratory flotation cell. *Minerals Engineering ,* Volume 24, pp. 1677-1686.

Jia, J., Wang, M. & Faraj, Y., 2015. Evaluation of EIT systems and algorithms for handing full void fraction range in two-phase flow measurements. *Neasurenebt Science and Technology,* Volume 26, p. 015305.

Jin, H., Yang, S., Wang, M. & A, W. R., 2007. Measurement of gas holdup profiles in a gas liquid cocurrent bubble column using electrical resistance tomography. *Flow measurement and Instrumentation ,* Volume 18, pp. 191-196.

Johnson, W. J., D'Appolonia & Monroeville, P. A., 2003. *Application of electrical resistance method for detection of underground mine workings..* lexington, Geophysical technologies for detecting underground coal mine voids, .

Joseph, S. & Shah, Y. T., 1984. *A two-bubble class model for churn-turbulent bubble column slurry reactors..* s.l., ACS Symp. Ser. 27, 149-167..

Jun, W. et al., 2015. Prediction of gas-liquid interfacial area in valve trays. *AIChE,* Volume 00, pp. 00-00.

Kantarci, N., Fahir, B. & Kutlu, O. U., 2005. Bubble column reactors. *Process Biochemistry,* Volume 40, pp. 2263-2283.

Kara, S., Kelkar, B., Shah, Y. & Carr, N., 1982. Hydrodynamics and axial mixing in a three-phase bubble column. *Ind Eng Chem Process Des Dev,* Volume 21, p. 584–94.

Kato, Y. & Nishiwaki, A., 1972. Longitudinal dispersion coefficient in a liquid in a bubble column. *Chem. Eng. ,* Volume 12, pp. 182-187.

Kawagoe, K., Inoue, T., Nakao, K. & Otake, T., 1976. Flow-pattern and gas holdup conditions in gas-sparged contactors.. *Int J Chem Eng ,* Volume 6, p. 176–83 .

Kawase, Y., 1990;. The energy dissipation rate concept for turbulent heat and mass transfer in drag-reducing fluids.. *Int Commun Heat Mass Trans,* Volume 17, p. 155–66.

Kawase, Y., Halard, B. & Moo-Young, M., 1987. *Chem. Eng. Sci. 42 ,* p. 1609–1617.

Kawase, Y. & Moo-Young, M., 1989. Mixing time in bioreactors.. *Journal of Chemical Technology and Biotechnology,* Volume 44, p. 63–75.

Kawase, Y., Umeno, S. & Kumagai, T., 1992. *Chem. Eng. J. ,* Volume 50, p. 1–7.

Kennard, E. H., 1938. *Kinetic Theory of Gases.* s.l.:McGraw-Hill, New York.

Kim, W. K. & Lee, K. L., 1987. Coalescence Behaviour of Two Bubbles in Stagnant Liquids. *J. of Chem. Eng. of Japan,* Volume 449, p. 20.

Kirkpatrick, R. D. & Lockett, M. J., 1974. The Influence of Approach Velocity on Bubble Coalescence. *Chem. Eng. Sci,* Volume 29, p. 2363 .

Koide, K., Hirahara, T. & Kubota, H., 1966. Average Bubble Diameter, Slip Velocity and Gas Holdup of Bubble Swarms. *Kagaku Kogaku,* Volume 30, pp. 712-718.

Koide, K., Takazawa, A., Komura, M. & Matsunga, H., 1984. Gas holdup and volumetric liquid phase mass transfer coefficient in solid-suspended bubble column. *J Chem Eng Jpn,* Volume 17, p. 459–66.

Kolmogorov, A. N., 1949. On the breakage of drops in a turbulent flow. *Dokl. Akad. Navk. SSSR ,* Volume 66, p. 825–828.

Krishna, R. et al., 1997. Gas holdup in slurry bubble columns: effect of column diameter and slurry concentrations.. *AIChE J ,* Volume 43, p. 311–6.

Krishna, R. et al., 1997. Gas holdup in slurry bubble columns: effect of column diameter and slurry concentrations. *AIChE J,* Volume 43, p. 311–6.

Krishna, R., Wilkinson, P. & Van, D. L., 1991. A model for gas holdup in bubble columns incorporating the influence of gas density on flow regime transitions. *Chem Eng Sci,* Volume 46, p. 2491–6.

Kuboi, R., Komasawa, I. & Otake, T., 1972a. Behaviour of Dispersed Particles in Turbulent Liquid Flow. *J. Chem. Eng. Japan,* Volume 5, p. 349.

Kuboi, R., Komasawa, I. & Otake, T., 1972b. Collision and Coalescence of Dispersed Drops in Turbulent Liquid Flow. *J. Chem. Eng. Japan,,* Volume 5, p. 423.

Laari, A. & Turunen, I., 2003. Experimental Determination of Bubble Coalescence and Break-up Rates in a Bubble Column Reactor. *Canadian Journal of Chemical Engineering,* Volume 81(3-4), pp. 395-401.

Laari, A. & Turunen, I., 2005. Prediction of coalescence properties of gas bubbles in a gas-liquid reactor using persistence time measurements. *IChemE,* 83(A7), pp. 881-886.

Lage, P. L. C., 1996. *The non-uniform bubble size distribution in bubble columns: the choice of bubble mean diameter for mass transfer.* s.l., Proc. of XXVI ENEMP (Brazillian Congress on particulate SYstems) II : .631-636.

Lehr, F. & Mewes, D., 2001. A transport equation the interfacial area density applied to bubble column. *Chemical Engineering Science. ,* Volume 56, pp. 1159-1166.

Leonard, C. et al., 2015. Bubble column reactors for high pressure and high temperatures operation. *Chemical Engineering Research and Design,* Volume 100, pp. 391-421.

Lesparre, N., Andy, A., Dominique, G. & Florence, N., 2011. *Electrical impedance tomography in geophysics, application of EIDORS..* Bath, UK, Conf EIT 2011.

Levenspiel, 1972. *Chemical reaction engineering. J..* New York.: VViley and Sons.

Levich, V. G., 1962. *Physicochemical Hydrodynamics.* NJ: Prentice-Hall, Engle-wood Cliffs .

Li, H. & Prakash, A., 2000. Influence of slurry concentrations on bubble population and their rise velocities in three-phase slurry bubble column. *Powder Technol,* Volume 113, p. 158–67.

Li, H. & Prakash, A., 2001. Survey of heat transfer mechanisms in a slurry bubble column. *Can J Chem Eng,* 79(717–25).

Lionheart, W., Polydorides, N. & Borsic, A., 2004. *Electrical impedance tomography : methods, history and applications.* s.l.:Institute of physics publishing, ISBN 0750309520.

Lockett, M. & Kirkpatrick, R., 1975. Ideal bubbly flow and actual flow in bubble columns. *Trans Inst Chem Eng,* Volume 53, p. 267–73..

Long, T., 2006. *An on-line velocity flow profiling system using electrical resistance tomography,* Cape Town, South Africa: University of Cape Town, South Africa.

Luo, H., 1993. *Coalescence, breakup and liquid circulation in bubble column reactors.,* Trondheim, Norway: Ph.D thesis, Department of Chemical Engineering, The institute of Norwegian institute.

Luo, X. et al., 1999. Maximum stable bubble size and gas holdup in high-pressure slurry bubble columns. *AIChE J,* Volume 45, p. 665–85.

Majumder, S., Kundu, G. & Mukherjee, D., 2006. Bubble size distibution and gas-liquid interfacial area in a modified downflow bubble column. *Chemical Engineering Journal,* Volume 122, pp. 1-10.

Mangartz, K. H. & Th, P., 1980. Untersuchungen zur Gasphasendispersion in Blasens&ulenreaktoren.. *Verfahrenstechnik (Mainz) ,* Volume 14, pp. 40-46.

Mangertz, K. H. & Pilhofer, T., 1981. The interpretation of mass transfer measurements in bubble columns considering dispersion in both phases. *Chem. Engr. Sci.,* Volume 31, pp. 1069-1077.

Mann, R. et al., 1997. Application of electrical resistance tomography to interrogate mixing processes at plant scale. *Chemical Engineering Science ,* Volume 52, p. 2087–2097.

Marco, M. & Mewes, D., 1999. Interfacial area density in bubbly flow. *Chemical Engineering and Processing,* Volume 38, pp. 307-319.

Martinez, C. et al., 2010. Considerations on bubble fragmentation models. *J. fluid mech. vol.,* Volume 661, p. 159 – 177.

Maxwell, J., 1873. *A Treatise on Electricity and Magnetism.* Oxford: Clarendon Press.

Mendelson, H. D., 1967. The prediction of bubble terminal velocities from wave theory. *AIChE J.,* Volume 13, pp. 250-253.

Metherall, P., Barber, D., Smallwodd, R. & Brown, B., 1996. Three-dimensional electrical impedance tomography. *Nature,* Volume 380, pp. 509-512.

Mitre, J., Takahashi, C., Ribeiro, J. & Lage, P., 2010. Analysis of breakage and coalescence models for bubble columns. *Chemical Engineering Science,* Volume 65, pp. 6089-6100.

Miyauchi, T., Rufusaki, S., Morooka, S. & lkeda, Y., 1981. In: New York: Academic Press, pp. 275-448.

Motarjemi, M. & Jameson, J. G., 1978. Mass transfer from very small bubbles - the optimum bubble size for aeration. *Chem Eng. Sci. ,* Volume 33, pp. 1415-1423.

Mott, C., 2006. High-efficiency gas-lqiuid contacting. *www.mottcorp.com/resoruce/pdf/sparging.pdf.*

Nagel, O., Kurten, H. & Hegner, B., 1979. Design of gas-liquid reactors: mass transfer area and input of Energy.. In: G. V. T. a. N. H. A. F. Durst, ed. *wo-phase momentum heat and mass transfer in chemical process and engineering systems.* Washington DC: Hemisphere Publ. Corp., pp. 2, 835.

Nambiar, D. K. R., Kumar, R., Das, T. R. & Gandhi, K. S., 1992. A New Model for the Breakage Frequency of Drops in Turbulent Stirred Dispersions. *Chem. Eng. Sci.,* Volume 47, p. 2989.

Nauman, E., 2008. *Chemical reactor design, optimization, and scaleup.* Second Edition ed. s.l.:Wiley.

Nikolaos, A., Aikaterini, A. & Spios, V. P., 2007. *Experimental study of bubble formation at porous spargers.* Leipzig, Germany, ICMF.

Okonkwo, A., Wang, M. & Azzopardi, B., 2012. Characterisation of a high concentration ionic bubble column using electrical resistance tomography. *Flow measurement and instrumentation. ,* 12(S0955-5986), pp. 00118-5 .

Oolman, T. & Blanch, H. W., 1986a. Bubble Coalescence in Air-Sparged. *Bioreactors. Biotech. Bioeng.,* Volume 28, p. 578.

Oolman, T. & Blanch, H. W., 1986b. Bubble Coalescence Stagnant Liquids. *Chem. Eng. Commun. ,* Volume 43, p. 237 .

Oztijrk, S. S., Schumpe, A. & Deckwer, W. D., 1987. Organic liquids in a bubble column: Hold-ups and mass transfer coefficients. *AIChE J. B, ,* pp. 1473-1480..

Ozturk, S., Schumpe, A. & Deckwer, W., 1987. Organic liquids in a bubble column: holdups and mass transfer coefficients. *AIChE J ,* Volume 33, p. 1473–80.

Pakzad, L., Ein-Mozzafari, F. & Chan, P., 2008. Using electrical resistance tomography and computational fluid dynamics modelling to study the formation of cavern in the mixing of pseudoplastic fluids possessing yield stress. *Chem. Engr Sci.,* Volume 63, pp. 2508-2522.

Patel, S. A., Daly, J. G. & Bukur, D. B., 1989. Holdup and interfacial area measurements using dynamic gas disengagement.. *AIChE ,* Volume 35, pp. 931-942.

Pinheiro, P., Loh, W. & Dickin, F., 1998. Three-dimensional Reconstruction Algorithm for Electrical Resistance Tomography. *IEE Proc.-Sci. Meas. Technol,* Issue 3, p. 145.

Pino, L. Z. et al., 1992. Effect of operating conditions on gas holdup in slurry bubble columns with a foaming liquid.. *Chem Eng Commun ,* Volume 117, p. 367–82.

Polydorides, N. & Lionheart, W., 2002. A MATLAB Toolkit for three-dimensional electrical impedance tomography: a contribution to the electrical impedance and diffuse optical reconstruction software project. *Meas. Sci. T Institute of Phyiscs Publishing,* Volume 13, pp. 1871-1883.

Prakash, A., Margaritis, A. & Li, H., 2001. Hydrodynamics and local heat transfer measurements in a bubble column with suspension of yeast. *Biochem Eng J ,* Volume 9, p. 155–63.

Prakash, A., Margaritis, A. & Li, H., 2001. Hydrodynamics and local heat transfer measurements in a bubble column with suspension of yeast.. *Biochem Eng J. ,* Volume 9, p. 155–63.

Prince, M. J. & Blanch, H. W., 1990. Bubble Coalescence and Break-up in Air-Sparged Bubble Columns.. *AIChE J. ,* 36(10).

Ramkrishna, D. & Borwanker, J. D., 1973. A puristic analysis of population balance. *Chemical Engineering Science. ,* Volume 28, pp. 1423-1435.

Randall, E., Long, T. & Sutherland, A., 2007. *The UCT Electrical Resistance Tomography instrument and its applications..* South Africa, The South African Institute of Mining and Metallurgy. Tomography symposium..

Randolph, A. D., 1964. A population balance for countable entities. *Canadian J. Chem. Eng.,* Volume 42, pp. 280-281.

Ribeiro, C. P. & Lage, P. L., 2004. Experimental study on bubble size distributions in a direct-contact evaporator. *Brazilian Journal of Chemical Engineering,* 21(01), pp. 69-81.

Ricard, F., Brechtelsbauer, C., Xu, X. & Lawrence, C., 2005. Monitoring of multiphase pharmaceutical processes using electrical resistance tomography. *Chemical Engineering Research and Design,* Volume 83, pp. 794-805.

Riquelme, A., Desbiens, A., Delvillar, R. & Maldonado, M., 2016. Predictive control of the bubble size distrobution in a two-phase pilot flotation column. *Mineral Engineering,* Volume 89, pp. 71-76.

Robert, M. W. et al., 2002. In situ imaging of paste extrusion using electrical impedance tomography. *Meas. Sci. Technol,* Volume 13, p. 1890.

Rodgers, T. et al., 2009. Tomographic imaging during semibatch reactive precipitation of barium sulphate in a stirred vessel. *Chemical Engineering Research and Design,* 87(4), pp. 615-626.

Rollbusch, P. et al., 2015. Bubble columns operated under industrially relevant conditions - current understanding of design parameters. *Chemical Engineering Science,* Volume 126, pp. 660-678.

Ross, H., Benjamin, J., Chow, W. & Adler, A., 2009. *EIT measurement of heart and lung perfusion..* University of Manchester, UK, 10th int. Conf. Biomed. Appl. Electrical Impedance Tomography .

Ruzicka, M. C., Zahadnik, J., Drahos, J. & Thomas, N. H., 2001. Homogeneous–heterogeneous regime transition in bubble columns.. *Chem. Eng Sci. ,* Volume 56, p. 4609–26.

Sailesh. B, K., Davood, M. & Milorad. P, D., 1997. Gas holdup measurements in bubble columns using computed tomography. *AIChE,* Volume 43, pp. 1414-1428.

Sattar, M., Naser, J. & Brooks, G., 2013. Numerical Simulation of two-phase flow with bubble break-up and coalescence coupled with population balance modeling. *Chemical ENgineering and Processing: Process Intensification,* Volume 70, pp. 66-76.

Saxena, S., Rao, N. & Saxena, A. C., 1990. Heat-transfer and gas-holdup studies in a bubble column: air–water–glass bead system. *Chem Eng Commun,* Volume 96, p. 31–55.

Schumpe, A. & Deckwe, W. D., 1981. Determination of interfacial areas in non-newtonian gas-liquid flow. *Paper presented at the ACM meeting, Atlanta.*

Schumpe, A. & Grund, G., 1986. The gas disengagement technique for studying gas holdup structure in bubble columns. *Can J Chem Eng,* Volume 64, p. 891–6.

Shah, Y., Godbole, S. & Deckwer, W., 1982. Design parameters estimations for bubble column reactors. *AIChE J.,* Volume 28, p. 353–379.

Shah, Y., Kelkar, B., Godbole, S. & Deckwer, W., 1982. Design parameters Estimations for bubble column reactors. *AIChE J.,* Volume 28, p. 353–379.

Shah, Y. T. & Deckwer, W. D., 1983. Hydrodynamics of bubble columns. In: A. A. S. P. A. A. Eds. N. P. Cheremisinoff and R. Gupta, ed. *In: Handbook of fluid in motion*, pp. 583-620.

Shah, Y. T., Joseph, S., Smith, D. N. & A, R. J., 1985. Two-bubble class model for churn-turbulent bubble column reactor. *Ind. Eng. Chem. Proc. Des. Dev.,* Volume 24, pp. 1096-1104.

Shah, Y. T., Kelkar, B. G., Godbole, S. P. & Deckwer, W. D., 1982. *AIChE J. 28,* p. 353–379..

Shimizu, K., Takada, S., Minekawa, K. & Kawase, Y., 2000. Phenomenological model for bubble column reactors: prediction of gas hold-ups and volumetric mass transfer coefficients. *Chemical Engineering Journal ,* Volume 78, p. 21–28.

Sriram, K. & Mann, R., 1977 . Dynamic gas disengagement a new technique for assessing the behaviour of bubble columns. *Chemical Engineering Science,* Volume 32, pp. 571-580.

Steinemann, J. & Buchholz, R., 1984. Application of an electrical conductivity microprobe for the characterization of bubble behaviour in gas-liquid bubble flow. *Part. Charact. ,* Volume 1, pp. 102-107 .

Stephenson, D., Rodgers, T., Mann, R. & York, T., 2009. *Application of three-dimensional electrical impedance tomography to investigate fluid mixing in a stirred vessel.* London , 13th European Conference on Mixing.

Stephenson, D., York, T. & Mann, R., 2007. *Performance and Requirement of Process ERT Instruments.* Bergen, Norway, 5th World Congress on Industrial Process Tomography.

Stevenson, R., 2006. *Analysis of particle suspension and mixing in biological systems: an application of tomography,* Cape Town: Ph.D thesis, University of Cape Town, South Africa.

Sudhakaran, H., 2010. *Application of electrical resistance tomography in evaluating the influence of nozzle design on the gas hold-up distribution in boiling bubble column reactors.* Beijing, 6th World conference on Industrial process tomography.

Tadaki, T. & Maeda, S., 1961. On the shape and the velocity of single air bubbles rising in velocity liquids. *Kagaku Kogaku ,* Volume 25, pp. 254-264 .

Tao, D., Manuchehr, S. & Andy, A., 2008. EIT image reconstruction with four dimensional regularization. *Med Biol Eng Comput ,* Volume 46, pp. 889-899.

Tao, D., Manuchehr, S. & Andy, A., 2008. EIT image reconstruction with four dimensional regularization. *Med Biol Eng Comput ,* Volume 46, p. 889–899.

Tennekes, H. & Lumley, J. L., 1972. *A First Course in Turbulence.* Cambridge, MA: The MIT Press.

Thorat, B. N. & Joshi, J. B., 2004. Regime transition in bubble columns: experi-mental and predictions. *Exp Therm Fluid Sci. ,* Volume 28, p. 423–30.

Tossavainen, O., Vauhkonen, M., Heikkinen, L. & Savolainen, T., 2004. Estimating shapes and freesurfaces with electrical impedance tomography. *Meas Sci Technol ,* Volume 15, p. 1402–1411.

Ueyama, K. & Miyauchi, T., 1976. Determination of Mean Bubble diameters based on Observation by a Two Point Electric Probe. *Kagaku Kogaku, Ronbunshu,* 2(430).

Ueyama, K. & Miyauch, i. T., 1979. Properties of recirculating turbulent two phase flow in gas bubble columns. *AlChE J. z, ,* pp. 258-266.

Vandu, C. O. & Krishna, R., 2004. Volumetric mass transfer coefficients in slurry bubble columns operating in churn-turbulentflow regime. *Chem Eng Process ,* Volume 43, p. 987–95.

Van, K., W, D. & Hoftijzer, P., 1950. Studies of gas bubble formation. *Chem Eng. Progr.,* 46(29).

Vauhkonen, P., Vauhkonen, M., Savolainen, T. & Kaipio, J., 1999. Three-dimensional electrical impedance tomography based on the complete electrode model.. *IEEE Trans Biomed Eng ,* 46(9), p. 1150–1160.

Veera, U. P., Kataria, K. L. & Joshi, J. B., 2004. Effect of superficial gas velocity on gas hold-up profiles in foaming liquids in bubble column reactors. *Chem Eng J ,* Volume 99, p. 53–8.

Vijayan, M., Schlaberg, H. & Wang, M., 2007. Effects of sparger geometry on the mechanism of flow pattern transition in a bubble column. *Chemical Engineering,* Volume 130, pp. 171-178.

Vijayan, M., Schlaberg, H. & Wang, M., 2007. Effects of sparger geometry on the mechanism of flow pattern transition in a bubble column. *Chemical Engineering Journal,* Volume 130, pp. 171-178.

Wachi, S. & Nojima, Y., 1990. Gas-phase dispersion in bubble columns. *Chem. Eng. Sci. a,,* pp. 901-905.

Waldo, C., Roelof, L., Coetzer, J. & Randhir, R., 2012a. Semianalytical bubble-flow models for the development of a novel bubble column simulator. *Ind. Eng. Chem. Res.,* Volume 51, pp. 7398-7409.

Waldo, C., Roelof, L., Coetzer, J. & Randhir, R., 2012b. Response surface strategies in constructing statistical bubble flow model for the development of a novel bubble column simulation approach. *Computer and chemical Engineering,* Volume 36, pp. 22-34.

Walters, J. & Blanch, H. W., 1983. Liquid Circulation Patterns and their Effect on Gas Holdup and Axial Mixing in Bubble Columns. *Chem. Eng. Commun.,* Volume 19, p. 243.

Wells, P. N. T., 2005. "Sir Godfrey Newbold Hounsfield KT CBE. 28 August 1919 - 12 August 2004: Elected F.R.S. 1975". *Biographical Memoirs of Fellows of the Royal Society,* Volume 51, p. 221–210.

Wikipedia, 2014. Allan McLeod Cormack.. *[ONLINE] Available at:http://en.wikipedia.org/wiki/Allan_McLeod_Cormack. .*.

Wikipedia, 2014. Tomography. *http://en.wikipedia.org/wiki/Tomography*.

Wilkinson, A. J. et al., 2005. A 1000-measurement frames/second ERT data capture system with real-time visualization. *IEEE Sens J ,* p. 300 – 307.

William, L., Nicholas, P. & Andrea, B., 2002. *The recostruction problem.* David Holder ed. Manchester Institute for Mathematical Sciences, School of Mathematics, The University of Manchester, ISSN 1749-9097.

Williams, 1999. Industrial Monitoring of Hydrocyclone Operation, *Minerals Engineering,* 12 (10), pp. 1245-1252.

Wu, Y., Ong, B. J. & Al-Dahhan, M. H., 2001. Predictions of gas hold-up profiles in bubble column reactors. *Chem Eng Sci ,* Volume 56, p. 1207–10.

Yorkey, T., Webster, J. & Tompkins, W., 1987. Comparing reconstruction algorithms for electrical impedance tomography. *IEEE Trans Biomed Eng ,* Volume 34, p. 843–852.

Yu, Y. & Kim, S. D., 1990. Bubble properties and local liquid velocities in the radial direction of concurrent gas-liquid flow. *Chem Eng. Sci.,* Volume 45, pp. 313-320.

Appendix A

Tables of graphical results in Chapter 4 and the area average of conductivity distribution with time during gas disengagement process

Table A1.1. The maximum, minimum and TACD values of the area within the first electrode layer for 3 repeated measurements for superficial gas velocities ranging from 0.002-0.016 m/s.
Key - U_g represents gas flow rates (m/s).

U_g (m/s)	Max. value of cond. (unit)			Mean value of cond. (unit)			Min. value of cond. (unit)		
Meas.	1	2	3	1	2	3	1	2	3
0.002	8.41	10.77	8.89	-3.6	-3.6	-3.63	-37.54	-40.43	-36.26
0.003	9.69	11.13	11.33	-4.81	-4.84	-4.76	-54.1	-58.64	-60.7
0.004	12.19	10.05	11.4	-5.75	-6.15	-5.47	-70.83	-62.49	-65.15
0.005	10.53	9.45	7.92	-7.83	-7.35	-7.74	-80.86	-77.99	-72.67
0.006	11.42	9.01	9.02	-8.31	-8.09	-8.29	-94.29	-87.63	-84.75
0.007	14.13	22.47	11.19	-9.58	-7.52	-9.88	-100.51	-108.58	-106.36
0.008	11.11	15.13	11.13	-10.89	-10.92	-10.78	-116.22	-117.05	-122.63
0.009	13.49	11.15	9.38	-11.8	-12.21	-11.73	-124.53	-132.92	-120.75
0.010	19.46	11.94	17.67	-13.56	-14.13	-12.41	-146.62	-132.8	-134.74
0.016	17.76	25.31	16.98	-24.72	-23.99	-24.79	-231.59	-239.66	-235.35

Table A1.2. The maximum, minimum and TACD values of the area within the second electrode layer for 3 repeated measurements for superficial gas velocities ranging from 0.002-0.016 m/s.

V_g (m/s)	Max. value of cond. (unit)			Mean value of cond. (unit)			Min. value of cond. (unit)		
Meas.	1	2	3	1	2	3	1	2	3
0.002	8.08	7.81	6.23	-3.2	-3.72	-3.98	-36.73	-36.45	-31.81
0.003	8.37	10.86	9.36	-6.09	-5.33	-5.54	-49.3	-55.05	-45.64
0.004	12.57	10.85	12.25	-7.59	-7.68	-5.99	-49.95	-58.19	-58.91
0.005	15.49	14.59	15.65	-10.71	-9.31	-10.1	-76.5	-93.07	-75.8
0.006	20.15	14.13	19.01	-11.27	-9.98	-10.99	-95.68	-87.74	-90.32
0.007	23.96	127.67	19.91	-12.01	-10.11	-12.37	-106.1	-166.83	-114.29
0.008	34.3	79.37	21.82	-11.77	-14.56	-15.06	-133.4	-128.11	-135.18
0.009	16.54	30.96	22.71	-16.78	-16.2	-17.84	-160.47	-142.76	-146.39
0.010	42.61	26.39	48.7	-17.03	-19.7	-17.01	-172.41	-158.83	-169.78
0.016	60.30	98.63	65.92	-36.91	-32.83	-37.28	-375.55	-374.62	-359.64

Table A1.3. The maximum, minimum and TACD values of the area within the third electrode layer for 3 repeated measurements for superficial gas velocities ranging from 0.002-0.016 m/s.

V_g (m/s)	Max. value of cond.			Mean value of cond.			Min. value of cond.		
Meas.	1	2	3	1	2	3	1	2	3
0.002	7.44	7.46	7.15	-4.67	-4.47	-4.92	-34.33	-37.81	-34.24
0.003	7.98	9.65	8.43	-8.1	-7.29	-7.33	-51.58	-43.54	-52.11
0.004	11.00	11.21	11.76	-9.02	-9.46	-9.19	-60.74	-54.72	-55.98
0.005	11.13	13.86	13.33	-12.87	-10.97	-11.33	-73.7	-86.17	-74.17
0.006	22.08	16.45	17.42	-14.51	-12.69	-13.87	-101.89	-89.37	-98.96
0.007	22.86	30.16	29.95	-15.92	-15.32	-15.51	-119.98	-140.25	-128.86
0.008	95.72	26.17	18.07	-16.01	-18.24	-18.93	-16.01	-128.23	-130.65
0.009	40.51	29.87	29.09	-20.86	-20.24	-20.41	-154.83	-183.42	-144.44
0.010	45.34	33.52	40.2	-22.45	-22.82	-22.99	-197.98	-159.86	-173.35
0.016	121.63	107.36	65.38	-45.02	-40.97	-45.86	-353.51	-355.69	-386.08

Table A1.4. The maximum, minimum and TACD values of the area within the fourth electrode layer for 3 repeated measurements for superficial gas velocities ranging from 0.002-0.016 m/s.

V_g (m/s)	Max. value of cond.			Mean value of cond.			Min. value of cond.		
Meas.	1	2	3	1	2	3	1	2	3
0.002	8.33	9.22	8.81	-4.45	-4.13	-4.13	-30.55	-33.78	-28.11
0.003	9.24	8.99	9.33	-7.51	-6.66	-7.29	-41.64	-39.69	-42.32
0.004	10.64	11.67	10.62	-8.24	-9.39	-9.87	-54.93	-47.71	-52.85
0.005	11.34	12.26	14.43	-11.55	-11.69	-10.27	-61.83	-68.16	-70.10
0.006	17.36	17.22	20.65	-13.04	-12.96	-12.64	-75.01	-84.85	-96.67
0.007	24.94	30.32	24.07	-15.09	-16.23	-15.11	-113.74	-109.46	-131.37
0.008	53.95	19.18	26.08	-18.00	-17.33	-17.91	-144.17	-116.40	-150.28
0.009	44.50	33.33	36.40	-21.31	-20.11	-20.49	-161.58	-161.35	-215.20
0.01	37.37	31.91	47.50	-22.2	-23.21	-23.90	-183.59	-161.00	-177.08
0.016	61.14	81.45	67.58	-47.72	-45.04	-45.5	-430.03	-471.64	-354.35

Table A1.5. The mean of maximum, minimum and TACD of the area within the first electrode averaged over the number of measurements.

U_g (m/s)	Averaged over 3 repeated measurement		
	Mean(σ^{max})	Mean($\bar{\sigma}_A^f$)	Mean(σ^{min})
0.002	9.36	-3.61	-38.08
0.003	10.72	-4.80	-57.81
0.004	11.21	-5.79	-66.16
0.005	9.30	-7.64	-77.17
0.006	9.82	-8.23	-88.89
0.007	15.93	-8.99	-105.15
0.008	12.46	-10.86	-118.63
0.009	11.34	-11.91	-126.07
0.010	16.36	-13.37	-138.05
0.016	20.02	-24.50	-235.53

Table A1.6. The mean of maximum, minimum and TACD values of the area within the second electrode averaged over the number of measurements.

U_g (m/s)	Averaged over 3 repeated measurement		
	Mean(σ^{max})	Mean($\bar{\sigma}_A^f$)	Mean(σ^{min})
0.002	7.37	-3.63	-35.00
0.003	9.53	-5.65	-50.00
0.004	11.89	-7.09	-55.68
0.005	15.24	-10.04	-81.79
0.006	17.76	-10.75	-91.25
0.007	57.18	-11.50	-129.07
0.008	45.16	-13.80	-132.23
0.009	23.40	-16.94	-149.87
0.01	39.23	-17.91	-167.01
0.016	74.95	-35.67	-369.94

Table A1.7. The mean of maximum, minimum and the TACD of the area within the third electrode averaged over the number of measurements.

U_g (m/s)	Averaged over 3 repeated measurements		
	Mean(σ^{max})	Mean($\bar{\sigma}_A^f$)	Mean(σ^{min})
0.002	7.35	-4.69	-35.46
0.003	8.69	-7.57	-49.08
0.004	11.32	-9.22	-57.15
0.005	12.77	-11.72	-78.01
0.006	18.65	-13.69	-96.74
0.007	27.66	-15.58	-129.70
0.008	46.65	-17.73	-91.63
0.009	33.16	-20.50	-160.90
0.010	39.69	-22.75	-177.06
0.016	98.12	-43.95	-365.09

Table A1.8. The mean of maximum, minimum and the TACD of the area within the fourth electrode averaged over the number of measurements.

U_g (m/s)	Averaged over 3 repeated measurements		
	Mean(σ^{max})	Mean($\bar{\sigma}_A^f$)	Mean(σ^{min})
0.002	8.79	-4.24	-30.81
0.003	9.19	-7.15	-41.22
0.004	10.98	-9.17	-51.83
0.005	12.68	-11.17	-66.70
0.006	18.41	-12.88	-85.51
0.007	26.44	-15.48	-118.19
0.008	33.07	-17.75	-136.95
0.009	38.08	-20.64	-179.38
0.010	38.93	-23.10	-173.89
0.016	70.06	-46.09	-418.673

ERT images of gas dispersion at lower superficial gas velocity values are displayed in the following figures. When the superficial gas velocity values was 0.009m/s, the following images were obtained.

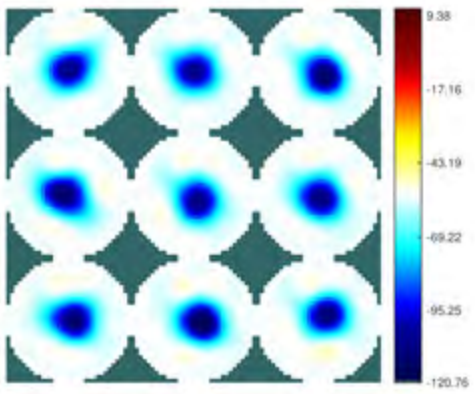

(a)

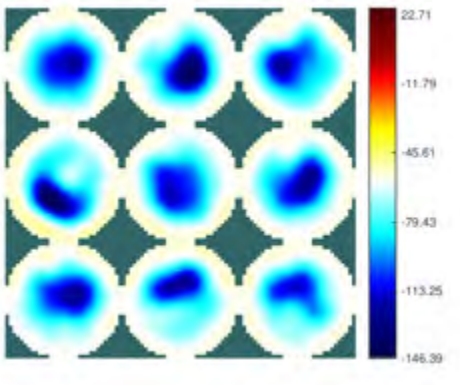

(b)

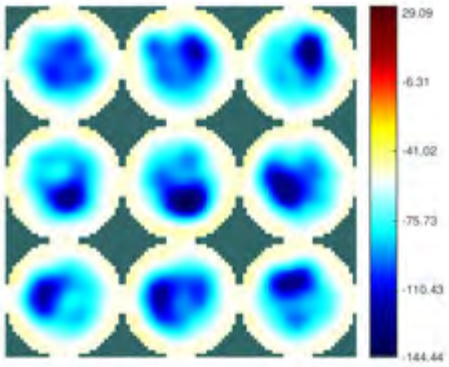

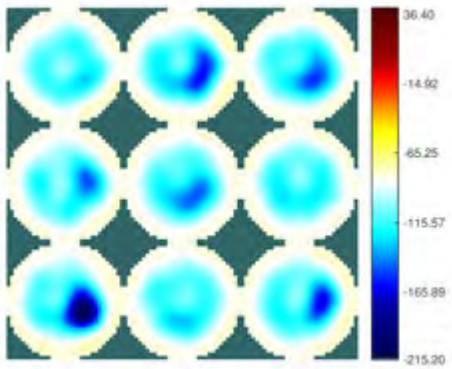

(c) (d)

Figure A1.1. ERT reconstruction of steady state dispersion at the superficial gas velocity of 0.009 m/s at the column cross-sectional area of data captured at 0.636 seconds time interval: (a) first section, (b) second section, (c) third section, (d) fourth section.

For the case of gas volumetric flow rate of 0.008m/s, the reconstructed images of the dispersion are shown below.

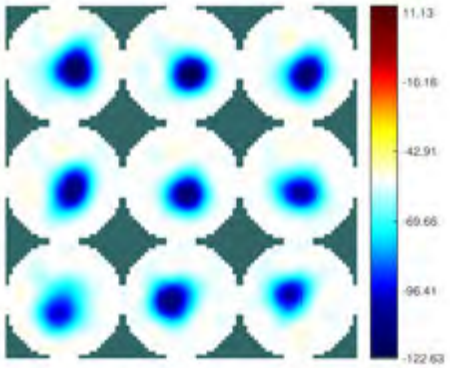

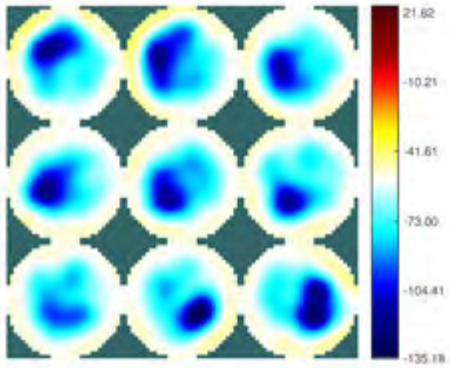

(a) (b)

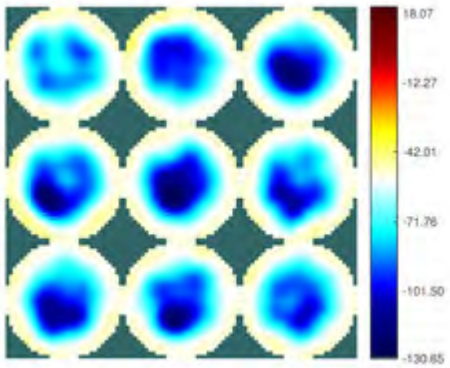

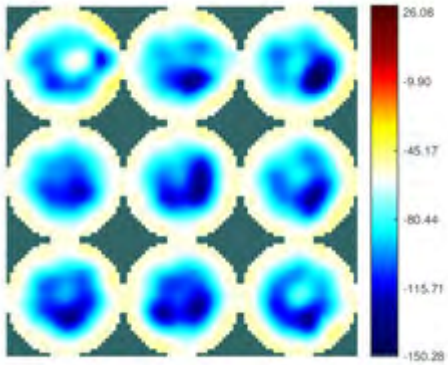

(c) (d)

Figure A1.2. ERT reconstruction of steady state dispersion at the superficial gas velocity of 0.008 m/s at the column cross-sectional area of data captured at 0.636 seconds time interval: (a) first section, (b) second section, (c) third section, (d) fourth section.

When the air inlet was reduced to 0.007m/s, the ERT images of the dispersed phase at target sections of the column are displayed below.

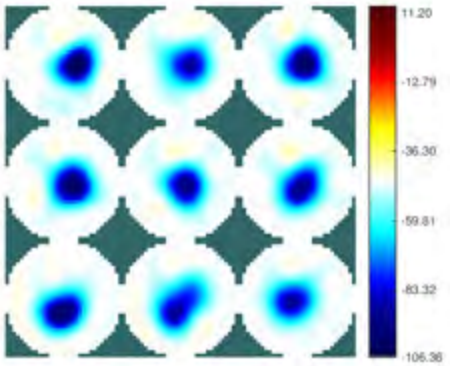

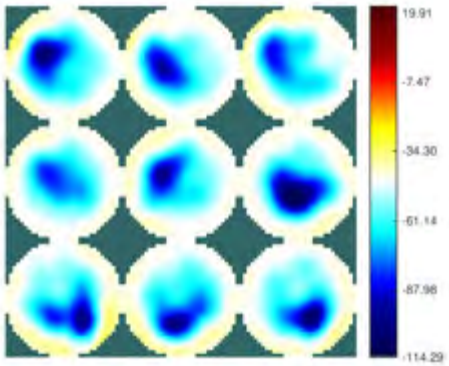

(a) (b)

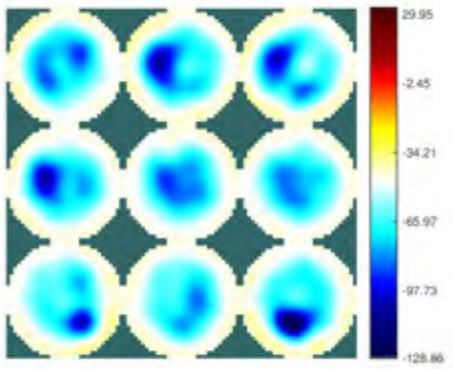

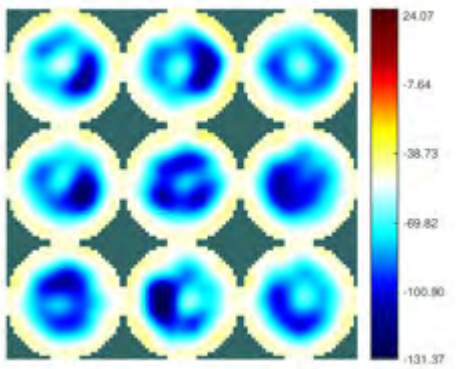

(c) (d)

Figure A1.3. ERT reconstruction of steady state dispersion at the superficial gas velocity of 0.007 m/s at the column cross-sectional area of data captured at 0.636 seconds time interval: (a) first section, (b) second section, (c) third section, (d) fourth section.

When the air inlet was reduced to 0.006m/s, the ERT images of the dispersed phase at target sections of the column are displayed below.

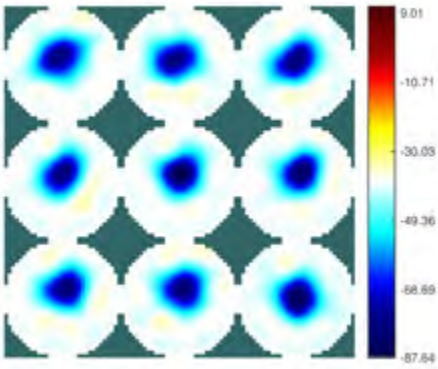

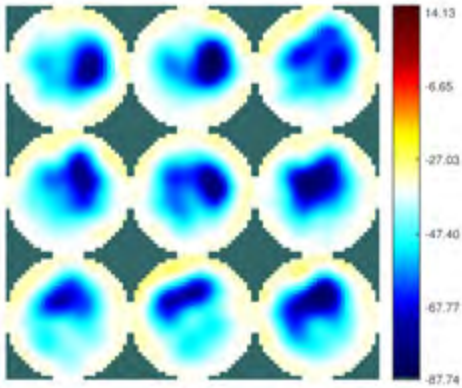

(a) (b)

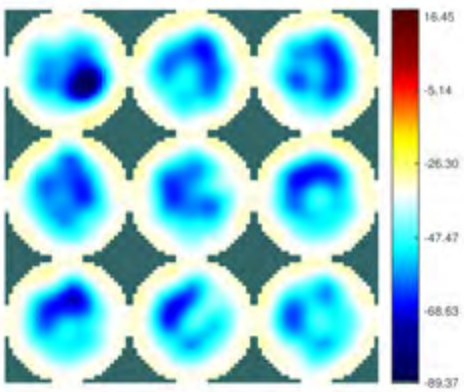

(c)

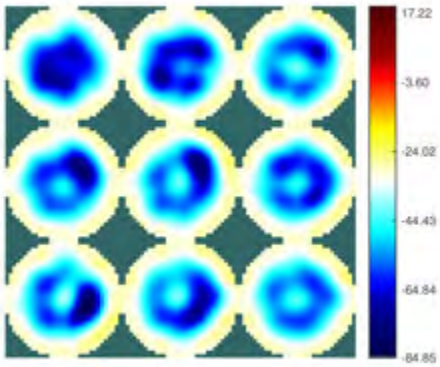

(d)

Figure A1.4. ERT reconstruction of steady state dispersion at the superficial gas velocity of 0.006 m/s at the column cross-sectional area of data captured at 0.636 seconds time interval: (a) first section, (b) second section, (c) third section, (d) fourth section.

The ERT images of the gas phase on further reduction of the gas inlet velocity of 0.005 m/s are presented below.

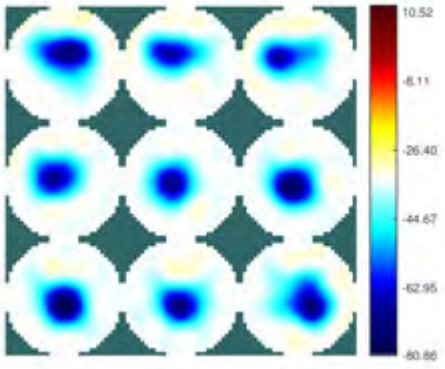

(a)

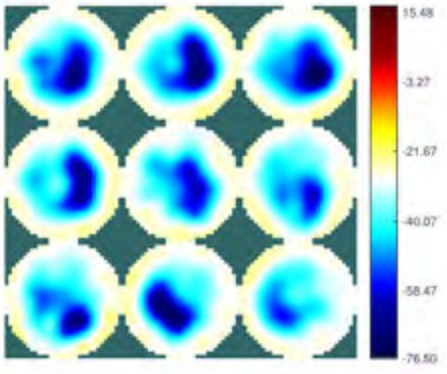

(b)

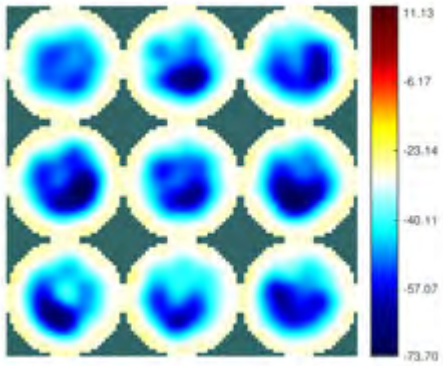

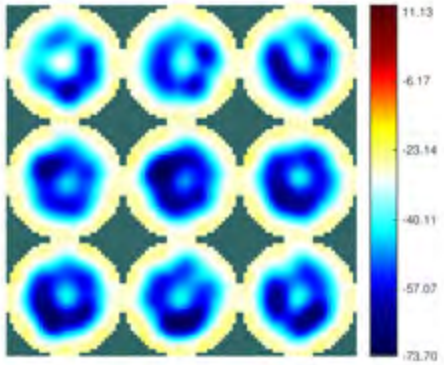

(c)

(d)

Figure A1.5. ERT reconstruction of steady state dispersion at the superficial gas velocity of 0.005 m/s at the column cross-sectional area of data captured at 0.636 seconds time interval: (a) first section, (b) second section, (c) third section, (d) fourth section.

When the inlet gas superficial velocity was reduced to 0.004 m/s, the following images are the scan of the dispersed phase in the continuous water phase.

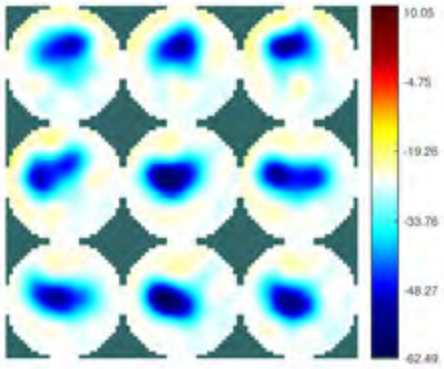

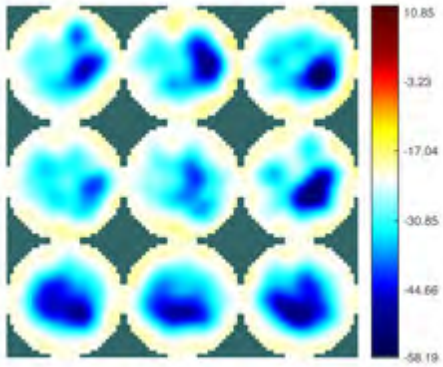

(a)

(b)

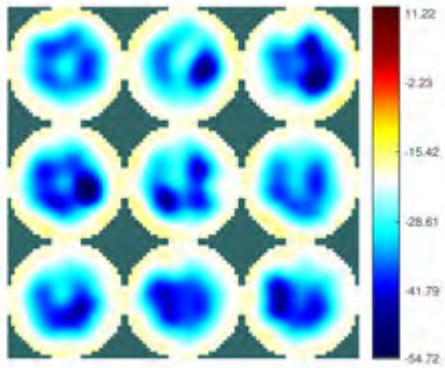

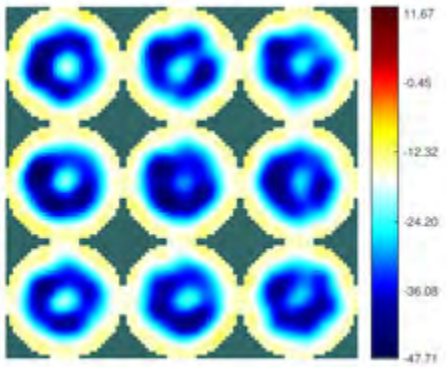

(c)

(d)

Figure A1.6. ERT reconstruction of steady state dispersion at the superficial gas velocity of 0.004 m/s at the column cross-sectional area of data captured at 0.636 seconds time interval: (a) first section, (b) second section, (c) third section, (d) fourth section.

The reconstructed images of the dispersed phase on reducing the superficial gas velocity to 0.003 m/s are shown below.

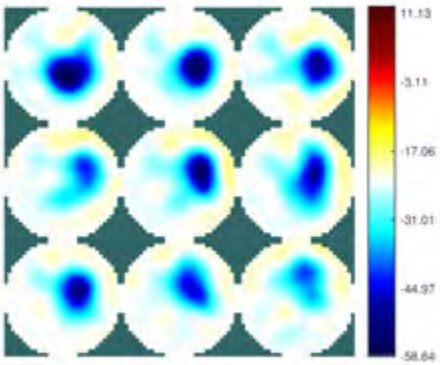

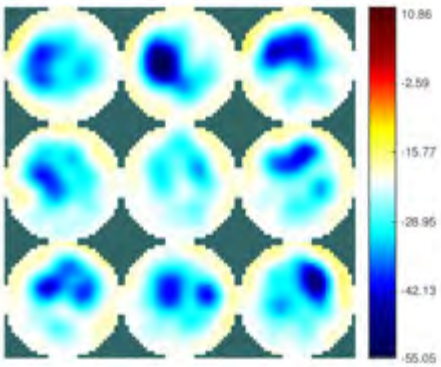

(a)

(b)

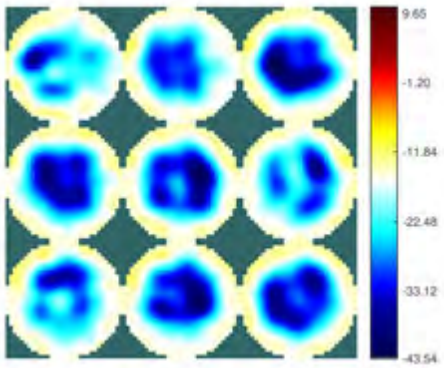

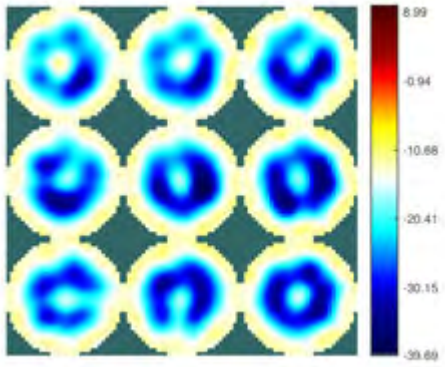

(c) (d)

Figure A1.7. ERT reconstruction of steady state dispersion at the superficial gas velocity of 0.003 m/s at the column cross-sectional area of data captured at 0.636 seconds time interval: (a) first section, (b) second section, (c) third section, (d) fourth section.

For the case of inlet superficial gas velocity of 0.002 m/s, the reconstructed images of the dispersion by the difference ERT algorithm are shown below.

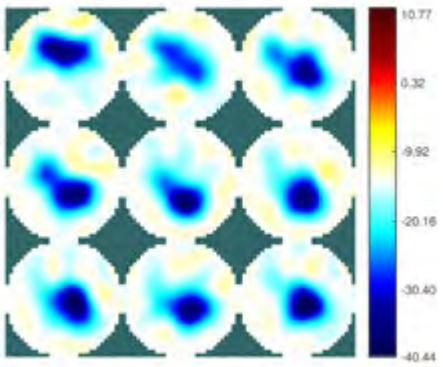

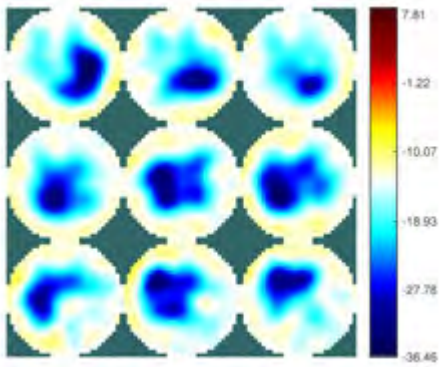

(a) (b)

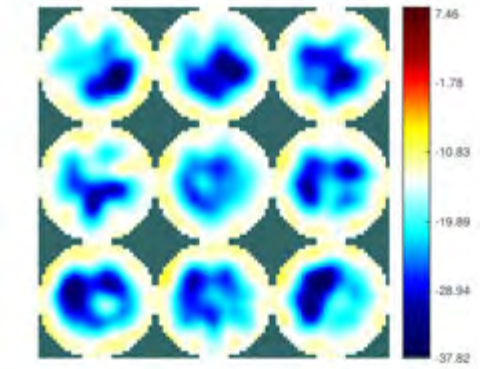

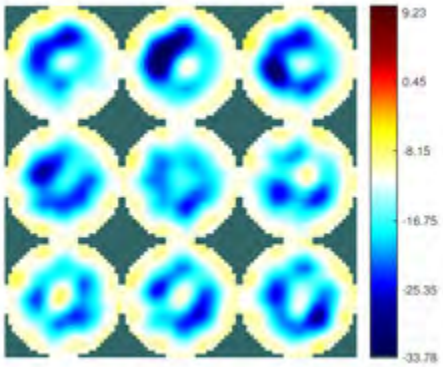

(c) (d)

Figure A1.8. ERT reconstruction of steady state dispersion at the superficial gas velocity of 0.002 m/s at the column cross-sectional area of data captured at 0.636 seconds time interval: (a) first section, (b) second section, (c) third section, (d) fourth section.

The reconstructed images of the continuous water phase before aeration of the fluid system are shown in Figure A1.9.

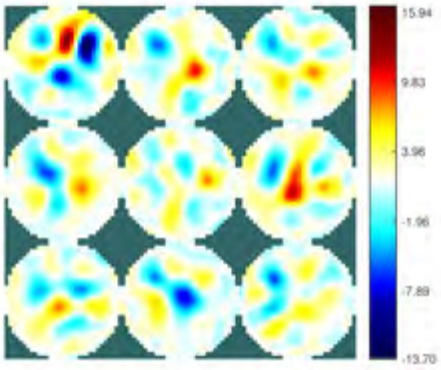

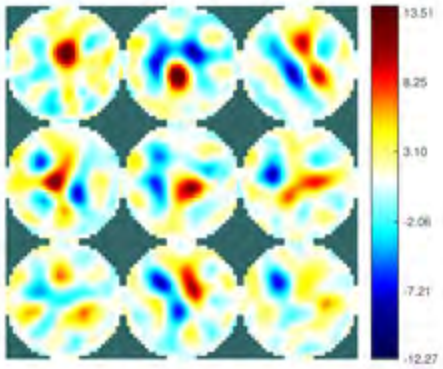

(a) (b)

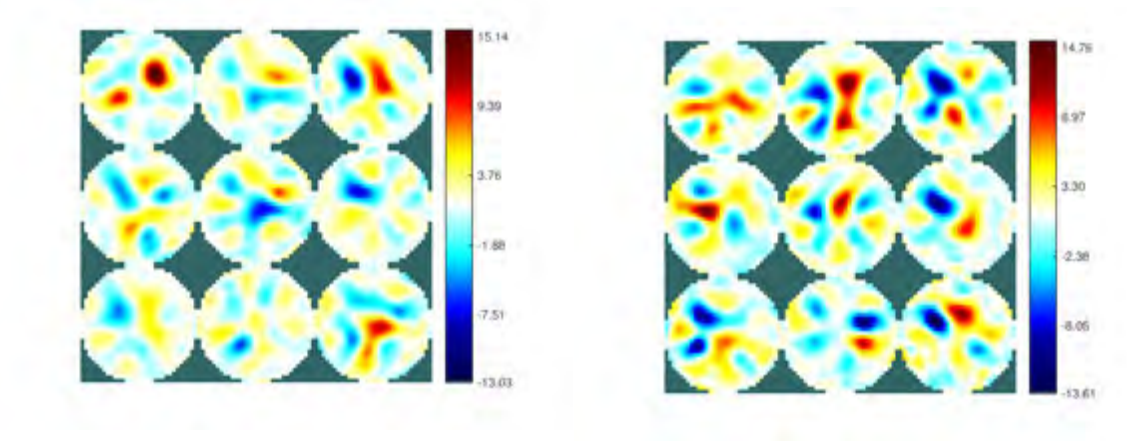

(c) (d)

Figure A1.9. ERT reconstruction of steady state dispersion at the superficial gas velocity of 0 m/s at the column cross-sectional area of data captured at 0.636 seconds time interval: (a) first section, (b) second section, (c) third section, (d) fourth section.

Table A1.9. Local gas void fraction, ε_g(%), as a function of superficial gas velocity (m/s).

u_g(m/s)	ε_g^2 (%)	ε_g^3 (%)	ε_g^4 (%)
H. of section (cm)	23	25	30
0.002	0.58±0.003	0.55±0.003	0.7±0.006
0.003	0.92±0.005	0.93±0.004	1.16±0.001
0.004	1.19±0.005	1.28±0.004	1.53±0.001
0.005	1.30±0.006	1.50±0.004	1.81±0.002
0.006	1.49±0.005	1.70±0.005	2.01±0.002
0.007	1.75±0.006	1.95±0.003	2.30±0.003
0.008	1.91±0.007	2.20±0.003	2.53±0.003
0.009	2.02±0.005	2.30±0.005	2.75±0.004
0.010	2.20±0.006	2.60±0.004	3.08±0.003
0.016	2.70±0.000	4.03±0.003	4.71±0.004

Table A1.10. The ERT mean conductivity difference values at layers 1, 2, 3 and 4 of the electrode arrays.

u_g (m/s)	Mean($\bar{\sigma}_A^f$) layer 1	Mean($\bar{\sigma}_A^f$) layer 2	Mean($\bar{\sigma}_A^f$) layer 3	Mean($\bar{\sigma}_A^f$) layer 4
0.002	-3.61	-3.63	-4.69	-4.24
0.003	-4.80	-5.65	-7.57	-7.15
0.004	-5.79	-7.09	-9.22	-9.17
0.005	-7.64	-10.04	-11.72	-11.17
0.006	-8.23	-10.75	-13.69	-12.88
0.007	-8.99	-11.50	-15.58	-15.48
0.008	-10.86	-13.80	-17.73	-17.75
0.009	-11.91	-16.94	-20.50	-20.64
0.010	-13.37	-17.91	-22.75	-23.10
0.016	-24.50	-35.67	-43.95	-46.09

Table A1.11. Computed ACD from captured ERT data frames with time during DGD process the first, second, third and fourth column sections after the steady state fluid flow at the gas flow rate of 0.016 m/s.

S/N	Ring 1	Ring 2	Ring 3	Ring 4	S/N	Ring 1	Ring 2	Ring 3	Ring 4
1	-16	-23	-30	-32	34	-11	-19	-27	-29
2	-16	-23	-30	-32	35	-11	-18	-27	-28
3	-16	-23	-30	-32	36	-10	-19	-26	-28
4	-15	-23	-30	-32	37	-11	-18	-26	-28
5	-15	-22	-30	-32	38	-10	-18	-26	-28
6	-15	-22	-29	-31	39	-11	-18	-26	-28
7	-15	-22	-28	-31	40	-11	-18	-26	-28
8	-14	-21	-29	-30	41	-11	-18	-26	-28
9	-13	-21	-28	-30	42	-10	-18	-26	-28
10	-14	-21	-28	-30	43	-10	-18	-25	-28
11	-13	-21	-28	-29	44	-11	-18	-26	-28
12	-13	-20	-28	-30	45	-10	-17	-25	-27
13	-12	-21	-28	-30	46	-10	-17	-25	-27
14	-13	-21	-28	-30	47	-11	-18	-25	-27
15	-13	-21	-28	-29	48	-10	-17	-25	-27
16	-13	-20	-28	-30	49	-10	-17	-25	-27
17	-13	-20	-28	-30	50	-10	-17	-24	-27
18	-12	-20	-28	-30	51	-10	-17	-25	-26
19	-12	-20	-28	-30	52	-10	-17	-24	-27
20	-12	-20	-28	-30	53	-10	-16	-24	-26
21	-12	-20	-27	-30	54	-10	-17	-24	-26
22	-12	-20	-27	-30	55	-10	-17	-24	-27
23	-12	-20	-27	-30	56	-10	-17	-24	-26
24	-12	-20	-27	-30	57	-10	-16	-24	-26
25	-11	-20	-27	-30	58	-10	-16	-24	-26
26	-11	-20	-27	-30	59	-10	-16	-24	-26
27	-11	-20	-27	-29	60	-10	-16	-24	-26
28	-11	-20	-27	-29	61	-9	-16	-23	-26
29	-12	-19	-27	-29	62	-9	-16	-23	-26
30	-11	-19	-27	-30	63	-10	-16	-22	-26
31	-11	-19	-27	-29	64	-9	-16	-22	-26
32	-11	-19	-27	-29	65	-9	-16	-22	-25
33	-11	-19	-27	-28	66	-9	-16	-23	-26

S/N	Ring 1 (cnt2.)	Ring 2 (cnt2.)	Ring 3 (cnt2.)	Ring 4 (cnt2.)	S/N	Ring 1 (cnt2.)	Ring 2 (cnt2.)	Ring 3 (cnt2.)	Ring 4 (cnt2.)
67	-9	-16	-22	-26	10	-5	-14	-20	-23
68	-8	-16	-23	-25	10	-5	-13	-20	-23
69	-9	-15	-22	-25	10	-5	-14	-19	-23
70	-9	-16	-22	-25	10	-5	-13	-20	-23
71	-8	-16	-22	-25	10	-5	-13	-20	-23
72	-8	-15	-22	-25	10	-5	-13	-20	-23
73	-8	-15	-21	-25	10	-4	-14	-20	-23
74	-8	-16	-22	-25	10	-4	-13	-20	-22
75	-8	-15	-22	-25	10	-4	-13	-20	-23
76	-8	-15	-22	-24	11	-4	-13	-20	-22
77	-7	-15	-22	-25	11	-4	-13	-20	-22
78	-7	-15	-22	-25	11	-4	-13	-20	-22
79	-7	-15	-22	-24	11	-4	-13	-20	-22
80	-7	-15	-22	-24	11	-4	-13	-20	-22
81	-7	-14	-22	-24	11	-4	-13	-20	-22
82	-7	-15	-22	-24	11	-4	-12	-20	-22
83	-7	-14	-21	-24	11	-4	-12	-20	-22
84	-6	-14	-21	-24	11	-4	-12	-19	-22
85	-6	-14	-21	-24	11	-4	-12	-19	-22
86	-7	-14	-21	-24	12	-4	-12	-20	-22
87	-6	-14	-21	-24	12	-3	-12	-19	-22
88	-6	-14	-21	-24	12	-4	-12	-19	-21
89	-6	-14	-21	-24	12	-3	-12	-19	-21
90	-6	-15	-21	-24	12	-3	-11	-19	-22
91	-6	-14	-21	-24	12	-3	-12	-19	-21
92	-6	-14	-21	-24	12	-4	-11	-19	-22
93	-6	-14	-21	-24	12	-3	-12	-19	-22
94	-6	-14	-21	-24	12	-4	-12	-19	-21
95	-5	-13	-21	-24	12	-4	-12	-18	-21
96	-5	-14	-21	-23	13	-3	-11	-19	-21
97	-5	-14	-20	-24	13	-3	-11	-19	-21
98	-5	-14	-20	-24	13	-3	-11	-19	-21
99	-5	-14	-20	-24	13	-3	-11	-19	-21
100	-5	-14	-20	-23	13	-3	-11	-18	-21

S/N	Ring 1 (cnt3.)	Ring 2(cnt3.)	Ring 3 (cnt3.)	Ring 4 (cnt3.)	S/N	Ring 1 (cnt3.)	Ring 2 (cnt3.)	Ring 3 (cnt3.)	Ring 4 (cnt3.)
135	-3	-11	-19	-20	169		-8	-16	-19
136	-3	-11	-19	-20	170		-8	-16	-19
137	-3	-11	-18	-21	171		-7	-16	-19
138	-2	-11	-18	-20	172		-7	-16	-20
139	-3	-10	-18	-20	173		-7	-16	-20
140	-3	-10	-18	-20	174		-7	-16	-19
141	-3	-10	-18	-20	175		-7	-16	-19
142	-3	-10	-19	-20	176		-7	-16	-20
143	-3	-10	-18	-21	177		-7	-16	-19
144	-2	-10	-18	-20	178		-7	-16	-19
145	-3	-10	-18	-20	179		-7	-16	-19
146		-10	-18	-21	180		-7	-16	-19
147		-9	-18	-21	181		-6	-16	-19
148		-10	-18	-21	182		-6	-15	-19
149		-9	-18	-20	183		-7	-16	-19
150		-9	-17	-20	184		-6	-16	-19
151		-9	-17	-20	185		-6	-15	-19
152		-9	-17	-20	186		-6	-15	-19
153		-9	-17	-20	187		-6	-15	-19
154		-9	-17	-20	188		-6	-15	-19
155		-9	-17	-20	189		-6	-15	-19
156		-9	-17	-20	190		-5	-15	-19
157		-8	-17	-20	191		-6	-15	-19
158		-9	-17	-19	192		-5	-14	-18
159		-8	-17	-20	193		-5	-14	-19
160		-8	-17	-19	194		-6	-14	-19
161		-8	-17	-20	195		-5	-15	-18
162		-8	-17	-19	196		-6	-14	-18
163		-8	-17	-20	197		-5	-14	-18
164		-8	-17	-20	198		-5	-14	-18
165		-8	-16	-19	199		-5	-14	-18
166		-8	-16	-20	200		-5	-14	-18
167		-8	-16	-19	201		-5	-14	-18
168		-8	-16	-20	202		-5	-13	-18

S/N	Ring 1 (cnt4.)	Ring 2 (cnt4.)	Ring 3 (cnt4.)	Ring 4 (cnt4.)	S/N	Ring 1 (cnt4.)	Ring 2 (cnt4.)	Ring 3 (cnt4.)	Ring 4 (cnt4.)
203		-5	-13	-18	237		-3	-10	-17
204		-4	-14	-18	238		-3	-10	-16
205		-5	-13	-18	239		-3	-10	-17
206		-4	-13	-18	240		-2	-10	-16
207		-4	-13	-18	241		-3	-9	-16
208		-5	-13	-17	242		-3	-10	-16
209		-5	-13	-18	243			-9	-16
210		-4	-13	-18	244			-9	-16
211		-5	-12	-17	245			-9	-16
212		-4	-13	-18	246			-9	-16
213		-4	-13	-17	247			-8	-16
214		-4	-13	-18	248			-8	-16
215		-4	-12	-17	249			-9	-16
216		-4	-12	-17	250			-8	-16
217		-4	-12	-17	251			-8	-16
218		-4	-12	-18	252			-8	-16
219		-4	-12	-17	253			-8	-16
220		-4	-12	-17	254			-8	-16
221		-3	-11	-17	255			-8	-16
222		-4	-11	-18	256			-7	-16
223		-4	-11	-17	257			-7	-16
224		-3	-11	-17	258			-7	-16
225		-3	-11	-17	259			-7	-15
226		-3	-11	-17	260			-7	-15
227		-3	-10	-17	261			-7	-15
228		-4	-11	-17	262			-7	-16
229		-2	-11	-17	263			-7	-16
230		-3	-11	-17	264			-7	-15
231		-3	-10	-17	265			-7	-15
232		-3	-10	-17	266			-7	-15
233		-3	-11	-17	267			-6	-15
234		-3	-10	-17	268			-7	-15
235		-3	-10	-17	269			-6	-15
236		-3	-10	-17	270			-6	-15

S/N	Ring 1 (cnt5.)	Ring 2 (cnt5.)	Ring 3 (cnt5.)	Ring 4 (cnt5.)	S/N	Ring 1 (cnt5.)	Ring 1 (cnt5.)	Ring 2 (cnt5.)	Ring 4 (cnt5.)
271			-6	-15	309			-4	-12
272			-6	-15	310			-3	-12
273			-6	-14	311			-3	-11
274			-6	-14	312			-3	-11
275			-6	-14	313			-3	-11
276			-6	-14	314			-3	-11
277			-6	-14	315			-3	-11
278			-5	-14	316			-3	-11
279			-6	-14	317			-3	-11
280			-6	-14	318			-3	-11
281			-5	-14	319			-3	-10
282			-5	-14	320			-3	-10
283			-5	-14	321			-3	-10
284			-5	-14	322			-3	-10
285			-5	-14	323			-3	-10
286			-5	-13	324			-3	-10
287			-5	-13	325			-3	-10
288			-5	-14	326			-3	-9
289			-5	-13	327			-3	-9
290			-4	-13	328			-3	-9
291			-5	-13	329				-9
292			-4	-13	330				-10
293			-4	-13	331				-9
294			-4	-13	332				-9
295			-4	-12	333				-9
296			-4	-13	334				-9
297			-4	-13	335				-9
298			-4	-13	336				-9
299			-4	-13	337				-8
300			-4	-12	338				-9
301			-4	-12	339				-8
302			-4	-13	340				-8
303			-4	-12	341				-8
304			-4	-12	342				-8
305			-3	-13	343				-8
306			-4	-12	344				-8
307			-3	-12	345				-7
308			-4	-12	346				-8

S/N	Ring 1 (cnt6.)	Ring 2 (cnt6.)	Ring 3 (cnt6.)	Ring 4 (cnt6.)	S/N	Ring 1 (cnt6.)	Ring 2 (cnt6.)	Ring 3 (cnt6.)	Ring 4 (cnt6.)
347				-8	385				-4
348				-7	386				-4
349				-7	387				-4
350				-8	388				-4
351				-7	389				-4
352				-7	390				-4
353				-7	391				-4
354				-7	392				-4
355				-7	393				-4
356				-7	3944				-4
357				-7	395				-3
358				-6	396				-3
359				-6	397				-3
360				-6	398				-4
361				-6	399				-3
362				-6	400				-3
363				-6	401				-3
364				-6	402				-3
365				-6	403				-3
366				-6	404				-3
367				-5	405				-3
368				-6	406				-3
369				-5	407				-3
370				-6	408				-3
371				-5	409				-3
372				-6	410				-3
373				-5	411				-3
374				-5	412				-3
375				-5	413				-2
376				-5	414				-3
377				-5	415				-2
378				-5	416				-3
379				-4	417				-2
380				-5	418				-3
381				-5	419				-3
382				-4	420				-3
383				-5	421				
384				-4	422				

Table A1.12. The axially averaged SMBDs, bubble volumes, local BNDD and the axially averaged BNDD of bubble size classes at superficial gas velocity of 0.016 m/s.

$\overline{vol^{b}_{32,}}(r)$ (cm^3)	$\overline{d^{ERT}_{32,J}}$ (cm)	$n^{ERT}_{z,1}(r_j)$ (cm^{-3})	$n^{ERT}_{z,2}(r_j)$ (cm^{-3})	$n^{ERT}_{z,3}(r_j)$ (cm^{-3})	$n^{ERT}_{z,4}(r_j)$ (cm^{-3})	$\bar{n}^{ERT}_{z}(r_j)$ (cm^{-3})
25.85	3.67		1.48	2.99	3.37	2.6
15.98	3.12	5.18	1.48	2.76	5.90	4.1
4.29	2.02	35.31	9.17	6.95	11.09	10.3
4.12	1.99		27.54	18.71	18.08	20.1
2.17	1.61		59.21	44.60	38.85	44.0
0.78	1.14	181.30	99.75	121.22	45.33	77.9
0.51	0.99	206.77	202.84	209.83	93.66	134.2
0.33	0.86	286.10	228.81	260.47	183.82	210.0
0.11	0.60	1680.65	526.95	435.36	283.24	403.4
0.05	0.46	4379.55	772.31	504.88	366.80	584.5
0.03	0.39	6821.87			1033.39	1259.7

Appendix B

Computer code for ERT image reconstruction of gas dispersion

The MATLAB code for image reconstruction of the 2 phase air-water system for the calculation of area average of conductivity distribution at cross sections of the column and gas void fractions by the ERT technique is found in Section 1 of the software file, which is accessible on the web link https://sourceforge.net/projects/bubble-column-model/?source=typ_redirect

Appendix C

Computer code for PBM simulation of bubble swarm at steady state in the direction of axial length of the column

The developed algorithm coded in MATLAB for the simulation of bubble column phenomena depending on bubble size and axial length of the column by the framework of Population Balance Model could be found in Section 2 of the software file, which is accessible on the web link https://sourceforge.net/projects/bubble-column-model/?source=typ_redirect

Appendix D

Computer code for solving the derived mathematical model for advection transport of bubble population in the process of dynamic gas disengagement

The developed algorithm coded in MATLAB for solving the derived mathematical model for the advection transport of bubble population in the process of dynamic gas disengagement is found in Section 3 of the software file that is accessible on the web link https://sourceforge.net/projects/bubble-column-model/?source=typ_redirect

Appendix E

Method of characteristics for solving a model of dynamic gas disengagement

By the method of characteristics, a first order PDE of the form

$$a(t,z)\,{}^{\partial C_j(t,z)}/_{\partial t} + b(t,z)\,{}^{\partial C_j(t,z)}/_{\partial z} = w(t,z) \tag{E.1}$$

for $j = 1,2,3,\dots N$

has a solution $C_j(t,z)$ if at each point (t,z) on the surface of the solution $S = \{t,z,C(t,z))\}$,

$$(a(t,z),b(t,z),w(t,z)) \cdot \left({}^{\partial C_j(t,z)}/_{\partial t}, {}^{\partial C_j(t,z)}/_{\partial z}, -1\right) = 0 \tag{E.2}$$

The normal to the surface S at the point $(t,z,C(t,z))$ is given by $N(t,z) = \left({}^{\partial C_j(t,z)}/_{\partial t}, {}^{\partial C_j(t,z)}/_{\partial z}, -1\right)$. From Eq.(E.2), if the vector $(a(t,z),b(t,z),w(t,z))$ is perpendicular to $\left({}^{\partial C_j(t,z)}/_{\partial t}, {}^{\partial C_j(t,z)}/_{\partial z}, -1\right)$ at each point $\big(t,z,C(t,z)\big)$, then the vector $(a(t,z),b(t,z),w(t,z))$ lies in the tangent plane to S.

By the condition of Eq.(E.2), a solution is sought such that at each point $\big(t,z,C(t,z)\big)$ on the surface of the solution, the vector $(a(t,z),b(t,z),w(t,z))$ lies in the tangent plane. To construct such a solution, a curve C' which lies on the surface is considered. Curve C' is parameterized by s such that at each point on the curve C', the vector $(a(t(s),z(s)),b(t(s),z(s)),w(t(s),z(s)))$ is tangent to the curve.

By this approach, the curve $C' = \{t(s),\ z(s),\ C(t(s),z(s))\}$ will satisfy the following system of ODEs

$$\frac{dt}{ds} = a(t(s),z(s)) \tag{E.3}$$

$$\frac{dz}{ds} = b(t(s),z(s)) \tag{E.4}$$

$$\frac{dC(t(s),z(s))}{ds} = w(t(s),z(s)) \tag{E.5}$$

Curve $C'$of this kind is referred to as integral curve or characteristic curve for the vector $(a(t,z), b(t,z), w(t,z))$ and Eq.(E.3) – Eq.(E.5) are known as characteristic equations.

Accordingly, in order to solve Eq.(7.14) , a search for an integral curve for the vector field

$$\left(a(t,z) = 1, b(t,z) = u_{b,j}(z,t),\ w(t,z) = \left(\frac{1}{\rho_g} \frac{D\rho_g}{D_t} + \frac{\dot{n} a_p}{\alpha_g \rho_g / \mu_g} \right) \partial \left(v' C_j(z,t) \right) \Big/ \partial v \right)$$

associated with the PDE of each bubble class will be made.

Appendix F

ERT measurement sequences for image reconstruction

Table A1.13. Selection of 13 data per stimulation yielding 208 data out of 256 data from 16 current stimulation through adjacent electrodes in a ring. Shaded readings are unused leaving out valid 13 data plotted for each of 16 "u" curves.

S/N	E1 /2	E2 /3	E3 /4	E4 /5	E5 /6	E6 /7	E7 /8	E8 /9	E9 /10	E10 /11	E11 /12	E12 /13	E13 /14	E14 /15	E15 /16	E16 /1
1	■	■														■
2	■	■	■													
3		■	■	■												
4			■	■	■											
5				■	■	■										
6					■	■	■									
7						■	■	■								
8							■	■	■							
9								■	■	■						
10									■	■	■					
11										■	■	■				
12											■	■	■			
13												■	■	■		
14													■	■	■	
15														■	■	■
16	■														■	■

Table A1.14. Selection of 12 data per stimulation yielding 192 data out of 256 data from 16 current stimulation through adjacent electrodes in a ring. Shaded readings are unused leaving out valid 12 data plotted for each of 16 “u” curves.

S/N	E1/2	E2/3	E3/4	E4/5	E5/6	E6/7	E7/8	E8/9	E9/10	E10/11	E11/12	E12/13	E13/14	E14/15	E15/16	E16/1
1	■							■	■							■
2	■	■							■	■						
3		■	■							■	■					
4			■	■							■	■				
5				■	■							■	■			
6					■	■							■	■		
7						■	■							■	■	
8							■	■							■	■
9	■							■	■							■
10	■	■							■	■						
11		■	■							■	■					
12			■	■							■	■				
13				■	■							■	■			
14					■	■							■	■		
15						■	■							■	■	
16							■	■							■	■

Table A1.15. The gas void fraction and their differences along the height of column computed with and without corrected model for the rate of coalescence at discrete axial length in the column.

z_i	ε_i^{Cor} (%)	$\Delta\varepsilon_i^{Cor}$ (%)	ε_i^{Unc} (%)	$\Delta\varepsilon_i^{Unc}$ (%)	z_i	ε_i^{Cor} (%)	$\Delta\varepsilon_i^{Cor}$ (%)	ε_i^{Unc} (%)	$\Delta\varepsilon_i^{Unc}$ (%)
0.000	0.03	0.00	0.03	0.00	0.68	0.03	0.00	0.03	5.24
0.007	0.03	0.00	0.03	0.05	0.71	0.03	0.00	0.03	5.54
0.014	0.03	0.00	0.03	0.10	0.74	0.03	0.00	0.03	5.83
0.022	0.03	0.00	0.03	0.14	0.77	0.03	0.00	0.03	6.14
0.029	0.03	0.00	0.03	0.19	0.81	0.03	0.00	0.03	6.45
0.061	0.03	0.00	0.03	0.41	0.84	0.03	0.00	0.03	6.76
0.094	0.03	0.00	0.03	0.63	0.87	0.03	0.00	0.03	7.07
0.126	0.03	0.00	0.03	0.86	0.90	0.03	0.00	0.03	7.40
0.158	0.03	0.00	0.03	1.09	0.94	0.03	0.00	0.03	7.72
0.191	0.03	0.00	0.03	1.32	0.97	0.03	0.00	0.03	8.06
0.223	0.03	0.00	0.03	1.55	1.00	0.03	0.00	0.03	8.39
0.255	0.03	0.00	0.03	1.79	1.03	0.03	0.00	0.03	8.73
0.288	0.03	0.00	0.03	2.03	1.07	0.03	0.00	0.03	9.08
0.32	0.03	0.00	0.03	2.28	1.10	0.03	0.00	0.03	9.43
0.35	0.03	0.00	0.03	2.53	1.13	0.03	0.00	0.03	9.79
0.39	0.03	0.00	0.03	2.78	1.16	0.03	0.00	0.03	10.15
0.42	0.03	0.00	0.03	3.04	1.19	0.03	0.00	0.03	10.51
0.45	0.03	0.00	0.03	3.30	1.22	0.03	0.00	0.03	10.80
0.48	0.03	0.00	0.03	3.56	1.25	0.03	0.00	0.03	11.09
0.51	0.03	0.00	0.03	3.83	1.27	0.03	0.00	0.03	11.39
0.55	0.03	0.00	0.03	4.11	1.30	0.03	0.00	0.03	11.68
0.58	0.03	0.00	0.03	4.38					
0.61	0.03	0.00	0.03	4.67					
0.64	0.03	0.00	0.03	4.95					

Table A1.16. The local and global SMBD of bubble size in classes at u_g of 0.01m/s.

$d_{32,1,j}$ (cm)	$d_{32,2,j}$ (cm)	$d_{32,3,j}$ (cm)	$d_{32,4,j}$ (cm)	$\overline{d_{32,}}$ (cm)
2.254	2.381	2.860	2.258	2.425
1.427	2.041	2.401	2.004	2.200
0.000	1.787	1.983	1.659	1.619
0.000	1.517	1.677	1.352	1.455
0.000	1.224	1.504	1.104	1.262
1.002	0.954	1.180	0.870	0.987
0.000	0.667	0.884	0.696	0.831
0.000	0.485	0.778	0.603	0.665
0.658	0.381	0.709	0.540	0.543
0.412	0.306	0.629	0.491	0.514
0.000	0.000	0.562	0.440	0.404

Table A1.17. The volume of gas disengaging from local sections of the column at varied time for gas flow at 0.01m/s.

Volume of gas (cm^3) released to atmosphere during DGD vs time (s)							
$t_{1,j}^{GD}$ (s)	$\Delta vol_{1,j}^{g}$ (cm^3)	$t_{2,j}^{GD}$ (s)	$\Delta vol_{2,j}^{g}$ (cm^3)	$t_{3,j}^{GD}$ (s)	$\Delta vol_{3,j}^{g}$ (cm^3)	$t_{4,j}^{GD}$ (s)	$\Delta vol_{4,j}^{g}$ (cm^3)
0.3922	39.59	0.8586	36.39	1.1607	38.47	1.8126	62.78
0.4929	55.79	0.9275	26.13	1.2667	60.72	1.9239	76.09
0.5883	61.94	0.9911	47.32	1.3939	8.26	2.1147	126.63
0.7261	111.32	1.0759	55.29	1.5158	19.57	2.3426	115.12
0.9169	104.79	1.1978	62.37	1.6006	119.16	2.5917	145.85
		1.3568	85.99	1.8073	65.25	2.9203	122.99
		1.6218	92.21	2.0882	60.77	3.2648	93.12
		1.9027	70.65	2.226	49.39	3.5086	55.65
		2.1465	45.52	2.332	53.33	3.7047	41.13
		2.3956	35.18	2.4751	31.82	3.8849	46.80
				2.6182	44.07	4.1075	54.32